UAB
Universitat Autònoma de Barcelona

Nanophotonic Biosensors for Rapid and Precision Diagnostics in Global Infectious Threats

Beatriz Serrano do Couto

ADVERTIMENT. L'accés als continguts d'aquesta tesi queda condicionat a l'acceptació de les condicions d'ús establertes per la següent llicència Creative Commons: https://creativecommons.org/licenses/?lang=ca

ADVERTENCIA. El acceso a los contenidos de esta tesis queda condicionado a la aceptación de las condiciones de uso establecidas por la siguiente licencia Creative Commons: https://creativecommons.org/licenses/?lang=es

WARNING. The access to the contents of this doctoral thesis it is limited to the acceptance of the use conditions set by the following Creative Commons license: https://creativecommons.org/licenses/?lang=en

UAB
Universitat Autònoma
de Barcelona

Doctorat en Bioquímica, Biologia Molecular i Biomedicina

Departament de Bioquímica i Biologia Molecular

Nanophotonic Biosensors for Rapid and Precision Diagnostics in Global Infectious Threats

Doctoral Thesis – 2026

Beatriz Serrano do Couto

Author

Dr. Maria Soler

Director

Prof. Ana Paula Candiota

Tutor

ICN2
Institut Català de Nanociència
i Nanotecnologia

Abstract

This PhD Thesis focuses on the development and analytical validation of nanophotonic biosensors for the rapid, precise molecular diagnosis of infectious diseases of major global health relevance. The increasing emergence of zoonotic pathogens, the global burden of sexually transmitted infections (STIs), and the accelerating spread of antimicrobial resistance (AMR) underscore the need for diagnostic technologies that provide timely, actionable information for surveillance, outbreak preparedness, and clinical decision-making. In this context, label-free photonic biosensors offer a promising approach for decentralized molecular diagnostics, combining high sensitivity, real-time monitoring, and compatibility with future miniaturized point-of-need platforms.

The Thesis addresses two challenges: the surveillance of zoonotic coronaviruses at the animal–human interface, and the diagnosis of bacterial STIs together with resistance-associated genetic markers. Two photonic technologies developed within the NanoBiosensors and Bioanalytical Applications (NanoB2A) group were employed and compared: surface plasmon resonance (SPR) and bimodal waveguide interferometry (BiMW). Both were investigated for the direct, label-free detection of pathogen-specific nucleic acid sequences (RNA and DNA), giving access to clinically and epidemiologically relevant genetic information unattainable through conventional antigen- or antibody-based assays. A major contribution is the establishment of robust nucleic acid biofunctionalization strategies for gold and silicon nitride surfaces—optimizing surface chemistries, probe immobilization, hybridization conditions, and regeneration protocols—providing the stable, reproducible biorecognition interfaces underpinning all subsequent applications.

Building on these advances, biosensor assays were developed for coronavirus RNA targets relevant to human and animal health, including signal amplification, assay transfer between platforms, and validation with synthetic targets, in vitro transcribed RNA, and animal-derived samples. Beyond their analytical performance, these studies demonstrate the applicability of photonic biosensors to wildlife and veterinary surveillance, an area underexplored despite its importance for pandemic preparedness. The work was further extended to bacterial STI pathogens and AMR-associated mutations, with novel assays for *Neisseria gonorrhoeae* and *Chlamydia trachomatis* and for the discrimination of a clinically relevant single-nucleotide mutation linked to ciprofloxacin resistance—showing that photonic biosensors can not only identify infectious agents but also provide genetic information directly relevant to antimicrobial stewardship and precision treatment.

Overall, this Thesis establishes a comprehensive framework for label-free nucleic acid detection with nanophotonic biosensors and demonstrates its versatility across distinct infectious disease applications, advancing photonic biosensing as a complementary diagnostic technology with strong potential for integration into multiplexed, automated, and portable platforms.

Resumen

Esta Tesis Doctoral se centra en el desarrollo y la validación analítica de biosensores nanofotónicos para el diagnóstico molecular rápido y preciso de enfermedades infecciosas de gran relevancia para la salud global. La emergencia de patógenos zoonóticos, la carga mundial de las infecciones de transmisión sexual (ITS) y la propagación de la resistencia a los antimicrobianos (RAM) evidencian la necesidad de tecnologías diagnósticas capaces de proporcionar información oportuna para la vigilancia, la preparación frente a brotes y la toma de decisiones clínicas. En este contexto, los biosensores fotónicos sin marcaje ofrecen una estrategia prometedora para el diagnóstico molecular descentralizado, al combinar elevada sensibilidad, monitorización en tiempo real y compatibilidad con futuras plataformas miniaturizadas de uso en el punto de necesidad.

La Tesis aborda dos retos: la vigilancia de coronavirus zoonóticos en la interfaz animal-humano y el diagnóstico de ITS bacterianas junto con marcadores genéticos de resistencia. Para ello se emplearon y compararon dos tecnologías fotónicas desarrolladas en el grupo de Nanobiosensores y Aplicaciones Bioanalíticas (NanoB2A): la resonancia de plasmón superficial (SPR) y la interferometría de guía de onda bimodal (BiMW). Ambas se investigaron para la detección directa y sin marcaje de secuencias de ácidos nucleicos específicas de patógenos (ARN y ADN), permitiendo acceder a información genética de relevancia clínica y epidemiológica no disponible mediante ensayos convencionales basados en antígenos o anticuerpos. Una de las principales contribuciones es el establecimiento de estrategias robustas de biofuncionalización sobre superficies de oro y nitruro de silicio, optimizando las químicas de superficie, la inmovilización de sondas, las condiciones de hibridación y los protocolos de regeneración.

A partir de estos avances, se desarrollaron ensayos de biosensado para dianas de ARN de coronavirus relevantes para la salud humana y animal, incluyendo amplificación de señal, transferencia entre plataformas y validación con dianas sintéticas, ARN transcrito in vitro y muestras de origen animal. Estos estudios demuestran la aplicabilidad de los biosensores fotónicos en la vigilancia de fauna silvestre y veterinaria, un ámbito poco explorado pese a su importancia para la preparación frente a pandemias. El trabajo se extendió además a patógenos bacterianos causantes de ITS y a mutaciones asociadas a la RAM, con nuevos ensayos para *Neisseria gonorrhoeae* y *Chlamydia trachomatis* y para la discriminación de una mutación de un solo nucleótido asociada a la resistencia a ciprofloxacino.

En conjunto, esta Tesis establece un marco integral para la detección de ácidos nucleicos sin marcaje mediante biosensores nanofotónicos y demuestra su versatilidad en distintas aplicaciones en enfermedades infecciosas, impulsando el biosensado fotónico como tecnología diagnóstica complementaria con potencial para su integración en plataformas multiplexadas, automatizadas y portátiles.

Resumo

Esta Tese de Doutoramento centra-se no desenvolvimento e na validação analítica de biossensores nanofotónicos para o diagnóstico molecular rápido e preciso de doenças infecciosas de grande relevância para a saúde global. A emergência de agentes patogénicos zoonóticos, o peso global das infeções sexualmente transmissíveis (IST) e a propagação da resistência aos antimicrobianos (RAM) evidenciam a necessidade de tecnologias de diagnóstico capazes de fornecer informação atempada para a vigilância, a preparação face a surtos e a tomada de decisões clínicas. Neste contexto, os biossensores fotónicos sem marcação constituem uma abordagem promissora para o diagnóstico molecular descentralizado, combinando elevada sensibilidade, monitorização em tempo real e compatibilidade com futuras plataformas miniaturizadas de utilização no ponto de necessidade.

A Tese aborda dois desafios: a vigilância de coronavírus zoonóticos na interface animal-humano e o diagnóstico de IST bacterianas juntamente com marcadores genéticos de resistência. Para tal, foram utilizadas e comparadas duas tecnologias fotónicas desenvolvidas no grupo de Nanobiossensores e Aplicações Bioanalíticas (NanoB2A): a ressonância de plasmão de superfície (SPR) e a interferometria de guia de onda bimodal (BiMW). Ambas foram investigadas para a deteção direta e sem marcação de sequências de ácidos nucleicos específicas de agentes patogénicos (ARN e ADN), permitindo o acesso a informação genética de relevância clínica e epidemiológica não acessível através de ensaios convencionais baseados em antigénios ou anticorpos. Uma das principais contribuições é o estabelecimento de estratégias robustas de biofuncionalização em superfícies de ouro e nitreto de silício, otimizando as químicas de superfície, a imobilização das sondas, as condições de hibridação e os protocolos de regeneração.

Com base nestes avanços, desenvolveram-se ensaios de biossensorização para alvos de ARN de coronavírus relevantes para a saúde humana e animal, incluindo amplificação de sinal, transferência entre plataformas e validação com alvos sintéticos, ARN transcrito in vitro e amostras de origem animal. Estes estudos demonstram a aplicabilidade dos biossensores fotónicos na vigilância de fauna selvagem e veterinária, uma área pouco explorada apesar da sua importância para a preparação face a pandemias. O trabalho foi ainda alargado a agentes patogénicos bacterianos causadores de IST e a mutações associadas à RAM, com novos ensaios para *Neisseria gonorrhoeae* e *Chlamydia trachomatis* e para a discriminação de uma mutação de um único nucleótido associada à resistência à ciprofloxacina.

Globalmente, esta Tese estabelece um quadro abrangente para a deteção de ácidos nucleicos sem marcação através de biossensores nanofotónicos e demonstra a sua versatilidade em diferentes aplicações em doenças infecciosas, impulsionando a biossensorização fotónica como tecnologia de diagnóstico complementar com potencial para integração em plataformas multiplexadas, automatizadas e portáteis.

Acknowledgements

This thesis is the result of several years of work, learning, challenges, and personal growth. Along the way, many people contributed to this journey in different ways, through their guidance, support, knowledge, friendship, and encouragement. I would like to express my sincere gratitude to all those who were part of this important chapter.

I would like to begin by expressing my deepest gratitude to Dr. Maria Soler, my thesis director, for giving me the opportunity to enter this field during my Master's degree and for trusting me to continue this work as a PhD student. Her guidance has been fundamental throughout the development of this thesis and has greatly shaped the way I approach science, research, and problem-solving.

I am especially grateful for her constant support, availability, and dedication during these years. Maria was always there when I needed advice, motivation, or direction, particularly in moments when I felt lost or uncertain. I deeply appreciate the thoughtful balance with which she guided me: she knew when to challenge me and help me improve, but also when to recognise my efforts and encourage me to keep moving forward. Her clear, objective, and constructive perspective often helped me regain confidence, organise my thoughts, and find the best way to continue.

I am profoundly thankful for her generosity, commitment, and patience, as well as for the time and care she devoted to this work, even during particularly demanding moments in her own life. Her passion for science, her professional achievements, and her organised and thoughtful way of working have been a true source of inspiration. I deeply admire not only the scientist she is, but also the way she combines ambition, dedication, kindness, and humanity. I feel very fortunate to have had her as my supervisor and to have learned from her during these years.

I would also like to sincerely thank Prof. Laura Lechuga for giving me the opportunity to carry out my doctoral research within the NanoB2A group. Being part of this group allowed me to work in a highly stimulating scientific environment and to learn from a team with great experience in the field of optical biosensors. I am very grateful for the opportunity to develop this thesis in such an inspiring and multidisciplinary research setting.

I would also like to acknowledge all the collaborators involved in the CoNVat, MUSECV, and TYPLEX projects, whose contributions were essential to the work presented in this thesis.

I am thankful to all the members of the NanoB2A group, past and present: Mari Carmen, Jessica, Ju, Patri, Jhonattan, Eloy, Celia, Andres, Raquel, Piotr, Jordi, Sofia, Bárbara, Alejandro, Mari Cruz, Olalla, Pablo, Cristina, Victor, Marta, and Mehdi, for sharing this journey with me. Thank you for your help in the laboratory, for sharing your knowledge, experience, and different perspectives, and for the conversations, laughter, and small moments that made everyday work more enjoyable. A special thanks to Razia for the coffees, the conversations, and the companionship during many long days in the lab.

To my friends in Barcelona, thank you for becoming my family away from home. Thank you for all the “planazos”, for your support, and for making these years so much more special. Thank you for making this city feel more like home. You were an important part of this journey, far beyond the thesis.

To my friends in Portugal, thank you for staying close despite the distance. Thank you for the messages, calls, visits to Barcelona, and for never letting time or distance weaken our friendship. Your presence, even from far away, reminded me of where I come from and of the people who have been with me since the beginning.

Finally, I would like to thank my entire family and João for their unconditional love, patience, and support throughout this journey. I could not have reached this point without you. Thank you for always being there, for encouraging me during the moments when I felt tired, frustrated, or unsure of myself, and for reminding me that I was capable of reaching the end. Your visits, care, motivation, and constant presence gave me strength when I needed it most. This thesis would not have been possible without your love and support.

To everyone who has been part of this path, in any way, thank you.

Table of contents

Abstract ..... **i**

Resumen ..... **ii**

Resumo ..... **iii**

Acknowledgements ..... **iv**

1. Introduction **9**

1.1. Global Burden of Emerging & Antimicrobial-Resistant Infectious Diseases 9

1.1.1. Emerging viral threats 10

1.1.2. Bacterial Infections and antimicrobial resistance (AMR) 12

1.2. Current Diagnostic Technologies: Strengths and Limitations 13

1.2.1. Molecular Diagnostics 14

1.2.2. Rapid Antigen and Serological Tests 16

1.2.3. Culture-based Methods 17

1.3. Biosensors for Precision and Point-of-Care Applications 19

1.3.1. Plasmonic biosensor technologies 21

1.3.2. Silicon-photonic biosensing technologies 28

2. Motivation and objectives **35**

3. Materials and Methods **38**

3.1. Surface Plasmon Resonance (SPR) platform 38

3.1.1. SPR experimental set-up 38

3.1.2. SPR sensor chips fabrication and cleaning 39

3.2. Bimodal Waveguide (BiMW) Interferometer platform 40

3.2.1. BiMW experimental set-up 40

3.2.2. BiMW sensor chips fabrication and cleaning 41

3.3. Chemical reagents and biological materials 42

3.4. Sensor biofunctionalization protocols 43

3.4.1. Gold-based surface biofunctionalization 43

3.4.2. Silicon-based surface biofunctionalization 43

3.5. Hybridization assays 44

3.6. Data analysis and statistics 44

4. Development of nucleic acid-based photonic biosensors **47**

4.1. Fundamentals of Nucleic Acid Hybridization Assays 47
4.2. Target selection and probe design considerations 48
4.2.1. Target selection 48
4.2.2. DNA probe design 49
4.3. Sensor Surface Biofunctionalization 50
4.3.1. Gold-based sensor surfaces 52
4.3.2. Silicon-based sensor surfaces 56
4.4. Hybridization assay 68
4.5. Conclusions 71
5. Photonic biosensors for screening of zoonotic coronaviruses 74
5.1. Zoonotic viruses and surveillance strategies 74
5.2. Target selection and probe design 76
5.3. SPR biosensor for CoV RNA detection 78
5.3.1. Biofunctionalization of the sensor surface 79
5.3.2. Hybridization buffer optimization 79
5.3.3. Sensitivity and specificity of SPR coronavirus RNA detection 81
5.3.4. Signal amplification of CoV RNA 86
5.3.5. Preliminary validation with real animal samples 90
5.4. BiMW biosensor for CoV RNA detection 91
5.4.1. Biofunctionalization of the sensor surface 91
5.4.2. Direct detection of synthetic coronavirus RNA targets 92
5.4.3. In vitro transcribed (IVT) RNA analysis 94
5.4.4. Validation with animal samples 96
5.5. Summary and conclusions 100
6. Photonic biosensors for screening of sexually transmitted bacteria and antibiotic resistance 103
6.1. STI Epidemiology and antimicrobial resistance challenges 103
6.2. Target selection and probe design 105
6.3. BiMW biosensor for bacterial DNA detection 107
6.3.1. Sensor biofunctionalization and assay optimization 107
6.3.2. Detection of *N. gonorrhoeae* and *C. trachomatis* synthetic DNA targets 109
6.3.3. Detection of antibiotic resistance in *N. Gonorrhoea*e DNA 111
6.3.4. Validation in real cells 114
6.4. Conclusions 120

7. General conclusions and future perspectives 123

A. Annex 128

A.1. Introduction 128

A.2. Optimization of the APTES silanization route 128

A.3. Optimization of the crosslinking chemistry 129

A.4. Analytical comparison of the optimized configurations 130

A.5. Conclusions 131

Publications 132

Abbreviations and Acronyms 134

List of figures 139

List of tables 146

Bibliography 147

Nanophotonic Biosensors for Rapid and Precision Diagnostics in Global Infectious Threats

Chapter 1

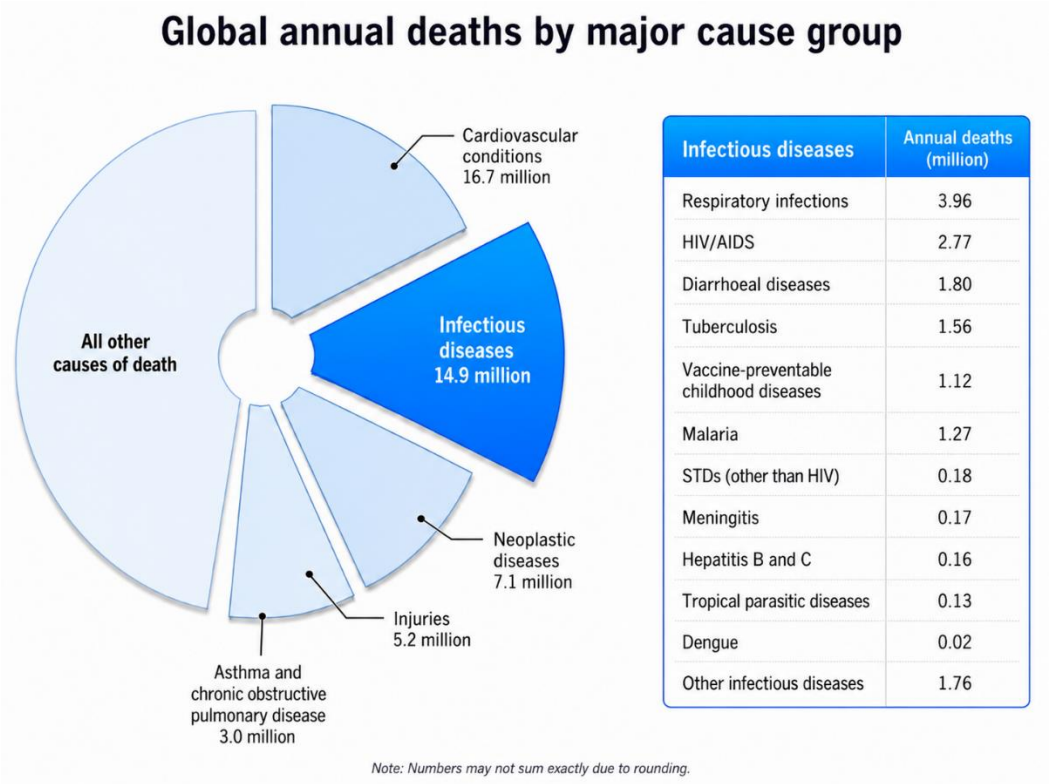
INTRODUCTION

This chapter provides a general introduction to the global burden of infectious diseases, mainly focusing on the role of biosensor devices as rapid diagnostic tools in the clinical and biomedical environment. After a brief overview of the most pressing emerging viral threats and of the growing problem of antimicrobial-resistant bacterial infections, the current diagnostic technologies are reviewed, pointing out their strengths and limitations for clinical practice and point-of-care settings. Special attention is given to biosensors as a promising alternative for precision and decentralized diagnostics, and in particular to label-free optical biosensors. Finally, we discuss plasmonic and silicon-photonic biosensing technologies, highlighting their principles, advantages, and potential for the rapid and sensitive detection of infectious agents.

1. Introduction

1.1. Global Burden of Emerging & Antimicrobial-Resistant Infectious Diseases

Infectious diseases have historically shaped human civilisation and remain a leading cause of morbidity and mortality worldwide. Despite substantial advances in public health, including vaccination programmes, antimicrobial therapies, improved sanitation, and diagnostic technologies, they continue to account for an estimated 10–13 million deaths per year globally.[1] As illustrated in **Figure 1.1**, infectious diseases collectively remain the third leading cause of death globally, behind cardiovascular disease and cancer, and the leading cause in low- and middle-income countries (LMICs). Lower respiratory infections, tuberculosis (TB), HIV/AIDS, and diarrhoeal diseases consistently rank among the leading infectious killers: in 2023 alone, lower respiratory infections were responsible for approximately 2.5 million deaths, TB for around 1.4 million, and AIDS-related illnesses for approximately 630,000.[2,3]



Infectious diseases	Annual deaths (million)
Respiratory infections	3.96
HIV/AIDS	2.77
Diarrhoeal diseases	1.80
Tuberculosis	1.56
Vaccine-preventable childhood diseases	1.12
Malaria	1.27
STDs (other than HIV)	0.18
Meningitis	0.17
Hepatitis B and C	0.16
Tropical parasitic diseases	0.13
Dengue	0.02
Other infectious diseases	1.76

Figure 1.1 Worldwide leading causes of death.

The burden is profoundly unequal. In low-income countries, infectious diseases account for nearly 44% of all deaths, driven by structural determinants including limited healthcare infrastructure, inadequate sanitation, and restricted access to vaccines and therapeutics.[4] However, infectious diseases are not restricted to resource-limited settings. Population ageing, global travel, urban density, and the accelerating emergence of antimicrobial resistance ensure that high-income countries remain substantially exposed. The COVID-19

pandemic made this explicitly clear: with over 770 million confirmed cases and more than 7 million reported deaths globally, it caused healthcare system collapse in some of the world's wealthiest nations and generated profound societal disruption, from healthcare system overload and interrupted essential services to lasting health sequelae in millions of survivors. But COVID-19 is not an isolated event; it is the most recent in a long series of infectious disease crises that have demonstrated how rapidly a localized outbreak can escalate into a global emergency.[5]

In recognition of this persistent threat, the WHO consistently identifies infectious diseases as a central priority in the global health agenda. Among its top ten global health threats, a substantial proportion relate directly to infectious pathogens, including pandemic influenza, novel respiratory viruses, and antimicrobial resistance.[6] Between 1996 and 2023, WHO emergency event reports documented over 3,000 outbreak events worldwide reflecting not only the breadth of the infectious disease landscape but also its accelerating complexity.[7] Two threats in particular stand out for their epidemic and pandemic potential: the emergence of novel zoonotic viruses and the global rise of antimicrobial-resistant bacteria.

1.1.1. Emerging viral threats

The emergence of novel viral pathogens represents one of the most significant challenges to global health security. Most emerging infectious diseases, approximately 60% of all known and up to 75% of newly emerging human pathogens, are zoonotic in origin, arising from animal reservoirs that collectively harbour an estimated 540,000 to 850,000 viruses with potential to infect humans, the vast majority uncharacterised.[8,9] RNA viruses are disproportionately represented among these threats, a consequence of their error-prone replication: lacking proofreading activity, RNA-dependent RNA polymerases generate mutation rates of 10^{-4} to 10^{-6} substitutions per nucleotide per cycle, sustaining a continuous pool of variants, referred to as a *quasispecies*, from which mutants with altered host tropism, transmissibility, or immune evasion are rapidly selected. In segmented RNA viruses, genetic reassortment between co-infecting strains can generate novel phenotypes abruptly, as occurs in influenza; in non-segmented RNA viruses, recombination fulfils a similar role. Together, these mechanisms give RNA viruses an exceptional capacity to cross species barriers and establish in new host populations.[10,11]

The COVID-19 pandemic, caused by SARS-CoV-2, is the defining example of this threat in the contemporary era. A *betacoronavirus* of likely bat origin, SARS-CoV-2 binds the human angiotensin-converting enzyme 2 (ACE2) via its spike protein (S) receptor-binding domain, with cellular entry further facilitated by a polybasic furin cleavage site at the S1/S2 boundary.[12–15] Seeded globally within weeks through international travel networks, it caused over 7 million recorded deaths, substantially more when excess mortality is considered, and infection fatality rates approximately twice as high in LMICs as in high-income nations.[16–19] Beyond its direct health toll, the pandemic contracted global gross domestic product (GDP) by an estimated 3.4% in 2020 alone,[20] with total economic losses projected at USD 13 trillion,[4] reflecting the cascading consequences of supply chain disruption, healthcare system overload, and the absence of rapid detection capacity in the critical early phase of emergence. The sequential emergence of variants of concern carrying spike

mutations that altered transmissibility and immune evasion further demonstrated that pandemic management cannot assume a static pathogen.[21] COVID-19, however, is only the latest in a series of zoonotic emergences that have repeatedly overwhelmed unprepared health systems. Other notable examples of viruses that have caused, or continue to pose, significant epidemic or pandemic threats include:

Influenza A viruses, whose capacity for antigenic shift and reassortment enables the periodic generation of pandemic strains. H5N1, recently detected in North American dairy cattle, causes sporadic human infections with a case-fatality rate exceeding 60%,[22,23] while seasonal influenza causes approximately 5 million severe cases and up to 650,000 deaths annually.[24]

Ebola virus (EBOV, *Filoviridae*), with case-fatality rates of 25–90% and recurrent outbreaks in sub-Saharan Africa.[25] The 2014–2016 West African epidemic caused over 28,600 cases and 11,000 deaths, the largest in recorded history.[26]

Nipah virus (NiV, *Henipavirus*), a bat-borne paramyxovirus causing severe encephalitis with a case-fatality rate of 40–75%, documented human-to-human transmission, and no approved vaccine or antiviral.[27]

Dengue virus (DENV), endemic in over 100 countries and placing half the global population at risk. Sequential infection with different serotypes can precipitate severe disease through antibody-dependent enhancement (ADE).[28] The 2023 season was the largest on record, with over 5 million cases and 5,000 deaths.[29]

Zika virus (ZIKV), whose 2015–2016 outbreak across the Americas was linked to congenital microcephaly and Guillain–Barré syndrome, prompting a WHO-declared public health emergency of international concern across 86 countries and territories.[30]

Chikungunya virus (CHIKV) and other arboviruses, whose geographic ranges have expanded significantly with climate-driven shifts in *Aedes* mosquito distribution, establishing transmission in previously non-endemic regions of Europe and the Americas.[31]

Mpox virus (MPXV), which caused another WHO-declared public health emergency of international concern in 2022 and 2024, demonstrating sustained human-to-human transmission well beyond its historical endemic range in Central and West Africa.[32]

Indeed, even as these lines are being written, the world is witnessing a confirmed hantavirus outbreak aboard a cruise ship, already associated with fatalities and cases involving individuals from multiple nationalities, further underscoring the persistent global threat posed by zoonotic pathogens.[33]

The increasing frequency of such emergence events reflects the systematic expansion of anthropogenic pressures that erode the ecological barriers between human populations and wildlife reservoirs. Deforestation and agricultural intensification bring humans and livestock into sustained contact with previously isolated reservoir species; rapid urbanization concentrates populations in conditions favourable to amplification and spread; and the international trade in live animals creates high-density interspecies

interfaces that can seed novel pathogens globally before their significance is recognized. Climate change compounds all of these drivers by reshaping the distribution of both reservoir hosts and arthropod vectors, extending the range of dengue- and Zika-transmitting *Aedes* mosquitoes into previously temperate regions and altering seasonal transmission windows.[34] Mathematical modelling indicates that the frequency of emerging disease events has increased significantly over the past century and is likely to continue, with estimates of a substantial probability of future pandemic events comparable to or exceeding COVID-19 within the coming decades.[35]

Addressing this trajectory requires moving from reactive outbreak response to proactive, risk-targeted surveillance. This is the central ambition of the One Health framework, which recognises that human, animal, and environmental health must be monitored and managed in an integrated manner. Critical to this ambition is the availability of rapid, sensitive, and field-deployable diagnostic tools capable of detecting and characterising novel pathogens at the earliest stages of emergence, in the geographic settings where spillover occurs and before centralised laboratory infrastructure can be mobilised. It is precisely this diagnostic gap that the present work seeks to address.[36,37]

1.1.2. Bacterial Infections and antimicrobial resistance (AMR)

Bacterial pathogens are directly responsible for an estimated 7.7 million deaths annually, and a growing proportion of this burden is driven by antimicrobial resistance (AMR).[38] In 2019, AMR was directly attributable to 1.27 million deaths and associated with a further 4.95 million,[39] placing it among the leading infectious causes of death globally. Without effective intervention, projections forecast approximately 1.91 million attributable deaths per year by 2050.[40] Beyond mortality, resistant infections add an average of 7.4 days to hospital stays and nearly double the risk of in-hospital mortality compared to susceptible infections.[41] At the system level, AMR is estimated to cost the global healthcare system USD 412 billion annually in additional treatment costs, alongside USD 443 billion in lost productivity,[42] with the World Bank projecting GDP losses of USD 1–3.4 trillion per year by 2030 if current trends continue.[43]

AMR arises when bacteria evolve mechanisms that render antimicrobial agents ineffective. At the molecular level, this occurs through spontaneous chromosomal mutations that alter antibiotic targets, or through the acquisition of resistance genes via horizontal gene transfer (HGT) mediated by mobile genetic elements such as plasmids, transposons, and integrons. The latter is of particular concern because these elements frequently carry multiple resistance determinants simultaneously and can disseminate across unrelated bacterial species, enabling rapid and broad resistance spread.[44,45] The main resistance mechanisms include:

Enzymatic inactivation of antibiotics, most critically by extended-spectrum beta-lactamases (ESBLs, e.g., CTX-M, SHV), which hydrolyse penicillins and cephalosporins, and by carbapenemases (KPC, NDM-1, OXA-type), which additionally inactivate carbapenems, the last-resort beta-lactam class.[46–48]

Target site modification, including mutations in *gyrA* and *parC* conferring fluoroquinolone resistance, mutations in *rpoB* underlying rifampicin resistance in *Mycobacterium*

tuberculosis, and acquisition of *mecA* in *Staphylococcus aureus*, encoding PBP2a, a modified penicillin-binding protein with reduced beta-lactam affinity that defines the methicillin-resistant S. *aureus* (MRSA) phenotype.[49,50]

Reduced antibiotic accumulation, through overexpression of efflux pumps that actively expel drugs from the cell and downregulation of outer membrane porins that limit entry, frequently acting in combination to produce high-level multidrug resistance.

These mechanisms can act individually or in combination, giving rise to multidrug-resistant (MDR), extensively drug-resistant (XDR), or pan-drug-resistant (PDR) phenotypes for which few or no treatment options remain.

The WHO Bacterial Priority Pathogens List classifies the organisms of greatest clinical concern across critical, high, and medium priority tiers.[51] Carbapenem-resistant *Enterobacterales* (particularly *Klebsiella pneumoniae* and *Escherichia coli*), carbapenem-resistant *Acinetobacter baumannii*, MRSA, and rifampicin-resistant *M. tuberculosis* lead the critical tier, collectively responsible for the majority of AMR-attributable deaths and a disproportionate share of healthcare expenditure worldwide. Among community-acquired pathogens, *Neisseria gonorrhoeae* was recently classified as high priority: having developed resistance to successive antibiotic classes and showing emerging resistance to third-generation cephalosporins, its current last-line treatment.[52]

A central driver of both the clinical and economic burden of AMR is the absence of rapid diagnostics at the point of care. Without timely identification of the causative pathogen and its resistance profile, clinicians' default to empirical broad-spectrum therapy, sustaining the selective pressure that accelerates resistance, while standard culture-based susceptibility testing requires 24 to 72 hours and is unavailable in most primary care or resource-limited settings. The WHO has identified rapid, point-of-care diagnostics as a strategic priority in AMR control, recognising that new antibiotics alone cannot address resistance without the infrastructure to guide their appropriate use. Developing sensitive, specific, and accessible diagnostic platforms capable of identifying resistant pathogens within minutes is therefore both a clinical and public health imperative, and a central motivation for the work presented in this thesis.[53]

1.2. Current Diagnostic Technologies: Strengths and Limitations

Accurate, timely, and accessible diagnostics are central to the effective management and control of infectious diseases. Diagnostic technologies guide clinical decision-making, enable appropriate treatment selection, support epidemiological surveillance, and are essential for outbreak containment. Over recent decades, substantial advances have been made in diagnostic methodologies, ranging from conventional culture-based techniques to highly sensitive molecular assays and rapid point-of-care tests.[54]

Despite this progress, no single diagnostic approach fully meets the demands of modern infectious disease management. Key challenges persist, including the need for rapid turnaround times, high sensitivity and specificity, multiplexing capability, affordability, and adaptability to decentralized or resource-limited settings. The growing complexity of infectious threats, particularly the emergence of novel viruses and the global rise of AMR

bacteria discussed in the previous section, has further exposed important limitations in current diagnostic paradigms.

This section provides an overview of the principal diagnostic technologies currently used in clinical microbiology, namely molecular diagnostics, rapid antigen and serological tests, and culture-based methods, highlighting their strengths as well as their inherent limitations.

1.2.1. Molecular Diagnostics

Molecular diagnostics encompasses a broad range of techniques that detect pathogens through the identification of specific nucleic acid sequences. Unlike traditional methods based on pathogen culture or antigen detection, molecular approaches exploit the unique genetic signatures of microorganisms, enabling highly specific identification at the species, subtype, or even strain level.[54,55]

Nucleic acid-based detection offers several intrinsic advantages. First, genomic sequences provide unparalleled molecular specificity, allowing discrimination between closely related organisms. Second, enzymatic amplification enables the detection of extremely low amounts of pathogen-derived material, often down to a few copies per reaction. This is particularly important in early-stage infections, asymptomatic carriers, and samples with low pathogen load.

Among these technologies, the polymerase chain reaction (PCR) and its variants remain the cornerstone of molecular diagnostics (**Figure 1.2**). PCR relies on cyclic enzymatic amplification of target DNA sequences using sequence-specific primers. Through repeated cycles of denaturation, annealing, and extension, target sequences are exponentially amplified, allowing highly sensitive detection.

For RNA pathogens, particularly relevant in the context of emerging viruses, reverse transcription PCR (RT-PCR) is employed, in which viral RNA is first converted into complementary DNA (cDNA) prior to amplification. Quantitative real-time PCR (qPCR) further enhances this approach by incorporating fluorescent probes or dyes, enabling real-time monitoring of amplification and providing both qualitative and quantitative information on pathogen load. These features have established qPCR as the gold standard for the

detection of numerous viral and bacterial infections, including respiratory viruses, bloodstream infections, and sexually transmitted pathogens.[56]

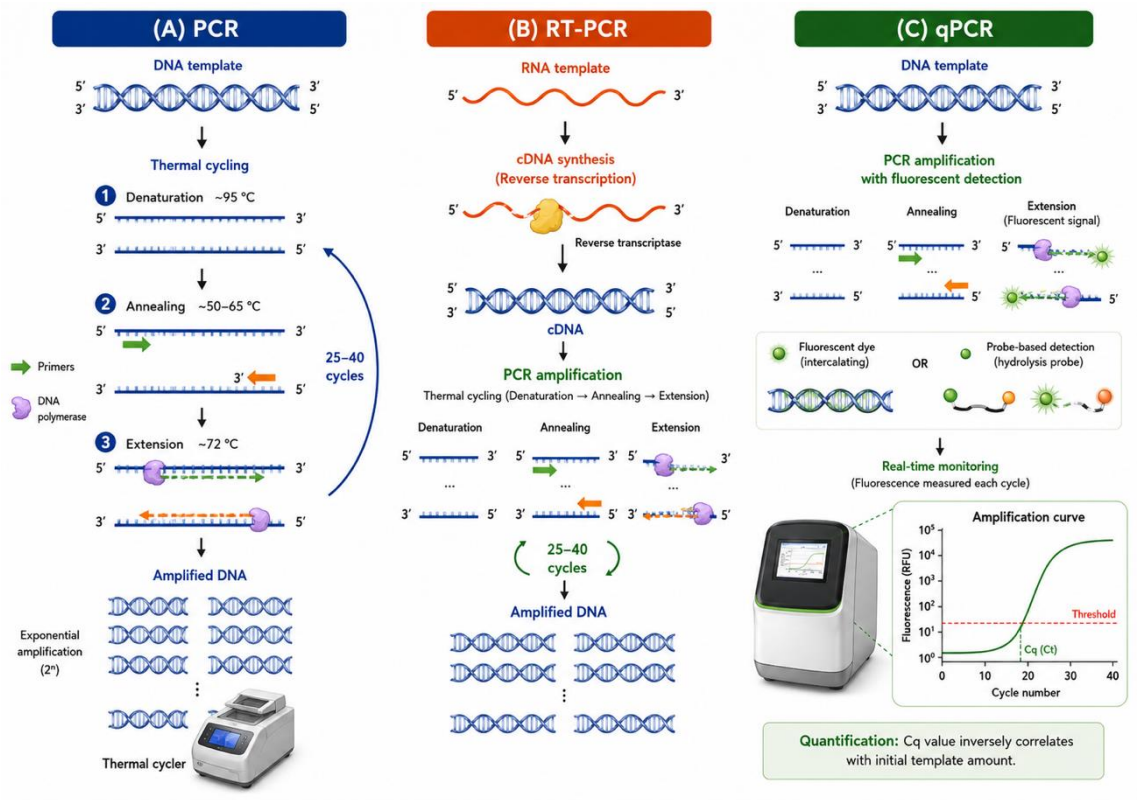


Figure 1.2 Schematic representation of PCR, RT-PCR and qPCR. Adapted from Adams et al.[56]

Beyond targeted amplification methods, advances in sequencing technologies have significantly expanded the scope of molecular diagnostics. Next-generation sequencing (NGS) enables the massively parallel sequencing of millions of DNA fragments, allowing comprehensive genomic analysis of pathogens. This includes whole-genome sequencing, metagenomic sequencing, and transcriptomic profiling. NGS has proven particularly valuable for pathogen discovery, outbreak investigation, antimicrobial resistance gene detection, and the study of microbial evolution and transmission dynamics.[57,58]

However, despite their high analytical performance, molecular diagnostics present several limitations that constrain their broader implementation. PCR-based assays typically require prior knowledge of target sequences, limiting their ability to detect unknown or highly divergent pathogens. They are also susceptible to contamination, which can lead to false-positive results, and may detect non-viable organisms, complicating the interpretation of clinical relevance.[55]

NGS technologies, while highly informative, remain resource-intensive. Their implementation requires complex workflows, including nucleic acid extraction, library preparation, sequencing, and advanced bioinformatics analysis. Turnaround times can range from hours to days, and costs remain significantly higher than conventional assays,

although these continue to decrease. The lack of standardised pipelines and regulatory frameworks poses additional challenges for routine clinical adoption.

Overall, molecular diagnostics represent a powerful and indispensable component of modern infectious disease detection. However, their reliance on specialised infrastructure, trained personnel, and relatively long processing times limits their accessibility, particularly in decentralised or point-of-care settings.

1.2.2. Rapid Antigen and Serological Tests

Another widely employed class of diagnostic approaches relies on the detection of proteins rather than nucleic acids, targeting either pathogen-derived antigens that signal active infection or host-produced antibodies that report immune response. Rapid diagnostic tests (RDTs), particularly those based on lateral flow immunoassays (LFAs), have emerged as essential tools for decentralised and point-of-care testing. These assays are designed to provide fast, simple, and cost-effective detection of infection-related biomarkers, often within 10 to 30 minutes and without the need for specialised equipment.[59,60]

LFAs operate through capillary-driven flow along a porous membrane containing immobilised biological recognition elements, typically antibodies. When a liquid sample is applied, it migrates along the membrane and interacts with labelled detection antibodies. If the target analyte is present, immune complexes form and are captured at defined test lines, producing a visible signal, commonly as a coloured band (**Figure 1.3**).

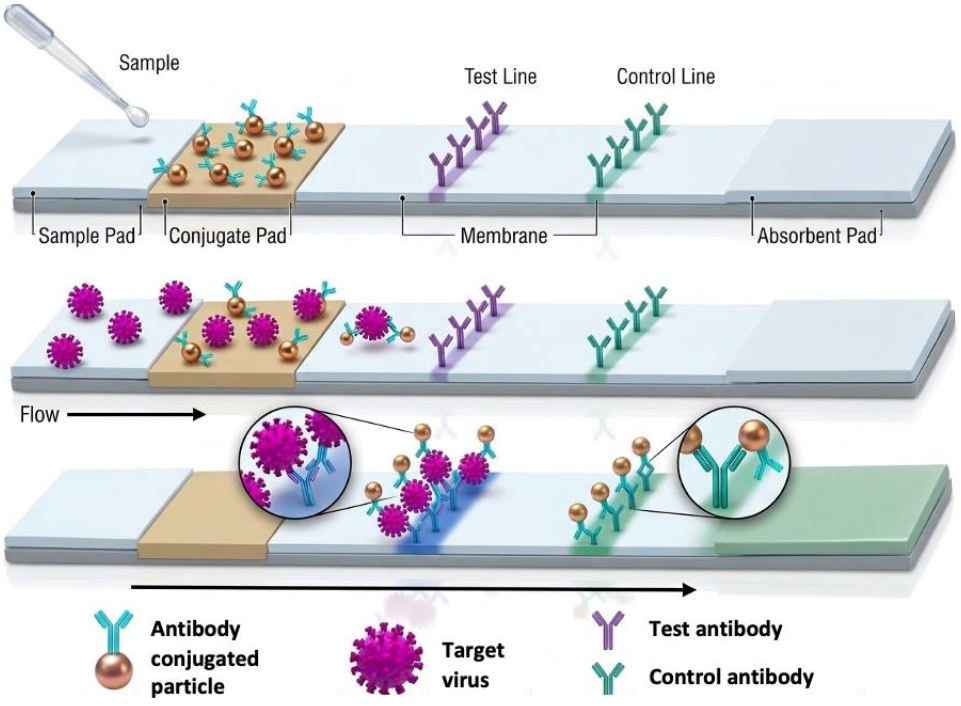


Figure 1.3 Schematic representation of a lateral flow immunoassay (LFA).

Rapid antigen tests detect pathogen-derived proteins and are most effective during the acute phase of infection, when viral or bacterial antigen levels are high. These tests have been widely deployed for respiratory viruses, including influenza and SARS-CoV-2, as well

as for certain bacterial pathogens. Their primary advantages include speed, ease of use, low cost, and suitability for large-scale screening and outbreak control.[61]

However, antigen-based assays generally exhibit lower sensitivity compared to nucleic acid amplification techniques. Their performance is highly dependent on viral or bacterial load, sample quality, and timing relative to infection onset. As a result, false-negative results may occur, particularly in early or late stages of infection.

Serological assays, in contrast, detect the host immune response rather than the pathogen itself. These tests measure antibodies produced following infection, typically immunoglobulin M (IgM), immunoglobulin A (IgA), and immunoglobulin G (IgG). IgM antibodies are usually associated with early immune responses, whereas IgG antibodies indicate past exposure or longer-term immunity.

Serological testing plays a crucial role in epidemiological studies, seroprevalence surveys, and the evaluation of immune responses following infection or vaccination. For example, in viral infections such as those caused by coronaviruses, antibodies directed against structural proteins, such as the spike or nucleocapsid proteins, can provide insights into exposure history and immune status. Nevertheless, serological assays are not suitable for early diagnosis of active infection due to the delay between pathogen exposure and antibody production, which can range from several days to weeks. Cross-reactivity with related pathogens may also reduce specificity, and antibody levels may wane over time, complicating interpretation.

In summary, rapid antigen and serological tests provide accessible and scalable diagnostic solutions, particularly valuable for point-of-care and population-level screening. However, their limitations in sensitivity, timing, and specificity necessitate their use in combination with other diagnostic modalities.

1.2.3. Culture-based Methods

Despite the advantages offered by molecular and immunoassay-based diagnostics, culture-based methods remain the foundation of clinical microbiology, particularly for bacterial infections and antimicrobial susceptibility testing. These techniques rely on the isolation and growth of viable microorganisms from clinical samples under controlled laboratory conditions.

In a typical workflow, samples are inoculated onto selective or non-selective culture media and incubated under defined environmental conditions, including temperature, atmospheric composition, and nutrient availability. Over time, microorganisms proliferate and form visible colonies, which can be further characterised based on morphology, staining properties, and biochemical assays. More recently, technologies such as matrix-assisted laser desorption/ionisation time-of-flight (MALDI-TOF) mass spectrometry have enhanced the speed and accuracy of bacterial identification following culture (**Figure 1.4**).[62,63]

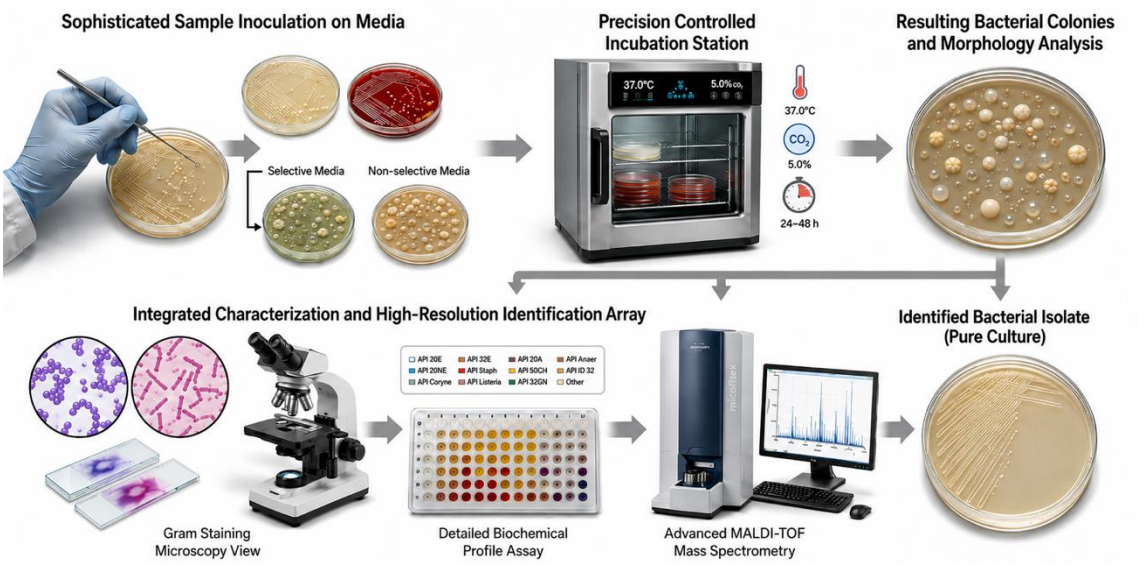


Figure 1.4 Schematic representation of culture-based methods workflow for bacterial identification.

A major advantage of culture-based methods is their ability to provide phenotypic information. In particular, antimicrobial susceptibility testing (AST) can be performed by exposing bacterial isolates to antibiotics and measuring growth inhibition. This allows clinicians to determine whether a pathogen is susceptible, intermediate, or resistant to specific antimicrobial agents, guiding targeted therapy. While molecular tests can detect specific known resistance genes, they cannot anticipate novel resistance mechanisms or fully characterise the functional susceptibility of an isolate, which is why culture-based AST remains the reference standard for AMR determination.[62]

Despite these strengths, culture-based diagnostics suffer from several critical limitations. The most significant is their inherently slow turnaround time. Depending on the organism, culture and susceptibility testing may require 24 to 72 hours or longer, with some pathogens such as *M. tuberculosis* requiring weeks. This delay often necessitates empirical treatment with broad-spectrum antibiotics, which can contribute to the development and spread of antimicrobial resistance.[64]

Additionally, culture-based methods are restricted to organisms capable of growing under laboratory conditions. Many clinically relevant pathogens are fastidious, slow-growing, or viable but non-culturable, leading to false-negative results and incomplete pathogen detection. Polymicrobial infections can further complicate interpretation, as dominant species may outcompete others in culture. Variability in culture conditions, including media composition and incubation parameters, can also affect reproducibility and standardisation across laboratories. Furthermore, these methods require dedicated laboratory infrastructure and trained personnel, limiting their applicability in resource-limited or point-of-care settings.[65]

Importantly, although culture remains the reference standard for antimicrobial susceptibility testing, its integration into diagnostic workflows often creates a bottleneck, delaying actionable results. This is particularly problematic in the context of rapidly

progressing infections and the global rise of AMR, where timely and precise treatment decisions are critical.[66]

Collectively, while culture-based methods provide indispensable phenotypic information, their limitations in speed, sensitivity, and scalability highlight the need for alternative diagnostic approaches capable of delivering rapid, accurate, and comprehensive results, an unmet need that motivates the development of next-generation biosensor-based platforms discussed in the following section.

1.3. Biosensors for Precision and Point-of-Care Applications

The diagnostic limitations discussed in the previous section have motivated the development of analytical platforms that can simplify detection workflows while preserving sensitivity, specificity, and quantitative capability. Biosensors represent one of the most relevant technological approaches in this context. Rather than replacing established laboratory methods, they offer complementary strategies for applications in which rapid analysis, reduced sample processing, portability, or real-time monitoring are required.[67,68]

A biosensor is an integrated analytical device that combines a biological or biomimetic recognition element with a physicochemical transducer. The recognition element provides molecular selectivity by interacting specifically with the target analyte, whereas the transducer converts the recognition event into a measurable signal. Depending on the intended application, the biorecognition element may consist of antibodies, nucleic acid probes, enzymes, receptors, aptamers, peptides, molecularly imprinted polymers, or other synthetic affinity ligands. This modular architecture allows the same transduction principle to be adapted to different targets by modifying the surface recognition chemistry (**Figure 1.5**).[69,70]

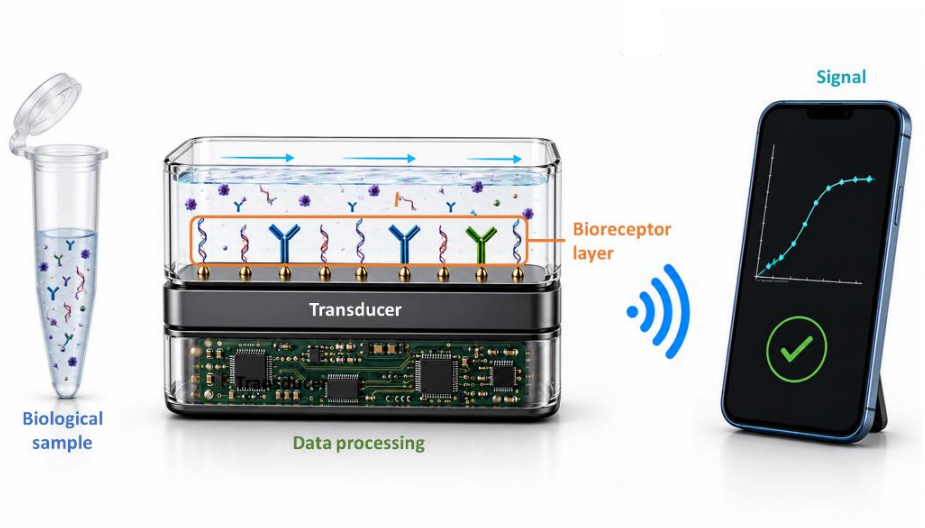


Figure 1.5 Schematic representation of a biosensor.

In infectious disease diagnostics, biosensors can be designed to detect pathogen-derived nucleic acids, proteins, toxins, whole viral or bacterial particles, antimicrobial resistance markers, or host-response biomarkers. The analytical signal originates from a physicochemical change occurring at the sensing interface after target recognition. This

change may involve variations in charge, current, impedance, mass, mechanical stress, temperature, refractive index, optical phase, intensity, or resonance conditions, depending on the transduction mechanism employed.[71]

Biosensors are commonly classified as electrochemical, optical, mechanical, thermal or magnetic according to their transduction strategy. Each class presents specific strengths and limitations regarding sensitivity, robustness, cost, miniaturization, multiplexing capability, and compatibility with biological samples. Among them, optical biosensors are particularly relevant because they interrogate biomolecular interactions through changes in light properties, being compatible with miniaturized formats, remote optical readout, multiplexed detection, and, in many configurations, label-free operation.[69]

Label-free optical biosensors detect molecular interactions directly through the physical changes produced at the sensor surface. This avoids additional labelling steps, reduces assay complexity, and limits possible interference caused by labels. In addition, continuous optical readout enables real-time monitoring of association and dissociation processes. Therefore, label-free platforms can provide information not only on analyte presence or concentration, but also on binding kinetics, affinity, and interaction specificity.[67]

Within optical biosensing, **evanescent wave-based sensors** constitute an important group of label-free technologies. Their operating principle relies on the interaction between a confined electromagnetic field and molecular binding events occurring close to the sensor surface. When light is confined at an interface, guided through an optical waveguide, coupled to a resonant structure, or used to excite a surface optical mode, part of the electromagnetic field extends beyond the physical boundary of the material into the surrounding medium (**Figure 1.6**). This non-propagating component is known as the evanescent field. Its intensity decays exponentially with distance from the surface, so it probes only a shallow region near the interface, typically within tens to hundreds of nanometres.[69,72,73]

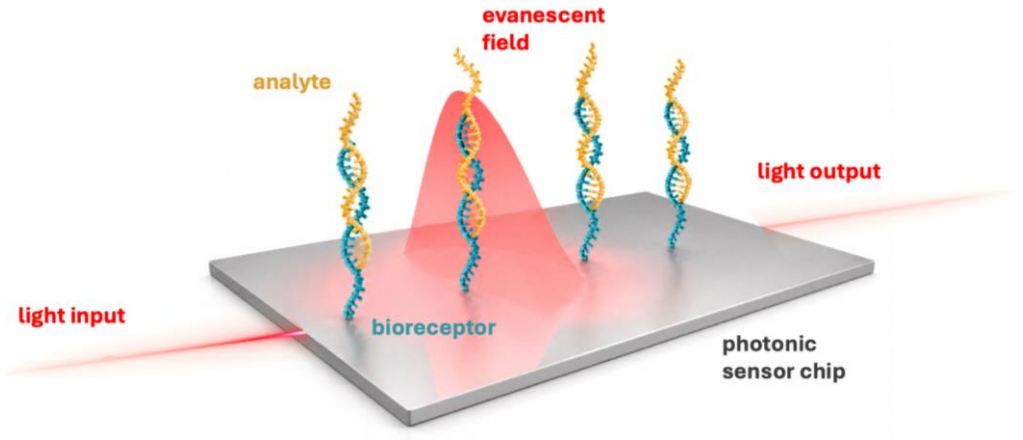


Figure 1.6 Schematic representation of an evanescent-wave biosensor. DNA probes (cyan) immobilized on the sensor surface hybridize with their complementary targets (yellow); the evanescent field (red) decays exponentially away from the interface.

This short penetration depth is essential for biosensing. The sensor surface is functionalized with specific bioreceptors, and target binding modifies the local optical environment within the region sampled by the evanescent field. In most label-free configurations, this modification is mainly associated with a change in the local refractive index caused by the accumulation of biomolecular material at the surface. The optical mode is sensitive to this perturbation, which can be measured quantitatively in real time as a change in intensity, phase, resonance wavelength, resonance angle, effective refractive index, or interference pattern.[72]

Compared with other biosensor formats, evanescent wave optical biosensors provide a distinctive combination of high surface sensitivity, direct optical readout, real-time monitoring, and robustness. Electrochemical biosensors are often compact and cost-effective, but their performance can be influenced by electrode fouling, ionic strength, and electroactive interferents, while mechanical biosensors often require strict control of mechanical stability and fluidic conditions. Their planar geometry also facilitates integration with microfluidics, automated sample handling, surface patterning, and sensor arrays. These characteristics are important for the development of compact diagnostic platforms with reduced reagent consumption and multiplexing capability. [74]

However, analytical performance depends on both the optical transducer and the biochemical interface. Optical field confinement, penetration depth, receptor immobilization, receptor orientation, surface density, antifouling strategy, mass transport, and signal processing all influence sensitivity, specificity, and reproducibility. For this reason, evanescent wave biosensor development requires the integration of biochemistry, surface chemistry, optics, micro- and nanofabrication, microfluidics, and analytical validation. This multidisciplinary perspective is particularly relevant in the context of this thesis, where biosensor development is approached both as a biochemical recognition problem and as assay design and optimization approach.[73]

Among evanescent wave-based optical biosensors, two technological families are especially relevant for label-free biomolecular detection: plasmonic biosensors and silicon photonic biosensors. Plasmonic platforms exploit surface electromagnetic modes supported at metal–dielectric interfaces, whereas silicon photonic platforms rely on guided optical modes in integrated waveguide structures. The following sections describe the physical principles, technological implementations, and state of the art of these two approaches, with emphasis on their application to infectious disease diagnostics.[69]

1.3.1. Plasmonic biosensor technologies

Surface plasmon resonance (SPR) is one of the earliest and most established examples of evanescent wave-based optical biosensing.[75] Since its introduction as a sensing principle in the early 1980s and subsequent commercialization in 1990, SPR has become a reference technique for the real-time and label-free characterization of biomolecular interactions, including antigen–antibody binding, nucleic acid hybridization, receptor–ligand recognition, and drug–target interactions.[76]

Plasmonic biosensors exploit the coupling of light to collective oscillations of free electrons in metallic films or nanostructures, being gold, silver or aluminium the most commonly employed plasmonic metals. In conventional SPR, these oscillations propagate along a planar metal–dielectric interface, whereas in nanostructured platforms they can be confined to metallic nanoparticles, nanoholes, or related architectures. In both cases, the resonance condition is highly sensitive to the optical properties of the medium adjacent to the metal surface, allowing surface-bound molecular interactions to be monitored through changes in the optical response. The following section describes the physical principles and technological implementations of these approaches.[77]

1.3.1.1. Principles and Technologies

The physical basis of plasmonic biosensing is the excitation of collective oscillations of free electrons at metal–dielectric interfaces, known as surface plasmons. These oscillations arise from the interaction between an incident electromagnetic field and the conduction electrons of a metal, typically gold or silver, whose dielectric function exhibits a negative real component at optical frequencies. Depending on the geometry of the metallic structure and the excitation scheme, surface plasmons can either propagate along extended interfaces or remain confined to nanoscale structures.[78]

Among plasmonic sensing technologies, SPR represents the most established approach. SPR is based on the resonant excitation of surface plasmon polaritons (SPPs) at a planar metal–dielectric interface, as illustrated in **Figure 1.7.** SPPs are transverse-magnetic polarized electromagnetic waves coupled to coherent oscillations of conduction electrons. They propagate along the interface and decay exponentially in the direction perpendicular to it, extending into both the metal and the adjacent dielectric medium. This surface confined field makes the resonance sensitive to optical changes occurring close to the metal surface.[79]

The propagation constant of the SPP depends on the dielectric functions of both the metal (ε_m) and the adjacent dielectric medium (ε_d), and can be expressed as:

$$k_{SPP} = \frac{\omega}{c}\sqrt{\frac{\varepsilon_m \varepsilon_d}{\varepsilon_m + \varepsilon_d}} \qquad (1.1)$$

where ω is the angular frequency of light and c is the speed of light in vacuum. Since ε_d is directly related to the refractive index of the surrounding medium ($\varepsilon_d \approx n_d^2$), any variation in the refractive index at the metal surface modifies the SPP propagation constant. This refractive index dependence constitutes the physical basis of SPR biosensing.

In a biosensor configuration, the metal surface is functionalized with specific bioreceptors. Binding of the target analyte changes the local refractive index within the plasmonic sensing region, shifting the resonance condition. This shift is monitored optically and correlated with the biomolecular interaction occurring at the sensor surface.

Direct excitation of SPPs by free-space illumination is not possible because the in-plane momentum of incident photons is smaller than that required to excite the plasmon mode. Therefore, additional momentum must be provided to satisfy the phase-matching condition

between the incident light and the SPP. This is typically achieved using prism coupling, grating coupling, or waveguide-based excitation.

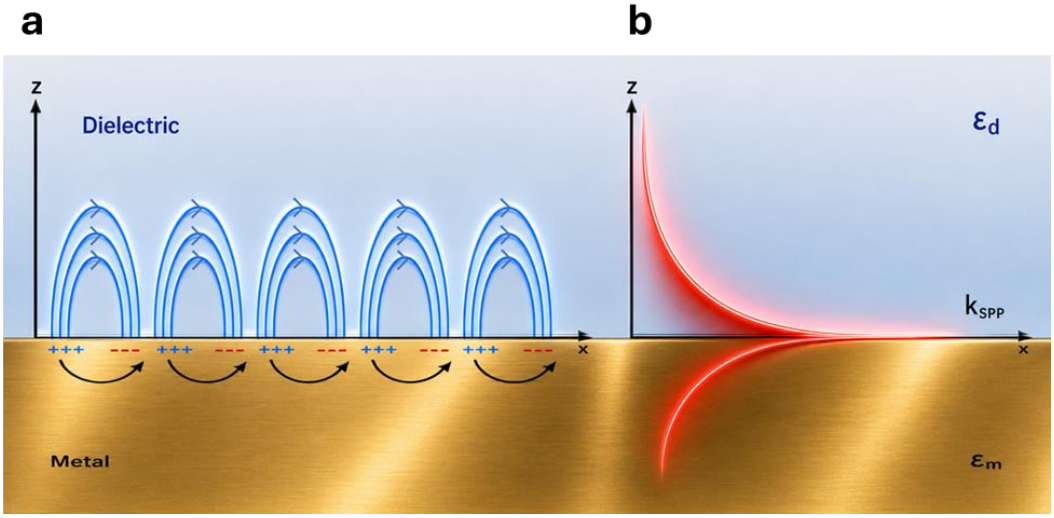


Figure 1.7 Schematic representation of a surface plasmon polariton (SPP) propagating along a metal–dielectric interface, illustrating: (**a**) the surface confined collective oscillation of free charges and (**b**) the transverse evanescent electromagnetic field extending

The most widely used configuration in SPR biosensing is the Kretschmann–Raether prism coupling geometry. In this configuration, a thin metal film, typically 40–50 nm of gold, is deposited on the base of a high-refractive-index prism, as shown in **Figure 1.8**. When p-polarized light undergoes total internal reflection (TIR) at the prism–metal interface, an evanescent field is generated that can transfer its momentum to the surface plasmon mode under specific resonance conditions.[80]

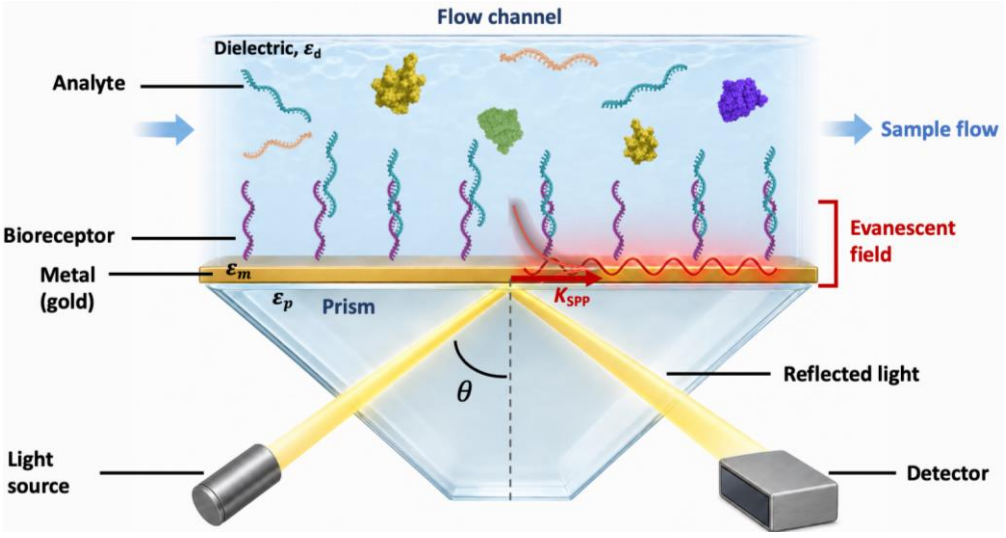


Figure 1.8 SPR biosensor based on prism-coupling Kretschmann configuration.

At the resonance angle or wavelength, efficient energy transfer occurs between the incident light and the SPP, resulting in a pronounced dip in the reflected light intensity. Changes in the refractive index near the metal surface shift this resonance condition, enabling the

detection of biomolecular binding events occurring within the evanescent sensing region, typically extending a few hundred nanometers from the surface (100-500 nm) (**Figure 1.9**).

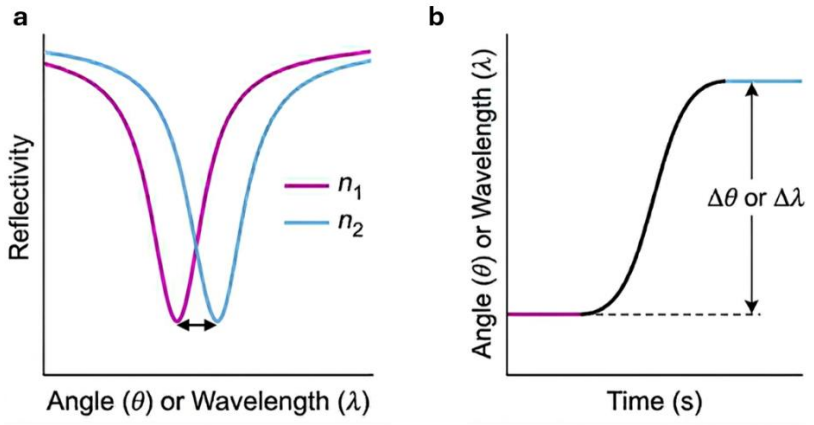


Figure 1.9 Spectral reflectivity dip and sensogram from SPR measurement methodology by wavelength-based interrogation.

The SPR signal can be interrogated using different detection schemes, depending on which property of the reflected light is monitored. In angular interrogation, the resonance condition is tracked as a shift in the angle of minimum reflectivity under monochromatic illumination. In wavelength interrogation, a broadband light source is employed and the resonance wavelength is monitored at a fixed incidence angle. Intensity-based interrogation measures variations in reflected light intensity at a fixed angle and wavelength, offering simpler instrumentation but typically lower sensitivity. Phase interrogation techniques detect changes in the phase of the reflected light, which varies sharply near resonance and can provide enhanced sensitivity, although they require more complex optical configurations.[75,77]

Alternative coupling strategies, such as grating coupling and waveguide-based excitation, have also been developed (**Figure 1.10**). In grating-coupled systems, periodic structures provide the additional momentum required for plasmon excitation through diffraction. In waveguide-based configurations, guided optical modes interact evanescently with a thin metal layer to excite the surface plasmon. These approaches are mainly explored for compact, integrated, and on-chip sensing platforms.[81]

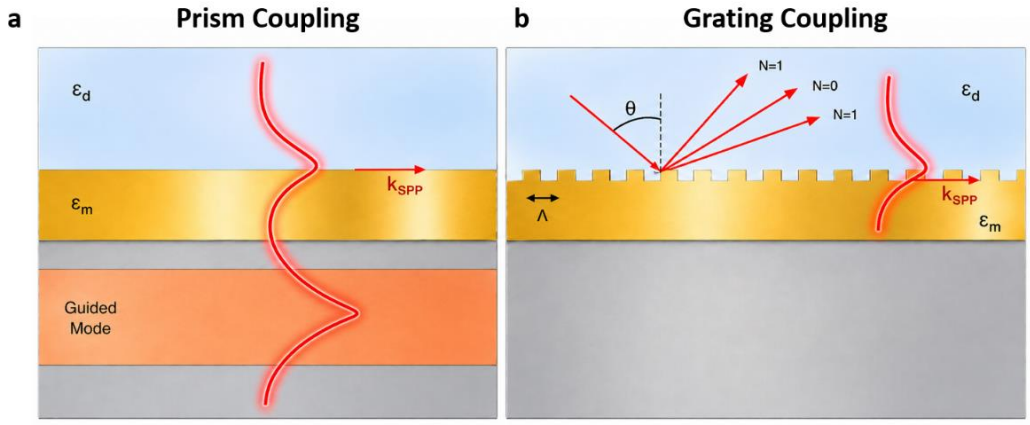


Figure 1.10 Schematic representation of SPR (**a**) grating coupling and (**b**) waveguide coupling.

Commercial SPR instruments have been widely adopted in biochemical and pharmaceutical research. Classical platforms such as Biacore systems (Cytiva) are based on prism-coupled SPR and are commonly used for real-time, label-free kinetic analysis of biomolecular interactions. Other commercial systems, including Reichert SPR instruments and BioNavis MP-SPR platforms, provide alternative implementations with similar optical configurations and expanded application capabilities. More compact platforms, such as Nicoya OpenSPR, aim to improve accessibility through simplified and miniaturized configurations.[82]

Overall, SPR technology combines high sensitivity, robustness, and label-free operation with the ability to monitor biomolecular interactions in real time. Typical SPR, LSPR and EOT-based plasmonic sensors achieve refractive-index resolutions on the order of 10^{-6} RIU, which determines the smallest detectable change in surface refractive index. This combination makes SPR a highly valuable tool for both fundamental research and emerging diagnostic applications. Meanwhile, ongoing technological developments are further driving its transition toward more compact, integrated, and potentially point-of-care compatible formats.

Following the development of propagating plasmon-based sensing platforms, advances in nanofabrication have enabled the implementation of plasmonic biosensors based on nanostructures, exhibiting either localized surface plasmon resonance (LSPR) or extraordinary optical transmission (EOT) phenomena:

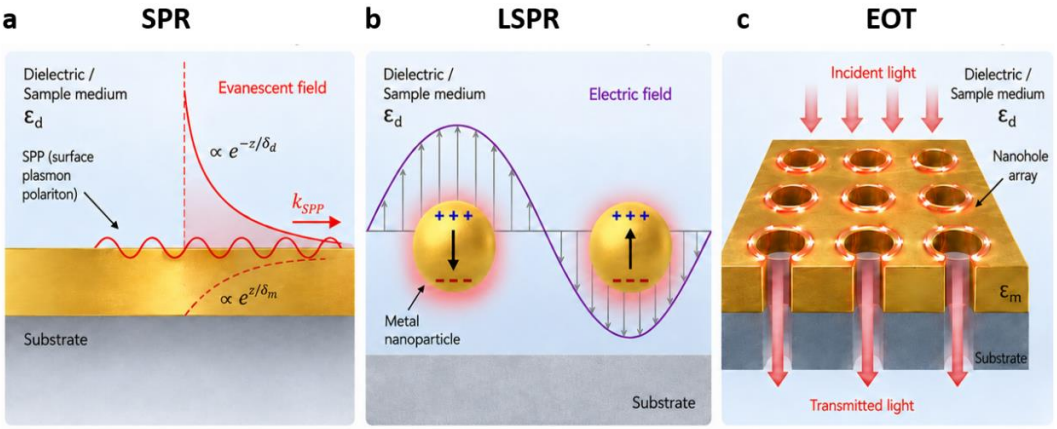


Figure 1.11 Schematic comparison of (**a**) SPR , (**b**) LSPR , and (**c**) EOT-based sensing, illustrating propagating vs localized fields and nanostructured platforms.

The **localized surface plasmon resonance (LSPR)** arises from the confinement of collective electron oscillations within metallic nanostructures such as nanoparticles, nanorods or nanodisks. When these nanostructures are illuminated, the incident electromagnetic field induces localized oscillations of conduction electrons, generating enhanced electromagnetic fields in the immediate vicinity of the nanostructure surface. This field is highly confined and decays rapidly, typically within a few tens of nanometers (10-50 nm), making LSPR particularly sensitive to molecular interactions occurring directly at the surface. Changes in the local refractive index caused by biomolecular binding events modify the resonance condition of the nanostructure, which can be detected as shifts in the optical spectrum (e.g., extinction or scattering). An important advantage of LSPR-based systems is that plasmon excitation can be achieved through direct illumination, without the need for additional coupling elements such as prisms, enabling simpler and more compact optical configurations.[58,72]

On the other hand, the **extraordinary optical transmission (EOT)** occurs through periodic arrays of subwavelength apertures in metallic films. In these systems, the interaction between incident light and surface plasmon modes supported by the periodic nanostructure leads to enhanced transmission at specific wavelengths. The spectral position of these transmission resonances depends on the geometry of the nanostructure and the surrounding dielectric environment. As in other plasmonic sensing approaches, biomolecular interactions near the surface induce changes in the local refractive index, resulting in measurable spectral shifts. Due to their compatibility with transmission-based measurements and large-area illumination, EOT platforms are particularly suitable for multiplexed detection and integration with imaging-based readout systems.[58]

Despite these advances, conventional surface plasmon resonance remains the most established and widely implemented plasmonic sensing technology in practical applications. LSPR and EOT platforms are still predominantly under development and are being actively explored to complement existing techniques by offering alternative configurations, miniaturization potential, and new functionalities.

1.3.1.2. Plasmonic Biosensors in Diagnostics

Plasmonic biosensors have been widely investigated for infectious disease diagnostics, demonstrating applications in the detection of whole viruses,[83] bacterial cells,[83] surface antigens,[85] nucleic acids,[86] toxins,[87] and host serological antibodies against pathogens.[88] Reported platforms include immunosensors for viral and bacterial antigen detection, sensors for direct identification of pathogen-specific DNA or RNA sequences, and serological assays for monitoring immune responses. In general, these technologies have achieved sensitivities ranging from the pico- to femtomolar (pM – fM) level for biomolecular targets, and in some cases single-virus or very low CFU/mL bacterial detection, while enabling rapid, label-free, and real-time analysis. These limits of detection are typically one to three orders of magnitude better than those of commercial lateral-flow immunoassays in the same matrices, which generally operate in the ng/mL range. Assay times are also markedly shorter: plasmonic measurements deliver a quantitative result in 15 to 30 min from a label-free, one-step protocol, compared with 1 to 3 h for RT-qPCR including sample preparation and 24 to 48 h for bacterial culture and antimicrobial susceptibility testing. Beyond these direct comparisons, plasmonic biosensors offer additional advantages including reduced sample preparation, multiplexing capability, quantitative analysis, and the possibility of miniaturization for point-of-care applications.

One of the main challenges in these plasmonic biosensor development is the detection of small targets or analytes present at very low concentrations. Since the sensing mechanism relies on refractive index changes occurring near the sensor surface, larger analytes such as viral particles, proteins or antibodies generally produce stronger signals than small biomolecules, including short nucleic acids, peptides, toxins, or low-molecular-weight proteins. Consequently, direct detection of these targets may generate signals close to the instrumental noise level, particularly in clinically relevant samples with low pathogen burden. To overcome this limitation, many plasmonic biosensors incorporate amplification or signal-enhancement strategies, such as nanoparticle labeling, sandwich assays, enzymatic reactions, or nucleic acid amplification methods, which increase the effective optical response and significantly improve sensitivity. However, these approaches often add complexity, increase assay time and cost, and may reduce robustness or suitability for decentralized testing. Therefore, an important challenge in the field remains achieving an optimal balance between analytical sensitivity, assay simplicity, reproducibility, and practical clinical implementation.[89]

The other major challenge for plasmonic biosensors is the analysis of complex biological samples under real clinical conditions. Matrices such as serum, plasma, saliva, urine, respiratory secretions, faecal extracts, or swab-derived samples contain high concentrations of proteins, salts, lipids, metabolites, nucleases, microorganisms, and cellular debris that can interfere with the sensing process. Because plasmonic sensors are inherently sensitive to refractive index changes occurring near the transducer surface, nonspecific adsorption of matrix components may generate false-positive signals, increase baseline drift, reduce signal-to-noise ratio, or hinder the accessibility of target molecules to the immobilized bioreceptors. In addition, matrix composition can vary significantly between patients and sample types, further affecting assay reproducibility and robustness. As a result, the development of antifouling surface chemistries, efficient blocking

strategies, reference sensing channels, optimized fluidics, and appropriate sample pretreatment protocols has become essential for reliable operation in real-world samples. Achieving accurate and reproducible detection directly in minimally processed clinical specimens remains one of the key requirements for the translation of plasmonic biosensors from laboratory demonstrations to routine diagnostic practice.[90]

Overall, plasmonic biosensors are highly useful for infectious disease assay development, but their translation is still constrained by sensitivity and selectivity limitations. For this reason, progress in the field depends on achieving a better compromise between analytical sensitivity and practical usability, supported by robust surface chemistry, controlled assay conditions, and validation in real biological matrices.

1.3.2. Silicon-photonic biosensing technologies

Silicon photonic biosensors constitute the second main family of evanescent wave-based optical biosensors considered in this thesis. In contrast to plasmonic platforms, where the optical response is associated with surface electromagnetic modes at metallic interfaces or nanostructures, silicon photonic sensors rely on dielectric waveguides and integrated optical circuits to guide and manipulate light on chip. This technological distinction enables compact sensor designs, multiplexed architectures, and compatibility with fabrication processes derived from the semiconductor industry.[91]

Silicon photonic biosensors are generally fabricated using silicon or silicon-based material platforms, particularly silicon-on-insulator and silicon nitride. Silicon-on-insulator (SOI) provides strong optical confinement due to the high refractive index contrast between silicon (Si) and silicon dioxide (SiO_2), enabling highly compact photonic structures. Silicon nitride (Si_3N_4) offers lower propagation losses, broader transparency in the visible and near-infrared spectral regions, and compatibility with aqueous biosensing conditions. These material platforms allow the implementation of different transducer architectures, mainly including resonant and interferometric devices.[92]

Among silicon photonic biosensors, the most widely developed platforms include microring resonators, photonic crystal sensors, and interferometric devices such as Mach–Zehnder interferometers (MZIs) and bimodal waveguide interferometers (BiMWs). Resonant structures, including microrings and photonic crystals, operate by monitoring shifts in resonance wavelength caused by binding-induced changes in the local refractive index near the sensor surface. In contrast, interferometric sensors detect variations in the effective refractive index through changes in the optical phase accumulated along the sensing region. In the following section, the fundamental sensing principles of these silicon photonic biosensor platforms are briefly introduced. Particular emphasis, however, is placed on the bimodal waveguide interferometer (BiMW), whose operating principle, design, and analytical performance are described in greater detail, as this technology constitutes the basis of the experimental work developed throughout this thesis.[74]

1.3.2.1. Principles and Technologies

The physical basis of silicon photonic biosensing is the perturbation of guided optical modes in integrated dielectric waveguides. In these structures, light is confined by the

refractive index contrast between the waveguide core and the surrounding medium. Changes occurring at the waveguide surface modify the effective refractive index of the guided mode, which can be detected as a variation in phase, transmitted intensity, or resonance wavelength depending on the device architecture.[93]

Silicon photonic biosensors can be implemented using different optical configurations, most commonly resonant and interferometric architectures. Resonant devices include microring resonators (miRR) and photonic crystals (PhC) (**Figure 1.12**). Microring resonators consist of closed-loop waveguides that support optical resonances at discrete wavelengths. Binding-induced changes in the effective refractive index shift the resonance wavelength, allowing detection through spectral monitoring. Their performance is strongly influenced by the quality factor, Q, with higher values corresponding to narrower resonance peaks and improved resolution of small wavelength shifts.[94,95]

Photonic crystals are based on periodic dielectric structures that generate photonic bandgaps, spectral regions in which light propagation is inhibited. The introduction of structural defects creates localized optical modes with strong electromagnetic confinement. Refractive index changes near the defect region shift the associated transmission, reflection, or resonance spectra. Although microring resonators and photonic crystals have been widely explored and utilized for biosensing, they are introduced here only as representative resonant platforms, since the main technology considered in this thesis is the bimodal waveguide interferometer.[94]

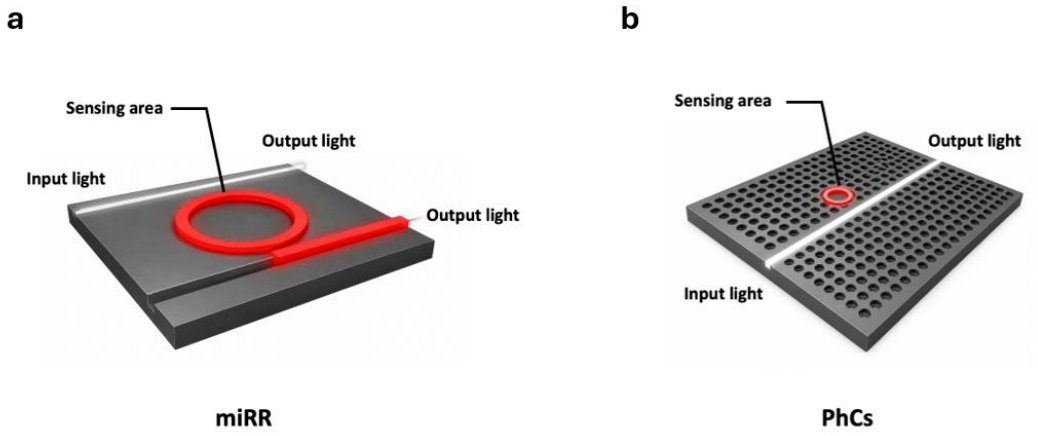


Figure 1.12 Schematic figure of (**a**) microring resonators (miRRs) and (**b**) photonic crystals (PhCs).

Interferometric sensors detect refractive index changes through phase variations accumulated during light propagation. In Mach–Zehnder interferometers (MZI), the input light is divided into a sensing arm and a reference arm (**Figure 1.13.a**). Binding events in the sensing arm modify its optical path length, and recombination with the reference arm converts the accumulated phase difference into an interference signal. This configuration can provide high sensitivity, but requires two spatially separated optical paths and stable reference conditions.[96]

Bimodal waveguide (BiMW) interferometers use a different configuration (**Figure 1.13.b**). Instead of separating the optical path into two arms, BiMW sensors rely on the propagation and interference of two optical modes within the same waveguide. These modes usually correspond to the fundamental mode and a higher-order mode of the same polarization, both propagating through a multimode sensing section. The signal originates from the phase difference accumulated between the two modes during propagation.[97]

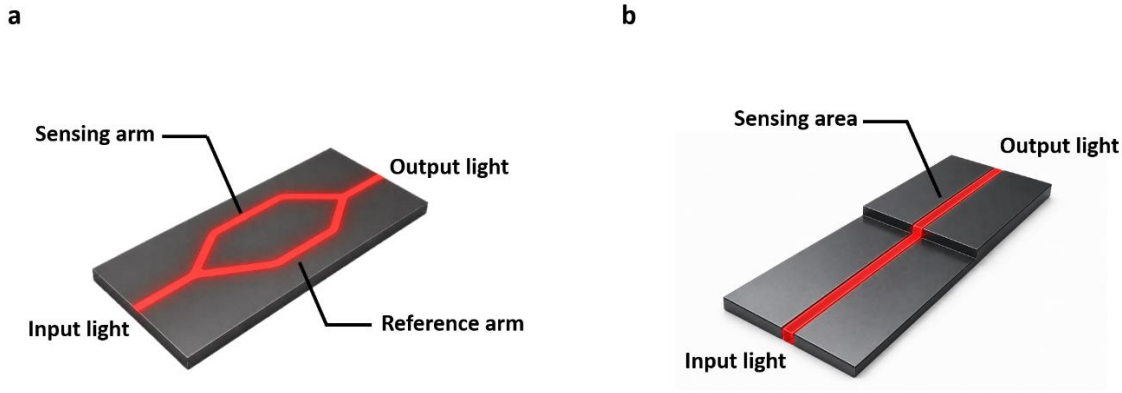


Figure 1.13 Schematic figure of (**a**) Mach–Zehnder interferometers (MZI) and (**b**) Bimodal waveguide (BiMW) interferometers.

A typical BiMW device consists of a bimodal sensing section inserted between two single-mode waveguides that act as input and output regions. The bimodal section is designed to support two propagating modes by increasing the waveguide width or height relative to the single-mode sections. Light entering from the input waveguide excites both modes in the bimodal region. After propagation along the sensing area, the modes interfere at the output transition, converting the accumulated phase difference into intensity modulation.[98]

The two modes are characterized by different propagation constants, $\beta_0$and β_1, and different effective refractive indices, $n_{\mathrm{eff},0}$ and $n_{\mathrm{eff},1}$. Their field distributions are also different. The fundamental mode is more confined within the waveguide core, whereas the higher-order mode extends further into the cladding region. The evanescent field typically penetrates 0.1–1 μm into the surrounding medium, allowing interaction with biomolecules immobilized on the waveguide surface or present in the adjacent fluidic channel. Because the two modes interact differently with this region, surface binding modifies their effective refractive indices unequally and changes their relative phase.[97]

The output optical intensity of a BiMW interferometer can be expressed as:

$$I_{\mathrm{out}} = I_0 + I_1 + 2\sqrt{I_0 I_1}\cos(\Delta\phi) \qquad (1.2)$$

where $I_0$and $I_1$are the intensities of the fundamental and higher-order modes, respectively, and $\Delta\phi$is the accumulated phase difference between them.

The general expression for the phase difference is:

$$\Delta\phi = \frac{2\pi}{\lambda}\left(n_{\mathrm{eff},1}L_1 - n_{\mathrm{eff},0}L_0\right) \qquad (1.3)$$

where λ is the optical wavelength, $L_0$and $L_1$are the propagation lengths of the two modes, and $n_{\mathrm{eff},0}$and $n_{\mathrm{eff},1}$are their effective refractive indices. In a BiMW sensor, both modes propagate along the same physical waveguide, so $L_0 = L_1 = L$. The phase difference therefore becomes:

$$\Delta\phi = \frac{2\pi}{\lambda}\left(n_{\mathrm{eff},1} - n_{\mathrm{eff},0}\right)L \qquad (1.4)$$

This expression shows that the signal depends on the modal effective-index difference. Any perturbation that changes the cladding refractive index modifies this difference and produces a measurable phase variation.

The refractive index sensitivity of a BiMW sensor is defined as:

$$S = \frac{\partial\Delta\phi}{\partial n_{\mathrm{clad}}} = \frac{2\pi L}{\lambda}\frac{\partial}{\partial n_{\mathrm{clad}}}\left(n_{\mathrm{eff},1} - n_{\mathrm{eff},0}\right) \qquad (1.5)$$

where $n_{\mathrm{clad}}$is the refractive index of the surrounding medium. Since the higher-order mode generally interacts more strongly with the cladding, its effective index is more sensitive to surface or bulk refractive index changes than that of the fundamental mode. The fundamental mode can therefore act as a quasi-reference, while the higher-order mode provides the dominant sensing response.[99]

Compared with MZIs, BiMW sensors provide a more compact interferometric architecture because both modes propagate within a single waveguide. This reduces the need for two separate arms and decreases common-mode perturbations, while preserving high phase sensitivity. As in other interferometric sensors, the phase sensitivity scales linearly with the interaction length. This represents an advantage compared with plasmonic biosensors, as the sensing area can be extended to enhance sensitivity.[97]

Reported refractive-index resolutions for BiMW sensors are typically in the 10^{-7}–10^{-8} refractive index units (RIU) range, depending on waveguide geometry, sensing length, optical setup, noise level, and signal processing. This performance, together with their compact layout, makes BiMW interferometers particularly relevant for the integrated biosensing strategy developed in this thesis.[99]

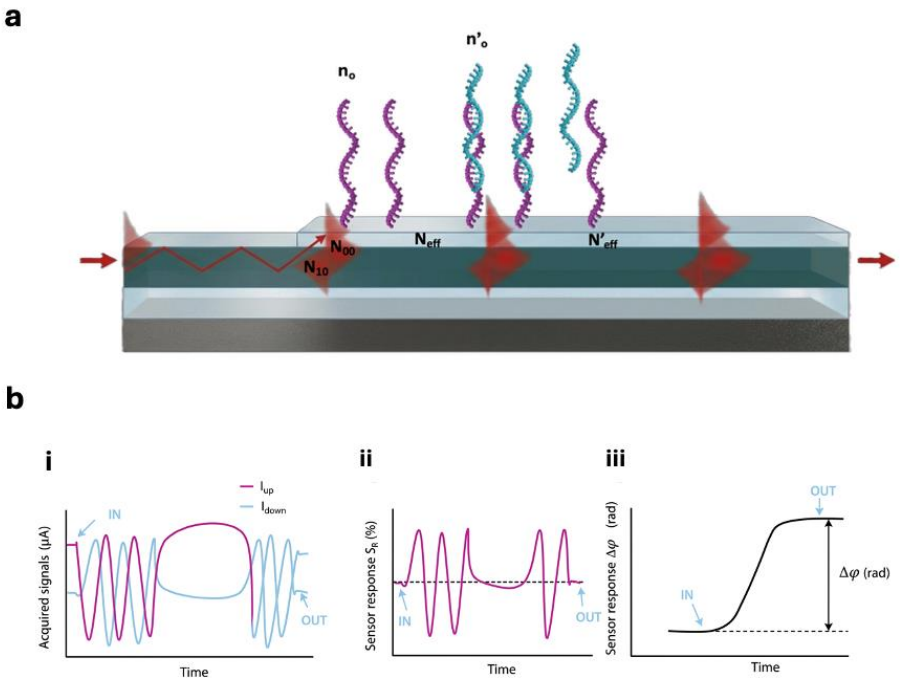


Figure 1.14 (**a**) Schematic illustration of the BiMW biosensor configuration. (**b**) Representative BiMW readout response: (**i**) raw Iup and Idown intensity signals; (**ii**) periodic interferometric signal associated with the sensor response during refractive index variation; and (**iii**) linearized sensor response obtained after all-optical modulation.[100]

1.3.2.2. Silicon Photonic Biosensors in Infection Diagnostics

Silicon photonic biosensors are particularly attractive for molecular diagnostics because they combine high sensitivity with chip-scale integration. In infectious disease diagnostics, this is relevant for assays that require low sample volumes, short analysis times, and parallel detection of several targets.[91]

Silicon photonic biosensors share with plasmonic devices the principle of evanescent-field, label-free detection, and the general sensitivity, matrix and translation challenges discussed in Section 1.3.1.2 apply equally to them. This section focuses on the aspects in which silicon photonic platforms differ from plasmonic ones, and on the specific challenges these differences introduce for infectious disease diagnostics.[69]

Silicon-photonic biosensors offer two main advantages over plasmonic platforms. First, interferometric devices in particular are intrinsically more sensitive, not because of how they are fabricated but because of their sensing mechanism: the optical signal accumulates as a phase shift over the entire light–analyte interaction length, rather than depending on a localized resonance condition. This translates into refractive-index resolutions about one order of magnitude better than those of plasmonic sensors (on the order of 10^{-7}–10^{-8} RIU versus ~10^{-6} RIU). Second, silicon devices are fabricated by lithographic patterning and etching of dielectric waveguides on a single wafer, using processes fully compatible with standard microelectronic (CMOS) technology. This compatibility enables low-cost, reproducible industrial-scale production, in clear contrast to plasmonic and especially nanoplasmonic devices, whose fabrication is more complex and not yet standardized, and gives silicon photonics far greater potential for

miniaturization and integration into automated, on-chip optical circuits, a key advantage for their translation into point-of-care diagnostic devices.

Despite these advantages, the main practical drawback of silicon photonics compared with plasmonics is surface chemistry. Plasmonic SPR benefits from the mature thiol–gold chemistry, which produces dense, self-assembled, well-ordered monolayers under simple ambient conditions and is the de facto standard for label-free immunoassays and oligonucleotide-based assays. Silicon-based surfaces lack an equivalent anchoring group: biofunctionalization proceeds through silanization of silanol-rich surfaces, followed by a cross-linker activation step and final probe coupling. Each of these steps is sensitive to silanol density, water content, silane concentration, temperature and curing time, and the resulting layers are generally less ordered and less reproducible than thiol–gold monolayers. Achieving uniform probe coverage, low nonspecific adsorption and stable baselines on silicon waveguides therefore requires more delicate process control and remains a technological challenge that directly conditions assay sensitivity, specificity and reproducibility.[94]

Operation in real samples is also more demanding. Many antifouling and regeneration protocols optimized over years for thiol–gold interfaces are not directly transferable to silicon: harsh regeneration solutions, in particular, can compromise the silane layer, and silicon-compatible blocking strategies are still less developed. Robust silicon-specific surface protocols, including adapted blocking layers, regeneration buffers and reference channels, are therefore an active area of research and a prerequisite for translating these platforms to clinical or surveillance use.[73]

Overall, silicon photonic biosensors provide a strong technological basis for miniaturized and multiplexed molecular diagnostics. Their high sensitivity makes them particularly relevant for early and precision diagnostics, but practical implementation depends on reliable silicon surface chemistry, accessible targets, and compatibility with complex samples. These challenges are central to the work developed in this Thesis.

Chapter 2

MOTIVATION AND OBJECTIVES

2. Motivation and objectives

Building on the diagnostic landscape described in Chapter 1, this PhD Thesis is aimed at the development and analytical validation of label-free photonic biosensor methodologies for the rapid molecular detection of two infectious disease challenges with high public-health relevance: the surveillance of zoonotic coronaviruses at the animal-human interface, and the diagnosis of bacterial sexually transmitted infections (STIs) together with AMR-associated genetic markers. To this end, the work has been carried out with two complementary photonic biosensing technologies consolidated within the NanoBiosensors and Bioanalytical Applications (NanoB2A) group at ICN2: an SPR platform, used as a versatile system for the development and optimization of nucleic acid hybridization assays, including the implementation of surface chemistry procedures and signal amplification strategies; and a BiMW interferometer, applied to the direct, label-free detection of DNA and RNA targets with improved intrinsic sensitivity and a layout compatible with future integration into compact point-of-care (PoC) devices.

The research has been framed within four competitive research projects that defined its biomedical scope and provided the clinical and epidemiological context for assay validation. On one hand, the **CoNVat** project (*Combating 2019-nCOV: Advanced nanobiosensing platforms for PoC global diagnostics and surveillance*, H2020, 101003544) and **MUSECOV** project (*Multi-scale Eco-evolution of Coronaviruses: from surveillance towards emergence prediction*, PCI2020-120687-2) focused on the development of photonic biosensors for zoonotic coronavirus detection and surveillance, and the specific tasks for this Thesis were carried out in collaboration with Prof. Jordi Serra-Cobo (University of Barcelona, Spain), who provided bat faecal samples for the analysis of mammalian alpha/beta-coronaviruses, and with Dr. Céline Courtillon (Agency for Food, Environmental and Occupational Health & Safety (ANSES), France), who provided in vitro transcribed RNA standards and chicken swab samples from controlled infectious bronchitis virus trials. On the other hand, the **TYPLEX** project (*Integrated prototype of a nanophotonic microchip biosensor for ultrasensitive multiplexed analysis of Sexually Transmitted Infections*, PDC2023-145891-I00) and the **DIGITS** project (*Rapid diagnostics of Sexually Transmitted Infections using Optical Nanotechnology,* 23S06145-001) addressed the application of photonic biosensors to the diagnosis of bacterial STIs and AMR profiling, targeting *Neisseria gonorrhoeae*, *Chlamydia trachomatis* and ciprofloxacin resistance-associated mutations in the gyrA gene, with tasks performed in collaboration with the Department of Microbiology of Vall d'Hebron University Hospital, led by Dr. Juan José González, which provided bacterial reference strains and contributed to the definition of clinically relevant diagnostic targets and validation strategies.

In particular, the main objectives outlined for this PhD Thesis are organized into four experimental chapters and include:

- **In Chapter 3**, description of the SPR and BiMW photonic biosensing platforms used throughout this Thesis, including their optical instrumentation, fluidic systems and signal acquisition, together with the establishment of a common methodological framework

covering sensor chip fabrication and cleaning, chemical reagents, biological materials, biofunctionalization protocols, hybridization conditions, regeneration procedures and data analysis methods.

- **In Chapter 4**, development of robust and reproducible nucleic acid-based biofunctionalization strategies on both gold (SPR) and silicon nitride (BiMW) sensor surfaces, including the systematic comparison of silanization chemistries, the optimization of probe density and hybridization conditions, and the assessment of the stability and reusability of the biofunctionalized interfaces over repeated hybridization and regeneration cycles.

- **In Chapter 5**, design, development and analytical validation of SPR and BiMW biosensor assays for the direct detection of viral RNA from SARS-CoV-2 (E and N genes), alpha/beta-coronaviruses and gamma-coronaviruses, including the implementation of an antibody-based signal amplification strategy and the evaluation of the developed assays against in vitro transcribed RNA and real animal samples (bat faeces and chicken swabs), within the framework of the CoNVat and MUSECOV projects.

- **In Chapter 6**, development of BiMW biosensor assays for the direct detection of bacterial DNA from *N. gonorrhoeae* and *C. trachomatis*, together with a hybridization strategy of controlled stringency for the discrimination of a single-nucleotide ciprofloxacin resistance-associated mutation in the gyrA gene, and validation of the optimized assay in lysed bacterial samples, within the framework of the TYPLEX and DIGITS projects.

The successful achievement of these objectives is intended to provide a coherent set of label-free photonic biosensor methodologies, evolving from the technological description and the consolidation of robust biorecognition interfaces toward their application in two clinically and epidemiologically relevant infectious disease scenarios. Together, these contributions aim to advance the role of photonic biosensors as complementary diagnostic tools within a One Health perspective for outbreak preparedness, STI screening and antimicrobial resistance monitoring.

Chapter 3

MATERIALS AND METHODS

A description of the materials, instrumentation and procedures employed throughout this doctoral work is summarized. A detailed explanation of both SPR- and BiMW-based biosensor figures is provided, followed by the fabrication and surface preparation protocols of the gold and silicon nitride sensor chips. A list of all chemical reagents, buffers and biological compounds used in the experimental work is also included. Finally, the chapter describes the biofunctionalization protocols, the hybridization and regeneration conditions, and the data analysis methods that constitute the common methodological framework of the experimental chapters presented in this dissertation.

3. Materials and Methods

3.1. Surface Plasmon Resonance (SPR) platform

3.1.1. SPR experimental set-up

The SPR device employed in this thesis is based on the Kretschmann prism-coupling configuration, in which transverse-magnetic polarized light is coupled through a prism to excite surface plasmon polaritons at the interface between a thin metallic film and the adjacent dielectric medium. Any biomolecular binding event occurring within the evanescent field modifies the local refractive index and produces a displacement of the resonance wavelength, which can be followed in real time.

The SPR platform used in this work was an in-house designed and fabricated system operating at a fixed incidence angle of θ = 70° (**Figure 3.1**)**.** All optical and fluidic components were integrated on a portable 20 × 20 cm^2 board, highlighting the compact character of the setup. The platform consisted of four main elements: a broadband light source, the plasmonic transducer, the detection module, and a microfluidic delivery system.

The plasmonic transducer consisted of 49 nm-thin gold-coated glass sensor chips. During SPR measurements, the gold-coated sensor chip was clamped between a trapezoidal glass prism and a custom-made Delrin flow cell. Refractive index matching oil with n ≈ 1.512 was used to ensure optical contact between the chip and the prism. The Delrin flow cell had an internal volume of 4 µL and was connected to the microfluidic system. The fluidic setup consisted of a syringe pump (Darwin Microfluidics, Paris, France) providing a constant flow rate and a manually operated injection valve (CHEMINERT®, VICI, Houston, TX, USA) equipped with a 100 µL loop for controlled sample injection.

The sensor surface was illuminated using a halogen light source (Thorlabs, Newton, NJ, USA) coupled to a collimator (C330TMEB, Thorlabs, Germany). The light was set to transverse-magnetic polarization using a linear polarizer (LPVIS050, Thorlabs, Germany**)** and coupled to the sensor chip through the prism. The reflected light was collected and fibre-coupled to a CCD spectrometer (Jaz, Ocean Optics, Largo, FL, USA). Reflectivity spectra were acquired every 3 ms, and 300 consecutive spectra were averaged to generate each resonance spectrum.

The SPR signal was monitored by tracking the displacement of the resonance wavelength, expressed as Δλ (nm)**.** Binding events at the gold surface increase the local refractive index and shift the resonance curve toward higher wavelengths, whereas desorption events decrease the refractive index and shift the resonance curve toward lower wavelengths. A software interface was also developed in Python for signal monitoring and data analysis (**Figure 3.2**). This enabled continuous monitoring of molecular association and dissociation events during the assay.

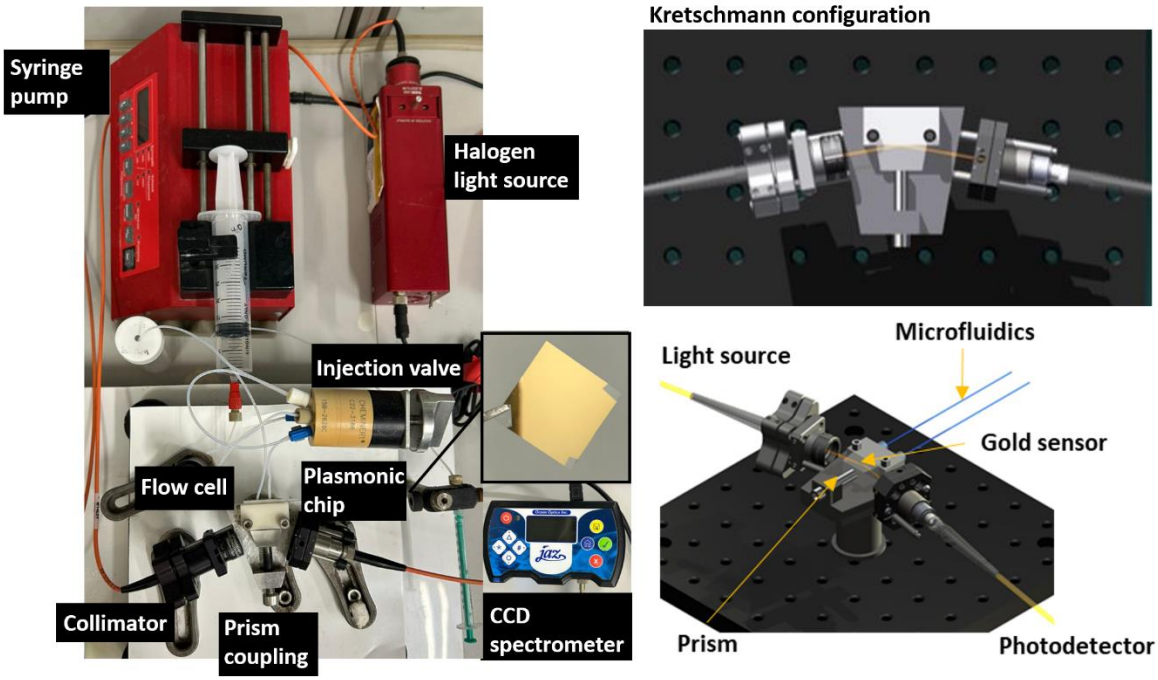


Figure 3.1 Photograph and schematic representation of the experimental SPR platform, showing the halogen light source, collimator, injection valve, syringe pump, prism coupling system, flow cell, plasmonic chip, and CCD spectrometer.

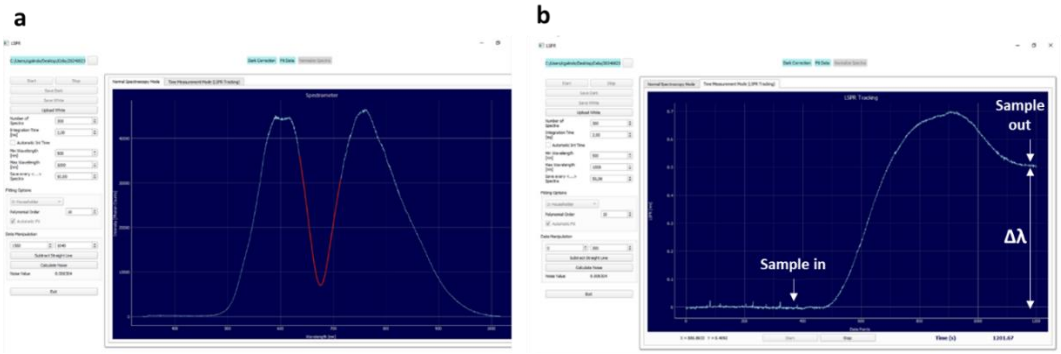


Figure 3.2 Screenshots of the homemade SPR readout software showing: (a) the wavelength reflectivity spectrum and (b) the sensogram tracking the SPR response in real time as wavelength shift, Δλ.

3.1.2. SPR sensor chips fabrication and cleaning

The SPR sensor chips were prepared on glass substrates by electron-beam metal evaporation using an AJA International Inc. ATC-8E Orion deposition system. Prior to metal deposition, glass coverslips (No. 4, 22 × 22 mm, Thermo Scientific Menzel-Glaser, Braunschweig, Germany) were used as supporting substrates. A thin titanium layer of 1 nm was first deposited to improve the adhesion of gold to the glass surface, followed by the deposition of a 49 nm gold layer. The resulting metal stack, composed of 1 nm Ti and 49 nm Au, provides the plasmonic interface required for surface plasmon excitation and is also compatible with thiol-based surface chemistry.

Before biofunctionalization, the gold chips were cleaned to remove organic residues and other surface contaminants that could interfere with the formation of the biorecognition

layer. The cleaning protocol consisted of consecutive heating at 60 °C and sonication for 1 min in solvents of increasing polarity, namely acetone, ethanol, and Milli-Q water. After this solvent cleaning step, the chips were dried under a nitrogen stream and activated for 20 min in a UV/Ozone ProCleaner Plus system (Bioforce Nanosciences, Utah, USA). Finally, the chips were rinsed with ethanol, dried again under nitrogen, and immediately used for chemical modification.

3.2. Bimodal Waveguide (BiMW) Interferometer platform

3.2.1. BiMW experimental set-up

The BiMW measurements were performed on a home-built interferometric platform (**Figure 3.3**). The system comprised a polarized diode laser, optical coupling elements, the BiMW sensor chip, a photodetector, a temperature stabilization module, and a microfluidic delivery system.

The BiMW sensor chip was mounted on a custom-made holder fixed to a three-axis translation stage, which allowed precise alignment and coupling of the input light into the waveguide. A Peltier thermoelectric cooler (TEC3-2.5, Thorlabs, New Jersey, USA), driven by a temperature controller, was positioned below the chip to minimize temperature fluctuations, reaching a stabilization accuracy of 0.01 °C. This is critical because the BiMW response is highly sensitive to thermally induced refractive-index changes.

Input light was provided by a TE-polarized diode laser operating at λ = 660 nm (Hitachi, Tokyo, Japan). The beam was conditioned and coupled into the BiMW sensor through a collimating lens (C240TME-D, Thorlabs, New Jersey, USA), a polarization-dependent isolator (IO-3D-660-VLP, Thorlabs, New Jersey, USA), and a 40× coupling objective (Achro, Leica, Wetzlar, Germany). The output intensity was recorded with a two-section photodetector (Hamamatsu Photonics, Hamamatsu, Japan) and digitized through an acquisition card.

Real-time signal acquisition and processing were handled by an in-house Python software (**Figure 3.4**). An all-optical phase-modulation method based on a trigonometric algorithm was applied to linearize the interferometric signal, so that the phase shift between the two propagating modes, expressed as $\Delta\phi$ (rad), could be continuously monitored and quantified.[101]

The fluidic system consisted of a five-channel polydimethylsiloxane (PDMS) microfluidic cell with channel dimensions of 1.25 mm width × 500 µm height × 18.5 mm length, a syringe pump (Darwin Microfluidics, Paris, France), and a six-port CHEMINERT® injection valve (VICI, Texas, USA). This configuration ensured a continuous flow of running buffer and the controlled injection of reagents and samples over the sensing area.

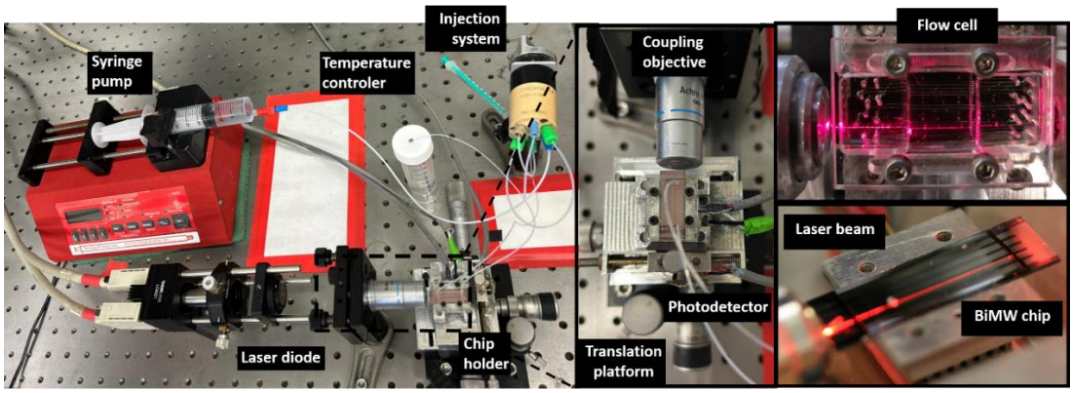


Figure 3.3 Photograph of the experimental BiMW platform and light-coupled BiMW waveguide, showing the diode laser, syringe pump, injection valve, flow cell, temperature controller, photodetector, and chip holder.

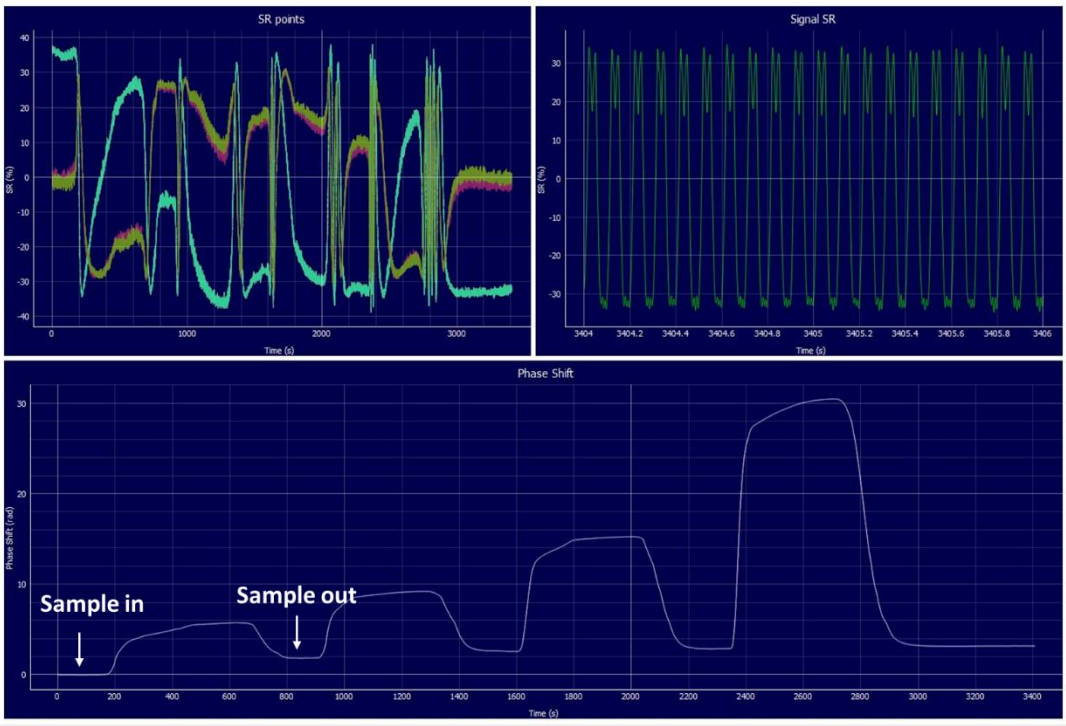


Figure 3.4 Screenshots of the homemade BiMW readout software showing the interferometric signal, SR values, and the real-time sensogram tracking the BiMW response as phase shift, Δϕ.

3.2.2. BiMW sensor chips fabrication and cleaning

The silicon-based BiMW sensor chips were fabricated at the Clean Room of the Microelectronic National Centre (IMB-CNM-CSIC, Barcelona, Spain), part of the Singular Scientific and Technical Infrastructures (ICTS) network. The process was based on standard microelectronic technology and combined photolithography and etching steps on a silicon wafer substrate.[102] Each wafer yielded 12 BiMW chips, with every chip integrating 20 BiMW sensors, 6 BiMW references (without sensing area), and 6 single-mode waveguides, all spaced 250 µm center-to-center (**Figure 3.5)**. Each chip measured 3 × 1 cm, and the rib waveguide had a cross-section of 3 µm in width and 1.5 nm in height.

The waveguide core is made of silicon nitride (Si_3N_4), chosen for its high refractive index (n_{core} = 2.00), its high density, and its chemical inertness against ion species, oxygen, and moisture permeation. The Si_3N_4 core is sandwiched between an upper and a lower cladding of silicon oxide (SiO_2), whose lower refractive index (n_{cladd} = 1.46) confines the optical mode within the core and minimizes propagation losses (Figure 3.5). In the bimodal section, the cladding is etched to define a 15 mm sensing area where the core is exposed to the external medium. The chip is operated with TE-polarized light at λ = 660 nm; in this regime both Si_3N_4 and SiO_2 are transparent (≈ 200–2000 nm), and biomolecules are essentially non-absorbent in the visible, which makes Si_3N_4 a particularly suitable core material for integrated-optics waveguide biosensors in the visible spectrum.

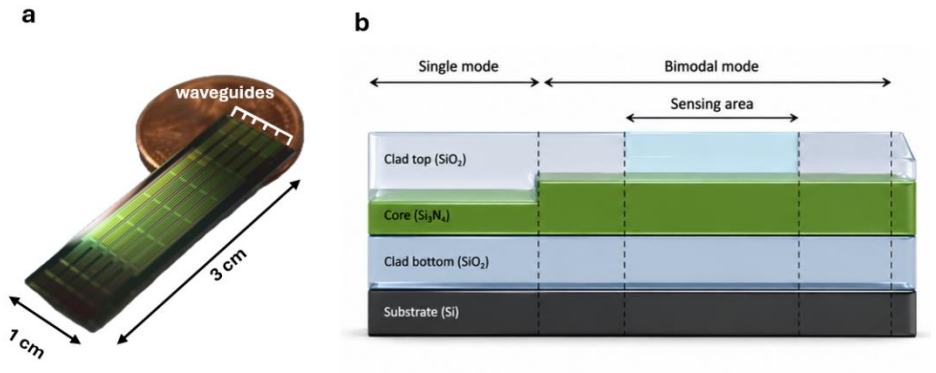


Figure 3.5 (**a**) Photography and (**b**) schematic overview of the BiMW interferometric sensor chip, showing the longitudinal layout of the single-mode and bimodal sensing regions.

Prior to biofunctionalization, the Si_3N_4 BiMW chips were cleaned and activated to remove contaminants and generate the surface hydroxyl groups required for silanization. The cleaning sequence consisted of consecutive sonication steps in acetone, ethanol, and Milli-Q water for 5 min at 60 °C, followed by a 10 min sonication in a 1:1 (v/v) methanol:hydrochloric acid (MeOH:HCl) mixture to eliminate residual organic contamination. The chips were then rinsed thoroughly with Milli-Q water and dried under a nitrogen stream.

Surface activation was performed to generate reactive hydroxyl groups on the Si_3N_4 surface. The chips were exposed to oxygen plasma using an Electronic Diener system (Ebhausen, Germany) for 5 min at a gas flow of 45 sccm, and subsequently immersed in 15% HNO_3 at 95 °C for 25 min. After activation, the chips were rinsed, dried, and used for ex situ silanization.

In experiments where piranha cleaning was used instead of nitric acid activation, the protocol consisted of treatment with H_2SO_4:H_2O_2 (3:1, v/v) after solvent cleaning and plasma treatment, followed by extensive rinsing with Milli-Q water and drying under nitrogen. The activated chips were used immediately for silanization to limit surface ageing and re-contamination.

3.3. Chemical reagents and biological materials

Organic solvents, including ethanol, acetone, and isopropanol, were obtained from PanReac AppliChem (Barcelona, Spain). (3-Aminopropyl)triethoxysilane (APTES), p-

phenylenediisothiocyanate (PDITC), N-hydroxysuccinimide polyethylene glycol maleimide (NHS-PEG-MAL), dimethyl sulfoxide (DMSO), toluene, dimethylformamide (DMF), pyridine, formamide (FA), and the reagents and salts used for buffer preparation were purchased from Merck (Darmstadt, Germany).

Phosphate-buffered saline (PBS, pH 7.4) was prepared at a final composition of 50 mM phosphate buffer, 750 mM NaCl, 33 mM Na_2HPO_4, and 2 mM EDTA. Saline-sodium citrate (SSC, pH 7.4) solutions were prepared from a 20× SSC stock solution containing 3 M NaCl and 0.3 M sodium citrate. Working SSC solutions were obtained by diluting the stock solution to 10× (1.5 M NaCl, 0.15 M sodium citrate), 7× (1.05 M NaCl, 0.105 M sodium citrate), 5× (0.75 M NaCl, 0.075 M sodium citrate), and 3× (0.45 M NaCl, 0.045 M sodium citrate).

Thiolated DNA probes, amine-modified DNA probes, biotinylated DNA probes, synthetic DNA targets, and the corresponding negative controls were synthesized and supplied by Microsynth AG (Balgach, Switzerland). Synthetic viral RNA target sequences were obtained from Integrated DNA Technologies, IDT (Newark, New Jersey, USA). The specific DNA and RNA sequences used in each assay are provided in the corresponding experimental chapters. Diethyl pyrocarbonate (DEPC)-treated water was used for the preparation of RNA solutions and buffers to ensure RNase-free conditions.

Hydroxyl-terminated thiolated polyethylene glycol lateral spacers, SH-PEG-OH, were purchased from Laysan Bio (Alabama, USA). Bond-Breaker™ TCEP solution, containing tris(2-carboxyethyl)phosphine hydrochloride, was purchased from Thermo Fisher Scientific (Waltham, Massachusetts, USA) and used for the reduction of thiolated oligonucleotides when required.

3.4. Sensor biofunctionalization protocols

3.4.1. Gold-based surface biofunctionalization

For gold sensor functionalization, direct thiol-functional DNA probe chemisorption was employed. This immobilization strategy was carried out entirely under flow conditions. The immobilization solution was prepared in 50 mM phosphate-buffered saline (PBS, pH 7.4) by mixing the thiolated DNA probe with a hydroxyl-terminated thiolated PEG lateral spacer (HO-PEG-SH). Before injection, the solution was treated with tris(2-carboxyethyl)phosphine hydrochloride (TCEP, 100 nM) at 36 °C for 30 min to reduce disulfide bonds and favour efficient thiol availability for gold attachment. After activation, the sensor chip was mounted in the SPR platform, and the immobilization solution was injected over the gold surface at a flow rate of 10 µL/min. Probe attachment occurred through Au–S chemisorption, while the lateral spacer was included to control probe density, reduce surface crowding, and improve probe accessibility for subsequent hybridization assays.

3.4.2. Silicon-based surface biofunctionalization

Different silicon-based sensor chips, including SiO_2-coated SPR chips and the BiMW sensor chips, were employed in this work in order to optimize and establish a robust

biofunctionalization procedure. Herein, we will only detail the protocol of the ultimately selected biofunctionalization protocol based on vapor-phase APTES silanization. Experimental details of the different tested strategies can be found in Annex A.

For vapor-phase silanization, the activated chips were placed in a vacuum desiccator with 100 µL of (3-aminopropyl)triethoxysilane (APTES). The desiccator was kept under vacuum for 5 min and then incubated for 1 h to allow APTES deposition on the sensor surface. After silanization, a curing step was performed at 120 °C for 20 min to stabilize the amine-functionalized layer.

The amine-functionalized surfaces were subsequently activated with 20 mM p-phenylenediisothiocyanate (PDITC) prepared in dimethylformamide (DMF) containing 10% pyridine. The chips were incubated with the PDITC solution for 2 h in the dark, enabling the formation of reactive isothiocyanate groups for covalent DNA probe attachment.

For in-flow probe immobilization, thiolated DNA probe solutions were prepared in 50 mM PBS (pH 7.4) supplemented with NaCl and EDTA and mixed with the HO-PEG-SH lateral spacer. Before immobilization, the solution was treated with TCEP (100 nM) at 36 °C for 20 min to reduce disulfide bonds and ensure the availability of thiol groups for coupling. The BiMW chip was then mounted in the experimental setup, and the immobilization solution was flowed over the sensor surface at 10 µL/min.

3.5. Hybridization assays

For detection assays, target solutions were generally prepared in 5× saline-sodium citrate buffer (SSC, pH 7.4) and the concentration of additives was adjusted according to the specific probe/target sequence and sensor response. Target solutions were injected over the functionalized sensor surface at a flow rate of 15 µL/min, and the hybridization process was monitored in real time. Negative controls were measured under the same conditions to assess assay specificity when required.

Regeneration was carried out by injecting 35% formamide (FA) after each hybridization step. This promoted dehybridization of the target strand from the immobilized DNA probe and allowed repeated hybridization–regeneration cycles on the same sensor chip.

3.6. Data analysis and statistics

Biosensor data were processed using Origin 8.0 software (OriginLab, Northampton, MA, USA). Statistical analyses were performed with GraphPad Prism (GraphPad Software, Inc., CA, USA). For analytical calibration assays, the mean sensor response and the corresponding standard deviation (SD) were plotted as a function of the target concentration. Synthetic RNA calibration curves were fitted by non-linear regression using a specific binding model with Hill slope. The limit of detection (LOD) was defined as the lowest target concentration that could be reliably distinguished from the blank signal, whereas the limit of quantification (LOQ) was defined as the lowest concentration that could be quantified with acceptable reliability. The LOD was calculated as the mean blank signal plus three times its standard deviation (mean blank + 3SD), while the LOQ was calculated as the mean blank signal plus ten times its standard deviation (mean blank + 10SD).

For biosensor validation using real samples, all measurements were performed blinded to the PCR classification, which was disclosed only after completion of the biosensor experiments and data analysis. To assess the agreement between the BiMW biosensor and RT-PCR analysis, a linear regression analysis was performed by comparing the RT-PCR cycle threshold (Ct) values with the corresponding biosensor signals.

Repeated measurements of the same sample were considered technical replicates and were not treated as independent observations; therefore, each biological sample was included only once in the statistical analysis. Differences between positive and negative sample groups were evaluated using the Kruskal–Wallis test, with statistical significance set at $p < 0.0001$.

Threshold values for sample classification were established from the negative control population using the median response plus two times the median absolute deviation (median + 2MAD). Samples giving responses lower than 0.9 × (median + 2MAD) were classified as negative, while samples giving responses higher than 1.1 × (median + 2MAD) were classified as positive. Responses falling within the intermediate interval, between 0.9 × (median + 2MAD) and 1.1 × (median + 2MAD), were considered indeterminates.[103]

Diagnostic performance was calculated from the number of true positives (TP), true negatives (TN), false positives (FP), and false negatives (FN), using the molecular reference method as comparator. Sensitivity (SE) was defined as TP/(TP + FN), specificity (SP) as TN/(TN + FP), positive predictive value (PPV) as TP/(TP + FP), and negative predictive value (NPV) as TN/(TN + FN). Receiver operating characteristic (ROC) curves were generated by plotting sensitivity against 1-specificity at different decision thresholds. The diagnostic accuracy of the biosensor was quantified by the area under the ROC curve (AUC), with values closer to 1 indicating higher discriminatory performance.

Chapter 4

DEVELOPMENT OF NUCLEIC ACID-BASED PHOTONIC BIOSENSORS

The development of robust and reproducible nucleic acid-based biofunctionalization strategies on both SPR and BiMW photonic platforms is described. A detailed comparison of different surface chemistry procedures on gold (SPR) and silicon nitride (BiMW) sensor surfaces is provided, including the systematic evaluation of silanization protocols and the optimization of probe density and lateral spacer ratios. The chapter also presents the optimization of the hybridization conditions, including pH, ionic strength and buffer composition, for the specific recognition of a model nucleic acid target. Finally, the stability and reusability of the biofunctionalized interfaces are assessed through repeated hybridization and regeneration cycles, establishing the biorecognition framework that supports the application-oriented chapters that follow.

4. Development of nucleic acid-based photonic biosensors

4.1. Fundamentals of Nucleic Acid Hybridization Assays

Nucleic acid-based biosensors detect specific nucleic acid sequences through complementary hybridization. A single-stranded DNA or RNA probe is immobilized on the sensor surface and binds selectively to a complementary target sequence in solution. DNA is typically found as a double-stranded helix, whereas RNA is generally single-stranded and often adopts secondary structures through intramolecular base pairing. Both are composed of four nucleotides—adenine (A), guanine (G), cytosine (C), and thymine (T) in DNA or uracil (U) in RNA. Hybridization proceeds via Watson–Crick base pairing, where A pairs with T (or U) and G pairs with C, generating duplex structures stabilized by hydrogen bonding. Alternative architectures such as triplexes, hairpins, and other secondary structures can also form under specific sequence and structural conditions (**Figure 4.1**).[104]

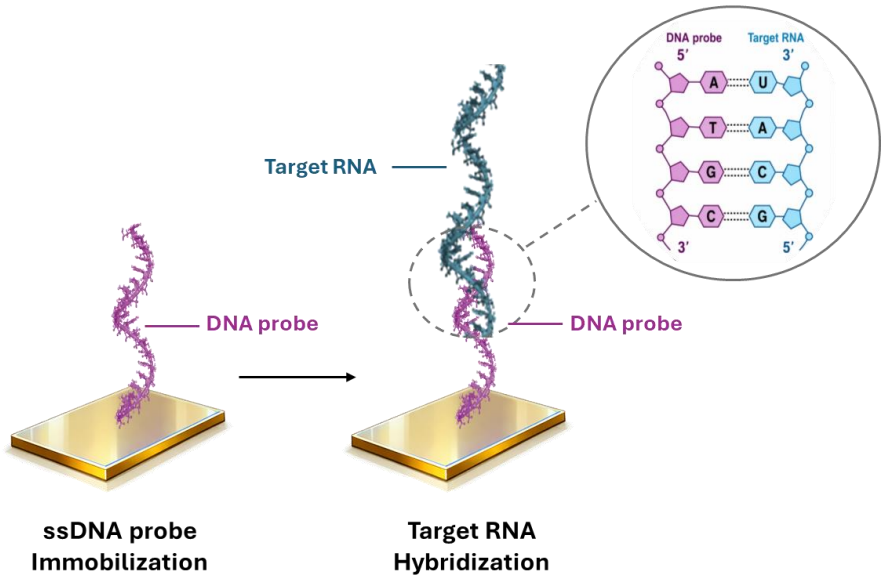


Figure 4.1 Schematic representation of DNA probe immobilization and hybridization process.

In evanescent-field-based biosensors, probe–target hybridization at the sensor surface produces a local refractive index change within the sensing field, which is detected by the optical transducer. The magnitude of the signal depends on the formation of nucleic acid complexes at the surface and, therefore, on the efficiency and specificity of the hybridization process.[105]

Probe design is therefore an initial key step in nucleic acid hybridization assays, since the immobilized strand must be complementary to the target region. The degree of complementarity determines the stability and specificity of the probe–target duplex: fully complementary sequences form stable hybrids, whereas mismatches weaken binding and reduce the sensor response. Nucleotide composition is also relevant, since GC-rich regions form more stable duplexes than AT- or AU-rich regions due to stronger hydrogen bonding and base-stacking interactions.[106]

Hybridization also requires that the target region be accessible to the immobilized probe. This is generally straightforward for short synthetic oligonucleotides or fragmented nucleic acids, whereas long DNA or RNA molecules may contain regions partially hidden by secondary structures. In the case of double-stranded DNA, the complementary strand must first be separated or locally displaced before the target can bind to the surface-bound probe.[107]

The physicochemical environment further modulates hybridization. Because nucleic acids carry negatively charged phosphate backbones, electrostatic repulsion between probe and target strands hinders duplex formation, particularly at high probe densities. Ionic strength screens these charges and promotes hybridization, while temperature regulates duplex stability and stringency: low-stringency conditions may favour nonspecific binding, whereas overly stringent conditions can destabilize even the correct probe–target duplex.[108]

In the following sections, we describe how each of these factors, including surface chemistry, probe density and orientation, hybridization conditions, and interface stability, has been systematically addressed and optimized for the nucleic acid biosensors developed in this thesis, providing the biorecognition foundation on which the application chapters are built.

4.2. Target selection and probe design considerations

4.2.1. Target selection

The development of a nucleic acid biosensor begins with two coupled decisions: which region of the target genome to detect, and how to design the complementary probe that will recognize it at the sensor surface. The first depends primarily on the biological question being addressed, including whether broad detection across strains or discrimination between closely related variants is required, while the second involves a set of sequence and structural parameters that govern hybridization efficiency, specificity, and the final sensor response. Both aspects are discussed below.

Target region selection is guided primarily by the diagnostic objective. For pathogen detection, conserved genomic regions are selected to recognize different strains of the same organism, whereas more variable regions are chosen to discriminate between closely related species, mutations, or variants. In all cases, the candidate region must be unique to the intended target: its sequence is compared against reference databases (for example, through BLAST alignment against the relevant genomes and against the host and commensal flora) to minimize cross-hybridization with non-target nucleic acids and ensure analytical specificity.

Beyond uniqueness, the biochemical properties of the region itself determine how efficiently it can be detected. A moderate GC content (approximately 40–60 %) is favoured, since GC-rich regions form stable intramolecular structures that compete with probe hybridization, whereas AT-rich regions yield weak, thermally unstable duplexes. Equally important is the accessibility of the region: single-stranded nucleic acids, and RNA in particular, fold into secondary structures (hairpins, loops, stems) that can sequester the target sequence and hinder probe binding, so regions predicted to be relatively

unstructured and single-stranded under the assay conditions are preferred. Repetitive elements, homopolymeric runs, and self-complementary motifs are likewise avoided, as they promote nonspecific binding and reduce the fraction of target available for hybridization.

4.2.2. DNA probe design

An important advantage of DNA-based biosensors is that DNA probes can be rationally designed and chemically synthesized with high reproducibility, allowing precise control over the nucleotide sequence, probe length, melting temperature (T_m), spacer region, and functional group used for surface immobilization. Probe design is therefore a critical step, as each of these parameters directly affects hybridization efficiency, specificity, and the final sensor response.[109]

The first step is target region selection. The probe is designed as the reverse complement of a specific region of the target nucleic acid, enabling selective recognition through Watson–Crick base pairing. For pathogen detection, conserved genomic regions are selected to detect different strains of the same organism, whereas more variable regions are chosen for discrimination between closely related species, mutations, or variants. The selected region should minimize cross-hybridization with non-target sequences and avoid regions that are not accessible for hybridization.

Several sequence parameters must be considered during probe design, including specificity, GC content, probe length, melting temperature, and the presence of self-complementary regions. GC content plays a central role in duplex stability, since GC base pairs form three hydrogen bonds versus two in AT pairs. Higher GC content increases duplex stability and T_m, but excessive GC content promotes secondary structures and nonspecific interactions, whereas very low GC content results in weak hybridization and reduced signal intensity. A moderate GC content is therefore preferred.[110]

Probe length involves a similar trade-off. Short probes provide better discrimination of single-base mismatches but form less stable duplexes and produce weaker signals, while longer probes yield more stable hybrids at the cost of increased secondary structure formation and reduced specificity. The melting temperature, closely related to both length and GC content, provides an estimate of the thermal stability of the probe–target duplex.[105]

Beyond sequence design, DNA probes can be end-modified for surface immobilization with functional groups such as thiol (–SH), amine ($–NH_2$), carboxylic acid (–COOH), or biotin. The choice of linker depends on the surface chemistry and immobilization strategy, and directly determines the stability and orientation of the probe at the interface.

To improve the accessibility of immobilized probes, vertical spacers are introduced between the nucleic acid sequence and the surface, increasing the probe-to-interface distance and reducing steric hindrance (**Figure 4.2**). Common spacers include short alkyl chains such as C6 and poly-thymine sequences, which provide flexibility and reduce interactions between the probe and the surface. Poly-thymine spacers are particularly advantageous in gold-based systems, since thymine exhibits relatively low affinity for gold

surfaces compared with other nucleobases, minimizing undesired probe–surface adsorption and maintaining the probe in an extended, accessible conformation.[73,111,112]

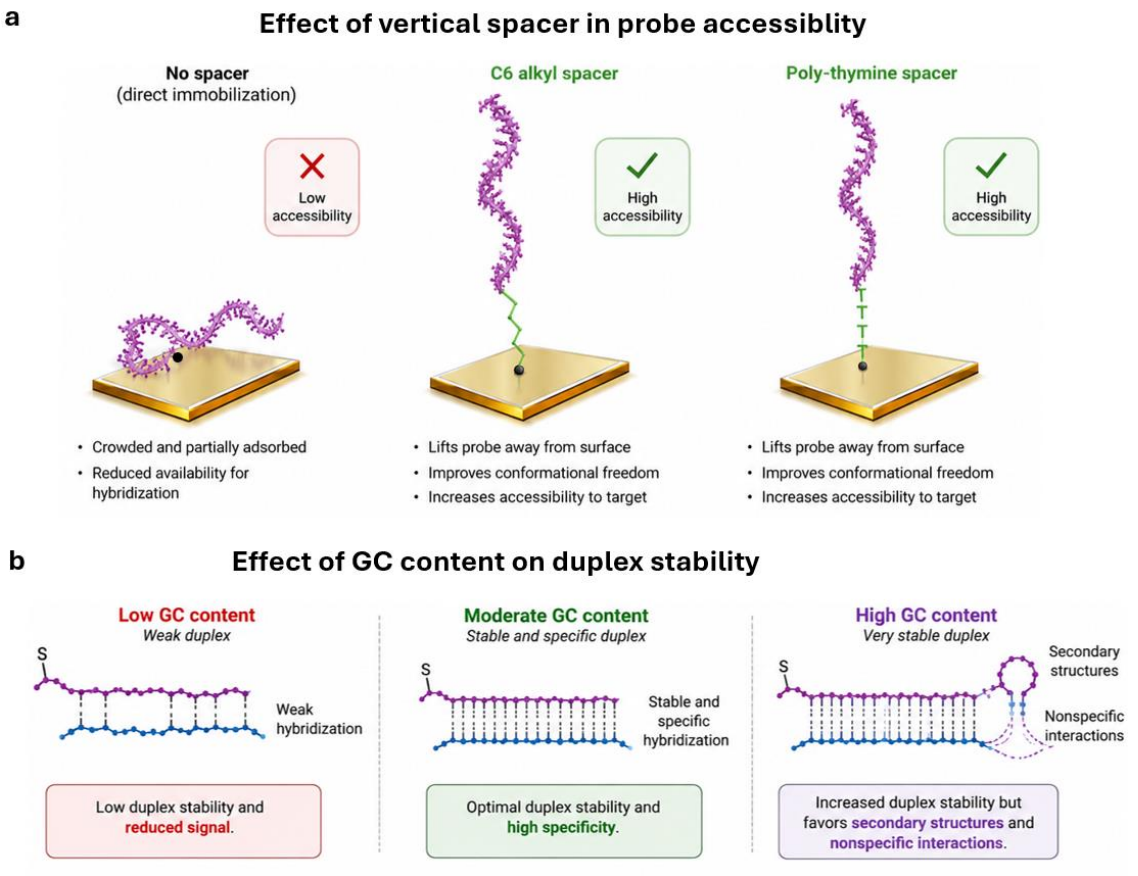


Figure 4.2 Schematic overview of DNA probe design parameters evaluated. (**a**) Influence of vertical spacers on probe orientation and target accessibility. (**b**) Influence of GC content on duplex stability, hybridization efficiency, and risk of secondary structures or

4.3. Sensor Surface Biofunctionalization

Effective biofunctionalization requires three concurrent conditions: (i) immobilization of a highly selective DNA probe ensuring specific interaction with the complementary target; (ii) controlled and uniform surface coverage with proper probe orientation, maximizing accessibility and hybridization efficiency; and (iii) strong attachment stability to withstand flow conditions and enable reproducible measurements over multiple assay cycles.[73]

The immobilization of DNA probes must preserve their structural integrity and accessibility. Probes that are poorly attached or adopt unfavourable conformations at the surface hybridize inefficiently, leading to reduced signal intensity. Probe density also plays a crucial role: excessive coverage generates steric hindrance and electrostatic repulsion between negatively charged strands, limiting target accessibility, whereas low density yields insufficient signal generation. An optimal balance between probe density and accessibility is therefore essential (**Figure 4.3**).[105]

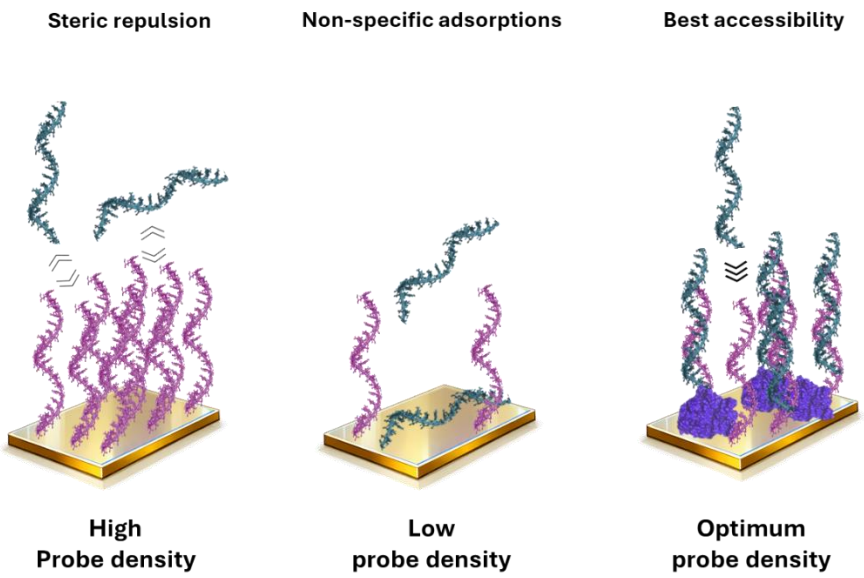


Figure 4.3 Surface coverage scheme: high, low, and optimum probe density

Probe accessibility is further influenced by spatial organization at the interface. Vertical spacers increase the probe-to-surface distance and reduce steric hindrance, while controlled lateral spacing between probes minimizes crowding effects and improves hybridization efficiency.[113]

Another critical factor is the stability of the immobilized layer. Weak attachment can result in probe desorption under flow conditions, compromising reproducibility and limiting the ability to perform multiple hybridization–regeneration cycles. The immobilization chemistry must therefore ensure robust and stable probe anchoring (**Figure 4.4**).

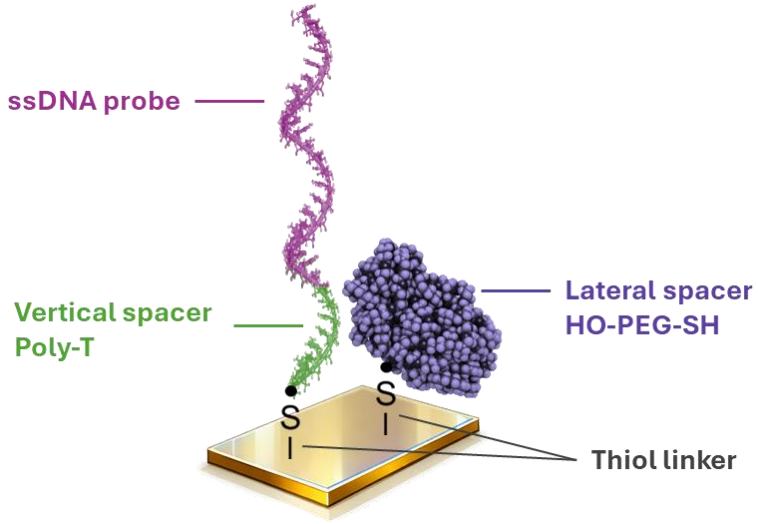


Figure 4.4 Schematic figure of thiolated single-stranded DNA probe with a vertical spacer (PolyT) and thiolated lateral spacer (HO-PEG-SH) immobilized on the gold surface.

The strategies required for effective biofunctionalization depend strongly on the nature of the sensor surface. The following sections systematically study DNA probe immobilization

on plasmonic and silicon photonic biosensors, with the aim of identifying the most robust and reproducible approach for efficient hybridization and reliable nucleic acid detection.

All optimization experiments in the following sections were performed with the same model probe and target, so that any observed differences reflect the immobilization strategy and surface chemistry under study. The model probe is a 25-nt DNA sequence with a moderate GC content of 52 %. The vertical spacer was adapted to each platform: a poly-T_{15} spacer was incorporated for the gold-based SPR system, taking advantage of the low affinity of thymine for gold to maintain the probe in an extended, accessible conformation, while a C_6 alkyl spacer was used for the silicon-based BiMW platform, where the surface chemistry does not require this passivation effect. As a model analytical target, a 50-nt synthetic RNA fragment was selected, with a GC content of 48 % and containing the 25-nt region fully complementary to the probe.

4.3.1. Gold-based sensor surfaces

4.3.1.1. Immobilization efficiency

The immobilization of thiol-modified DNA probes (SH–DNA) onto gold surfaces is a widely used and robust strategy for nucleic acid biosensor fabrication. This approach relies on the formation of strong Au–S bonds between the thiol group of the probe and the gold surface, enabling stable and reproducible probe attachment.

This direct chemisorption strategy allows the probe sequence to be presented at the interface for target hybridization, while providing sufficient stability under flow conditions. Compared to other immobilization approaches, thiolated DNA probes typically yield high surface coverage, which can be optimized by adjusting parameters such as probe concentration, ionic strength, and immobilization conditions.

As shown in **Figure 4.5**, the immobilization signal increased with higher probe-to-spacer ratios, reaching its maximum at 1:7 (**Figure 4.5a**), while increasing the probe concentration increased the signal to 2 µM, with no further gain at higher concentrations (**Figure 4.5b**). The higher immobilization observed at greater probe-to-spacer ratios is expected, since more probe molecules become attached to the surface. However, a higher immobilization signal does not necessarily indicate better sensing performance, as densely packed probes can hinder target accessibility through steric and electrostatic effects. The influence of probe density and concentration on the actual sensor response was therefore evaluated through

hybridization experiments, presented in the following section.

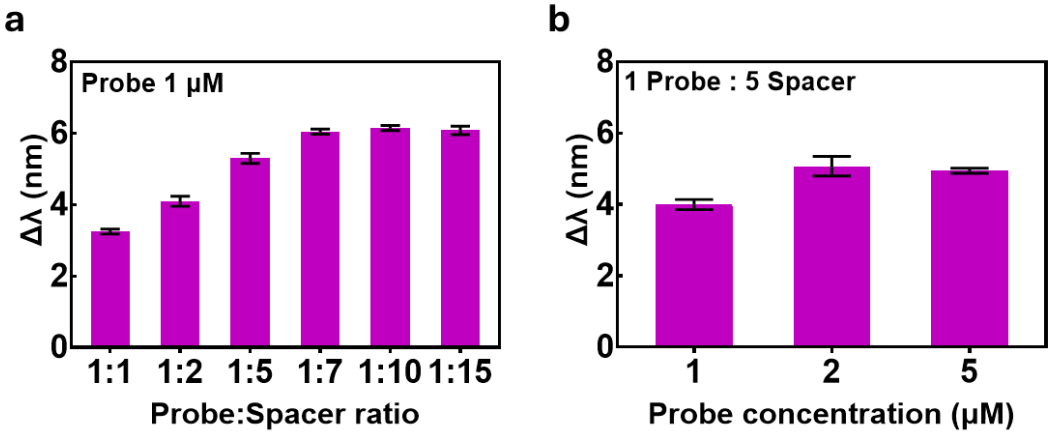


Figure 4.5 (**a**) Immobilization of DNA probe with different concentrations (1, 2 and 5 µM) and (**b**) lateral spacer ratios (1:1, 1:2, 1:5, 1:7, 1:10, 1:15).

4.3.1.2. Hybridization efficiency

The effect of probe density on hybridization performance was evaluated separately using a 100 nM RNA target, as shown in the following bar plots (**Figure 4.6**). Despite lower immobilization levels, intermediate probe-to-spacer ratios (particularly 1:5) yielded the highest hybridization response ($\Delta\lambda \approx 1.5$–$1.7$ nm). In contrast, conditions with higher probe density resulted in reduced hybridization signals, indicating that excessive surface coverage limits target accessibility due to steric hindrance and electrostatic repulsion.

While the sensor response confirm successful probe attachment, the hybridization results highlight the importance of controlling probe density to maximize accessibility. An optimal balance between probe coverage and spatial distribution is therefore required, with 2 µM probe concentration at a 1:5 probe-to-spacer ratio providing the best overall performance.

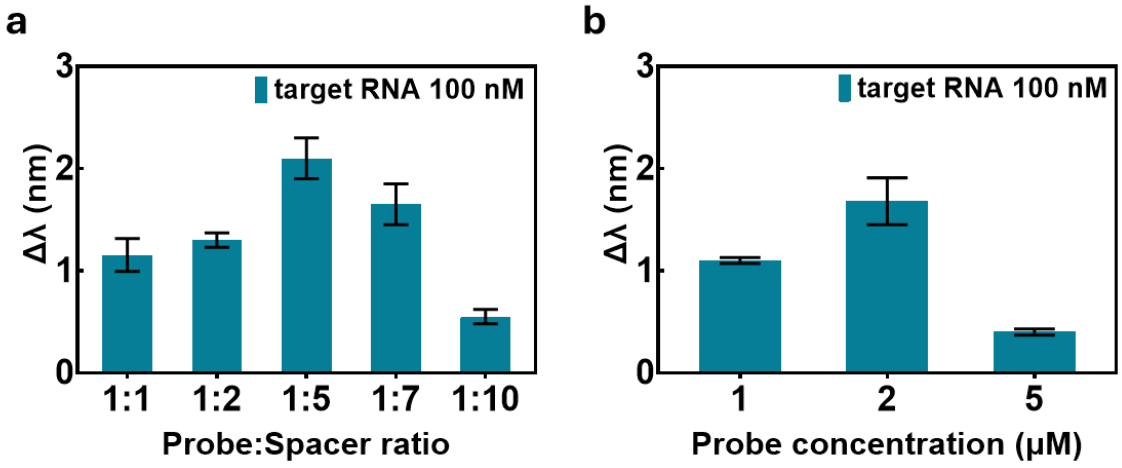


Figure 4.6 100 nM RNA sample hybridization signal with different (**a**) lateral spacer ratios (1:1, 1:2, 1:5, 1:7, 1:10) and (**b**) DNA probe concentrations (1, 2 and 5 µM).

Finally, to assess assay specificity, 100 nM target and non-complementary RNA sequences were injected under the same conditions (**Figure 4.7**). This control produced a negligible

signal, confirming minimal nonspecific interaction and the selectivity of the assay toward the complementary target.

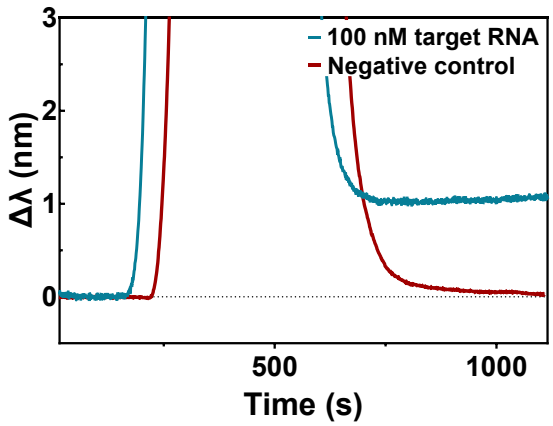


Figure 4.7 SPR hybridization response after injection of a 100 nM 50-nt complementary RNA model target and a 100 nM non-complementary RNA control on functionalized sensor surfaces.

4.3.1.3. Stability of the DNA probe layer

The stability of the immobilized DNA probe layer is a critical parameter for in-flow-based biosensors, and for performing repeated hybridization measurements with the same chip. After each target detection cycle, the bound complementary strand can be removed to regenerate the surface and restore the immobilized probe to its single-stranded state. An effective regeneration protocol should therefore promote dehybridization of the probe–target duplex while preserving the integrity, density, and hybridization capability of the immobilized DNA probe layer.

Regeneration of nucleic acid biosensors is commonly achieved by exposing the surface to chemical conditions that destabilize Watson–Crick base pairing. Several agents can be used for this purpose, including formamide, sodium hydroxide (NaOH), and urea. Formamide lowers the melting temperature of nucleic acid duplexes by weakening hydrogen bonding and reducing duplex stability, allowing strand separation under relatively mild conditions. NaOH promotes dehybridization by creating highly alkaline conditions that disrupt hydrogen bonding between nucleobases. Urea can also destabilize nucleic acid duplexes by interfering with hydrogen bonding and base-stacking interactions.[114,115]

In this thesis, formamide was selected as the regeneration agent because it provides efficient duplex destabilization under milder conditions than strongly alkaline treatments. This was particularly relevant for enabling a common regeneration protocol across both gold and silicon-based sensor platforms used in this thesis. Although gold–thiol probe layers tolerate strongly alkaline conditions such as NaOH, silicon-based surfaces are more sensitive to such treatments; formamide therefore provides a single regeneration strategy applicable to both platforms. Urea was also considered as a denaturing agent, but formamide was preferred because it is widely used for nucleic acid duplex destabilization and can be applied at room temperature without imposing strong pH changes on the surface. In addition, urea can denature proteins, which would make it incompatible with

biofunctionalization strategies based on affinity proteins (e. g. Biotin-Neutravidine); formamide therefore offers broader compatibility as a regeneration agent.

The effectiveness of this strategy was experimentally evaluated using 35% formamide as the regeneration solution. This concentration was selected because it was sufficient to promote dehybridization of the probe–target duplex while preserving the functionality of the immobilized probe layer. Repeated hybridization–regeneration cycles were performed, each consisting of target hybridization followed by exposure to the formamide solution (**Figure 4.8**).

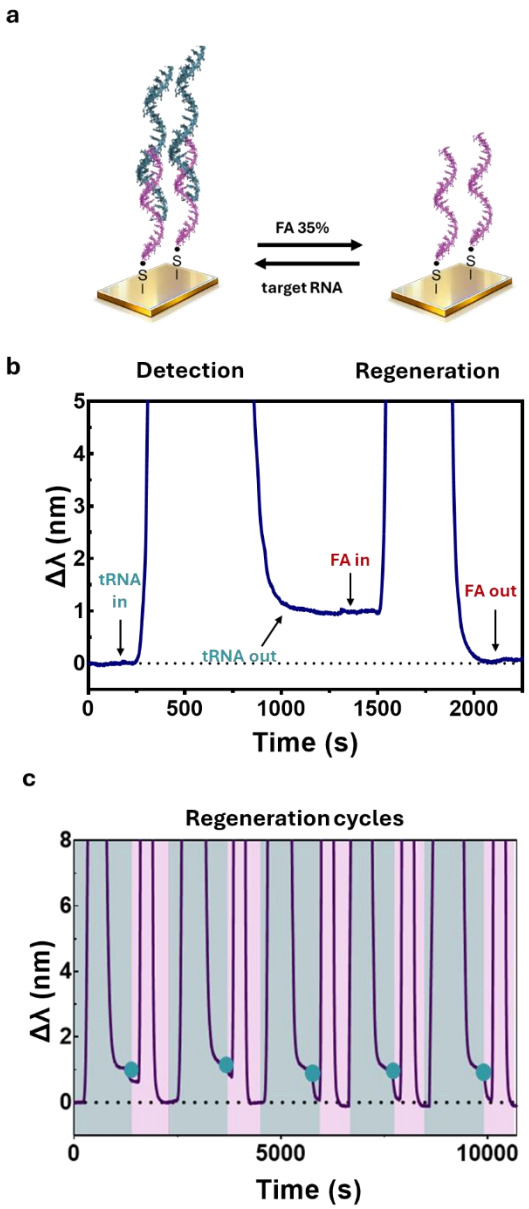


Figure 4.8 (**a**) Schematic representation and (**b**) SPR biosensor sensogram of regeneration of the DNA probe layer on gold surfaces using 35% formamide. (**c**) Repeated hybridization–regeneration cycles were performed to evaluate the stability and reusability of the sensing surface.

Consistent signal recovery was observed across multiple cycles, demonstrating that the sensing surface maintained its hybridization capability after repeated exposure to the regeneration solution. The system showed stable performance over approximately 30 cycles, with a coefficient of variation of approximately 25.0%. These results confirm that 35% formamide enables effective removal of the hybridized target while preserving the activity of the immobilized DNA probes, demonstrating the stability of the gold-based biofunctionalized surface for repeated nucleic acid detection assays.

4.3.2. Silicon-based sensor surfaces

Unlike gold-based sensors, where thiolated DNA probes can be directly immobilized through Au–S chemisorption, silicon-based biosensors require an intermediate functionalization layer. BiMW silicon nitride (Si_3N_4) surfaces do not provide a direct anchoring chemistry for thiol-modified oligonucleotides, and a chemical activation followed by the introduction of a functional scaffold bearing reactive groups is therefore required for DNA probe attachment.

This intermediate scaffold is generated through silanization, a reaction in which silane molecules react with surface hydroxyl groups of the oxidized Si_3N_4 surface to form a covalently anchored organic monolayer. Alkylsilanes have the general formula $R_nSiX_{(4-n)}$ and exhibit a dual chemical character: a hydrolysable group X (–Cl, –OMe, –OEt) that anchors the molecule to the inorganic surface, and an organic functional group R (–NH_2, –SH, –Cl, epoxy, among others) that provides the chemical handle for subsequent biomolecule attachment. The reaction of silane molecules with the surface silanol groups leads to the formation of siloxane bonds (Si–O–Si), which are both thermally and chemically stable.

The silanization reaction proceeds in two steps (**Figure 4.9**). First, the hydrolysable groups of the silane undergo hydrolysis to form silanols (Si–OH), which establish hydrogen bonds with the free hydroxyl groups present on the surface or with adsorbed water molecules. Second, condensation between adjacent silanols, with release of water molecules, leads to the formation of the covalent siloxane network. Water plays a catalytic role in this reaction, and its concentration must be carefully controlled to ensure reproducible monolayer formation.

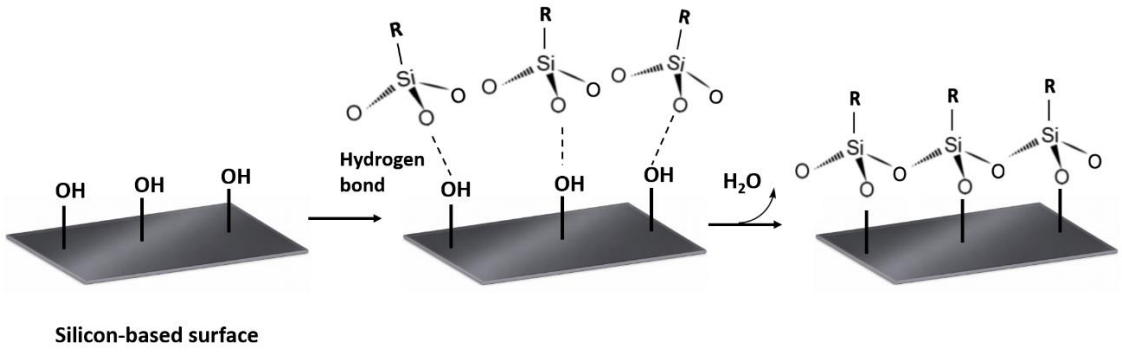


Figure 4.9 General scheme of the silanization reaction on Si_3N_4 surfaces: hydrolysis of the silane hydrolysable groups to silanols and subsequent condensation with surface hydroxyls to yield siloxane (Si–O–Si) bonds.

In this thesis, different silanization strategies were evaluated to functionalize the Si_3N_4 sensing surface and enable stable, accessible, and reproducible DNA probe immobilization, including different silane molecules and crosslinkers. Compared with gold–thiol chemistry, silanization is more sensitive to surface cleaning, hydroxylation, solvent conditions, humidity, and incubation time, all of which affect layer homogeneity and consequently the quality of the subsequent DNA probe immobilization. The control of the functionalized interface is therefore a critical step for silicon-based biosensors.

4.3.2.1. Hydrophilic polyethylene glycol (PEG)-based Silane strategies

Based on previous research performed within the group, we first tested the use of polyethylene glycol (PEG)-containing silane molecules for surface silanization. These molecules are considered to provide not only a functional scaffold but also a highly hydrophilic layer that aids minimizing nonspecific adsorptions of sample matrix components. [116–118]

Three PEG-silane molecules with different terminal functional groups were compared: carboxyl (–COOH), amine ($–NH_2$), and biotin. Each functional group provides a different mechanism for DNA probe attachment. The COOH-functionalized surface relies on activation of the carboxyl groups with N-(3-dimethylaminopropyl)-N'-ethylcarbodiimide hydrochloride (EDC) and N-hydroxysuccinimide (NHS), followed by covalent coupling with NH_2-modified DNA probes. The NH_2-functionalized surface introduces amine groups at the interface, which are subsequently activated with p-phenylene diisothiocyanate (PDITC) to allow covalent immobilization of modified DNA probes. And the biotin-functionalized surface uses neutravidin as an intermediate layer for the immobilization of biotinylated DNA probes (**Figure 4.10**).

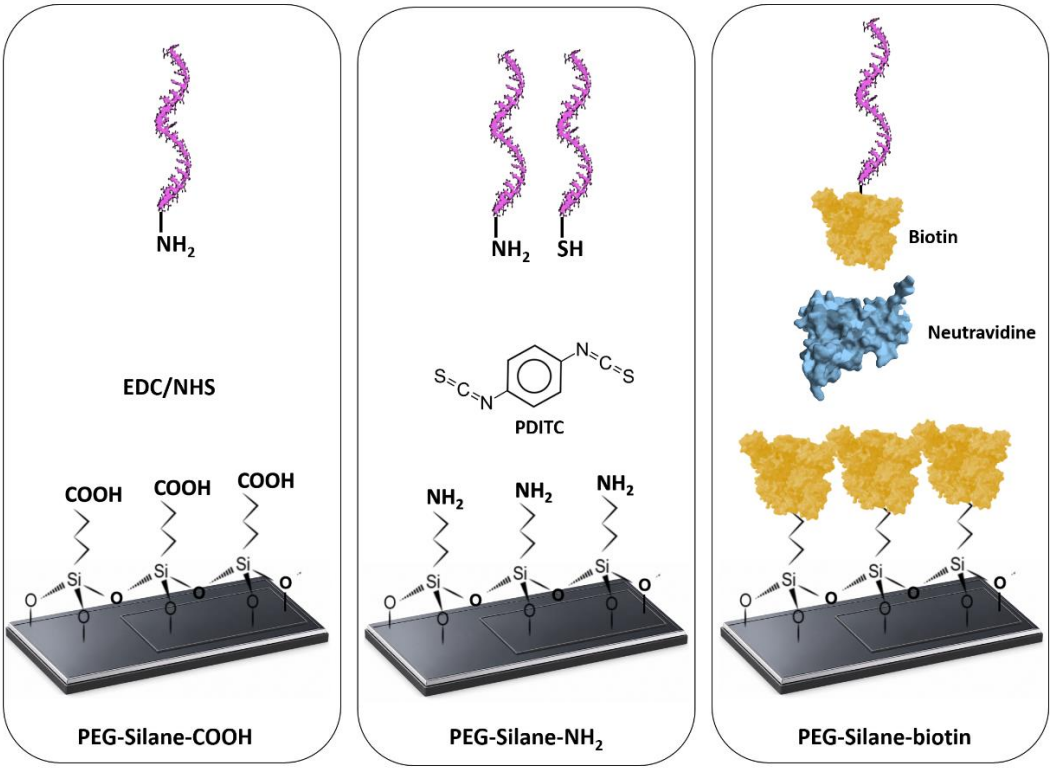


Figure 4.10 Schematic representation of the three PEG-silanes evaluated and their corresponding immobilization chemistries: PEG–silane–COOH/EDC–NHS/NH_2-DNA, PEG–silane–biotin/neutravidin/biotin-DNA, and PEG–silane–NH_2/PDITC/modified DNA probe.

PEG-silane–COOH functionalization

The PEG–silane–COOH strategy was first evaluated as a reference approach, since this chemistry had previously been successfully used in the group for protein and antibody immobilization. In this configuration, the silanized surface presents terminal carboxyl groups that can be activated with EDC/NHS chemistry, enabling covalent coupling with NH_2-modified biomolecules (**Figure 4.11**).

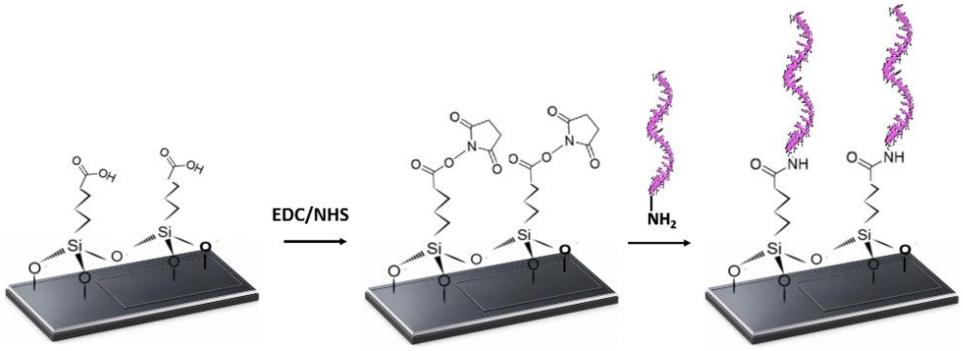


Figure 4.11 Schematic of PEG–silane–COOH functionalization, EDC/NHS activation, and NH_2-DNA probe immobilization.

The PEG–silane–COOH layer was formed by incubating the Si_3N_4 sensor surface with a 25 µg/mL PEG–silane solution in DMSO. The resulting carboxyl groups were activated using a 0.2 M EDC / 0.05 M NHS solution prepared in MES buffer and injected at a flow rate of 5 µL/min. NH_2-modified DNA probes were then immobilized in situ at concentrations of 2, 5, and 10 µM. Under these conditions, no significant immobilization signal was observed. The probe concentration was therefore further increased to 20 µM, a value considerably high for surface immobilization assays, in an attempt to force the coupling reaction and maximize the amount of DNA attached to the surface. Even at this high probe concentration, the immobilization signal remained very low, indicating limited DNA probe attachment. This reduced probe density directly affected hybridization performance, resulting in weak and poorly reproducible target responses: a 100 nM RNA target produced a phase shift of only ≈ 0.20 rad, confirming the limited sensitivity achieved with this biofunctionalization strategy (**Figure 4.12**).

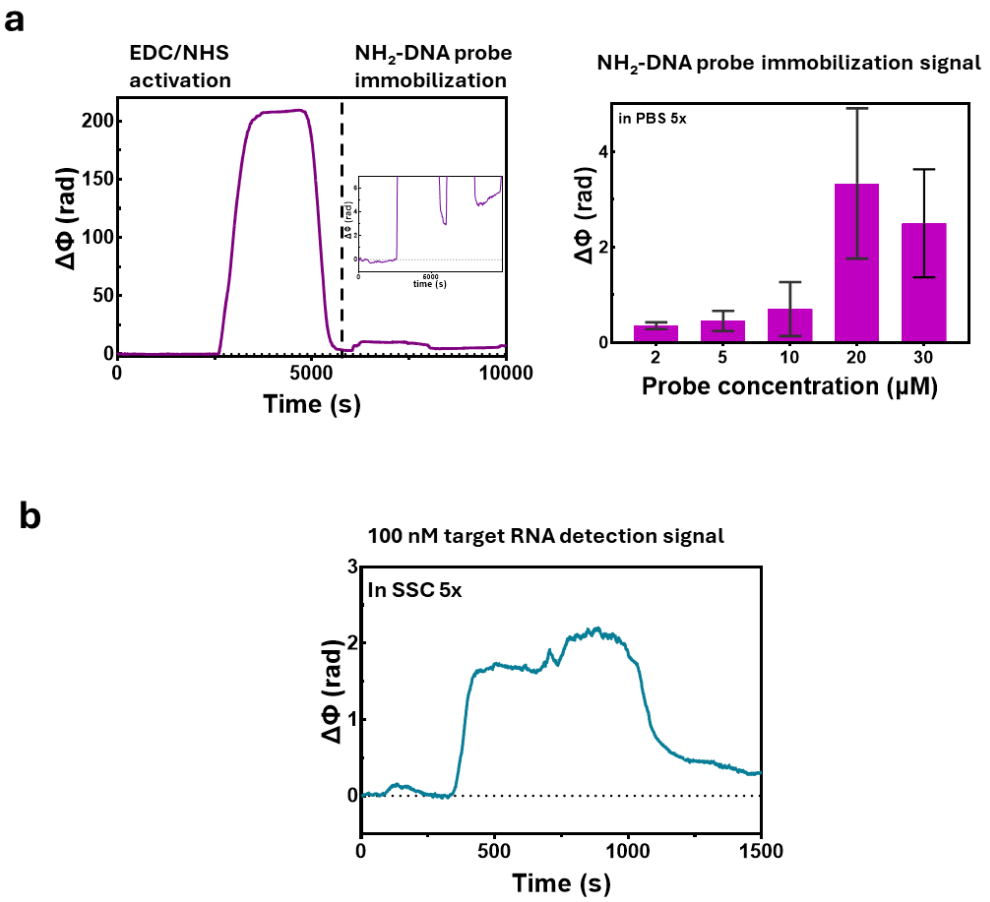


Figure 4.12 (**a**) Immobilization signals with different probe concentration (2, 5, 10, 20 and 30 μM) and (**b**) hybridization signals obtained using PEG–silane–COOH.

The low immobilization efficiency observed with the PEG–silane–COOH strategy can be explained by the specific requirements of EDC/NHS coupling when applied to DNA probes. This chemistry had previously worked well for antibody immobilization partly because antibodies contain multiple accessible primary amine groups, mainly from lysine residues, increasing the probability of covalent attachment to the activated carboxyl surface. In contrast, the NH_2-modified DNA probe used here contains only one terminal amine group per molecule, so the immobilization efficiency depends on the successful reaction of a single reactive site. In addition, EDC/NHS activation of carboxyl groups is time-sensitive: the activated NHS-esters are reactive only for a limited period and can lose activity through hydrolysis before reacting with the amino-modified probe. The combination of short-lived activated carboxyl groups and a single terminal amine on the DNA probe therefore reduces the probability of efficient covalent coupling, even when the PEG–silane–COOH layer is properly formed.[119]

PEG-silane–NH_2 functionalization

As a second strategy, amine-terminated PEG-silane (PEG–silane–NH_2) surfaces were evaluated to determine whether introducing surface amines, followed by a more stable crosslinking, could provide a more efficient covalent immobilization route for DNA probes. PDITC was selected as the bifunctional crosslinker because of its versatility: it reacts with primary amine groups on the surface to generate isothiocyanate groups, which can

subsequently react with different nucleophilic groups on DNA probes (i.e., amines or thiols) forming stable covalent bonds. PDITC is also a relatively short and rigid linker, minimizing the distance between the surface and the immobilized probe; this compact interface can be advantageous for surface confined hybridization assays, where the accessibility and orientation of the probe strongly influence the target response (**Figure 4.13**).



Figure 4.13 Schematic of PEG–silane–NH_2 functionalization, PDITC activation, and DNA probe immobilization.

The PEG–silane–NH_2 layer was prepared at 25 µg/mL in DMSO and incubated on the Si_3N_4 sensor surface, followed by activation with 20 mM PDITC in an *ex situ* step.[120] Probe immobilization was then carried out *in situ* at a flow rate of 5 µL/min using two probe chemistries: an amine-terminated probe and a thiol-modified probe (**Figure 4.14**).

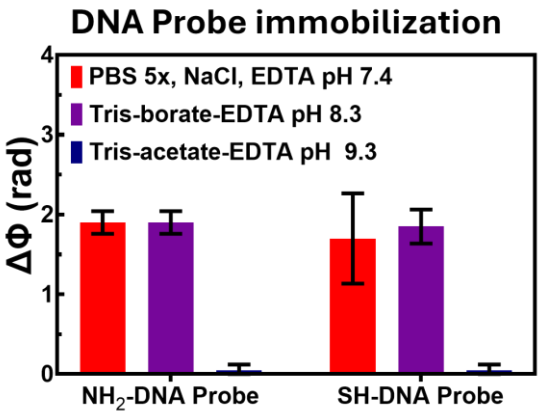


Figure 4.14 DNA probe immobilization on PEG–silane–NH_2 surfaces activated with PDITC. (bar plot of immobilization signal for the tested probe (-SH and -NH2)

The sensor signals obtained were very low or negligible for both probe chemistries, indicating that neither the NH_2- nor the SH-modified probes achieved efficient immobilization on the PEG–silane–NH_2 layer. Since two different probe terminations were evaluated and both failed, the limitation is unlikely to arise from the probe end group alone. Instead, the results suggest that the PEG–silane–NH_2 layer did not provide a sufficiently dense or accessible amine interface for efficient PDITC activation and subsequent probe coupling.

Biotin-functionalized PEG-silane surface

The biotin-functionalized PEG-silane was evaluated as a third approach for DNA probe immobilization. In this configuration, the sensor surface is first modified with PEG–silane–biotin, followed by neutravidin immobilization and subsequent attachment of biotinylated DNA probes (**Figure 4.15**).

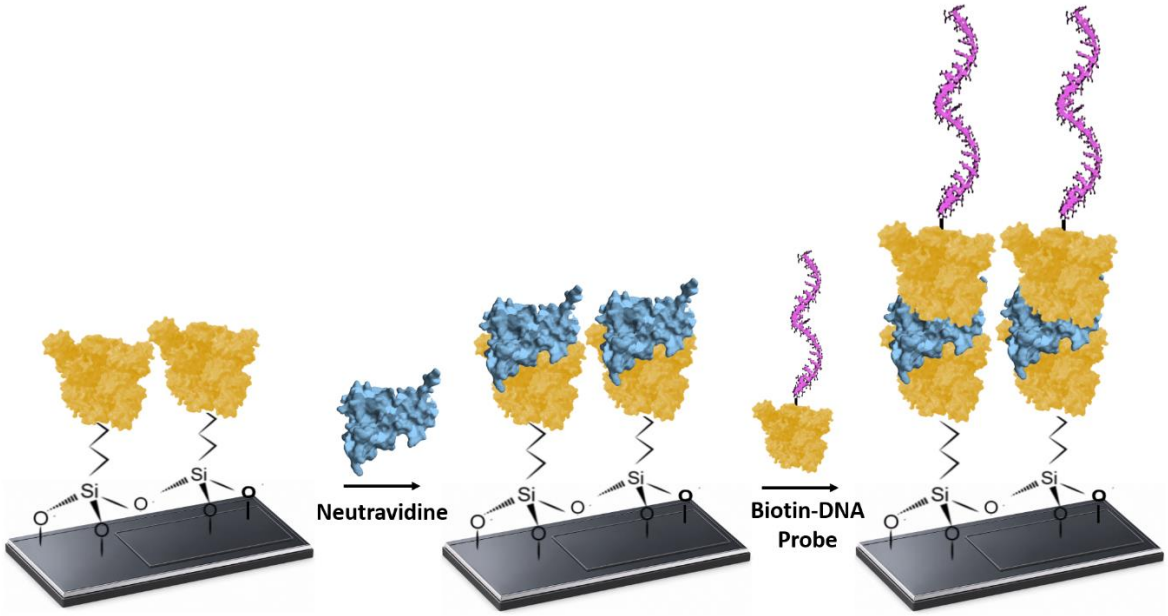


Figure 4.15 Schematic of PEG–silane–biotin functionalization, neutravidin immobilization, and biotin-DNA probe attachment.

The biotin–neutravidin interaction is one of the strongest non-covalent interactions used in biosensing, with a dissociation constant in the order of 10^{-15} M, making it an attractive strategy for achieving stable and specific probe immobilization while preserving a modular surface functionalization approach.[121] Compared with the previously tested COOH/NH_2 coupling strategies, this approach offers two important advantages. First, probe attachment does not depend on a short-lived activated ester intermediate, as occurs in EDC/NHS coupling. Second, neutravidin provides four biotin-binding sites, which increases the availability of binding sites at the surface and facilitates the immobilization of biotinylated DNA probes; even though each DNA probe contains only one biotin group, the neutravidin layer improves the organization and accessibility of the immobilization interface.[122]

The sensor surface was first modified with a PEG–silane layer functionalized with biotin groups at 25 µg/mL. Neutravidin was then immobilized *in situ* at concentrations of 10, 25, 50, and 100 µg/mL under a constant flow rate of 10 µL/min, in order to determine the optimal surface coverage (**Figure 4.16a**). The immobilization signal increased with neutravidin concentration up to 25 µg/mL, indicating progressive surface coverage. Above this value, the measured signal decreased, suggesting saturation of the available binding sites. Based on these results, 25 µg/mL was selected as the optimal neutravidin concentration.

Following this step, biotinylated DNA probes were immobilized *in situ* at concentrations of 2, 4, 10, and 33 µM (**Figure 4.16b**). The immobilization signal increased with probe concentration up to 10 µM, reflecting improved probe coverage and accessibility. At higher concentrations the signal decreased, indicating that excessive probe density can introduce steric hindrance effects that reduce binding efficiency. A 10 µM concentration was therefore selected for biotinylated probe immobilization.

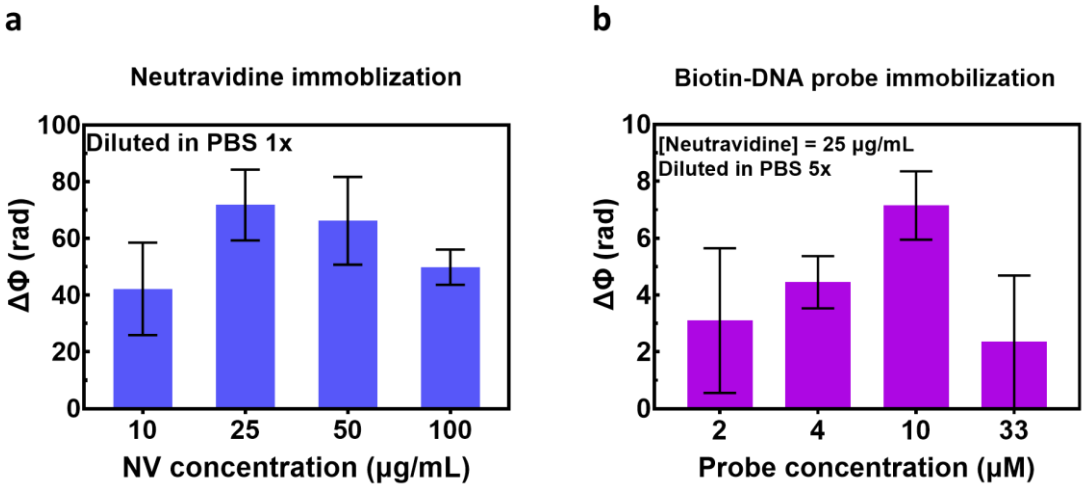


Figure 4.16 (**a**) Neutravidin immobilization saturation and (**b**) Biotin-DNA probe immobilization study.

Since the biotin-based strategy showed more promising immobilization than the COOH- and NH_2-based approaches, the influence of the immobilization buffer composition was further investigated (**Figure 4.17**). The incorporation of ethylenediaminetetraacetic acid (EDTA), sodium chloride (NaCl), and 1% FA in PBS 5× resulted in a noticeable increase in the immobilization signal. NaCl reduces the electrostatic repulsion associated with the negatively charged phosphate backbone of DNA through screening by Na^+ counterions; EDTA, as a chelating agent, can stabilize secondary structures and reduce nonspecific interactions; and the addition of a low percentage of FA partially destabilizes hydrogen bonding within nucleic acid secondary structures, reducing probe folding and improving accessibility to the target. In contrast, immobilization in tris-borate-EDTA buffer (TBE, pH 8.3) led to a lower signal, likely due to the different ionic composition and mildly basic pH, which may reduce favourable probe organization and biotin accessibility at the surface.[123]

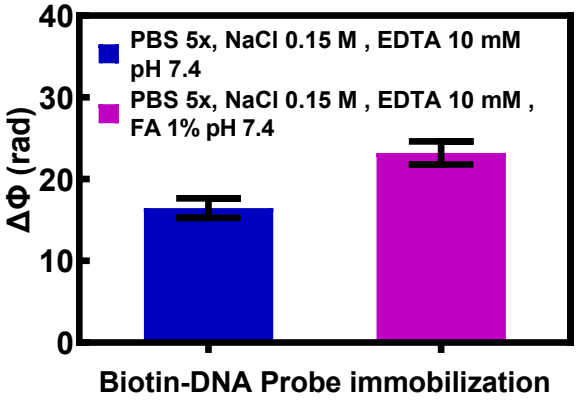


Figure 4.17 Effect of buffer composition on biotin-DNA probe immobilization.

To assess whether the higher immobilization signals translated into improved sensing performance, hybridization was evaluated by injecting a 100 nM RNA target complementary to the immobilized probe. Under the optimized immobilization conditions, the biotin-based surface produced a much stronger response than the previous PEG-silane strategies, reaching a phase shift of ≈ 3.9 rad (**Figure 4.18**). This result confirmed that the biotin–neutravidin architecture enabled efficient and accessible probe immobilization for RNA recognition.

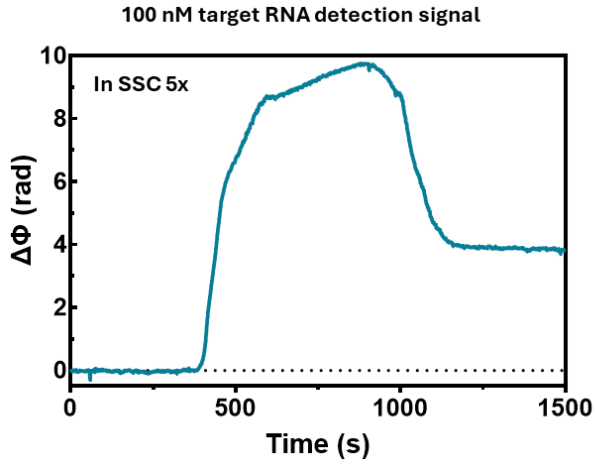


Figure 4.18 Sensogram showing DNA probe immobilization and subsequent hybridization with 100 nM RNA target on PEG–silane–biotin/neutravidin surfaces.

After evaluating the three PEG-silane strategies, their performance was compared in terms of protocol simplicity, DNA probe immobilization, hybridization response, and reproducibility (**Table 4.1**). All three approaches are experimentally simple and compatible with standard biosensor biofunctionalization workflows, but they differed markedly in immobilization and detection performance. The PEG–silane–COOH and PEG–silane–NH_2 strategies resulted in low or negligible probe immobilization and weak hybridization responses, whereas the PEG–silane–biotin strategy provided the highest immobilization and hybridization signals. This improvement is likely related to the high affinity of the biotin–neutravidin interaction and to the multiple biotin-binding sites available on neutravidin, although the reproducibility of the underlying silane layer remained a limitation.

Table 4.1 Comparison of different silanization strategies for DNA probe immobilization and RNA target detection on BiMW sensors.

Silane	***Immobilization strategy***	***Simplicity***	***Probe immobilization signal***	***Hybridization signal***
PEG–silane–COOH	EDC/NHS activation + NH_2-DNA probe	High	Low	Low (~0.20 rad at 100 nM target)
PEG–silane–NH_2	PDITC activation + NH_2- or SH-DNA probe	High	Negligible	Negligible
PEG–silane–Biotin	Neutravidin immobilization + biotin-DNA probe	High	Good	Very good (~3.9 rad at 100 nM target)

Unfortunately, although the biotin-based strategy gave the best immobilization and hybridization signals in this preliminary study, an excessive batch-to-batch variability was observed in subsequent experiments, limiting robustness and reproducibility. Therefore, an APTES-based silanization was investigated as a more controlled alternative for silicon-based biofunctionalization.

4.3.2.2. APTES-based silanization strategies

Among the available silanes, (3-aminopropyl)triethoxysilane (APTES) is the most widely used and well-characterized coupling agent for the biofunctionalization of silicon-based surfaces in biosensing, owing its terminal amino group suitable for subsequent crosslinker coupling, and its well-established reactivity with silanol-rich surfaces. Despite its widespread use, however, a large number of different APTES protocols have been reported, differing in solvent, concentration, deposition method, reaction time, and curing conditions, often yielding markedly different surface qualities. A systematic optimization is therefore necessary to identify reproducible conditions suitable for the silicon-based BiMW platform.

Owing to this variety of reported protocols, a preliminary optimization of the silanization conditions was first carried out on the SPR platform, taking advantage of its greater robustness and simpler handling compared with the BiMW waveguides, which makes it well suited for rapid screening of surface-chemistry parameters. This preliminary study, including the comparison of different silane chemistries and reaction conditions, is presented in detail in **Annex A**. The present section focuses on the strategies subsequently tested on the BiMW platform and on the criteria that led to the selection of the optimal protocol.

Immobilization efficiency

The first APTES protocol evaluated was based on liquid-phase silanization in anhydrous toluene. This solvent was selected because the presence of uncontrolled water during APTES deposition can promote excessive hydrolysis and polymerization of silane molecules in solution, leading to multilayer formation and poorly reproducible surfaces. To minimize this effect, 1% (v/v) APTES was prepared in water-free toluene, and the silanization was performed under controlled atmosphere. N,N-diisopropylethylamine (DIPEA, 0.5% v/v) was added to the reaction mixture to catalyze the silanization under low-water conditions. The objective was to favour APTES grafting onto the activated Si_3N_4 surface while limiting uncontrolled polymerization in the bulk solution.[124,125]

Using this protocol, DNA probe immobilization was achieved after PDITC activation (20 mM). For the selected condition of 2 µM thiolated DNA probe with a 1:2 probe-to-spacer ratio, relatively high immobilization signals were obtained, $\Delta\phi \approx 41.3$ rad (**Figure 4.19**). However, the coefficient of variation was CV = 38.0%, indicating poor reproducibility between independent silanization experiments. This suggests that, although toluene reduces bulk water content, the reaction remains highly sensitive to the amount of residual water present at the surface: a very low water content may limit APTES hydrolysis and reduce homogeneous grafting, whereas small uncontrolled differences in humidity can lead to variations in silane polymerization and surface coverage. The toluene-based protocol therefore allowed DNA immobilization but did not provide sufficient reproducibility for robust biofunctionalization.

APTES silanization in ethanol was then evaluated to improve the reproducibility of the liquid-phase process. Using 2% (v/v) APTES in ethanol followed by PDITC activation (20 mM), under the same DNA probe immobilization conditions, the ethanol-based protocol showed improved reproducibility, with a lower coefficient of variation (CV = 15.8%) (**Figure 4.19**). This improvement may be related to better surface wetting and to the presence of a controlled amount of residual water, which can facilitate APTES hydrolysis and condensation with surface hydroxyl groups. However, the variability remained higher than that obtained with vapor-phase silanization, indicating that liquid-phase deposition still provides limited control over silane layer formation.[126]

Vapor-phase APTES silanization provided the most reproducible immobilization response among the three evaluated strategies. After PDITC activation (20 mM), at the same fixed immobilization conditions, it produced an immobilization signal of $\Delta\phi = 52.2$ rad with the lowest coefficient of variation (CV = 7.20%). This indicates that vapor-phase deposition improves control over APTES layer formation by reducing uncontrolled polymerization in bulk solution, resulting in a more reproducible amine-functionalized interface for DNA probe attachment (**Figure 4.19**).[127–130]

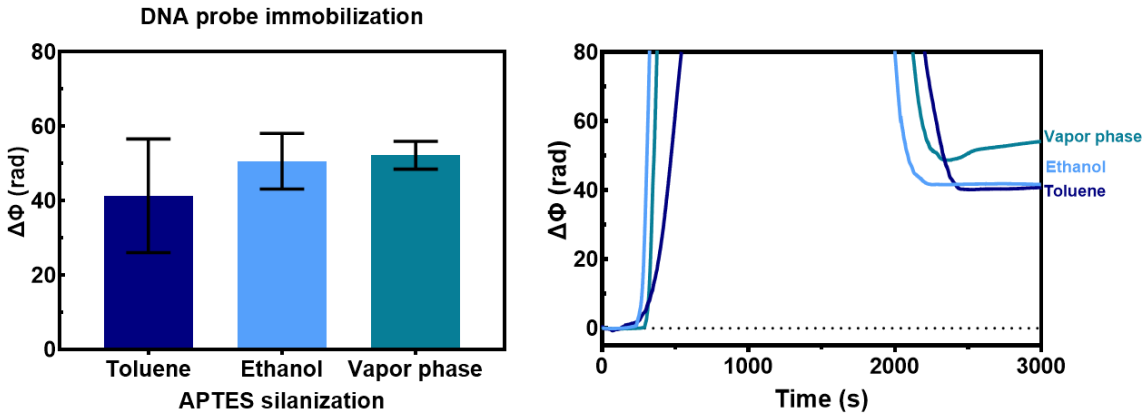


Figure 4.19 DNA probe immobilization sensor signals with different APTES silanizations: dilluted in toluene, ethanol, and vapor phase.

Hybridization efficiency

After the immobilization study, the same surfaces were tested with a 100 nM RNA target to evaluate probe accessibility (**Figure 4.20**). The toluene-based protocol produced a detectable hybridization signal of $\Delta\phi \approx 5.3$ rad, but the response remained highly variable, following the same trend observed for probe immobilization. The ethanol-based protocol improved the target response, reaching $\Delta\phi \approx 7.1$ rad. The vapor-phase strategy provided the highest hybridization response, with $\Delta\phi \approx 10.3$ rad, confirming it as the most reliable APTES silanization approach for BiMW biofunctionalization. This result confirms the successful transfer of the optimized surface chemistry to the BiMW platform and highlights the higher sensitivity of the interferometric transducer.

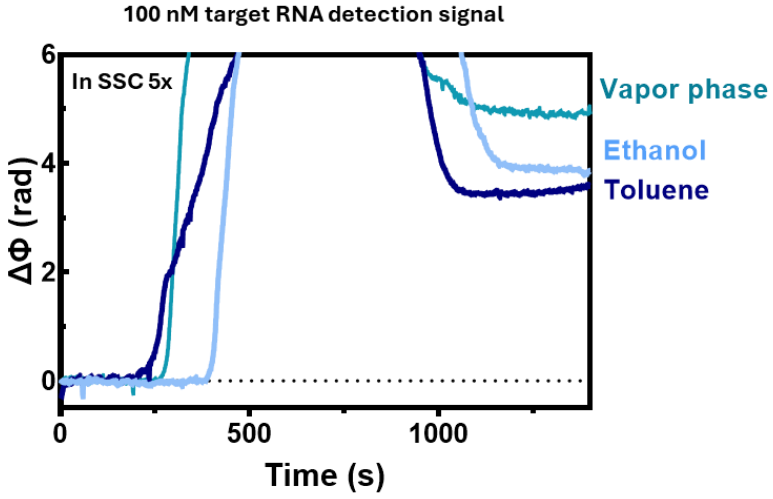


Figure 4.20 Hybridization response after injection of 100 nM RNA target on BiMW sensors functionalized with APTES/PDITC using toluene, ethanol, or vapor-phase silanization.

This result confirms vapor-phase APTES silanization as the most reliable strategy evaluated on the BiMW platform, in agreement with the trend previously observed on the SPR sensor (**Annex A**).

4.3.2.3. Stability of the DNA probe layer

The stability of the DNA probe layer immobilized through the vapor-phase APTES/PDITC strategy was evaluated by repeated hybridization–regeneration cycles. Since regeneration must remove the hybridized target without compromising the immobilized probe layer, two conditions were tested: 5 mM NaOH and 35% formamide.[86,125]

First, 5 mM NaOH was evaluated, following the strategy previously used for gold surfaces. However, this condition was not compatible with the Si_3N_4/APTES/PDITC interface. After NaOH exposure, the sensor showed poor baseline recovery, indicating deterioration of the functionalized surface (**Figure 4.21**). This behaviour is consistent with the limited stability of organosilane layers under alkaline conditions, where base-catalysed hydrolysis of siloxane bonds can disrupt the APTES layer and compromise DNA probe immobilization. Therefore, NaOH was discarded for BiMW regeneration.

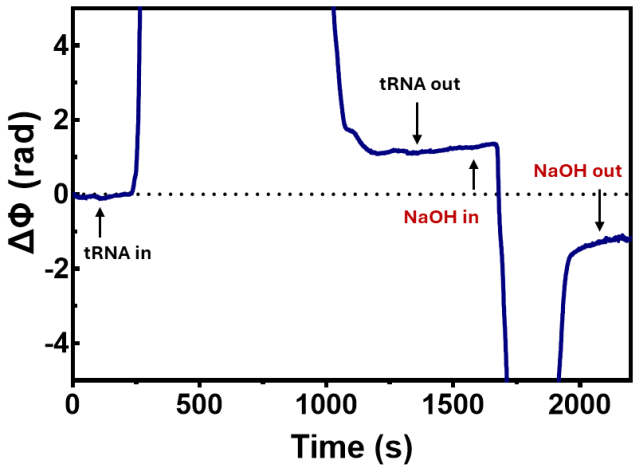


Figure 4.21 Regeneration with NaOH 5 mM using the BiMW sensor functionalized with vapor-phase APTES/PDITC.

Regeneration was then performed using 35% formamide, which destabilizes nucleic acid duplexes by lowering their melting temperature, allowing target removal under milder chemical conditions (**Figure 4.22**).

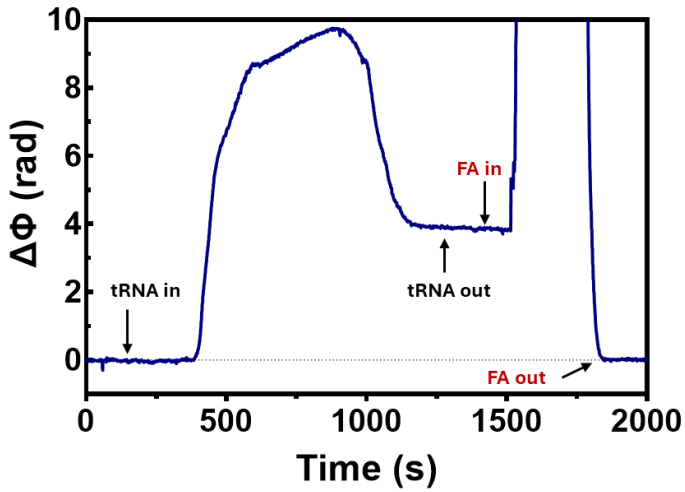


Figure 4.22 Regeneration with FA 35% using the BiMW sensor functionalized with vapor-phase APTES/PDITC.

Using this strategy, consistent signal recovery was observed over 20 hybridization–regeneration cycles, demonstrating that the Si_3N_4 sensing surface maintained its hybridization capability after repeated use. The system exhibited stable performance, with a coefficient of variation of approximately 25%. Although this variability indicates that repeated chemical and fluidic treatments still affect the response to some extent, the preservation of hybridization capacity confirmed that 35% formamide was compatible with the APTES/PDITC-functionalized BiMW surface and was therefore selected for subsequent assays.

4.4. Hybridization assay

Once the surface biofunctionalization strategies were established for both biosensor platforms (gold and silicon-based), attention was directed toward optimizing the hybridization assay with the complementary RNA target. Although the immobilization of DNA probes provides the necessary biorecognition element, efficient target detection at the sensor interface is not solely determined by sequence complementarity. Hybridization under surface confined conditions is influenced by a combination of physicochemical factors, including electrostatic interactions, steric constraints, and the conformational behaviour of both probe and target strands. A systematic study of the hybridization environment was therefore required in order to identify conditions that favour stable and reproducible duplex formation.[105,108,113]

To evaluate the influence of pH on hybridization efficiency, a set of representative buffer systems covering acidic, neutral, and mildly basic conditions was selected. Sodium acetate buffer at pH 4.5, saline-sodium citrate (SSC) buffer at pH 7.4, and Tris–EDTA (TE) buffer at pH 8.5 were chosen as model systems due to their widespread use in nucleic acid assays and their distinct physicochemical properties. As shown in **Figure 4.23**, the hybridization response exhibited a clear dependence on pH: the highest signals were obtained under near-neutral conditions, specifically at pH 7.4 using SSC buffer, while both acidic and mildly basic environments resulted in a noticeable decrease in signal intensity.

This behaviour can be understood by considering the chemical nature of nucleic acid interactions. At low pH, partial protonation of nucleobases interferes with Watson–Crick hydrogen bonding, destabilizing duplex formation. Under mildly basic conditions, changes in hydrogen bond stability and stronger electrostatic repulsion between negatively charged strands can also reduce hybridization efficiency. Neutral pH therefore provides the most favourable environment for RNA/DNA duplex formation at the sensor surface.

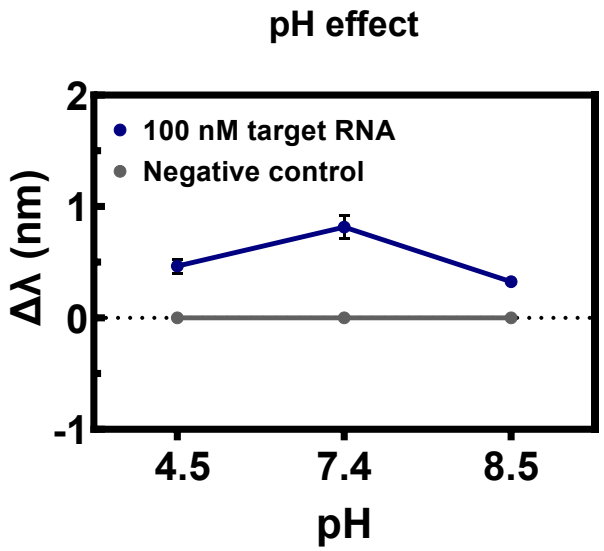


Figure 4.23 pH effect in target hybridization.

The role of ionic strength was then examined by varying the concentration of SSC buffer between 0.45 and 1.50 M. The ionic environment plays a central role in nucleic acid hybridization, since the negatively charged phosphate backbones of DNA and RNA strands generate electrostatic repulsion that can hinder duplex formation; increasing the salt concentration reduces this repulsion, facilitates strand approach, and stabilizes the hybridized structure.[131,132]

As shown in **Figure 4.24**, increasing ionic strength improved the hybridization signal up to an optimal value. The maximum response was obtained at 0.75 M SSC, corresponding to 5× SSC conditions, after which no further enhancement was observed. At higher salt concentrations the signal tended to plateau or slightly decrease, suggesting that beyond a certain point additional ionic strength does not improve hybridization and may instead promote undesirable effects such as stabilization of secondary structures in the RNA target or increased non-specific interactions. The optimal ionic strength therefore reflects a balance between efficient duplex formation and preservation of target accessibility.

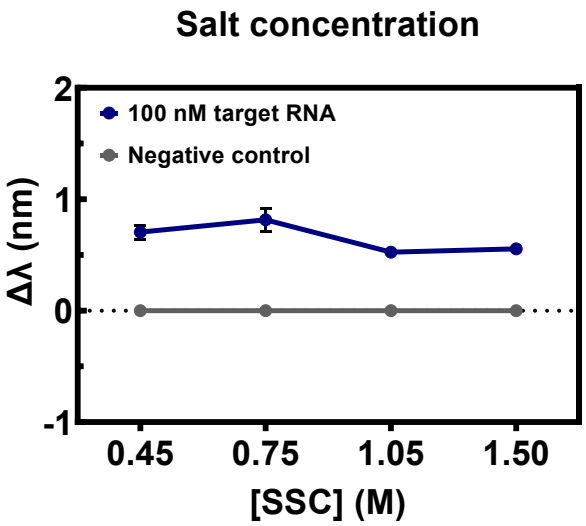


Figure 4.24 Salinity effect in target hybridization.

In addition to pH and ionic strength, the effect of buffer additives can be considered to further improve hybridization efficiency. As mentioned before, FA is widely used in nucleic acid assays as a denaturing agent, since it reduces the melting temperature of duplexes by weakening hydrogen bonding interactions. But this property is especially relevant for RNA target detection, which often adopt stable secondary structures that limit their availability for hybridization; partial destabilization of these structures by FA can therefore enhance target accessibility and promote more efficient binding to the immobilized probe (**Figure 4.25**).[123,133]

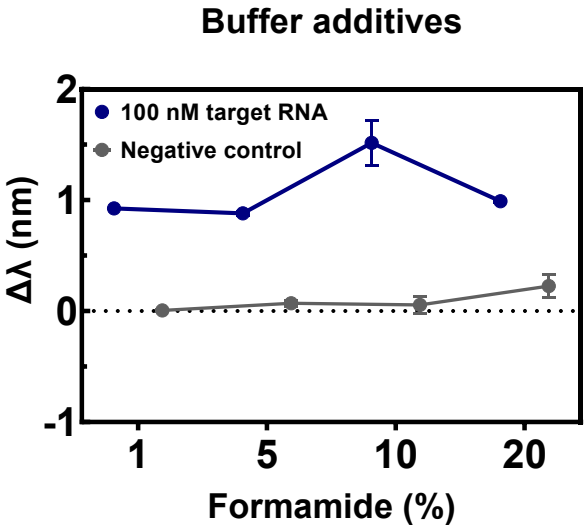


Figure 4.25 Formamide effect in target hybridization.

Beyond formamide, tetramethylammonium chloride (TMAC) can also be used as a hybridization additive, since it reduces the dependence of duplex stability on GC content and helps make hybridization conditions more uniform across different sequences. However, the effect of any such additive depends strongly on the specific target sequence,

probe design, surface chemistry, and sensor platform, and its concentration must therefore be optimized for each individual assay (**Figure 4.26**).[134]

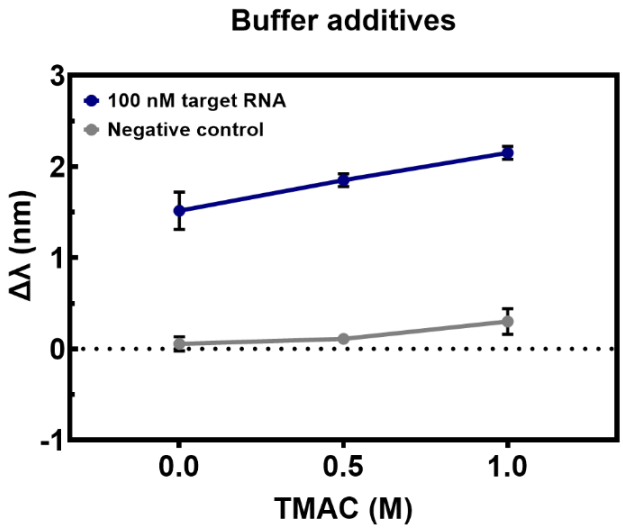


Figure 4.26 TMAC effect in target hybridization.

Based on these results, SSC buffer at pH 7.4 and 0.75 M was selected as a baseline hybridization condition for subsequent assay development. These conditions should not, however, be considered universal: hybridization efficiency depends strongly on the specific probe/target pair, including sequence composition, GC content, target length, and the presence of secondary structures. Even small changes in the nucleic acid sequence can modify the accessibility of the target region and the stability of the duplex formed at the sensor surface.

In addition, the optimal hybridization conditions may vary depending on the sensor platform, since parameters such as surface chemistry, probe density, and sensing mechanism can influence the balance between target signal and non-specific response. The final assay conditions must therefore be refined for each specific biosensor configuration. This is particularly relevant in the following chapters, where different hybridization conditions are used for the SPR and BiMW platforms.

4.5. Conclusions

We established biofunctionalization protocols for DNA probes on two transducer platforms: gold-based SPR sensors through direct Au–S chemisorption, and silicon-based BiMW sensors through vapor-phase APTES silanization combined with PDITC crosslinking. On gold, the systematic study of probe concentration and probe-to-spacer ratio identified an optimal compromise (2 μM probe, 1:5 ratio) that maximizes the hybridization response rather than probe loading, demonstrating that excessive probe density compromises target accessibility through steric and electrostatic effects. On silicon-based surfaces, three PEG-silane strategies (COOH, NH_2, and biotin) and three APTES deposition protocols (toluene, ethanol, and vapor phase) were compared, and vapor-phase APTES/PDITC was selected as the most reproducible chemistry, yielding an immobilization signal of $\Delta\phi \approx 52.2$ rad with a coefficient of variation of 7.20%. The optimized hybridization conditions (5× SSC, pH 7.4)

enabled the detection of the 50-nt RNA model target on both platforms, with the gold-thiol platform additionally validated against a non-complementary RNA control to confirm assay selectivity.

The presented methodology constitutes a versatile approach for the generation of nucleic acid–based biosensors on both gold and silicon-based surfaces. The vapor-phase APTES/PDITC chemistry is particularly suitable for the transfer of methodologies developed on SPR to the BiMW interferometer, allowing the higher sensitivity of the silicon platform to be exploited while preserving the modularity of probe design that makes thiol–gold chemistry attractive. Because PDITC reacts with a wide range of nucleophilic groups ($–NH_2$, –SH), the same biofunctionalized interface can be readily extended to other biorecognition elements requiring covalent anchoring to the sensor surface, supporting future development of multi-analyte BiMW assays in which probes for different biomarkers are immobilized on independent sensing arms of the same chip.

Finally, we demonstrated the reusability of both biofunctionalized interfaces through repeated hybridization–regeneration cycles using 35% formamide, which dehybridized the bound RNA target while preserving the immobilized probe layer. The gold surface supported approximately 30 stable cycles and the BiMW surface 20 cycles, both with a coefficient of variation of ~25%, confirming that the chemistries selected withstand repeated chemical regeneration without significant loss of activity, providing a reliable basis for repeated multi-cycle measurements and substantially reduce the cost per analysis by enabling reuse of the same sensor chip.

In summary, we developed a biofunctionalization and hybridization base for both SPR and BiMW photonic biosensors, comprising the probe immobilization chemistries, the optimized hybridization buffer, and the regeneration protocol, that will be applied in the following chapters for the development of nucleic acid–based assays targeting biomarkers of clinical relevance.

Chapter 5

PHOTONIC BIOSENSORS FOR THE SCREENING OF ZOONOTIC CORONAVIRUSES

The design, development and analytical validation of SPR and BiMW biosensor assays for the screening of zoonotic coronaviruses is presented. A detailed explanation of the probe design strategy for SARS-CoV-2 (E and N genes), alpha/beta-coronaviruses and gamma-coronaviruses is provided, followed by the development of direct hybridization assays on the SPR platform and the implementation of an antibody-based signal amplification strategy. The chapter also describes the transfer of the optimized assays to the BiMW interferometer for the direct, one-step detection of viral RNA, and their benchmarking against in vitro transcribed RNA standards. Finally, the developed biosensors are validated with viral RNA extracted from real animal samples (bat faecal samples and chicken swabs) provided by the collaborating laboratories within the CoNVat and MUSECOV projects, and their diagnostic performance is compared with the corresponding molecular reference methods.

5. Photonic biosensors for screening of zoonotic coronaviruses

This chapter focuses on the development of photonic biosensor assays for rapid coronavirus RNA screening within the framework of two European research projects: the CoNVaT project, funded by the European Commission under the H2020-SC1-PHE-CORONAVIRUS-2020 call (Grant Agreement No. 101003544), and the MUSECOV project, supported by the International Coordination of Research on Animal Diseases (ICRAD ERA-NET) and funded by the Spanish Ministry of Science and Innovation (Grant PCI2020-120687-2, funded by MCIN/AEI/10.13039/501100011033 and by the European Union NextGenerationEU/PRTR). The work was specifically carried out in collaboration with Prof. Jordi Serra-Cobo, University of Barcelona, for bat coronavirus samples, and Dr. Céline Courtillon, Ploufragan-Plouzané-Niort Laboratory of the French Agency for Food, Environmental and Occupational Health & Safety (ANSES, Ploufragan, France), for avian coronavirus samples. These collaborations guided the selection of biologically relevant targets and provided reference molecular methods and real animal samples for validation.

5.1. Zoonotic viruses and surveillance strategies

Coronaviruses represent a major group of zoonotic pathogens with the capacity to circulate in animal reservoirs and cross species barriers, leading to the emergence of human infections.[135,136] Members of the Coronaviridae family are classified into four genera: alpha-, beta-, gamma-, and delta-coronaviruses (**Figure 5.1**). Alpha-coronaviruses (α-CoV) and beta-coronaviruses (β-CoV) primarily infect mammals, particularly bats, whereas gamma-coronaviruses (γ-CoV) are mainly associated with avian species. Delta-coronaviruses (Δ-CoV) have also been identified in both birds and some mammalian hosts, highlighting the diversity and cross-species transmission potential of this viral family.[137–139]

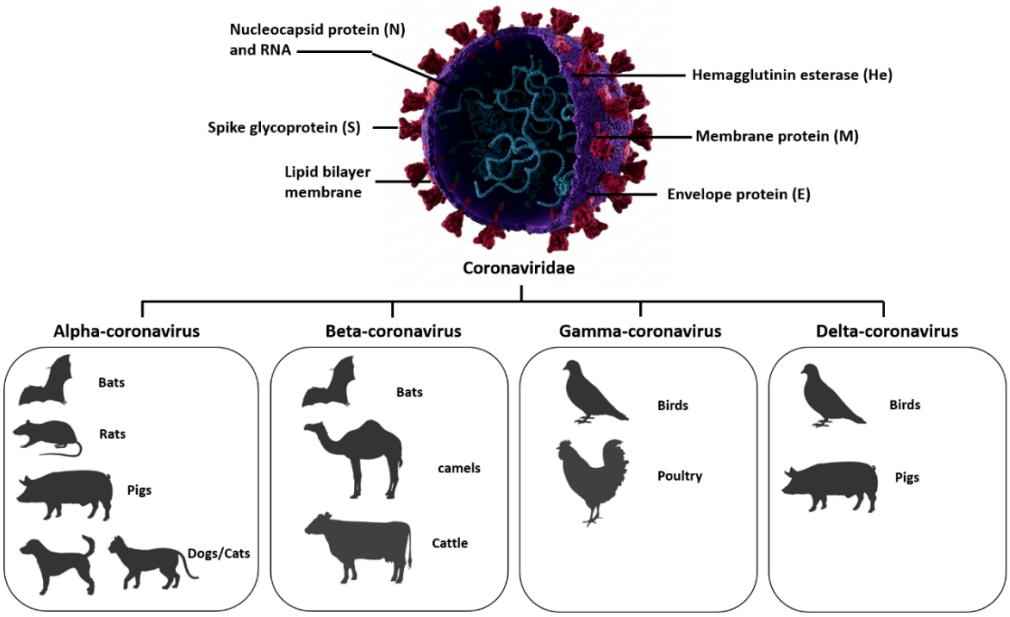


Figure 5.1 Schematic overview of coronavirus genera, main animal reservoirs, and surveillance targets addressed in this chapter.

The structure and genome organization of coronaviruses reflect a balance between genetic conservation and adaptability. Coronaviruses are enveloped viruses containing a single-stranded positive-sense RNA genome of approximately 30 kb, organized into a conserved 5' region encoding the replication machinery and a more variable 3' region encoding structural proteins, including spike (S), envelope (E), membrane (M), and nucleocapsid (N). During infection, discontinuous transcription generates subgenomic RNAs, leading to high intracellular expression of structural genes. However, the degree of conservation and expression of these regions varies across coronavirus genera, and therefore the selection of suitable detection targets must be tailored to each virus group.[140,141]

Nucleic acid amplification tests (NAATs), particularly RT-PCR, constitute the current standard for coronavirus detection. These methods rely on the amplification of specific genomic regions using sequence-specific primers and probes. Conserved regions within the RNA-dependent RNA polymerase (RdRp) gene are widely employed for the detection of alpha- and beta-coronaviruses, while the 5' untranslated region (5'-UTR) serves as a reliable target for gamma-coronaviruses.[142,143] For SARS-CoV-2 detection, the envelope (E) and nucleocapsid (N) genes emerged as optimal targets due to their high transcription levels and relatively conserved sequences, using the RdRp gene for confirmatory analysis. [144,145]

Despite their high analytical sensitivity and specificity, NAAT-based methods rely on enzymatic amplification, multi-step workflows, and controlled laboratory conditions. These requirements limit their applicability for rapid and decentralized surveillance, particularly in scenarios involving large-scale screening of animal reservoirs.[146,147]

Photonic biosensors offer a complementary strategy for viral detection by enabling rapid and simple readout of specific biomolecular recognition events. Previous research in our group has demonstrated the excellent diagnostic potential for COVID-19 either through serological detection or direct viral detection. Calvo-Lozano et al. developed a SPR serological assay for total SARS-CoV-2 antibodies in serum, reaching ng/mL detection limits and diagnostic sensitivity and specificity of 99% and 100%, respectively, validated with 120 clinical samples.[148] Giarola et al. later applied a related SPR serological strategy to domestic animals, detecting anti-SARS-CoV-2 antibodies in diluted serum with an LOD of 49.6 ng/mL and diagnostic sensitivity and specificity of 100% and 71.4%, respectively, also validated with over 70 animal clinical samples.[149] Ruiz-Vega et al. further demonstrated direct viral particle detection on the BiMW interferometric platform by functionalizing the sensor with bioengineered nanobodies targeting the SARS-CoV-2 spike receptor-binding domain, achieving an LOD of 178 $TCID_{50}$/mL in viral transport medium and a dynamic range of 10^2–10^6 $TCID_{50}$/mL in under 20 minutes.[118]

Despite these advances, for early detection and precision active surveillance of coronaviruses, molecular diagnostics based on nucleic acid detection remain essential, as viral RNA provides the most direct and timely indicator of active infection and viral circulation. In this context, the development of photonic biosensors for direct RNA detection presents important analytical and bioengineering challenges associated with assay design and surface functionalization. The performance of these systems strongly depends on the careful selection of probes and target regions, as well as on the

optimization of the hybridization conditions while considering factors such as RNA secondary structure formation, electrostatic interactions and probe accessibility, among others. Consequently, there is still a need for highly sensitive nucleic acid-based photonic biosensors capable of enabling rapid, amplification-free molecular diagnostics while maintaining the simplicity and real-time operation that characterize these optical sensing technologies.

The objective of this chapter was thereby to design, implement, and validate photonic biosensor assays for coronavirus RNA screening at three levels: SARS-CoV-2 as a clinically relevant model coronavirus, alpha/beta-coronaviruses associated with mammalian reservoirs, and gamma-coronaviruses associated with avian hosts. The assays were first developed on a SPR platform and then transferred to the BiMW interferometric biosensor to improve direct detection sensitivity.

5.2. Target selection and probe design

For SARS-CoV-2, the E and N genes are widely used in standard clinical RT-qPCR workflows because their high intracellular abundance contributes to improved sensitivity, while their genetic stability supports reliable detection across circulating variants. These properties make them equally suitable as hybridization targets.[144,145]

For the detection of alpha- and beta-coronaviruses circulating in mammalian hosts, highly conserved regions within the RdRp gene, corresponding to the non-structural protein 12 (nsp12), were selected. RdRp/nsp12 is commonly used in broad-range coronavirus surveillance because it contains conserved motifs shared across coronavirus groups while still providing sufficient sequence variability for phylogenetic identification. Detecting these viruses by PCR is, however, particularly challenging: alpha- and beta-coronaviruses circulating in wildlife reservoirs—especially bats—are highly diverse, and even within conserved regions sequence mismatches at primer-binding sites can reduce amplification efficiency and increase the risk of false negatives. This problem is amplified in animal and environmental samples, where viral loads are often low, RNA may be partially degraded, and the sample matrix (e.g., faeces or guano) can contain PCR inhibitors. Broad-range coronavirus detection therefore frequently requires nested or semi-nested RT-PCR protocols, in which a first amplification step is followed by a second amplification with an internal primer; this improves sensitivity and the probability of detecting divergent sequences at the cost of a longer, more complex, and contamination-prone workflow. The relevance of RdRp/nsp12 as a broad-range target was illustrated by Gouilh et al. (partner of the MUSECOV project), who screened more than 1500 bat faecal samples from western Europe and North Africa using a semi-nested RT-PCR targeting a conserved fragment of RdRp/nsp12 and detected a high diversity of alphacoronaviruses and a SARS-CoV-related betacoronavirus in *Rhinolophus ferrumequinum*.[143,150–152]

For avian gamma-coronaviruses (γ-CoVs), the 5' untranslated region (5'-UTR) was selected as the target. This region contains regulatory elements essential for viral transcription and is highly conserved among gamma-coronaviruses, and its suitability as a diagnostic target is supported by established molecular assays. Callison et al. reported a real-time RT-PCR targeting the 5'-UTR that enabled sensitive and specific detection of infectious bronchitis

virus (IBV) directly from clinical samples, including multiple IBV strains and closely related turkey coronaviruses, demonstrating both the conservation and inclusivity of this genomic region.[142,153]

Based on these considerations, 50-nucleotide RNA target sequences were defined for each coronavirus group, together with their complementary single-stranded DNA probes. The DNA probes were designed following the criteria established in Section 4.2.1: 5'-terminal thiol modification for covalent immobilization and a vertical spacer to improve probe flexibility and accessibility. For SPR probes, we employed a poly-thymine vertical spacer ($polyT_{15}$), as optimized in previous research from the group. For the BiMW probes, the $polyT_{15}$ spacer was replaced by a hexamethylene (C6) spacer to match the surface chemistry optimized for the silicon-based platform in Chapter 4. The full set of target and probe sequences used in this chapter is summarized in **Tables 5.1 and 5.2**.

Table 5.1 Target RNA and DNA probe sequences for SPR biosensor.

Target Coronavirus	Target Region	Target RNA sequence	DNA probe
alpha/beta-CoVs	RdRp – nsp12	AAC CAG GUG GAA CAU CAU CAG GUG AUG CCA CAA CUG CCU ACG CTA ATA GU	[Thiol]-$polyT_{15}$-TAG GCA GTT GTG GCA TCA CCT GAT G
gamma-CoVs	5' UTR	CCA AAC AAC CCC UGA GGU GAC AGG UUC UGG UGG UGU UUA GUG AGC AGA CA	[Thiol]-$polyT_{15}$-AAC ACC ACC AGA ACC TGT CAC CTC A
SARS-CoV-2	**E gene**	GUA UUC UUG CUA GUU ACA CUA GCC AUC CUU ACU GCG CUU CGA UUG UGU GC	[Thiol]-$polyT_{15}$-GCG CAG TAA GGA TGG CTA GTG TAA C
	N gene	UGC AAU CGU GCU ACA ACU UCC UCA AGG AAC AAC AUU GCC AAA AGG CUU CU	[Thiol]-$polyT_{15}$-CAA TGT TGT TCC TTG AGG AAG TTG T

Table 5.2 Target RNA and DNA probe sequences for BiMW biosensor.

Target Coronavirus	Target Region	Target RNA sequence	DNA probe
Alpha/Beta-CoVs	RdRp – nsp12	AAC CAG GUG GAA CAU CAU CAG GUG AUG CCA CAA CUG CCU ACG CTA ATA GU	[Thiol]-C_6-TAG GCA GTT GTG GCA TCA CCT GAT G
Gamma-CoVs	5' UTR	CCA AAC AAC CCC UGA GGU GAC AGG UUC UGG UGG UGU UUA GUG AGC AGA CA	[Thiol]-C6-AAC ACC ACC AGA ACC TGT CAC CTC A

5.3. SPR biosensor for CoV RNA detection

The first sensing strategy is based on an SPR biosensor for direct detection of viral RNA by surface hybridization. A single-stranded DNA probe complementary to the selected viral RNA target (Section 4.2) is immobilized on the gold sensor surface; upon injection of the complementary RNA, hybridization at the interface produces a local refractive index change that is monitored in real time by the SPR transducer. A schematic representation of the SPR biosensor system is shown in **Figure 5.2**.

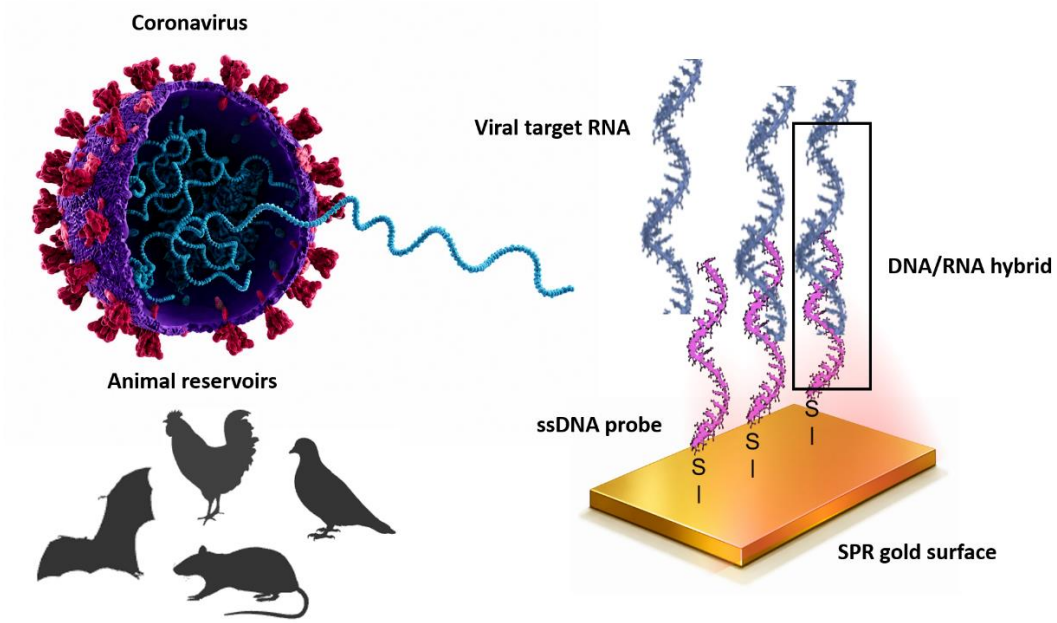


Figure 5.2 Schematic representation of the SPR biosensor system for coronavirus RNA detection.

5.3.1. Biofunctionalization of the sensor surface

The SPR gold surface was biofunctionalized using the thiol-based immobilization strategy optimized in Chapter 3. Thiolated DNA probes were co-immobilized with the PEG-based lateral spacer SH-PEG_{500}-OH to control probe density and minimize non-specific adsorption. The same conditions were applied to the four primary assays of this chapter: N gene, E gene, alpha/beta-CoVs, and gamma-CoVs. A combined N+E configuration is treated separately in Section 5.3.2 as a multi-target strategy.

Following the optimum conditions identified in Chapter 3, probes were immobilized at 2 µM with a 1:5 probe-to-spacer ratio in 5× PBS, pH 7.4, under in situ flow at 10 µL/min. Stable and reproducible immobilization sensograms were obtained for all assays, with wavelength shifts of $\Delta\lambda \approx 4–6$ nm (**Figure 5.3**). The similarity of the responses across targets confirms that immobilization was mainly governed by probe length and surface chemistry rather than by sequence composition. These conditions were therefore used for all subsequent SPR experiments.

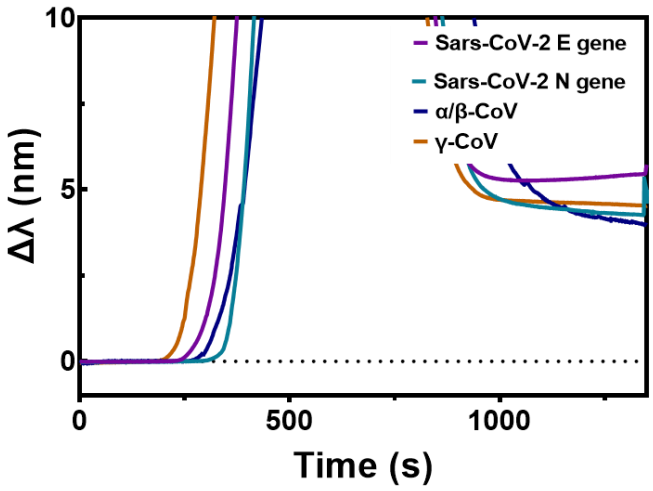


Figure 5.3 Sensograms of DNA probe immobilization.

5.3.2. Hybridization buffer optimization

Following probe immobilization, the hybridization assay was evaluated for all selected targets, including the SARS-CoV-2 N and E genes, alpha/beta-CoV, and gamma-CoV RNA sequences. Although general hybridization conditions were established in Chapter 3, further optimization was required to improve the sensitivity of the coronavirus RNA assays.

The effect of formamide was first evaluated at 1%, 5%, 10%, and 20% in 5× SSC (**Figure 5.4**). Increasing the formamide concentration enhanced the hybridization signal across all four targets, with 10% formamide producing the highest response. This trend indicates improved target accessibility and duplex formation at the sensor interface under moderately destabilizing conditions.

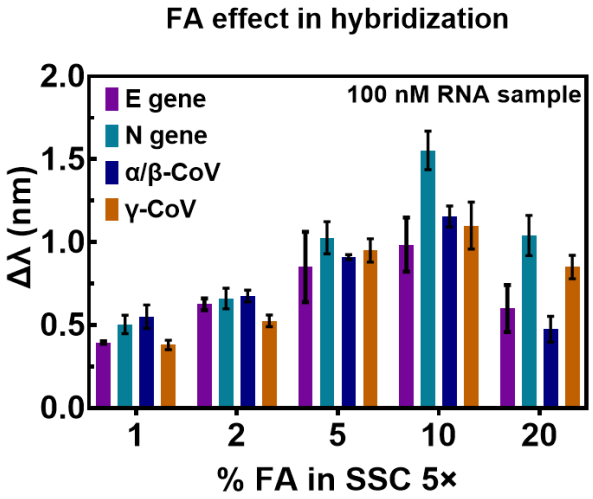


Figure 5.4 Effect of Formamide in SSC 5 × hybridization buffer on sensor response for different CoV RNA targets. Hybridization signals obtained for 100 nM RNA targets corresponding to SARS-CoV-2 N gene, E gene, alpha/beta-coronavirus, and gamma-coronavirus assays

To further enhance sensitivity, TMAC was evaluated as an additional buffer additive. TMAC reduces base-pairing bias and promotes more uniform duplex stability. At 1 M, TMAC further increased the hybridization signal but also produced a noticeable rise in non-specific responses. A combined formulation containing 10% formamide and a reduced TMAC concentration of 0.5 M restored assay specificity while preserving the signal enhancement, giving consistent improvement across all targets and negligible non-specific responses (**Figure 5.5**).

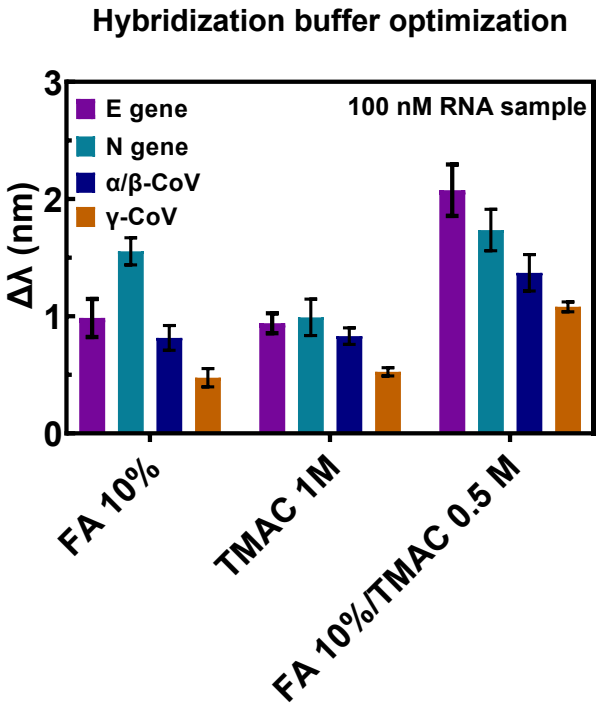


Figure 5.5 Effect of addtives in SSC 5 × hybridization buffer on sensor response for different CoV RNA targets. Hybridization signals obtained for 100 nM RNA targets corresponding to SARS-CoV-2 N gene, E gene, alpha/beta-coronavirus, and gamma-coronavirus assays.

Based on these results, 5× SSC (pH 7.4) supplemented with 10% FA and 0.5 M TMAC was selected as the optimal hybridization buffer for all subsequent SPR experiments.

5.3.3. Sensitivity and specificity of SPR coronavirus RNA detection

Under the optimized hybridization conditions, the analytical performance of the SPR assays was first evaluated for the SARS-CoV-2 E and N targets. Both produced clear and reproducible sensograms with well-defined binding, confirming efficient hybridization at the sensor interface (**Figure 5.6**).

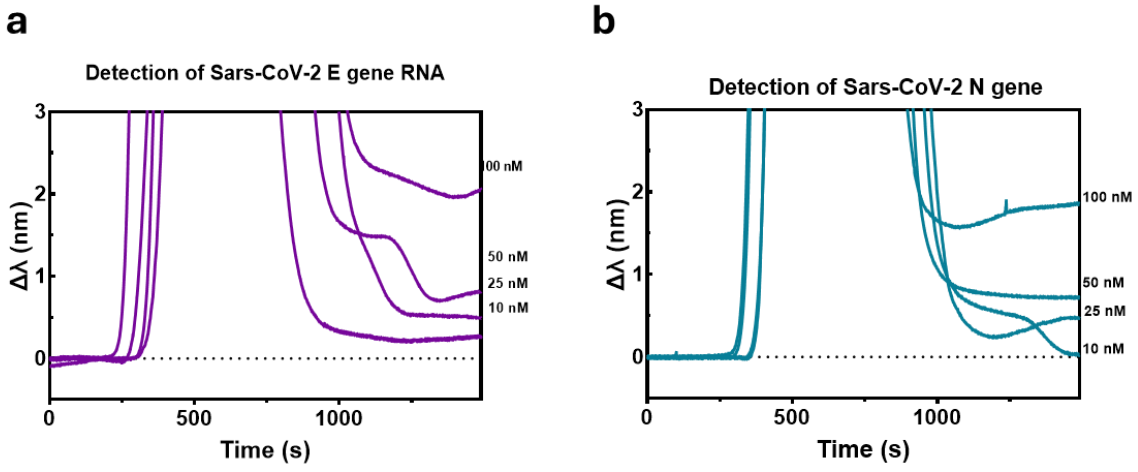


Figure 5.6 Sensograms of viral target detection SARS-CoV-2 (**a**) N and (**b**) E genes RNA.

The analytical performance of each assay was evaluated through calibration curves obtained over a defined concentration range (**Figure 5.7**). A concentration-dependent response was observed in both cases, enabling quantitative detection. The LODs achieved for the E gene was approximately 0.52 nM, while the N gene exhibited a slightly higher LOD of 1.51 nM. The difference in sensitivity between the E and N targets is attributed to sequence-dependent differences in secondary structure that modulate target accessibility and hybridization efficiency. Compared with previous direct SPR assays for nucleic acid detection, the sensitivity obtained here is within, and in some cases slightly better than, the reported range.

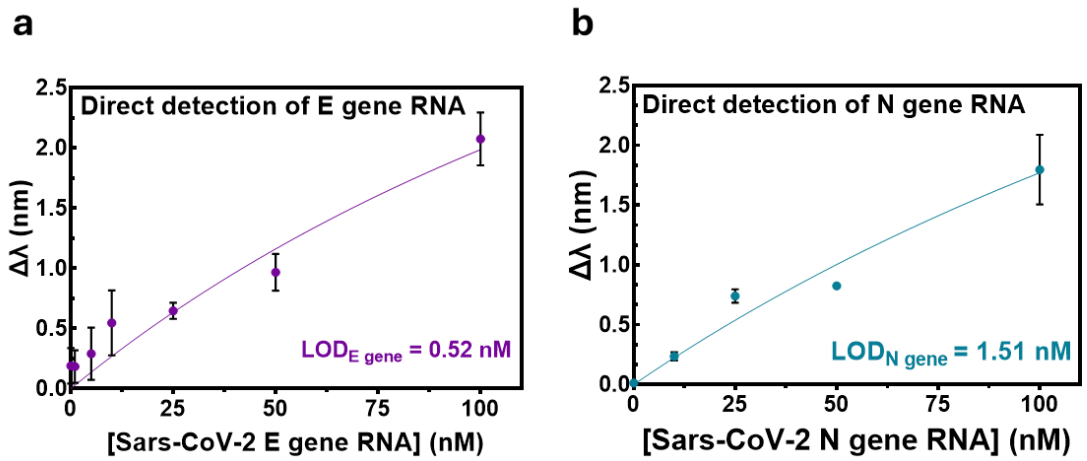


Figure 5.7 Calibration curves for (**a**) gene E and (**b**) N RNA detection.

Specificity was evaluated by injecting non-complementary RNA sequences under identical conditions (**Figure 5.8**). In all cases the sensor response was negligible, confirming that the signal arises from specific hybridization and that no cross-reactivity occurs between the tested sequences.

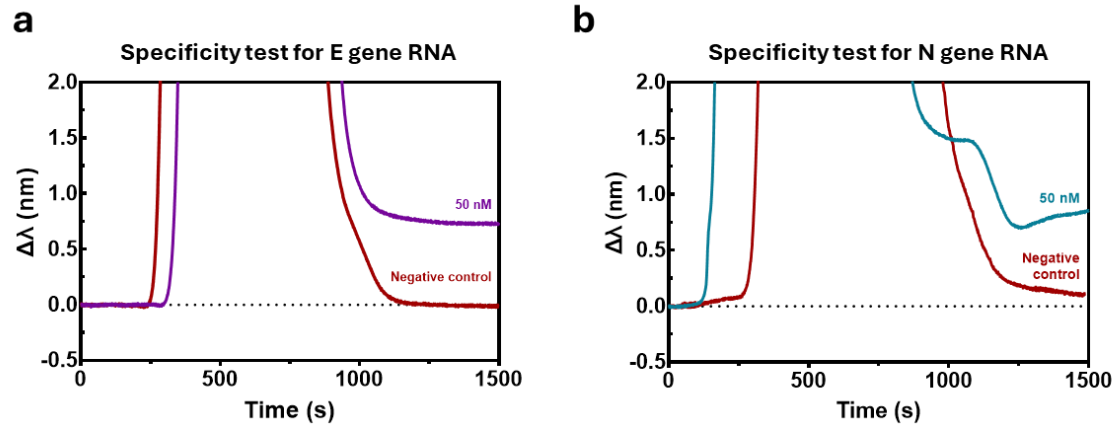


Figure 5.8 Sensograms showing specificity for (**a**) E gene and (**b**) N gene RNA detection.

To further improve detection robustness and sensitivity, a combined N+E configuration was also evaluated, mirroring the multi-region strategy used in clinical RT-PCR to reduce false negatives.[154] The two probes were co-immobilized on the same gold surface, keeping the total probe concentration at 2 μM (1 μM N + 1 μM E) and the same total probe-to-spacer ratio of 1:5. Successful co-immobilization was confirmed by the immobilization response, and the combined assay yielded an LOD of ≈ 1.50 nM (**Figure 5.9)**.

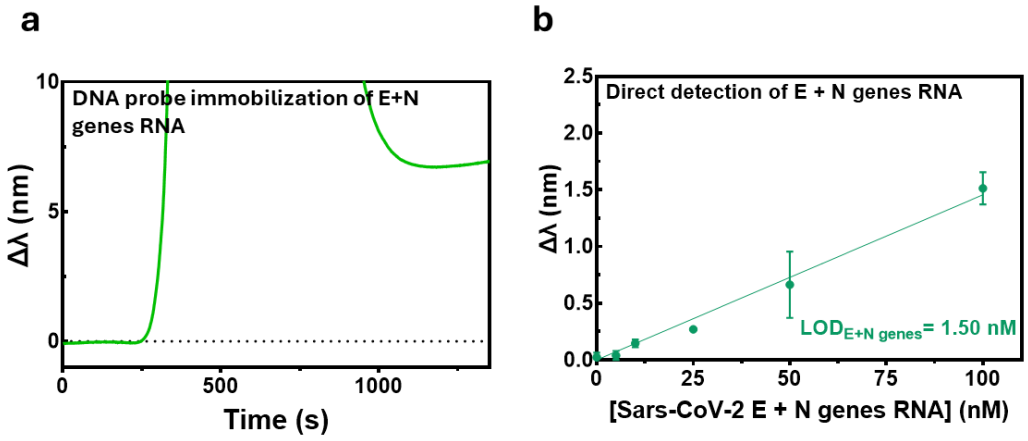


Figure 5.9 (**a**) Immobilization response and (**b**) calibration curve for gene E + N RNA detection.

The analytical sensitivity of the multi-target assay remained in the same range as that of the corresponding single-target assays, with no substantial gain in the limit of detection achieved on synthetic targets. Nonetheless, the relevant benefit of the multi-target configuration is not analytical but diagnostic: by simultaneously interrogating several conserved regions of the viral genome on the same sensor surface, the probability of capturing a positive signal from a clinical or environmental sample is increased, particularly in the presence of partial sequence variability, low viral load, or partially degraded RNA.

Following the optimization of the hybridization conditions, calibration curves were obtained for the alpha/beta-coronavirus RNA target under the selected buffer composition. As shown in **Figure 5.10**, the sensor response exhibited a clear concentration-dependent behaviour, enabling quantitative detection over the tested range. The limit of detection achieved for the alpha/beta-CoV assay was approximately 1.28 nM. Specificity was assessed by injecting non-complementary RNA sequences under identical experimental conditions. Negligible responses were observed, confirming that the sensor signals were associated with specific probe-target hybridization rather than non-specific adsorption or cross-reactivity between the tested sequences.

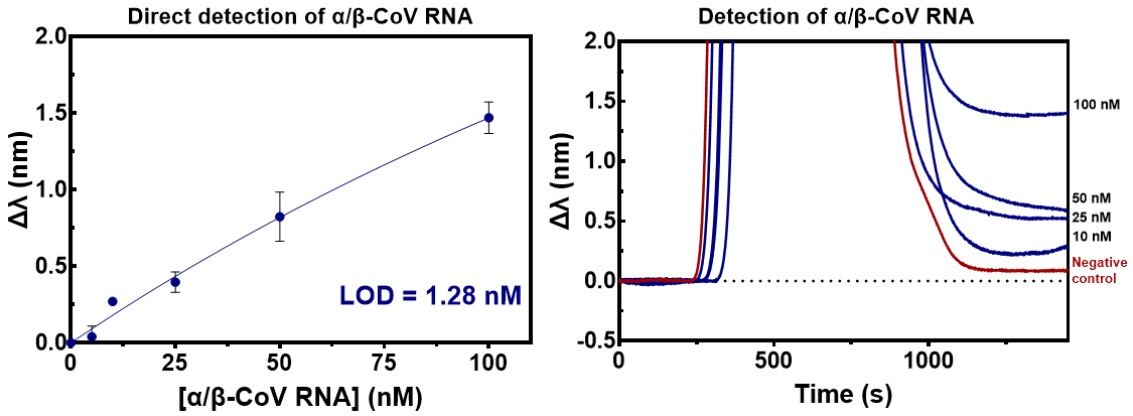


Figure 5.10 Calibration curves for alpha/beta-RNA detection and specificity sensogram.

Subsequently, the same experimental conditions were applied to the gamma-coronavirus RNA target. A similar concentration-dependent response was observed (**Figure 5.11**), confirming that the optimized hybridization conditions are transferable across different targets. The limit of detection obtained for the gamma-CoV assay was approximately 1.49 nM.

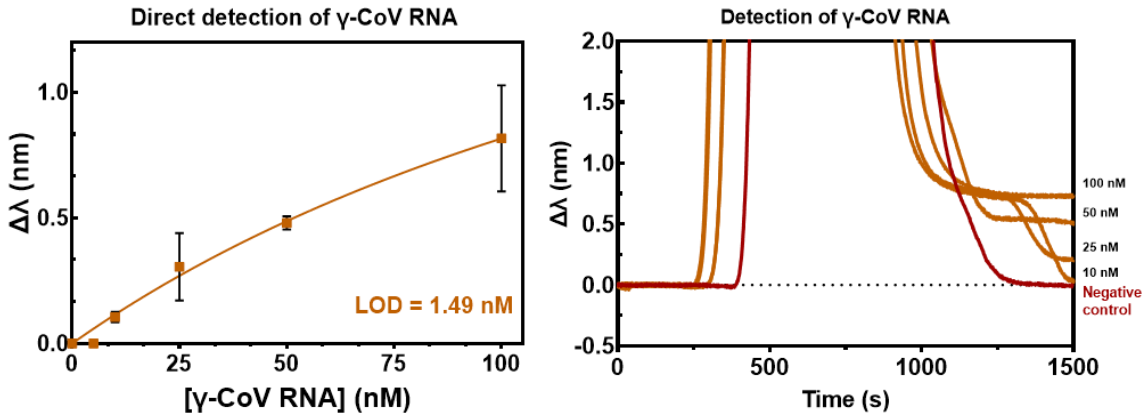


Figure 5.11 Calibration curves for gamma-RNA detection and specificity sensogram.

The comparable performance obtained for the alpha/beta- and gamma-CoV assays indicates that the optimized buffer supported hybridization across different coronavirus targets. The slightly different detection limits are likely associated with sequence-specific properties such as GC content, local folding, and accessibility of the hybridization region.

Direct detection of viral RNA has been reported in different formats of plasmonic biosensors, often using strategies to overcome the limited signal generated by nucleic acid targets. Qiu et al. developed a dual-functional LSPR biosensor combining localized surface plasmon resonance with a plasmonic photothermal effect, reaching an LOD of 0.22 pM for the SARS-CoV-2 RdRp sequence.[155] The photothermal step improved hybridization selectivity but added temperature-assisted operation to the assay. More recently, Chang et al. reported a highly sensitive SPR RNA sensor using 2D phosphorus-based nanosheets and AuNPs, achieving an LOD of 10 aM for SARS-CoV-2 RdRp and ORF1ab synthetic RNA sequences.[156] These works demonstrate how nanostructured and signal-enhanced

plasmonic systems can reach very low detection limits, but they also show that such sensitivity is often obtained using additional materials or controlled buffer conditions. In comparison, the direct SPR assays developed here are simpler, but their nanomolar detection limits confirm the sensitivity limitation of direct SPR detection for short RNA targets.

Considering that the synthetic targets used in this study consist of short 50-nt sequences, whereas real coronavirus genomes are approximately 30 kb in length, the effective mass associated with full-length RNA is approximately 600 times higher. Assuming a proportional relationship between molecular size and sensor response, the corresponding estimated limits of detection for full-length viral RNA fall in the low picomolar range, corresponding to approximately 10^5–10^6 copies/µL depending on the target (**Table 5.1**). These values were estimated from the measured nanomolar limits of detection by applying a 600-fold correction factor based on target length, with the individual assay-by-assay values summarized in **Table 5.3**. For the SARS-CoV-2 E gene assay, the estimated LOD is 0.87 pM, corresponding to approximately 5.2×10^5 copies/µL. For the N gene assay, the estimated LOD is 2.52 pM, corresponding to approximately 1.52×10^6 copies/µL. For the combined N+E assay, the estimated LOD is 2.50 pM, corresponding to approximately 1.51×10^6 copies/µL. For the alpha/beta-coronavirus assay, the estimated LOD is 2.13 pM, corresponding to approximately 1.28×10^6 copies/µL. Finally, for the gamma-coronavirus assay, the estimated LOD is 2.48 pM, corresponding to approximately 1.50×10^6 copies/µL. These values were estimated from the measured nanomolar limits of detection by applying a 600-fold correction factor based on target length.

Table 5.3 LODs obtained for the different coronavirus RNA assays.

Assay	Measured LOD (50 nt target)	Estimated LOD (full-length RNA)	Estimated copies/µL
SARS-CoV-2 E	0.52 nM	0.87 pM	5.2 × 10^5
SARS-CoV-2 N	1.51 nM	2.52 pM	1.52 × 10^6
SARS-CoV-2 N+E	1.50 nM	2.50 pM	1.51 × 10^6
alpha/beta-CoV	1.28 nM	2.13 pM	1.28 × 10^6
gamma-CoV	1.49 nM	2.48 pM	1.50 × 10^6

For SARS-CoV-2 detection, RT-qPCR assays targeting the E and N genes typically achieve detection limits in the range of approximately 50 to 200 copies/µL under practical implementation conditions.[144,145,157] Broad-range alpha/beta-CoV PCR assays generally exhibit lower sensitivity, with reported or inferred detection limits in the range of 10^2 to 10^3 copies/µL, mainly due to the use of degenerate primers and the reduced amplification efficiency associated with sequence variability. These limitations are expected to be even more pronounced for gamma-CoVs, which are genetically more divergent from the human beta-coronaviruses for which many molecular assays were originally optimized.[142,143,158]

In this context, the estimated detection limits obtained for full-length viral RNA with the developed SPR biosensor, ranging from approximately 5.2×10^5 to 1.5×10^6 copies/µL depending on the target, remain above those of conventional RT-qPCR. This difference highlights the need for an additional signal amplification strategy, which is addressed in the following section.

5.3.4. Signal amplification of CoV RNA

To overcome the sensitivity limit of direct SPR detection of short nucleic acid targets, a signal amplification strategy based on anti-DNA/RNA duplex antibodies was implemented. This approach, previously explored in SPR-based nucleic acid detection, exploits an antibody that selectively recognizes DNA/RNA hybrid duplexes formed at the surface after target capture. Antibody binding increases the effective mass accumulated at the interface and produces a larger optical response. Importantly, antibody recognition occurs only when the RNA target has hybridized with the immobilized DNA probe, so the amplification step also provides indirect specificity confirmation of duplex hybrid formation.[159,160]

The strategy consists of two sequential recognition events (**Figure 5.12**). First, the RNA target is captured by the immobilized DNA probe, producing a signal proportional to the target concentration. Second, an anti-DNA-RNA antibody is introduced, which binds specifically to the formed DNA/RNA duplex and contributes an additional, target-proportional signal that effectively amplifies the overall sensor response.[107]

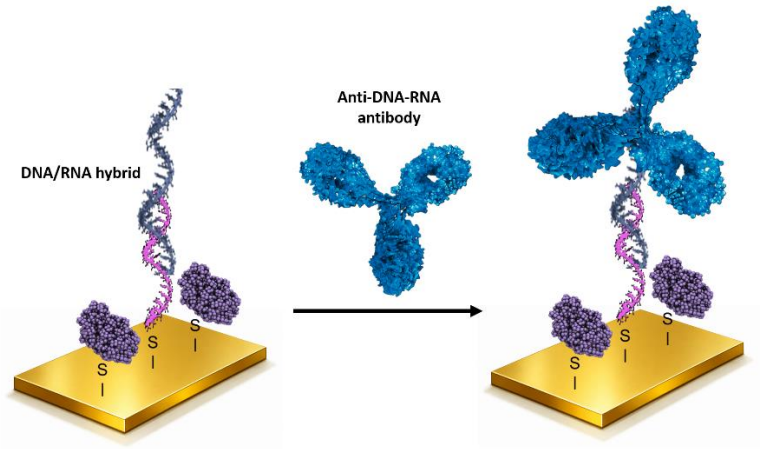


Figure 5.12 Illustration of Anti-DNA-RNA amplification strategy.

The amplification strategy was first optimized using the alpha/beta-CoV RNA target. This target was selected as a representative model due to its similar hybridization behaviour compared to the other RNA targets.

The alpha/beta-CoV target was chosen as the model for assay optimization because its hybridization behaviour is representative of the other RNA targets. Given the size of the antibody (≈ 150 kDa), sufficient interprobe spacing is required at the surface to allow access to the buried DNA/RNA hybrid. Increasing the spacer content improved the amplification signal, and a probe-to-spacer ratio of 1:7 produced the highest response (**Figure 5.13**).

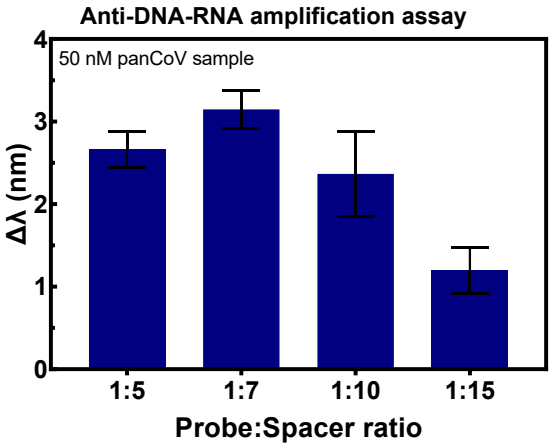


Figure 5.13 DNA probe spacing optimization for amplification assay.

The concentration of the anti-DNA–RNA antibody was subsequently optimized. The signal increased with antibody concentration and reached saturation at concentrations equal to or higher than 7 µg/mL (**Figure 5.14**), indicating that all available DNA/RNA hybrid binding sites were occupied. A concentration of 7 µg/mL was therefore selected for subsequent experiments.

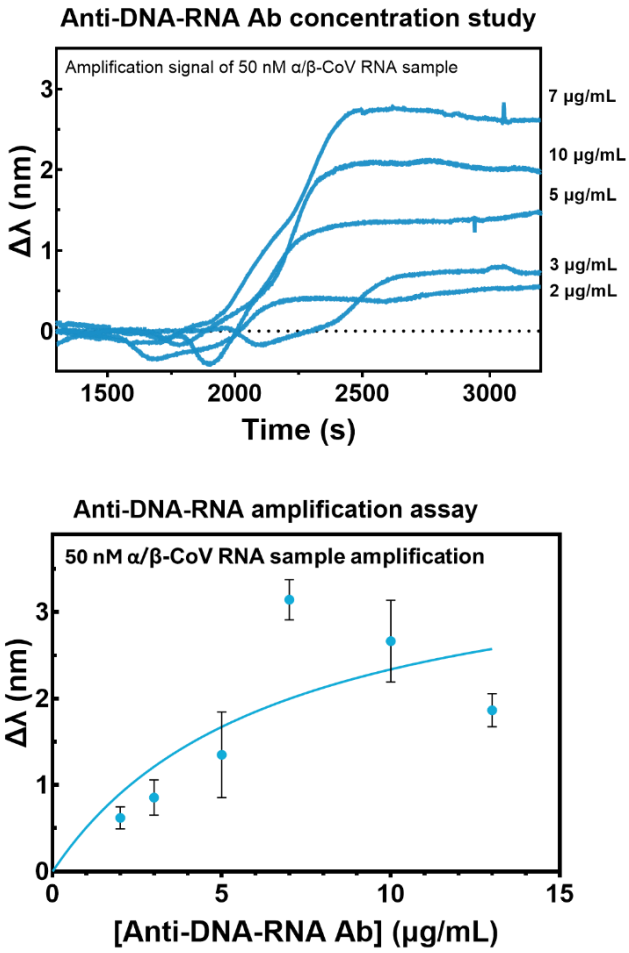


Figure 5.14 Evaluation of anti-DNA-RNA antibody concentrations for the optimization of the amplification assay,

Calibration curves obtained with the optimized amplified format showed a clear improvement in sensitivity over direct detection. For the alpha/beta-CoV assay, the LOD improved to ≈ 20 pM (**Figure 5.15**).

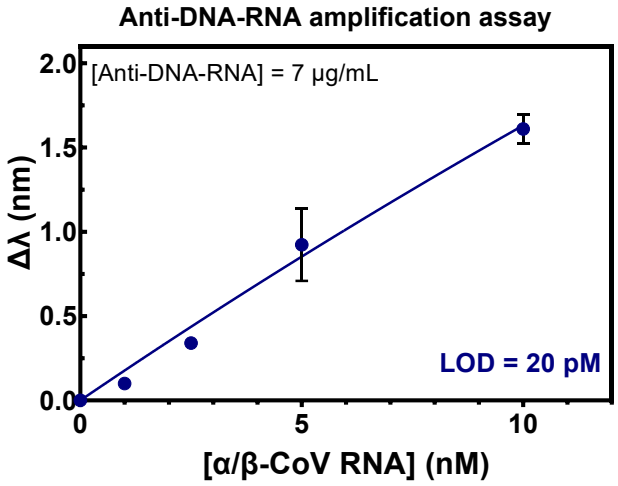


Figure 5.15 Calibration curve alpha/beta-CoV amplification assay.

To evaluate transferability, the same amplification conditions were applied to the gamma-CoV assay. The introduction of the amplification step produced a clear increase in sensor response compared with direct hybridization (**Figure 5.16**), allowing detection of the gamma-CoV target down to 38 pM. The LOD is slightly higher than for the alpha/beta-CoV target but confirms that the strategy is applicable across coronavirus sequences.

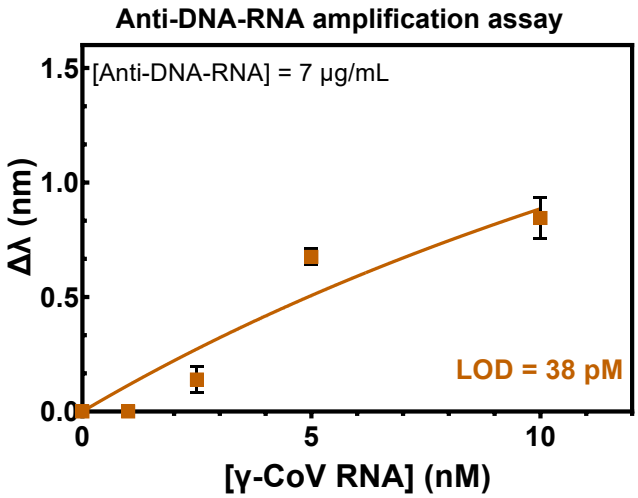


Figure 5.16 Calibration curve gamma-CoV amplification assay.

The results demonstrate that antibody-based signal amplification is effective for improving SPR detection of coronavirus RNA targets. Furthermore, the specificity of the amplification step was confirmed using non-complementary sequences, which resulted in negligible signal after antibody injection confirming, on one hand, that the antibody only binds to DNA/RNA hybrid duplexes and that the DNA probes only hybridize with the corresponding complementary RNA sequence (**Figure 5.17**).

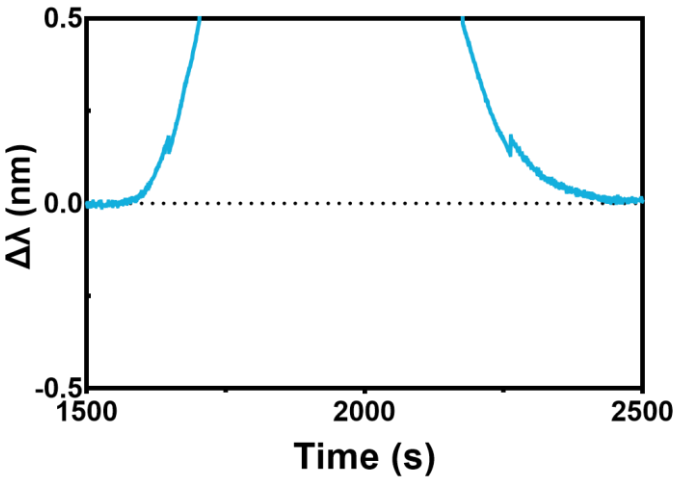


Figure 5.17 Amplification signal obtained for negative-control RNA sequences.

When converting molarity to copies/µL, the estimated limits of detection were approximately 2.0×10^4 copies/µL for the alpha/beta-CoV assay and 3.8×10^4 copies/µL for the gamma-CoV assay. These values indicate reasonable analytical performance

considering the genetic diversity of the selected coronavirus targets and the absence of enzymatic target amplification. As expected, the sensitivity remains lower than that of optimized NAATs, including RT-qPCR, nested or semi-nested PCR, digital PCR, and isothermal amplification methods such as RT-LAMP or RPA. The SPR strategy developed here, by contrast, relies on antibody-based signal amplification of the surface hybridization event, which preserves the simplicity of the workflow by avoiding target enzymatic amplification, thermal cycling, and primer- or polymerase-dependent reagents, while still enhancing sensitivity over the direct label-free format.

Signal amplification has also been used in other viral nucleic acid biosensors. For example, Diao et al. developed an SPR assay for HIV-related DNA using entropy-driven strand displacement and DNA tetrahedron nanostructures, achieving an LOD of 48 fM with a total assay time of approximately 60 min.[161] This type of strategy illustrates how amplification can improve sensitivity without enzymatic target amplification, but also shows the trade-off between analytical performance and assay complexity. The antibody-amplified SPR assay developed here follows the same general principle: it improves the sensitivity of direct hybridization while remaining simpler than nucleic acid amplification protocols.

Overall, the antibody-amplified SPR assay represents an intermediate strategy between direct SPR detection and NAAT-based diagnostics. It improves sensitivity compared with direct hybridization while preserving a relatively simple optical workflow. This compromise is particularly relevant for broad-spectrum coronavirus detection, where sequence variability can complicate primer-based amplification. These results supported the preliminary evaluation of the assay in real samples, as described in the following section.

5.3.5. Preliminary validation with real animal samples

To assess the applicability of the developed assay under realistic conditions, the amplified alpha/beta-CoV SPR assay was tested with RNA extracted from biological samples. The study was designed as a preliminary evaluation of whether the sensitivity achieved under controlled conditions is sufficient for viral RNA detection in real samples.

A panel of 24 RNA samples extracted from bat faeces was analysed. These samples were previously collected from wild animals and processed by the collaborating laboratory (Prof. Jordi Serra-Cobo, University of Barcelona (UB)), where viral RNA extraction and characterization were performed using semi-nested RT-PCR following the protocol described by Gouilh et al. The samples consisted of 19 PCR-positive and 5 PCR-negative specimens, providing a reference classification for comparison.[143]

The extracted RNA was directly introduced into the biosensor system without further treatment steps, using the optimized hybridization and amplification conditions described in the previous section. As shown in **Figure 5.18a**, the biosensor response enabled a clear discrimination between positive and negative samples. Most PCR-positive samples produced signals above the established threshold, while PCR-negative samples showed negligible responses. The distribution of the sensor signal for all samples is presented in **Figure 5.18.b**, together with the statistical analysis (Kruskal–Wallis test, $p < 0.0001$), confirming the significant difference between the two populations.

Based on this classification, the diagnostic performance of the assay was evaluated, yielding a sensitivity of 89%, specificity of 80%, positive predictive value (PPV) of 94%, and negative predictive value (NPV) of 67%. The sensitivity of 89% indicates that most PCR-positive samples were correctly identified, while the lower negative predictive value (67%) suggests that samples with low viral load may fall below the detection limit, leading to false negatives. Nevertheless, the current SPR assay still requires two sequential steps, target hybridization followed by antibody-based amplification, which increases the analysis time and operational complexity compared with a direct one-step assay. Considering these limitations, and to improve the sensitivity of direct coronavirus RNA detection, the optimized assay was subsequently transferred to the BiMW interferometric biosensor platform, as described in the next section.

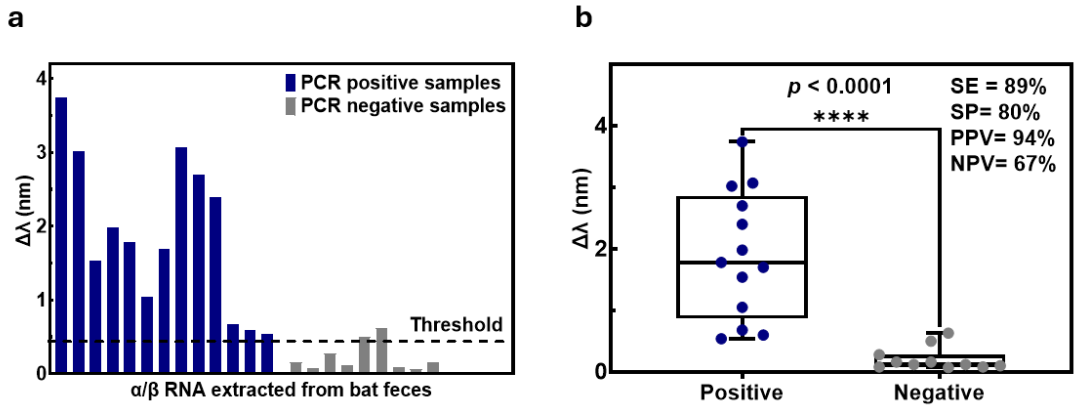


Figure 5.18 Preliminary validation of the alpha/beta-CoV amplification assay RNA extracted from bat feces: (**a**) discrimination between positive and negative samples and (**b**) statistical analysis (Kruskal–Wallis test, $p < 0.0001$).

5.4. BiMW biosensor for CoV RNA detection

5.4.1. Biofunctionalization of the sensor surface

Following development and preliminary validation on the SPR platform, the sensing strategy was transferred to the BiMW device to evaluate its performance using a more sensitive photonic transduction mechanism. The same biosensor design, based on the immobilization of specific DNA probes, was maintained to allow comparison between both platforms.

The motivation for the transfer was the higher sensitivity of interferometric biosensors to refractive index changes occurring close to the sensing surface. As shown in Chapter 4, however, analytical performance is not determined by the transducer alone: surface chemistry, probe density, and probe accessibility are also critical. The BiMW biofunctionalization was therefore performed using the optimized APTES/PDITC chemistry described in Chapter 4, in order to evaluate whether a more sensitive transducer combined with a controlled DNA probe layer could improve direct coronavirus RNA detection.

Briefly, the employed protocol used vapor-phase APTES deposition followed by 20 mM PDITC crosslinking for covalent immobilization of thiolated DNA probes. The probes were immobilized at 2 µM and co-functionalized with the PEG-based lateral spacer SH-PEG_{500}-

OH using a probe-to-spacer ratio of 1:2. Probe immobilization was monitored in real time using the BiMW platform. As shown in **Figure 5.19**, the sensograms exhibited a consistent increase in phase shift during probe attachment, reaching Δϕ = 52.2 ± 3.8 rad.

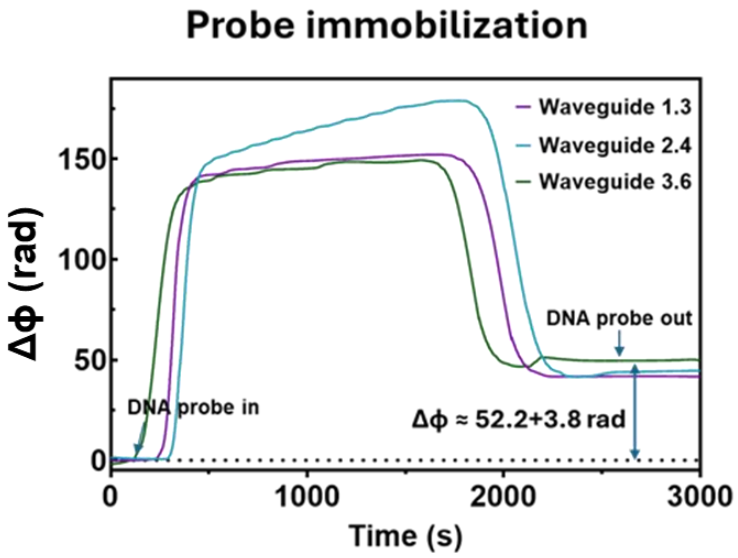


Figure 5.19 BiMW sensograms of DNA probe immobilization in different waveguides of the BiMW sensor chip over 2500 s.

5.4.2. Direct detection of synthetic coronavirus RNA targets

Following biofunctionalization, the detection of alpha/beta- and gamma-CoV RNA targets was evaluated using assay conditions derived from those previously optimized on the SPR platform. Given the differences in surface chemistry, signal acquisition, and data analysis between the SPR and BiMW platforms, a slight re-optimization of the hybridization conditions was required to account for the higher sensitivity of the interferometric sensor.

The hybridization buffer was based on 5× SSC, and the effect of FA concentration was re-evaluated in the BiMW platform. While higher FA concentrations (e.g., 10%) provided enhanced hybridization efficiency in SPR sensor, a different behaviour was observed in the BiMW sensor. As shown in **Figure 5.20**, increasing the FA percentage resulted in a noticeable increase in non-specific signal, particularly at concentrations above 1%, as evidenced by the response obtained for the negative control.

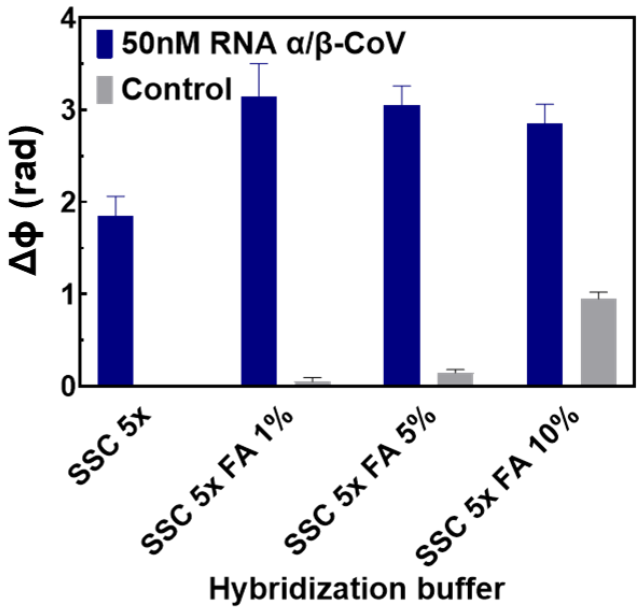


Figure 5.20 . Synthetic RNA target for α/β-CoV assay (blue histograms) and negative control (grey histograms) signals obtained with different formamide percentage (FA at 1, 5, and 10%).

This effect is likely related to the interaction of formamide with the BiMW sensor surface rather than to a true hybridization event. At higher FA concentrations, additive adsorption onto the functionalized surface or changes in the bulk refractive index can generate signal artefacts and apparent positive responses, even in the absence of complementary target binding. Therefore, the increased response observed at high FA percentages was considered nonspecific and not suitable for reliable target detection.

Based on these results, 1% formamide was selected for the BiMW biosensor, providing a balance between hybridization efficiency and specificity. Under these conditions, the biosensor maintained a strong response for the target RNA while minimizing non-specific interactions. The sensor surface could also be regenerated using a 35% formamide-based protocol, enabling repeated use without loss of performance.

The analytical performance of the BiMW biosensor was evaluated using synthetic RNA targets corresponding to alpha/beta- and gamma-coronavirus assays. Calibration curves were obtained by sequential injection of RNA solutions at concentrations ranging from 0.5 to 100 nM, with real-time monitoring of the sensor response (**Figure 5.21**). The alpha/beta-CoV assay achieved an LOD of 38 pM and an LOQ of 186 pM, while the gamma-CoV assay presented an LOD of 91 pM and an LOQ of 305 pM. The slightly higher detection limits obtained for the gamma-CoV target are likely related to sequence-dependent effects, such as secondary structure formation or reduced accessibility of the hybridization region.

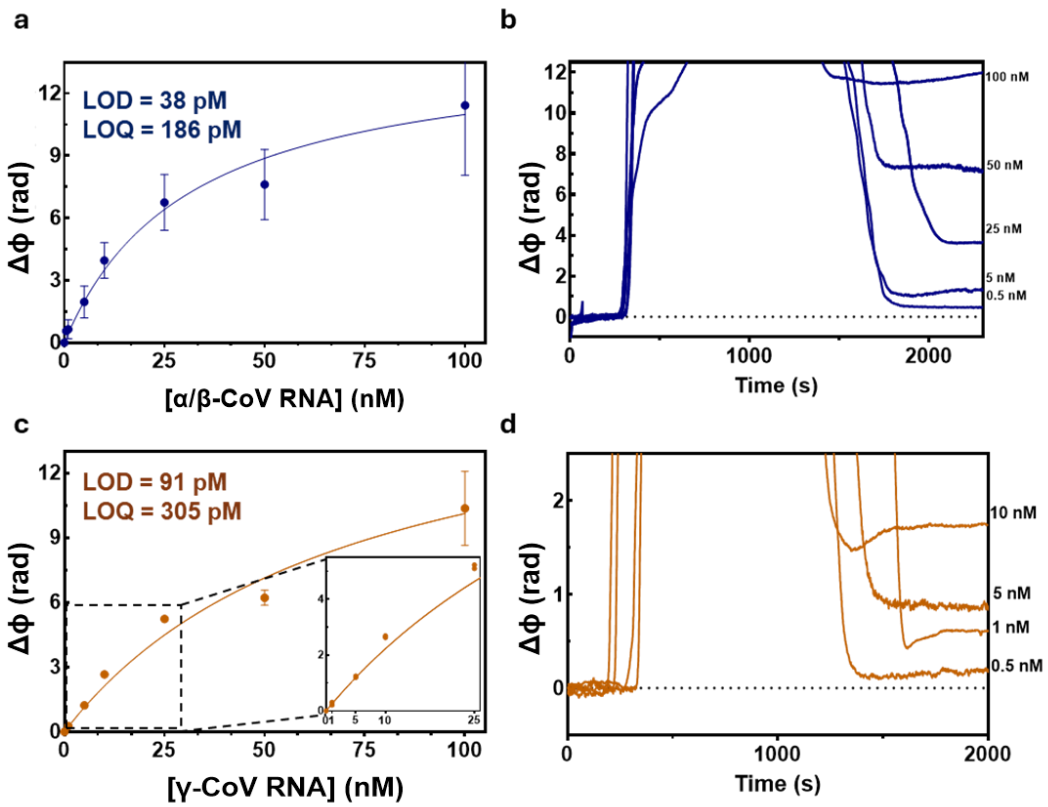


Figure 5.21 (**a**) Standard calibration curve using a synthetic RNA target at concentration range of 0.5-100 nM for the α/β-CoV biosensor assay; (**b**) Representative sensograms of the synthetic RNA targets for the α/β-CoV assay; (**c**) Standard calibration curve using a synthetic RNA target at concentration range of 0.5-100 nM for the γ-CoV biosensor assay; (**d**) Representative sensograms of the synthetic RNA targets for the γ-CoV assay.

These results represent a significant improvement compared to the direct assay of SPR biosensor, confirming the higher sensitivity of the BiMW sensor.[97,125] However, this comparison is still not directly equivalent to the PCR-based evaluation discussed in Section 4.3.3, since the calibration curves were obtained using short synthetic RNA oligonucleotides rather than longer RNA fragments resembling the amplified viral targets. Short synthetic targets are useful for controlled assay optimization, but they do not reproduce the molecular weight, folding, and accessibility constraints of longer viral RNA sequences. Therefore, in vitro transcribed RNA was subsequently evaluated as a larger and more representative target, allowing a more realistic comparison with PCR-based approaches.

5.4.3. In vitro transcribed (IVT) RNA analysis

In vitro transcribed (IVT) RNA corresponding to the gamma-CoV target was provided by our collaborators (Dr. Céline Courtillon, ANSES). Although IVT-RNA standards were available only for the gamma-CoV target, the analytical conclusions drawn from this experiment can reasonably be extended to the alpha- and beta-CoV assays, since all coronavirus targets in this work were detected using the same biofunctionalization, probe-immobilization, and hybridization conditions, and analytical performance in this BiMW format is governed

mainly by transducer sensitivity and hybridization thermodynamics rather than by virus-specific features.

The use of IVT RNA offers a well-defined system with controlled concentration while preserving a more realistic molecular structure compared to short synthetic oligonucleotides. This makes it particularly suitable for assessing the intrinsic sensitivity and quantitative performance of the BiMW biosensor.

Serial ten-fold dilutions of the IVT RNA were prepared, covering a concentration range from 10^{-2} to 10^{4} copies/µL, and were first characterized by RT-qPCR to confirm their concentration and linearity through the corresponding Ct values. The same set of samples was subsequently analysed using the BiMW biosensor. As shown in **Figure 5.22**, no measurable signal was observed for concentrations below 10 copies/µL, in agreement with the RT-qPCR-negative classification. A clear hybridization response was detected from 10 copies/µL onwards, increasing progressively with concentration up to 10^{4} copies/µL. This behaviour demonstrates a strong correlation between the biosensor signal, the IVT RNA concentration, and the RT-qPCR results. At higher concentrations, the response deviates from linearity, with the signal approaching a plateau. This effect is attributed to surface saturation phenomena, where the high density of target molecules limits the availability of accessible binding sites due to steric hindrance at the sensor interface.

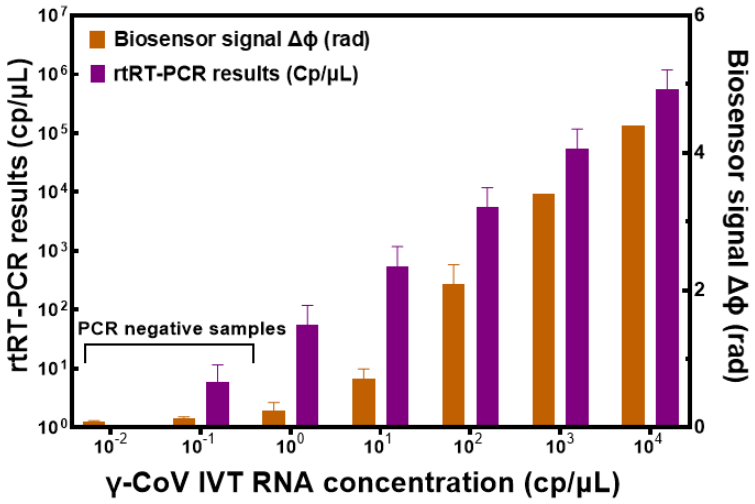


Figure 5.22 BiMW biosensor responses (orange) to serial 10-fold dilutions of gamma-CoV IVT RNA (from 10-2 to 104 copies/µL) compared with RT-qPCR results (purple).

To determine the LOD and LOQ of the assay, the sensor response was plotted as a function of IVT RNA concentration and fitted using a one-site binding model (**Figure 5.23**), revealing a typical saturation profile. Based on this analysis, the LOD and LOQ were estimated to be 1.52 copies/µL and 9.4 copies/µL, respectively.

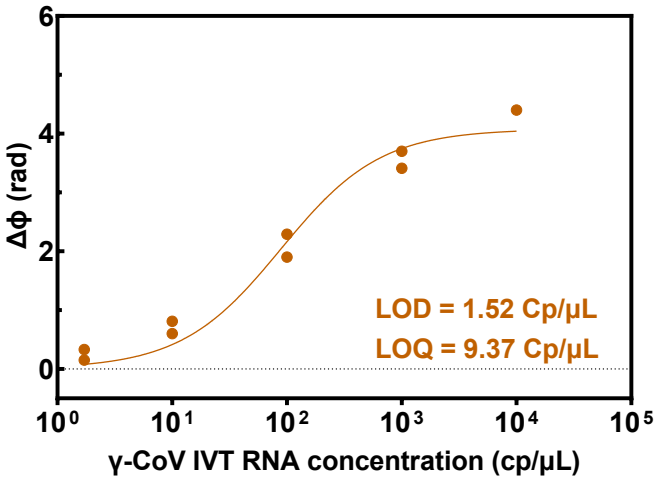


Figure 5.23 Calibration curve of biosensor signal versus RNA concentration fitted to a one-site specific binding model.

Finally, the analytical performance of the biosensor was benchmarked against RT-qPCR by correlating the sensor response with the corresponding Ct values (**Figure 5.24**). A strong inverse linear relationship was obtained (R^2 = 0.95), confirming the reliability of the BiMW biosensor for quantitative detection of gamma-CoV RNA across a broad concentration range.

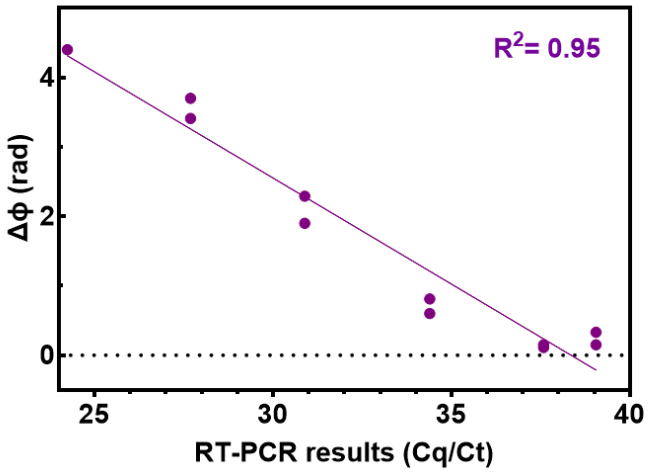


Figure 5.24 Benchmarking of the biosensor against RT-qPCR. All sensor signals are measured in duplicate.

5.4.4. Validation with animal samples

Following the controlled validation using IVT RNA, the performance of the BiMW biosensor was finally assessed and clinically validated using RNA extracted from animal samples corresponding to alpha/beta- and gamma-coronaviruses.

The alpha/beta-CoV assay was first evaluated using a set of bat faecal samples. These bat faecal samples were classified by semi-nested RT-PCR as 34 positives and 12 negatives. When measured using the BiMW biosensor, 27 samples were identified as positive and 19

as negative. Although discrepancies with respect to RT-PCR classification were observed, the biosensor responses showed a statistically significant distinction between positive and negative samples (Kruskal–Wallis test, $p < 0.0001$). The diagnostic performance of the assay yielded a sensitivity of 72% and a specificity of 83%, with a high positive predictive value (PPV = 93%) and a lower negative predictive value (NPV = 53%). These results indicate that positive detections are highly reliable, while samples with low viral loads may fall below the detection limit, leading to false negatives.

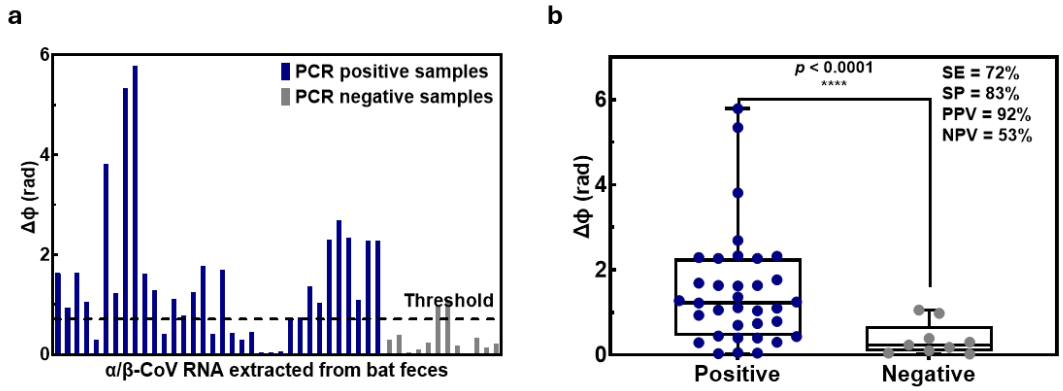


Figure 5.25 Validation of the BiMW biosensors: (**a**) Sensor signals for alpha/beta-CoV RNA extracted from bat feces samples (37 positive (blue) and 9 negative (grey), classified by the BiMW biosensor results). Negative samples according to RT-PCR are highlighted inside the grey box and (**b**) signal distribution and statistical analysis.

To further assess the diagnostic performance of the alpha/beta-CoV biosensor, a receiver operating characteristic (ROC) curve was constructed (**Figure 5.26**). The ROC analysis yielded an area under the curve (AUC) of 0.76, confirming the ability of the biosensor to discriminate between positive and negative samples.

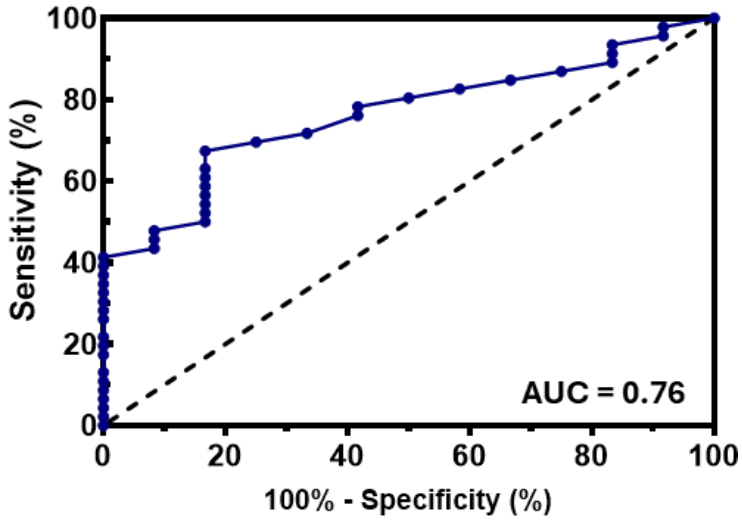


Figure 5.26 Statistical ROC analysis of alpha/beta-CoV BiMW assay.

This performance is consistent with the intrinsic challenges associated with wildlife samples. Bat-derived specimens typically present high viral diversity, low viral abundance,

and complex biological matrices, which can hinder detection. Moreover, the semi-nested RT-PCR method used as reference involves two amplification steps and provides exceptionally high sensitivity, representing a stringent benchmark for comparison.

After evaluating the alpha/beta assay with faecal bat samples, the gamma-CoV assay was validated using RNA extracted from chicken swab samples obtained from controlled animal trials (Céline Courtillon, ANSES). These samples were collected from specific pathogen-free (SPF) chickens experimentally infected with infectious bronchitis virus (IBV), providing a well-characterized dataset with known viral loads.

A total of 26 chicken samples were analyzed, including 17 RT-qPCR-positive and 9 negative samples. Positive samples covered a wide range of viral loads, with Ct values between 19.4 and 31.7, corresponding to concentrations from 4.1×10^5 to 1.7×10^2 copies/µL. The BiMW biosensor correctly identified 16 positive and 10 negative samples, showing strong agreement with RT-qPCR results. A clear relationship between viral load and sensor response was observed, with higher RNA concentrations producing stronger signals. Statistical analysis confirmed a significant distinction between positive and negative samples (Kruskal–Wallis test, $p < 0.0001$).

The gamma-CoV assay achieved a sensitivity of 88% and a specificity of 89%, with balanced predictive values (PPV = 94% and NPV = 80%). These figures are notably higher than those obtained for the alpha/beta-CoV assay, but a direct comparison between the two validation studies should be made with caution: the alpha/beta-CoV assay was benchmarked against a semi-nested RT-PCR reference, whose two-step amplification provides an exceptionally low detection threshold and thus classifies as positive a substantial fraction of samples lying below the reach of any direct, amplification-free method, whereas the gamma-CoV assay was benchmarked against single-step RT-qPCR. In addition, the gamma-CoV cohort was generated from SPF chickens under controlled experimental infection, yielding well-characterized viral loads and a homogeneous sample matrix, in contrast to the wildlife bat-faecal cohort used for the alpha/beta-CoV assay. Both factors contribute to the more favourable diagnostic figures obtained here, and the difference between the two studies

should be interpreted as a consequence of the validation conditions rather than of an intrinsic performance gap between the two surface-hybridization assays.

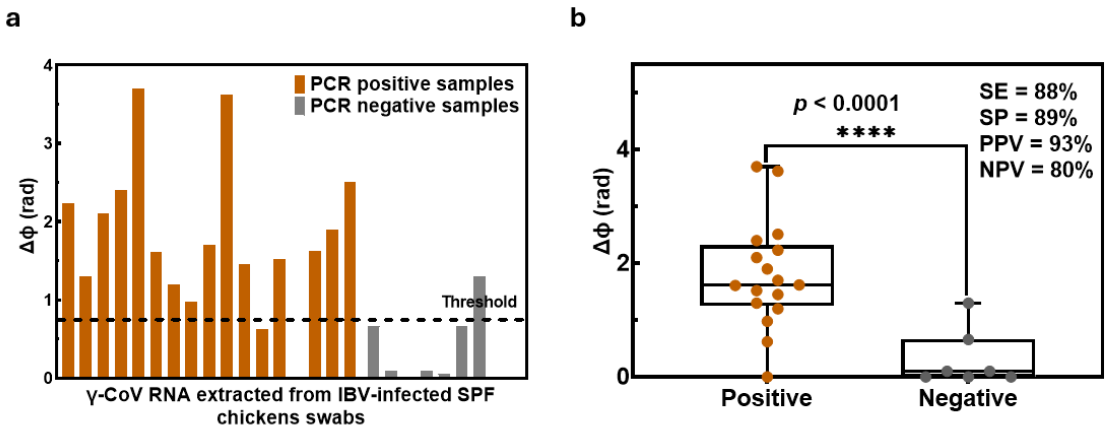


Figure 5.27 (**a**) Sensor signals for gamma-CoV RNA extracted from chicken swab samples (16 positive (orange) and 10 negative (grey), classified by the BiMW biosensor), negative samples according to RT-PCR are highlighted inside the grey box , and (**b**) signal distribution and statistical analysis.

For the gamma-CoV assay, ROC analysis was performed to quantitatively evaluate the classification performance of the biosensor (**Figure 5.28**). The resulting curve yielded an AUC of 0.92, indicating strong discrimination between positive and negative samples. This result agrees with the high sensitivity and specificity obtained for this assay.

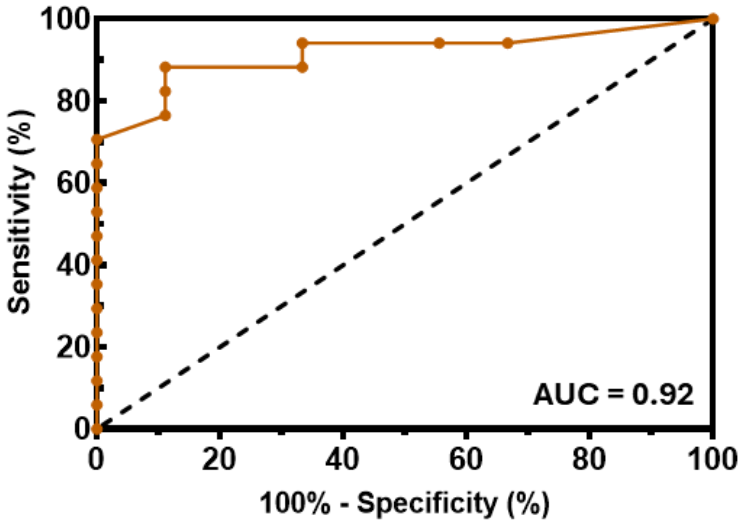


Figure 5.28 Statistical ROC analysis of gamma-CoV BiMW assay.

The difference between the alpha/beta- and gamma-CoV assays reflects the influence of sample type, viral load, and biological context on biosensor performance. In both cases, the high PPV values above 90% demonstrate that positive detections are highly reliable. However, the lower sensitivity and NPV in bat samples indicate that low viral-load specimens remain challenging for direct biosensing. In contrast, the gamma-CoV assay

was evaluated in a controlled infection model with well-defined viral concentrations, leading to a more balanced diagnostic profile.

These results are consistent with the limitations of label-free biosensors compared with amplification-based techniques.[162–164] RT-PCR benefits from enzymatic amplification and can detect extremely low target concentrations, while the BiMW biosensor relies on direct hybridization and optical signal transduction at the surface. Nevertheless, the BiMW assay offers important advantages in analytical speed and operational simplicity. Once RNA is available, detection can be completed within 10–15 min, reducing the turnaround time compared with conventional RT-PCR workflows.

5.5. Summary and conclusions

This chapter reports the development of SPR and BiMW biosensor assays for coronavirus RNA detection, with emphasis on rapid screening for zoonotic surveillance. The assays were designed around targets selected within the CONVAT and MUSECOV projects, covering SARS-CoV-2, alpha/beta-coronaviruses from mammalian reservoirs, and gamma-coronaviruses from avian hosts. Part of these results have been published in npj Biosensing: Serrano, B., Soler, M., Courtillon, C. *et al*. Rapid screening of animal coronaviruses in livestock and wildlife using a silicon photonics biosensor. *npj Biosensing* **3**, 26 (2026). https://doi.org/10.1038/s44328-026-00091-0.

The initial implementation on the SPR platform confirmed the feasibility of direct RNA detection through surface hybridization. Under optimized conditions, the SPR biosensor achieved LODs of 0.52 nM for the E gene, 1.51 nM for the N gene, 1.50 nM for the combined N+E assay, 1.28 nM for alpha/beta-CoV, and 1.49 nM for gamma-CoV targets. These results demonstrate the capability of the platform for coronavirus RNA detection, but also reveal the intrinsic sensitivity limitations of direct SPR detection for low-concentration nucleic acid targets.

To address this limitation, an antibody-based signal amplification strategy was implemented, reducing the LOD to 20 pM for gamma-CoV and 38 pM for gamma-CoV, corresponding to more than one order of magnitude improvement. The amplified alpha/beta-CoV SPR assay was then preliminarily evaluated using RNA extracted from bat faecal samples provided by the University of Barcelona. Despite the complexity of these wildlife samples and the stringent comparison with semi-nested RT-PCR, the biosensor discriminated positive and negative samples with 89% sensitivity, 80% specificity, and 94% PPV. These results showed that the SPR assay could detect coronavirus RNA in real animal samples, although low viral-load specimens remained challenging.

These constraints motivated the transfer of the biosensor design to the BiMW platform. The interferometric detection mechanism provided enhanced sensitivity by enabling the resolution of smaller refractive index changes associated with nucleic acid hybridization. As a result, direct detection without antibody amplification became feasible, with LODs of 38 pM for alpha/beta-CoV and 91 pM for gamma-CoV synthetic targets. The analytical performance was further evaluated using IVT gamma-CoV RNA, enabling controlled assessment with a longer and more representative RNA target. Under these conditions, the

biosensor achieved an LOD of 1.52 copies/μL and showed strong correlation with RT-qPCR results.

Validation with animal samples demonstrated that biosensor performance depends strongly on the biological context. The alpha/beta-CoV assay, evaluated in bat faecal samples, exhibited a sensitivity of 72% and specificity of 83%, with PPV of 93%, NPV of 53%, and AUC of 0.76. In contrast, the gamma-CoV assay, tested in chicken swab samples under controlled infection conditions, showed improved performance, with sensitivity of 88%, specificity of 89%, PPV of 94%, NPV of 80%, and AUC of 0.92. These differences reflect the effect of sample matrix, viral load, target accessibility, and reference method sensitivity.

The developed biosensors should be considered complementary tools for rapid screening and sample prioritization rather than replacements for confirmatory NAAT methods. Future work should focus on expanding the number and diversity of animal samples, improving sample preparation where needed, and adapting the assay to multiplexed detection of different coronavirus groups on the same chip. In this context, integrating photonic biosensors into One Health surveillance strategies could help reduce the diagnostic gap between human and animal health and support earlier detection of potential zoonotic threats.

Chapter 6

PHOTONIC BIOSENSORS FOR THE SCREENING OF BACTERIAL STIs AND ANTIBIOTIC RESISTANCE

The development and analytical validation of BiMW biosensor assays for the screening of bacterial STIs and antibiotic resistance markers is presented. A detailed explanation of the probe design strategy for N. gonorrhoeae (opa gene), C. trachomatis (ompA gene) and ciprofloxacin resistance-associated mutations in the N. gonorrhoeae gyrA gene is provided, followed by the optimization of the BiMW hybridization conditions for the specific detection of synthetic DNA targets. The chapter also describes the development of a hybridization strategy with controlled stringency for the discrimination of the single-nucleotide difference between the ciprofloxacin-resistant and wild-type gyrA sequences. Finally, a sample preparation workflow (bacterial lysis, DNA fragmentation and thermal denaturation) is established, and the optimized N. gonorrhoeae assay is validated in lysed bacterial samples within the framework of the TYPLEX and DIGITS projects.

6. Photonic biosensors for screening of sexually transmitted bacteria and antibiotic resistance

This chapter focuses on the application of the BiMW interferometric biosensor to the detection of bacterial sexually transmitted infections and antimicrobial resistance-associated genetic markers. The work targets two clinically relevant pathogens, *Neisseria gonorrhoeae* and *Chlamydia trachomatis*, as well as ciprofloxacin resistance in *N. gonorrhoeae* through mutations in the *gyrA* gene. The study was carried out in the context of the TYPLEX project (Grant PDC2023-145891-I00, funded by MCIU/AEI/10.13039/501100011033 and by the European Union NextGenerationEU/PRTR) and the DIGITS project (Ref. 23S06145-001, Research and Innovation project grants awarded by the Barcelona City Council, in partnership with the "la Caixa" Foundation), in collaboration with the Department of Microbiology of Vall d'Hebron University Hospital.

6.1. STI Epidemiology and antimicrobial resistance challenges

Chlamydia trachomatis and *Neisseria gonorrhoeae* are among the most prevalent bacterial STIs worldwide. Their control remains difficult because many infections are asymptomatic, allowing infected individuals to transmit the pathogen without seeking medical care. Transmission is further sustained by delayed diagnosis, limited access to screening, stigma, and insufficient surveillance programs. Therefore, improved diagnostic tools are needed not only for individual patient management, but also for infection control and public health surveillance.

Among community-acquired pathogens, *N. gonorrhoeae* was recently classified as a high-priority bacterial pathogen by the WHO, having developed resistance to successive antibiotic classes and showing emerging resistance to third-generation cephalosporins, its current last-line treatment. *C. trachomatis*, the most prevalent bacterial STI globally with over 127 million new cases per year, remains susceptible to current agents but its largely asymptomatic nature results in widespread undetected infection and reliance on untargeted empirical therapy.[165]

The healthcare consequences of undiagnosed bacterial STIs extend well beyond the acute infection. In the absence of timely detection and treatment, *C. trachomatis* infection can progress to pelvic inflammatory disease (PID), a leading cause of tubal factor infertility, ectopic pregnancy, and chronic pelvic pain in women, with an estimated 15% of untreated cases developing PID.[166,167] Neonatal transmission during delivery causes neonatal conjunctivitis and pneumonia, adding a further dimension of preventable morbidity. *N gonorrhoeae*, if untreated, causes similar reproductive complications, and the progressive erosion of treatment options due to AMR in *N. gonorrhoeae* directly compounds these outcomes: treatment failure leads to prolonged infection, higher rates of onward transmission, and greater risk of complications. Both pathogens disproportionately affect young adults and are subject to significant underdiagnosis due to the asymptomatic or paucisymptomatic nature of most infections, a pattern that sustains transmission chains silently and underscores the critical role of screening and point-of-care diagnostics in interrupting them.

These two pathogens differ markedly in their biological organization, which also influences diagnostic strategies. *N. gonorrhoeae* is a Gram-negative diplococcus with an outer membrane containing surface proteins such as opacity-associated proteins and porins, which contribute to host interaction and immune evasion. In contrast, *C. trachomatis* is an obligate intracellular bacterium with a biphasic developmental cycle, alternating between the infectious elementary body and the replicative reticulate body. Its outer membrane contains the major outer membrane protein (MOMP), encoded by the *ompA* gene, which is widely used as a molecular marker. These structural and biological differences are important because they affect sample processing, target accessibility, and the choice of genomic markers for nucleic acid-based detection.[168,169]

A schematic representation of *Chlamydia trachomatis* and *N. gonorrhoeae structure* is shown in **Figure 6.1**.

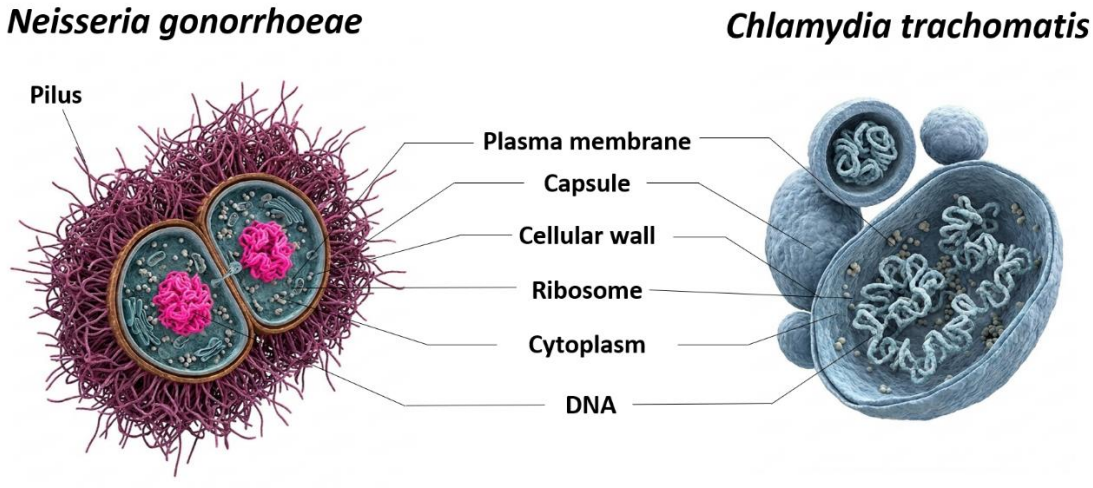


Figure 6.1 Schematic representation of *Chlamydia trachomatis* and *N. gonorrhoeae* structure.

From a diagnostic perspective, NAATs are currently the standard approach for the detection of *C. trachomatis* and *N. gonorrhoeae*, offering high sensitivity and specificity. However, they generally focus on pathogen identification and do not always provide antimicrobial susceptibility information. This creates an important limitation for *N. gonorrhoeae*, where treatment decisions are often made before resistance data are available.[170]

The clinical management of gonorrhoea is particularly complicated by the capacity of *N. gonorrhoeae* to acquire resistance to successive antibiotic classes. Resistance has emerged against sulfonamides, penicillins, tetracyclines, macrolides, and fluoroquinolones, progressively reducing available treatment options. As a consequence, ceftriaxone, an injectable third-generation cephalosporin, remains the main empirical treatment in many settings. Although effective, its widespread empirical use increases selective pressure on one of the last reliable therapeutic options.[171]

This context creates a clear need for diagnostic methods that can provide resistance information before treatment whenever possible. Ciprofloxacin susceptibility is a clinically relevant example. Fluoroquinolone resistance in *N. gonorrhoeae* is strongly associated with

point mutations in the quinolone-resistance-determining region of the *gyrA* gene, particularly at codon 91. Strains carrying a wild-type *gyrA* sequence at this position are generally associated with ciprofloxacin susceptibility, whereas resistant strains frequently carry mutations that alter DNA gyrase and reduce drug binding. Therefore, detection of *gyrA* mutations can support a more targeted treatment strategy, allowing ciprofloxacin to be used when susceptibility is predicted and preserving ceftriaxone for resistant infections or cases where susceptibility cannot be inferred.[172–174]

Current guidelines emphasize the importance of culture-based antimicrobial susceptibility testing and test-of-cure, but these approaches are limited by the fastidious nature of *N. gonorrhoeae*, the need for viable bacteria, strict sample transport conditions, and longer processing times. Molecular detection of resistance-associated mutations provides a faster and clinically actionable alternative, especially when integrated with pathogen identification in the same diagnostic workflow.[175,176]

Photonic biosensors have already shown promise for bacterial diagnostics, including whole-cell detection, bacterial DNA analysis and antimicrobial resistance marker detection.[177,178] In the STI field, Soler et al. reported a multiplexed nanoplasmonic biosensor based on gold nanohole arrays for the simultaneous detection of *C. trachomatis* and *N. gonorrhoeae* directly in urine samples. In that work, antibody-functionalized surfaces were used to detect whole bacteria, reaching limits of detection of 300 CFU/mL for *C. trachomatis* and 1500 CFU/mL for *N. gonorrhoeae*, without DNA extraction or amplification.[84] This demonstrated the potential of label-free optical biosensors for STI screening, but the assay targeted intact bacterial cells rather than pathogen-specific DNA sequences or resistance-associated mutations. Therefore, an important gap remains for biosensor platforms capable of combining bacterial nucleic acid detection with genetic AMR information.

In this context, the BiMW biosensor was applied to the detection of *N. gonorrhoeae*, *C. trachomatis*, and ciprofloxacin resistance-associated *gyrA* mutations. The objective was to evaluate whether a label-free photonic biosensor could support direct bacterial STI detection and provide a basis for future integration of pathogen identification and antimicrobial resistance profiling within the same platform.

6.2. Target selection and probe design

In this chapter, target selection was focused on three clinically relevant bacterial DNA markers: the *opa* gene for *N. gonorrhoeae* detection, the *ompA* gene for *C. trachomatis* detection, and the *gyrA* gene for ciprofloxacin resistance profiling in *N. gonorrhoeae*. These targets were selected to evaluate the applicability of the BiMW platform to two different diagnostic tasks: direct STI pathogen detection and discrimination of an antimicrobial resistance-associated point mutation.

For *N. gonorrhoeae* detection, the opacity-associated *opa* gene was selected as the diagnostic target. The *opa* genes encode a family of outer membrane proteins involved in host-cell adhesion, invasion and immune evasion. This target is particularly attractive for nucleic acid detection because it is present in multiple copies in the *N. gonorrhoeae*

genome, with approximately 11 copies per genome. The use of a multicopy target increases the effective number of detectable sequences per bacterial cell, which is advantageous for label-free biosensing approaches where no enzymatic amplification is used. For probe design, a conserved internal region shared across different *opa* variants was selected to improve inclusivity while minimizing potential cross-reactivity with closely related commensal *Neisseria* species.[179,180]

For *C. trachomatis* detection, the *ompA* gene was selected. This gene encodes the major outer membrane protein, one of the most abundant and immunologically relevant membrane components of *C. trachomatis*. The *ompA* gene has been widely used in molecular diagnostics and genotyping because it contains species-specific regions suitable for pathogen identification. In this work, a conserved region of *ompA* was selected to enable specific detection of *C. trachomatis* while maintaining compatibility with a short hybridization-based biosensor assay.[181–183]

In addition to pathogen detection, ciprofloxacin resistance in *N. gonorrhoeae* was addressed by targeting the *gyrA* gene. This gene encodes the A subunit of DNA gyrase, the molecular target of fluoroquinolone antibiotics. Resistance to ciprofloxacin is strongly associated with point mutations in the quinolone-resistance-determining region of *gyrA*, particularly at codon 91. These mutations alter the target enzyme and reduce fluoroquinolone binding.[184–187] Therefore, the *gyrA* target was selected not only for DNA detection, but also as a model to evaluate whether the BiMW biosensor could discriminate a single-nucleotide difference associated with antimicrobial resistance.[188]

The *gyrA* assay represents a more demanding analytical challenge than the *opa* and *ompA* assays. For pathogen detection, the objective is to distinguish the target organism from non-target organisms. For resistance profiling, the objective is to distinguish two highly similar sequences from the same species that differ by only one nucleotide. This requires not only efficient hybridization of the resistant target, but also suppression of hybridization with the wild-type sequence. Therefore, the *gyrA* assay was designed to evaluate both sensitivity and mismatch discrimination under controlled hybridization conditions.[62,104,189]

DNA probes were designed according to the principles described in Chapter 4. Each probe was selected as the reverse complement of the target region and evaluated according to length, GC content, melting temperature and absence of strong self-complementarity or secondary structures. These parameters were assessed using sequence-analysis software and AI-assisted design tools to support probe selection and compare candidate sequences before experimental validation. The final probes included a terminal thiol modification for covalent attachment to the functionalized BiMW surface, and a C_6 vertical spacer was incorporated to improve probe accessibility at the sensing interface.

For the AMR assay, the probe was designed so that the resistance-associated nucleotide was located within the hybridization region in a position suitable for mismatch discrimination between the mutant and wild-type sequences. Because the difference between both targets is only one nucleotide, the predicted melting temperature, GC content and position of the mismatch were particularly important for defining hybridization

conditions with sufficient stringency. This step was essential to favour detection of the resistant sequence while reducing hybridization with the wild-type sequence.[62,104]

In the first stage of assay development, short synthetic DNA targets were used to evaluate probe performance under controlled conditions. This allowed the sensitivity and specificity of each assay to be assessed before moving to bacterial samples, where genomic DNA release, fragmentation, denaturation and matrix effects strongly influence target accessibility and biosensor response.

The selected target sequences and their corresponding DNA probes are summarized in **Table 6.1**.

Table 6.1 DNA probes and target DNA sequences.

Assay	Target gene	Target DNA sequence	DNA probe
***N. gonorrhoeae* detection**	**opa**	5'- CTA AGG TGA TGA AGC ACC GG-3'	5'- SH-C_6-CCG GTG CTT CAT CAC CTT AG-3'
***C. trachomatis* detection**	**ompA**	5'- AAG CTT ATC CAG AAA CAA ATC G-3'	5'- SH-C_6- CGA TTT GTT TCT GGA TAA GCT T-3'
AMR detection	**gyrA**	5' - TTA ACT GCG AAA TCG CCG GC -3'	5'- SH-C_6-GCC GGC GAT TTC GCA GTT AA -3'
AMR specificity control	**gyrA** wild-type	5' - TTA ACT GCG GAA TCG CCG GC -3'	-

6.3. BiMW biosensor for bacterial DNA detection

6.3.1. Sensor biofunctionalization and assay optimization

The detection of *Neisseria gonorrhoeae* and *Chlamydia trachomatis* DNA was evaluated using the BiMW biosensor under the optimized surface biofunctionalization conditions established in Chapter 4. Based on those results, vapor-phase silanization with APTES followed by PDITC crosslinking was selected as the surface functionalization strategy, due to its reproducibility and its ability to generate homogeneous reactive surfaces for covalent probe immobilization.

Probe immobilization was monitored in real time using the BiMW phase shift as readout. As shown in **Figure 6.2**, both probes produced clear and reproducible immobilization signals, with phase shifts of approximately $\Delta\phi \approx 46.2$ rads. This confirmed the successful attachment of the *N. gonorrhoeae* and *C. trachomatis* probes under the selected conditions. The similar immobilization responses obtained for both probes suggest that probe attachment was mainly governed by the surface chemistry and immobilization protocol, rather than by major sequence-dependent differences between the probes.

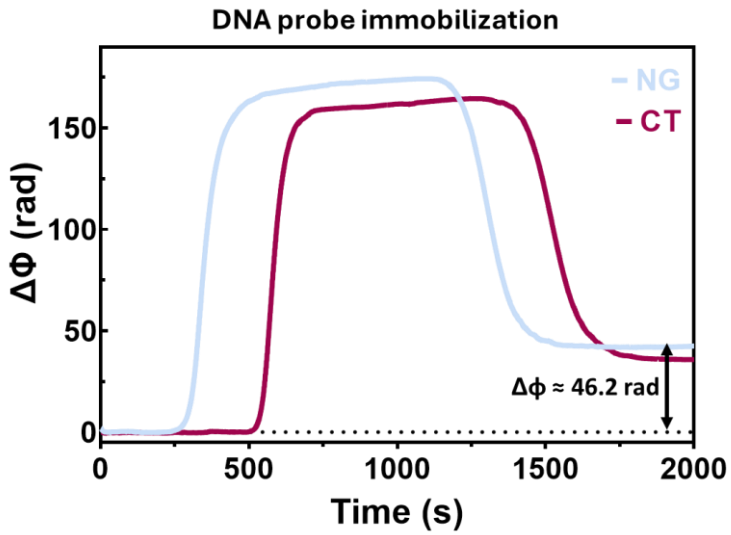


Figure 6.2 BiMW sensograms of the *N. gonorrhoeae* (NG) and *C. trachomatis* (CT) DNA probe immobilization.

Although general hybridization conditions were established in Chapter 3, the buffer composition was re-evaluated for the bacterial DNA targets used in this chapter. The synthetic targets designed for *N. gonorrhoeae* and *C. trachomatis* were short DNA oligonucleotides, with sequence-dependent differences in GC content and predicted duplex stability. Therefore, the hybridization conditions were adjusted to promote efficient target binding while minimizing nonspecific responses.

The effect of ionic strength was first assessed by testing SSC concentrations ranging from 2× to 7×. As shown in **Figure 6.3**, the highest and most reproducible hybridization responses for both *N. gonorrhoeae* and *C. trachomatis* were obtained using 2× SSC. Increasing the SSC concentration did not improve the signal and led to higher variability. This may indicate that, for these short DNA targets, higher ionic strength did not enhance productive hybridization at the surface and may have favoured nonspecific interactions or less controlled surface confined binding. Based on these results, 2× SSC was selected as the base hybridization buffer.

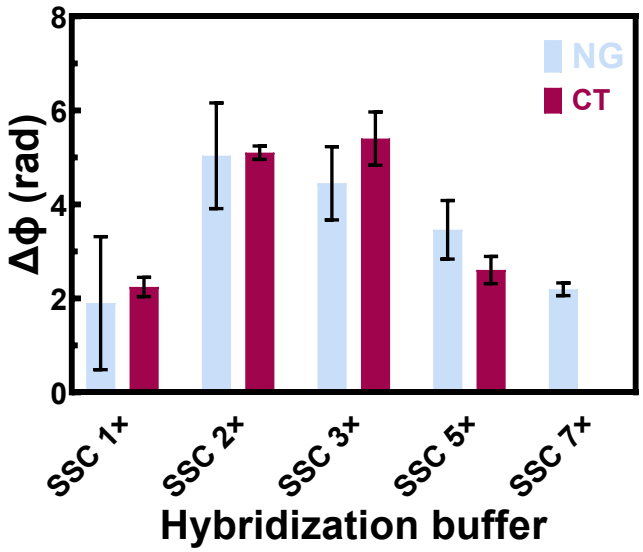


Figure 6.3 Bars graph with SSC salinity with NG and CT.

To further improve hybridization performance, formamide was incorporated into the buffer. The addition of 1% formamide improved signal stability and hybridization efficiency. At this low concentration, formamide can reduce weak secondary structures and improve strand accessibility without excessively destabilizing the probe–target duplex. Based on these results, 2× SSC supplemented with 1% formamide was selected as the optimized hybridization buffer for the detection of the synthetic bacterial DNA targets.

6.3.2. Detection of *N. gonorrhoeae* and *C. trachomatis* synthetic DNA targets

After confirming successful probe immobilization and selecting the hybridization buffer, the analytical performance of the BiMW biosensor was evaluated using short synthetic DNA targets corresponding to *N. gonorrhoeae* and *C. trachomatis*.

Under the optimized conditions, in **Figure 6.4**, calibration curves were obtained for both targets by injecting increasing concentrations of synthetic DNA (0.5 – 100 nM). A concentration-dependent response was observed in both assays, confirming that the BiMW biosensor enables quantitative detection of the selected bacterial DNA sequences. The LOD was 290 pM for *N. gonorrhoeae* and 171 pM for *C. trachomatis*.

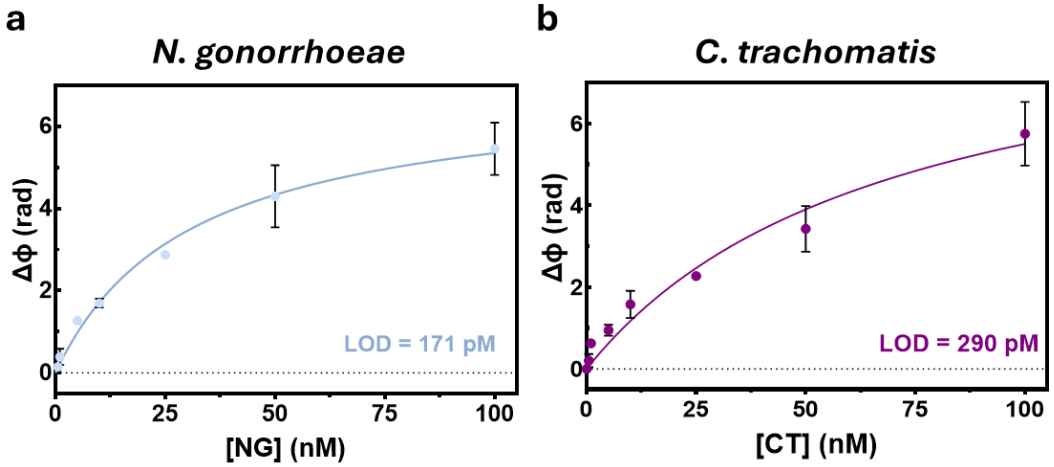


Figure 6.4 Calibration curve for (**a**) *N. gonorrhoeae* and for (**b**) *C. trachomatis*.

In parallel, specificity was assessed by injecting non-complementary DNA sequences under the same experimental conditions. Negligible responses were obtained for the non-target sequences, confirming that the observed signals were associated with specific probe–target hybridization rather than nonspecific adsorption or cross-reactivity at the sensor surface (**Figure 6.5**).

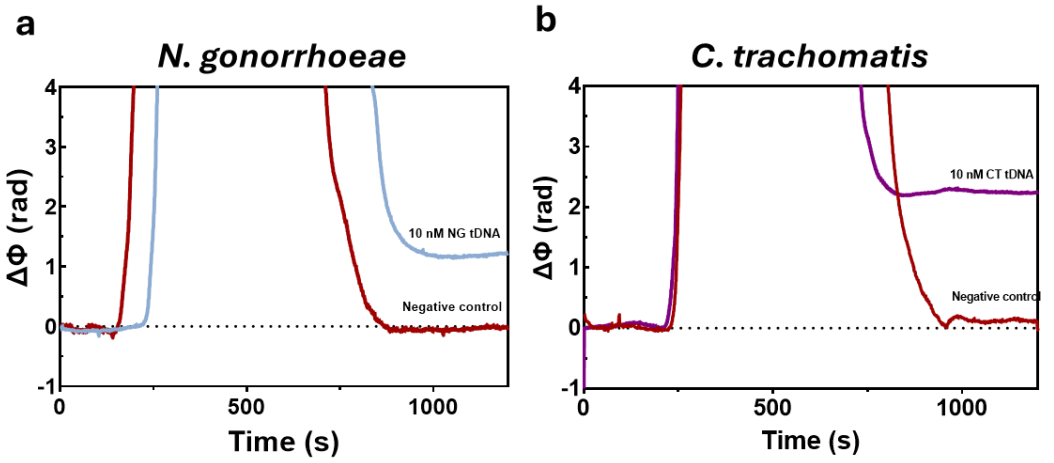


Figure 6.5 Specificity assay for (**a**) *N. gonorrhoeae* and (**b**) *C. trachomatis* synthetic DNA detection using non-complementary DNA controls.

The slightly improved sensitivity observed for *C. trachomatis* may be related to sequence-dependent differences in hybridization efficiency, including GC content, predicted duplex stability, or target accessibility. Since both assays used the same surface chemistry and hybridization buffer, the difference in LOD is most likely associated with the intrinsic properties of the probe–target pair rather than with the immobilization process.

The obtained LODs are reasonable for direct, amplification-free nucleic acid detection. For comparison, Kumar et al. reported a 10 pM LOD using a liquid crystal-assisted optical DNA biosensor for selective detection of N. *gonorrhoeae*.[190] Kaur et al. developed an SPR biosensor for Neisseria meningitidis DNA using a ZnO/Au thin-film sensor functionalized

with complementary DNA probes, obtaining an LOD of approximately 0.6 μM and a linear range between approximately 1.2 and 22 μM.[191] Other approaches have used signal enhancement to improve sensitivity; for example, gold nanoparticle-enhanced SPR was applied to the detection of *E. coli* 16S rRNA, reaching an LOD of approximately 0.1 pM.[192] These examples show that bacterial nucleic acid biosensors can reach different sensitivity ranges depending on the transducer, target type and use of amplification or enhancement strategies. The BiMW assay developed here provides direct, label-free detection of STI-related DNA targets within the picomolar range, without secondary probes, nanoparticles or enzymatic amplification.

6.3.3. Detection of antibiotic resistance in *N. Gonorrhoea*e DNA

After demonstrating the detection of *N. gonorrhoeae* and *C. trachomatis* synthetic DNA targets, the BiMW biosensor was applied to the detection of ciprofloxacin resistance-associated mutations in *N. gonorrhoeae*. This assay represents a more demanding analytical challenge than pathogen detection because it requires discrimination between two nearly identical DNA sequences. In this case, the resistant and wild-type *gyrA* targets differ by a single nucleotide.

The detection of this mutation relies on the difference in hybridization stability between the perfectly matched resistant target and the single-mismatch wild-type sequence. However, this thermodynamic difference is small, particularly in short oligonucleotides and under surface confined conditions. Therefore, the *gyrA* assay could not be optimized only to maximize the sensor signal, it also required conditions with sufficient stringency to suppress hybridization of the wild-type sequence.

The same probe immobilization conditions described in Section 5.3.1 were used, allowing direct comparison with the pathogen-detection assays. Initial experiments were performed using the hybridization buffer optimized for *N. gonorrhoeae* and *C. trachomatis* detection, composed of 2× SSC supplemented with 1% FA. Under these conditions, the resistant *gyrA* target produced a clear concentration-dependent response, confirming that the BiMW

biosensor was able to detect the AMR-associated sequence. As shown in **Figure 6.6**, the calibration curve obtained under these conditions yielded a limit of detection of 87 pM.

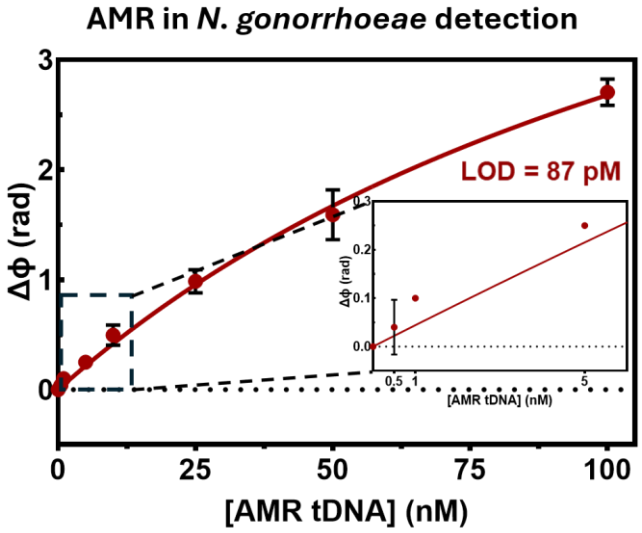


Figure 6.6 Calibration curve for detection of the ciprofloxacin resistance-associated *gyrA* sequence using 2× SSC + 1% FA.

However, when the wild-type *gyrA* sequence was tested under the same conditions, a significant response was also observed. This indicated that the buffer provided efficient hybridization, but not enough selectivity to discriminate the single-base mismatch. This distinction is critical for antimicrobial resistance profiling: a strong response to the resistant sequence is only useful if the assay can also minimize the signal from the susceptible wild-type sequence.

To improve mismatch discrimination, the hybridization buffer was further optimized. First, the FA concentration was increased to 5% to increase stringency by partially destabilizing probe–target duplexes. Although this condition reduced the overall signal intensity, it did not provide sufficient discrimination between the resistant and wild-type sequences. This suggests that increasing formamide alone mainly decreased hybridization efficiency without selectively suppressing the mismatched duplex. TMAC was then evaluated as a specificity-enhancing additive. TMAC can reduce the influence of base composition on duplex stability and is commonly used to improve mismatch discrimination in nucleic acid hybridization assays. At 1 M TMAC, the wild-type signal was strongly reduced, but the specific response from the resistant target also decreased markedly, indicating overly stringent conditions. Reducing the TMAC concentration to 0.5 M provided a better balance, preserving the resistant-target response while suppressing hybridization with the wild-type sequence (**Figure 6.7**).

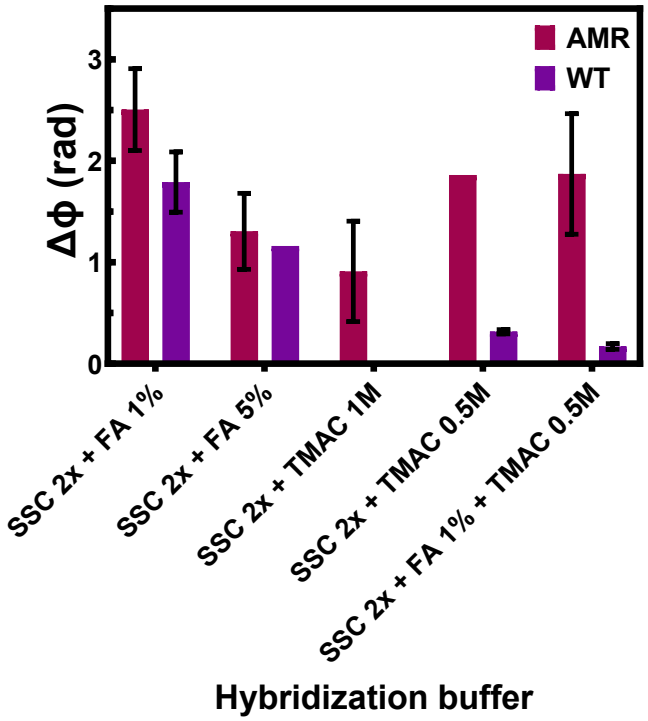


Figure 6.7 Optimization of hybridization stringency for discrimination between resistant and wild-type gyrA sequences.

Based on these results, 2× SSC + 1% FA + 0.5 M TMAC was selected as the optimal buffer for resistance-associated mutation detection. Under these conditions, the biosensor clearly distinguished the resistant *gyrA* target from the wild-type sequence, demonstrating that the BiMW platform can be adapted for single-base mutation discrimination when hybridization stringency is carefully controlled.

A new calibration curve was then obtained for the resistant *gyrA* target under the optimized specificity conditions, yielding a limit of detection of 189 pM (**Figure 6.8**).

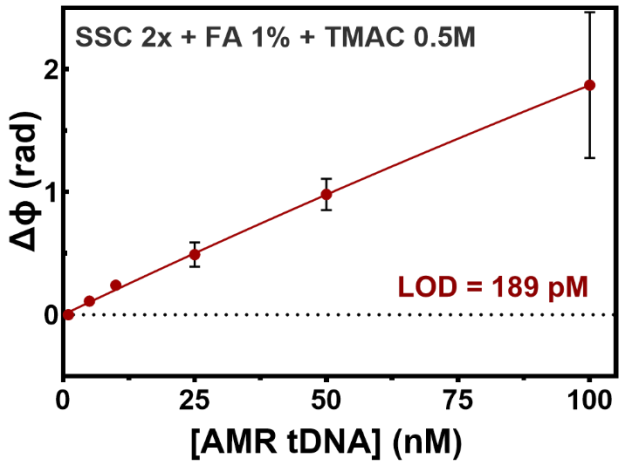


Figure 6.8 Calibration curve of *N. gonorrhoeae* AMR with optimized buffer.

The increase in LOD from 87 pM to 189 pM reflects the expected trade-off between sensitivity and specificity. Under the initial buffer conditions, the resistant *gyrA* target was detected with higher sensitivity, but the wild-type sequence also produced a significant response. Therefore, this condition was not suitable for resistance profiling. After increasing the hybridization stringency with 0.5 M TMAC, the wild-type signal was suppressed and the resistant sequence could be selectively detected, although with a moderate loss of sensitivity. For this reason, the 189 pM LOD represents the relevant analytical performance of the assay for ciprofloxacin resistance-associated mutation detection.

Previous BiMW biosensors have demonstrated very high sensitivity for bacterial AMR gene detection. Maldonado et al. reported direct, label-free detection of unamplified multidrug-resistance genes, targeting *bla*CTX-M-15 and *bla*NDM-5 in bacterial genomic DNA, with LODs of 30 aM and 24–28 aM, respectively.[188] This work demonstrated the strong potential of BiMW interferometry for AMR diagnostics. However, the analytical problem addressed here is different. Detection of a complete resistance gene confirms the presence or absence of a genetic determinant, whereas the present *gyrA* assay requires discrimination between two nearly identical sequences differing by a single nucleotide. Therefore, the LOD obtained in this work is higher, but its relevance lies in the achieved mismatch discrimination. For ciprofloxacin resistance profiling, specificity against the wild-type sequence is as important as sensitivity, because a false resistant signal would directly affect treatment interpretation.

The relevance of *gyrA*-based ciprofloxacin resistance testing is already demonstrated by commercial molecular assays such as ResistancePlus® GC and the VIASURE *N. gonorrhoeae* ciprofloxacin-resistant Real Time PCR kit.[193] These assays target the *gyrA* codon 91 region and report very high diagnostic performance, with analytical sensitivities down to a few DNA copies per reaction. However, they rely on real-time PCR amplification, fluorescent readout, dedicated instrumentation, and amplification reagents, which increases workflow complexity and prevents fully direct label-free detection.

In contrast, biosensor-based detection of this specific *N. gonorrhoeae gyrA* resistance-associated mutation remains much less explored. The results obtained here show that the BiMW platform can be adapted for direct, label-free, and amplification-free discrimination of a clinically relevant point mutation. Although the preliminary sensitivity level achieved in this work is lower than PCR-based methods and lower than previous BiMW assays targeting full AMR genes, the ability to distinguish a single-base difference is a critical step toward integrating pathogen detection and resistance profiling in the same photonic biosensor platform.

6.3.4. Validation in real cells

After demonstrating the detection of short synthetic DNA targets, the applicability of the BiMW biosensor was evaluated using real *N. gonorrhoeae* bacterial samples provided within the collaboration with Vall d'Hebron University Hospital. This step was necessary to assess the assay under conditions closer to real diagnostic samples, where sample preparation, target accessibility and matrix effects become critical.

The transition from synthetic targets to bacterial samples introduces an important analytical challenge. The synthetic DNA targets used in the previous sections were short oligonucleotides of 20–22 nucleotides, specifically designed to be fully accessible to the immobilized probes. In contrast, bacterial samples contain long double-stranded genomic DNA inside intact cells. *N. gonorrhoeae* has a genome of approximately 2.2 Mbp, meaning that the selected *opa* target region is embedded within a much larger genomic structure and is not directly accessible for surface hybridization.

Direct detection of bacterial DNA therefore requires a sample preparation workflow capable of converting genomic DNA into a format compatible with hybridization at the sensor surface. This involves bacterial lysis, DNA fragmentation and DNA denaturation. Lysis releases genomic DNA into solution, fragmentation reduces DNA size and improves target accessibility, and thermal denaturation separates the complementary strands immediately before biosensor analysis. Rapid cooling on ice was used to limit re-annealing before injection over the sensor surface.

The compatibility of the sample matrix with the label-free BiMW sensor must also be considered. Lysed bacterial samples contain not only target DNA, but also proteins, lipids, membrane fragments, salts, metabolites and other cellular components released during lysis. Since the sensor detects refractive index changes close to the surface, nonspecific adsorption of lysate components can generate background signal, baseline drift or reduced reproducibility. Adsorbed proteins or membrane fragments can also block access to the immobilized DNA probes, reducing hybridization efficiency.

To establish a suitable protocol, different lysis, fragmentation, denaturation and buffer conditions were evaluated. Two lysis strategies were initially investigated: enzymatic lysis using lysozyme and detergent-assisted thermal lysis using SDS combined with heating.

The lysozyme-based approach resulted in weak and unstable signals, with no clear dependence on bacterial concentration, indicating insufficient DNA release or poor compatibility with the sensing interface. As shown in **Figure 6.9**, synthetic *N. gonorrhoeae* target DNA diluted in the lysis buffer was included as a control to evaluate whether the buffer perturbed hybridization, interacted nonspecifically with the biofunctionalized surface or generated bulk refractive index effects. The results showed that buffer compatibility had to be evaluated before transferring the assay from purified synthetic targets to lysed bacterial samples.

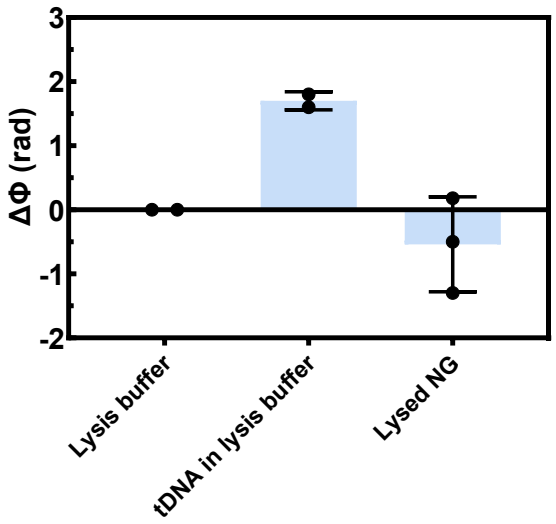


Figure 6.9 Evaluation of lysozyme-based lysis and lysis-buffer compatibility of 10^7 CFU/mL sample.

In contrast, detergent-assisted thermal lysis provided more consistent and reproducible responses. SDS disrupts bacterial membranes and denatures proteins, while heating promotes cell disruption and DNA release. Compared with enzymatic lysis, this protocol does not require specific enzyme activity or long incubation times, making it more compatible with simplified diagnostic workflows.

Different SDS concentrations and heating times were evaluated, including 0.1–1% SDS and 10–15 min at 95°C. Within the tested conditions, no major differences were observed as a function of heating time. Therefore, 1% SDS and 10 min at 95 °C were selected due to simplicity, efficient DNA release and compatibility with the biosensor response.

As shown in **Figure 6.10**, the SDS-based thermal lysis protocol produced measurable responses for lysed *N. gonorrhoeae*, indicating that bacterial DNA was released and that the target sequence could be detected after sample treatment. In the same experiment, synthetic *N. gonorrhoeae* DNA diluted in the lysis buffer was included as a positive hybridization control. However, the lysed *Pseudomonas aeruginosa* control also produced a noticeable background response, indicating that lysed bacterial samples release components that can interact nonspecifically with the biofunctionalized surface. Therefore, the SDS-based lysis protocol improved DNA release, but matrix-related background signals still needed to be controlled.

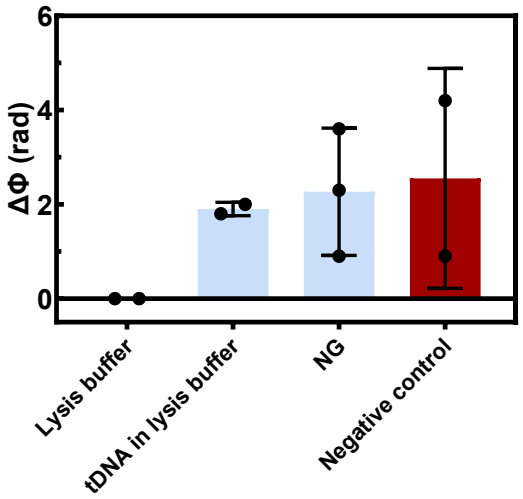


Figure 6.10 10^6 CFU/mL sample lysed with SDS 1% and 10min incubation at 95ºC.

To reduce this background, the hybridization buffer was further optimized. Tween 20 at 0.5% was incorporated as a non-ionic surfactant to reduce nonspecific adsorption, mainly by limiting hydrophobic interactions. This reduced the background signal. Dextran sulfate at 1 mg/mL was then introduced as a polyanionic crowding agent to increase hybridization efficiency by increasing the effective local concentration of target DNA near the sensor surface. This led to higher signal intensity.

The combination of both additives provided the best overall performance, yielding more specific and reproducible signals compared to SSC buffer alone. Therefore, SSC supplemented with Tween 20 and dextran sulfate was selected for subsequent experiments with lysed bacterial samples (**Figure 6.11**).

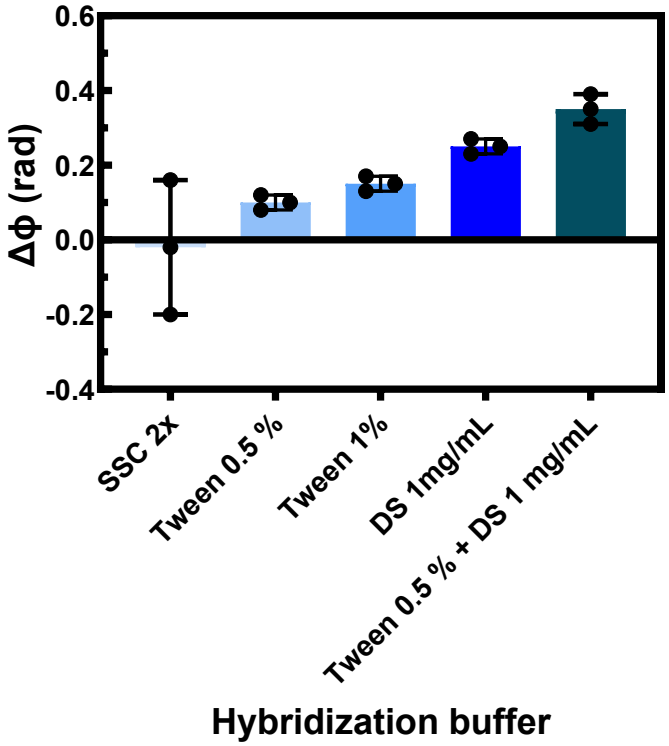


Figure 6.11 Antifouling additives effect in hybridization buffer for 10^6 CFU/*mL N. gonorrheae* samples.

Based on these results, the final sample preparation workflow consisted of detergent-assisted thermal lysis, followed by sonication and thermal denaturation immediately prior to analysis, using the optimized hybridization buffer containing Tween 20 and dextran sulfate.

To assess assay specificity, a non-target bacterial control, *Pseudomonas aeruginosa*, was analyzed under the same conditions. The control produced a negligible response compared to the target samples, confirming that the optimized protocol reduced nonspecific background and that the measured signal was mainly associated with specific hybridization of *N. gonorrhoeae* DNA (**Figure 6.12**).

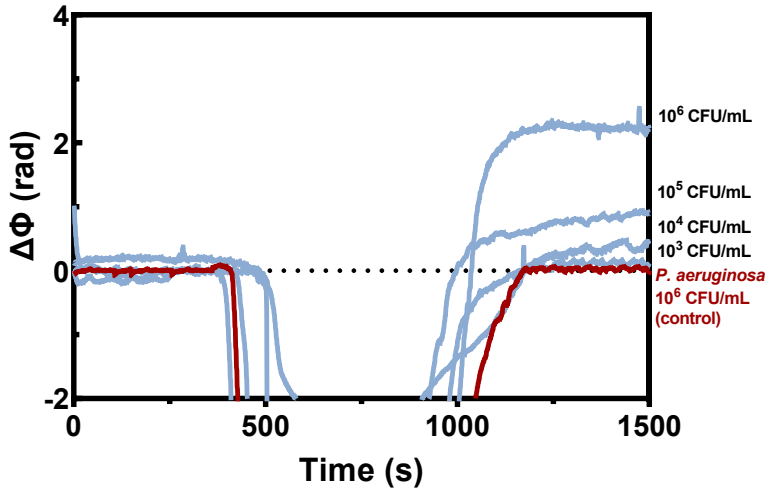


Figure 6.12 Sensograms of *N. gonorrhoeae* and negative control (*P. aeruginosa*) detection.

At lower concentrations, a linear response was observed, enabling quantitative analysis. From these measurements, an LOD of 2.29 × 10^3 CFU/mL was determined (Figure 5.X), demonstrating that the BiMW biosensor can detect *N. gonorrhoeae* DNA from lysed bacterial samples without nucleic acid amplification.

This value is higher than the sensitivity obtained with synthetic DNA targets, as expected. In bacterial lysates, the target sequence is embedded within long double-stranded genomic DNA and must be released, fragmented, denatured and maintained as an accessible single-stranded region for hybridization. Incomplete denaturation, rapid re-hybridization of complementary strands and limited accessibility of the target region are likely the main factors limiting sensitivity. In contrast, the synthetic DNA targets used in the previous sections were short, purified and directly available for hybridization.

The reproducibility of the assay was evaluated through the coefficient of variation, which was approximately 12%. This value indicates good repeatability considering the complexity of lysed bacterial samples, the presence of matrix components and the absence of signal amplification. Nevertheless, sample preparation remains a critical limitation. DNA fragmentation, denaturation, prevention of strand re-annealing and target accessibility should be further refined to improve the sensitivity of direct bacterial DNA detection.

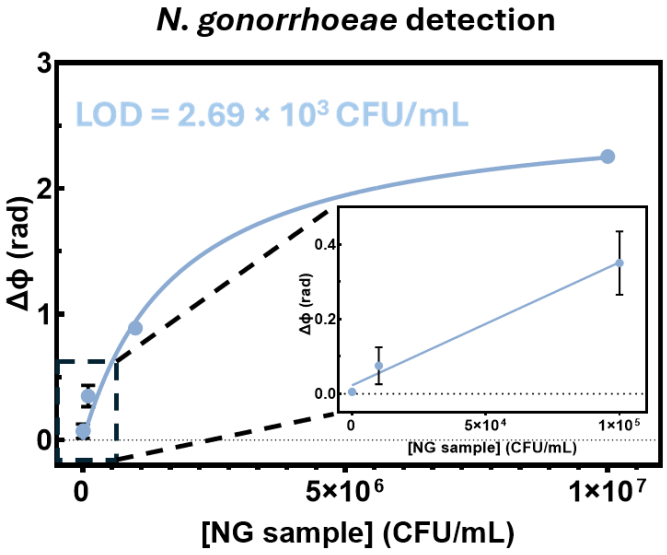


Figure 6.13 Calibration curve for *N. gonorrhoeae* real samples.

The obtained LOD is higher than that typically achieved by NAATs, which can reach detection limits in the range of 10–100 CFU/mL equivalent or a few genome copies per reaction.[194] However, the performance of the BiMW biosensor is comparable to culture-based methods, which typically exhibit detection limits in the range of 10^2–10^3 CFU/mL.[187] Unlike amplification-based techniques, the proposed approach enables direct, label-free detection without enzymatic amplification during the biosensor assay.

These results demonstrate that successful detection in bacterial samples depends strongly on sample preparation. The combined optimization of lysis, DNA fragmentation, denaturation and hybridization buffer composition was essential to achieve reliable detection. Although the sensitivity remains lower than amplification-based methods, the BiMW biosensor provides a direct and label-free approach with potential for further development in STI diagnostics.

6.4. Conclusions

This chapter demonstrated the application of the BiMW interferometric biosensor to the detection of STI-related bacterial DNA and antimicrobial resistance-associated mutations. The work focused on three clinically relevant targets: *N. gonorrhoeae*, *C. trachomatis* and a ciprofloxacin resistance-associated mutation in the *N. gonorrhoeae* gyrA gene.

Using short synthetic DNA targets, the BiMW biosensor enabled specific detection of *N. gonorrhoeae* and *C. trachomatis*, with LODs of 290 pM and 171 pM, respectively. These results confirmed that the selected probes, surface chemistry and hybridization conditions were suitable for direct detection of STI-related DNA targets without amplification or labelling. Although these sensitivities are lower than those typically achieved by NAATs, they are consistent with the expected performance of an amplification-free biosensor based on surface hybridization.

A key result of this chapter was the detection of ciprofloxacin resistance-associated *gyrA* mutations. Under standard hybridization conditions, the resistant target was detected with

an LOD of 87 pM, but the wild-type sequence also produced a significant response. By increasing hybridization stringency using TMAC, selective discrimination of the resistant sequence was achieved, with an LOD of 189 pM. This result highlights the trade-off between sensitivity and specificity in single-base mutation detection: conditions that maximize signal intensity are not necessarily suitable for selective AMR profiling. Compared with previous BiMW assays targeting complete AMR genes such as blaCTX-M-15 and blaNDM-5, where attomolar LODs were achieved, the sensitivity obtained here is lower, but detecting a full resistance gene is not equivalent to discriminating a single-base mutation within *gyrA*; the contribution of this work lies in demonstrating direct, label-free discrimination of a clinically meaningful resistance-associated point mutation.

Placing these results in the broader context of photonic bacterial diagnostics highlights the specificity of the strategy followed in this thesis. Previous interferometric photonic biosensors have addressed bacterial pathogens such as *Staphylococcus aureus*, *Pseudomonas aeruginosa* and *Helicobacter pylori,* reaching limits of detection below 100 CFU/mL with assay times shorter than 15 min and diagnostic performance above 90 % in clinical samples;[195] however, those works rely on antibody-based recognition of surface antigens or intact cells. Antibody-based bacterial assays are inherently constrained by the phase and antigenic variation of bacterial surface structures across strains and by the technical difficulty of producing reproducible, high-affinity antibodies against intact cells or surface epitopes. Genomic DNA detection, in contrast, can be directed at conserved or species-specific chromosomal regions, providing a sequence-defined recognition element that is uniform across strains and naturally compatible with simultaneous interrogation of resistance-associated markers, as demonstrated here for the *gyrA* mutation. Fewer studies have addressed this combination of direct DNA detection and label-free discrimination of single-nucleotide resistance markers in STI pathogens, which is the niche this work contributes to.

The transition from synthetic targets to bacterial samples required additional optimization. A workflow based on SDS-assisted thermal lysis, DNA fragmentation, thermal denaturation and buffer optimization enabled detection of N. gonorrhoeae from lysed bacterial samples with an LOD of 2.29×10^3 CFU/mL and a coefficient of variation of approximately 12 %. This sensitivity is lower than that of NAATs, which benefit from target amplification, but it is within the range expected for a direct, label-free approach and comparable to non-amplified optical bacterial detection strategies. The real-sample experiments also showed that sample preparation remains one of the main practical limitations of the current assay: the lysis and fragmentation protocol is compatible with laboratory implementation but is not yet integrated or automated for decentralized testing, and incomplete fragmentation, inefficient denaturation, re-hybridization of the genomic duplex and nonspecific adsorption from lysate components can all reduce sensitivity and reproducibility. Future optimization should therefore focus on improving DNA accessibility and minimizing matrix effects, particularly if the assay is transferred to clinical samples such as urine or swabs.

In summary, this chapter demonstrates that the BiMW biosensor can be adapted for direct detection of STI-related bacterial DNA and for discrimination of a ciprofloxacin resistance-associated *gyrA* mutation. The platform should not be viewed as a replacement for NAATs

in terms of sensitivity, but as a complementary approach offering label-free detection, real-time monitoring and compatibility with integrated pathogen and resistance-marker analysis.

Future work will focus on implementing these assays in a multiplexed BiMW format, enabling simultaneous detection of *N. gonorrhoeae*, *C. trachomatis* and *gyrA*-associated resistance markers within a single measurement. Further development should also address the integration of sample preparation steps, lysis, fragmentation and denaturation, into a simplified workflow suitable for decentralized testing. Since the BiMW platform is compatible with multi-channel detection, this approach could be extended to larger STI panels and additional antimicrobial resistance markers, supporting faster and more informative diagnostics for sexually transmitted infections.

7. General conclusions and future perspectives

This PhD Thesis demonstrates the potential of photonic biosensors for the rapid and precise molecular diagnosis of emerging health threats. The work has focused on the development of label-free optical biosensing strategies for the detection of infectious disease biomarkers, with particular emphasis on two urgent biomedical challenges: the surveillance of zoonotic coronaviruses and the diagnosis of bacterial sexually transmitted infections, including antimicrobial resistance-associated mutations. The combination of nanophotonic transduction, molecular biology, surface chemistry and analytical validation has allowed the development of biosensor methodologies capable of detecting specific DNA and RNA sequences with short assay times and without the need for enzymatic amplification during the biosensing step.

The work in this PhD Thesis involved the design, optimization and evaluation of two complementary photonic biosensing platforms: an SPR biosensor and a BiMW interferometric biosensor. The SPR platform was employed as a robust and versatile tool for the development of nucleic acid hybridization assays and for the evaluation of signal enhancement strategies. The BiMW platform, due to its higher sensitivity, was applied for direct DNA and RNA detection with improved analytical performance. Both platforms enabled real-time monitoring of biomolecular recognition events and demonstrated the value of evanescent-wave photonic biosensors for the development of rapid diagnostic methodologies. In particular, the BiMW biosensor showed strong potential for future integration in compact, multiplexed and automated platforms.

The main general conclusions that can be drawn from this work are the following:

Several biofunctionalization strategies have been developed for the construction of nucleic acid-based photonic biosensors on both gold and silicon nitride surfaces. For the SPR platform, thiolated DNA probes were immobilized onto gold sensor chips through Au–S chemistry, using PEG spacers to improve probe accessibility and reduce steric hindrance at the sensing surface. For the BiMW platform, a silanization strategy based on vapor-phase APTES followed by PDITC activation was implemented for the covalent immobilization of DNA probes on Si_3N_4 chips. The optimization of these surface chemistries was essential to obtain reproducible probe attachment, efficient hybridization and specific biosensor responses. These results confirm that the analytical performance of nucleic acid biosensors depends not only on the optical transducer, but also on the quality, organization and stability of the biorecognition layer.

The SPR biosensor enabled the development of direct RNA hybridization assays for coronavirus-related targets. Specific detection of SARS-CoV-2-related sequences, alpha/beta-coronavirus sequences and gamma-coronavirus sequences was achieved, demonstrating the suitability of the platform for the study and optimization of viral RNA biosensing strategies. Although direct SPR detection was limited at low target concentrations, the incorporation of an anti-DNA/RNA antibody amplification step significantly improved the analytical response, reducing the limits of detection to the picomolar range. These results show that SPR is a useful platform for the development of

nucleic acid-based assays and for the evaluation of amplification strategies when higher sensitivity is required.

The transfer of the coronavirus assays to the BiMW interferometric platform improved the direct detection of viral RNA targets while maintaining a label-free format. The BiMW biosensor achieved limits of detection of 38 pM for alpha/beta-coronavirus synthetic targets and 91 pM for gamma-coronavirus synthetic targets, without requiring antibody amplification or enzymatic target amplification during detection. More importantly, when the gamma-coronavirus assay was evaluated using in vitro transcribed RNA, the platform reached a limit of detection of 1.52 copies/µL and a limit of quantification of 9.4 copies/µL. These results demonstrate the high sensitivity of BiMW interferometry for the detection of low-abundance nucleic acid targets and support its application in rapid molecular screening.

The coronavirus biosensors were successfully evaluated using animal-derived samples relevant to One Health surveillance. In bat faecal samples, the alpha/beta-coronavirus BiMW assay differentiated positive and negative samples with 72% sensitivity, 83% specificity and an AUC of 0.76. In chicken swab samples from controlled infection studies, the gamma-coronavirus assay showed stronger diagnostic performance, reaching 88% sensitivity, 89% specificity and an AUC of 0.92. These results demonstrate that photonic biosensors can be applied beyond synthetic targets and controlled buffer conditions, although sample matrix, viral load and target accessibility remain important factors influencing diagnostic performance.

This work also contributes to an important gap in the current field of diagnostic biosensors. Although the One Health framework recognizes the close relationship between human, animal and environmental health, most biosensor developments remain mainly focused on human clinical applications. However, animal reservoirs play a central role in the emergence, maintenance and transmission of zoonotic pathogens. The validation of the coronavirus biosensors using bat and chicken samples therefore represents an important step toward the use of photonic biosensing technologies in veterinary and wildlife surveillance. In this context, the developed biosensors may provide complementary tools for the rapid screening and prioritization of samples at the animal–human interface.

The BiMW platform was also adapted to the detection of bacterial sexually transmitted infections. Specific detection of *Neisseria gonorrhoeae* and *Chlamydia trachomatis* synthetic DNA targets was achieved with limits of detection of 290 pM and 171 pM, respectively. These results demonstrate that the optimized BiMW biofunctionalization and hybridization conditions can be applied not only to viral RNA detection, but also to bacterial DNA targets. The ability to detect these pathogens without labels or enzymatic amplification highlights the versatility of the platform and its potential relevance for faster STI screening strategies.

A novel BiMW biosensing strategy was developed for the detection of a ciprofloxacin resistance-associated mutation in the *N. gonorrhoeae* gyrA gene. This assay represented a particularly demanding analytical challenge, since the resistant and wild-type sequences differed by only one nucleotide. By increasing the stringency of hybridization using TMAC,

the response of the wild-type sequence was strongly reduced while maintaining the detection of the resistant target. The optimized assay achieved a limit of detection of 189 pM. These results show that the BiMW biosensor can provide not only pathogen identification, but also genetic information related to antimicrobial resistance, which is highly relevant for future diagnostic approaches aimed at guiding treatment and supporting antimicrobial stewardship.

The analysis of lysed *N. gonorrhoeae* samples demonstrated the feasibility of applying the BiMW biosensor to more complex bacterial material, while also identifying the main limitations that must be addressed in future work. The platform detected lysed bacterial samples with a limit of detection of 2.29×10^3 CFU/mL and a coefficient of variation of approximately 12%. This performance was achieved without enzymatic amplification and is comparable to some culture-based approaches. However, the results also showed that direct bacterial DNA detection is strongly dependent on sample preparation, particularly cell lysis, genomic DNA fragmentation, strand denaturation and target accessibility. These steps will be critical for the future analysis of clinical samples.

In the context of bacterial STIs, the relevance of these results extends beyond the analytical demonstration. The global burden of *N. gonorrhoeae* and *C. trachomatis* infections remains very high, and *N. gonorrhoeae* has been classified among the high-priority bacterial pathogens for which new diagnostic and therapeutic strategies are urgently needed, due to the progressive loss of treatment options driven by AMR. Treatment decisions are currently empirical and rarely informed by resistance information, accelerating the spread of resistance and the consumption of last-line antibiotics. The BiMW biosensors developed here address this gap by enabling rapid, label-free identification of the pathogen and a clinically actionable resistance marker within the same platform. Conceptually extensible to other STIs and resistance markers, this approach positions photonic biosensing as a relevant tool for antimicrobial stewardship and for slowing AMR progression in the bacterial STI field.

Overall, the results obtained in this Thesis indicate that photonic biosensors should be considered as complementary diagnostic tools for RT-qPCR, conventional NAATs or culture-based methods. Their main value lies in the possibility of reducing the complexity of the detection step, providing real-time and label-free readout, and enabling rapid sample screening. In viral surveillance, this could be useful for identifying samples that require confirmatory molecular analysis. In STI and AMR diagnostics, it could support faster detection of pathogens and resistance-associated genetic markers, helping to reduce the delay between testing and appropriate therapy administration.

At present, the biosensors developed in this Thesis still require operation within a laboratory environment, since sample preparation, fluidic handling and optical instrumentation need controlled experimental conditions. Nevertheless, their fast readout and label-free operation already provide important advantages at the analytical detection stage. By decoupling the biosensor response from enzymatic amplification, the BiMW platform reduces assay complexity and processing time during detection, positioning it as a

promising complementary technology for time-sensitive surveillance and diagnostic applications.

Future work should focus on the integration of these biosensing strategies into more complete and user-friendly diagnostic workflows. In the particular case of bacterial targets, further optimization of sample preparation will be required, especially for cell lysis, genomic DNA fragmentation, strand denaturation and prevention of re-hybridization.

Further studies should also evaluate the performance of the developed assays in larger and more diverse sample collections. For coronavirus surveillance, this should include additional wildlife, livestock and companion animal samples, covering different matrices, viral loads and geographical origins. For STI and AMR diagnostics, validation should progress toward clinically relevant samples such as urine and genital, rectal or pharyngeal swabs, as well as broader panels of *N. gonorrhoeae* strains carrying different resistance-associated markers. These studies will be necessary to establish robust diagnostic thresholds and to define the most appropriate use of the biosensor within real diagnostic workflows.

The development of multiplexed biosensor formats represents another important future direction. The BiMW platform is especially suitable for this purpose because several sensing channels can be integrated on the same chip. For zoonotic surveillance, multiplexing could allow the simultaneous detection of different coronavirus groups or other viral families with spillover potential. For STI diagnostics, the same platform could combine the detection of *N. gonorrhoeae*, *C. trachomatis* and multiple antimicrobial resistance markers in a single assay. This would increase the diagnostic value of the platform and provide more complete information for clinical or epidemiological decision-making.

Ongoing developments within the research group toward the integration and automation of multiplexed photonic biosensor chips, together with compact optical and fluidic components, represent an important step toward the future translation of this technology. The consolidation of sample handling, target recognition and optical detection into a compact system could bring these biosensors closer to the point of need while preserving the analytical performance demonstrated in the current laboratory-based configuration.

In conclusion, this PhD Thesis has demonstrated the potential of photonic biosensors for the rapid molecular detection of emerging health threats. By addressing both zoonotic coronavirus surveillance and bacterial STI/AMR diagnostics, this work shows that label-free optical biosensing can be adapted to different infectious disease targets and can provide relevant analytical information in short timeframes. The methodologies developed here establish a solid basis for future integrated, multiplexed and portable biosensor platforms with potential application in One Health surveillance, outbreak preparedness and antimicrobial resistance monitoring.

Annex

OPTIMIZATION STUDY FOR SENSOR SURFACE SILANIZATION USING THE SPR BIOSENSOR

This Annex complements the silicon-surface biofunctionalization study of Chapter 4 (Development of Nucleic Acid-Based Photonic Biosensors). It compiles the preliminary screening of silanization and crosslinking conditions carried out on the SPR platform, which is referred to in that chapter and which guided the selection of the protocol later implemented on the BiMW interferometer.

A. Annex

A.1. Introduction

Establishing a robust biofunctionalization chemistry on silicon-compatible surfaces requires the optimization of two coupled steps: the silanization that anchors a reactive organic layer to the silanol-rich surface, and the crosslinking that couples the DNA probe to it. Identifying suitable conditions involves testing a large number of variables—silanization solvent and concentration, deposition method, and crosslinking chemistry. For this kind of extensive screening, the SPR biosensor is the more convenient platform: surface plasmon resonance sensor is a well-established, more user-friendly and robust to operate than the more specialized BiMW interferometer. The silanization and crosslinking conditions were therefore screened on SPR, and only the best-performing combination was carried forward to the BiMW platform (Chapter 4).

For the results to be transferable, the SPR sensor must present the same surface chemistry as the BiMW waveguides. This was achieved using custom SPR chips coated with a thin SiO_2 overlayer (10 nm) on the gold film:[196] the SiO_2 surface is silanol-rich and chemically equivalent to the native oxide that forms on the Si_3N_4 BiMW surface after cleaning, so that APTES silanization and probe coupling proceed through the same reactions on both platforms. The SPR set-up and the general biofunctionalization and hybridization protocols are described in Chapter 3 (Materials and Methods); only the conditions specific to this screening are given below. The same 25-nt thiolated DNA probe and 50-nt complementary RNA model target used in Chapter 4 were employed, and the resonance-wavelength shift (Δλ) recorded on probe immobilization was used as the readout to compare conditions.

A.2. Optimization of the APTES silanization route

The deposition of the APTES layer governs the density and homogeneity of the amine groups available for the subsequent probe-coupling step, and therefore conditions the reproducibility of the whole interface. Three silanization approaches were compared on SPR platform, using the immobilization signal of the thiolated probe (after PDITC coupling) as the readout (**Figure A.1**).

Liquid-phase silanization in anhydrous toluene was tested first, since water-poor, non-polar media are expected to suppress premature silane hydrolysis and bulk polymerization. SiO_2 surfaces were exposed to 1 % and 2 % (v/v) APTES in anhydrous toluene, with 0.3 % (v/v) *N,N*-diisopropylethylamine (DIPEA) as catalyst, under nitrogen for 1 h. Both concentrations yielded comparable immobilization signals ($\Delta\lambda \approx 2.5$ nm), confirming the formation of a functional amine layer, but with substantial batch-to-batch variability (CV ≈ 30.8 %). This variability is consistent with the well-known sensitivity of trialkoxysilane chemistry to trace water, which triggers localized hydrolysis and siloxane clustering, yielding a chemically functional but structurally non-uniform interface—a limitation for biosensors, where reproducibility depends on nanometric control of the interfacial layer.

Ethanol was evaluated next as a more accessible and environmentally benign solvent. A concentration study (1–5 % APTES) showed improved immobilization, with 2 % APTES giving

the highest and most reproducible signals across independent chips (Δλ ≈ 5.10 nm, CV ≈ 20.0 %). The stronger signal is consistent with greater surface coverage, although the faster hydrolysis of the ethoxysilane groups in ethanol favours thicker, less ordered multilayers that can compromise long-term stability and probe accessibility through steric crowding.

Finally, vapor-phase silanization under reduced pressure was tested to decouple silane deposition from solution-phase hydrolysis equilibria. Exposure of activated chips to APTES vapor yielded an immobilization signal comparable in magnitude to the optimal ethanol condition (Δλ ≈ 5.50 nm) but with markedly improved reproducibility (CV ≈ 11.9 %). Because the ethanol and vapor routes gave similar signal magnitudes, total amine density alone does not determine coupling efficiency; the improved reproducibility of the vapor route most likely reflects greater lateral uniformity and reduced nanoscale roughness, parameters not captured by mass-sensitive measurements but known to influence interfacial assays. Vapor-phase APTES was therefore identified as the most reproducible silanization route, in agreement with the trend subsequently confirmed on the BiMW platform (Chapter 4).[197–199]

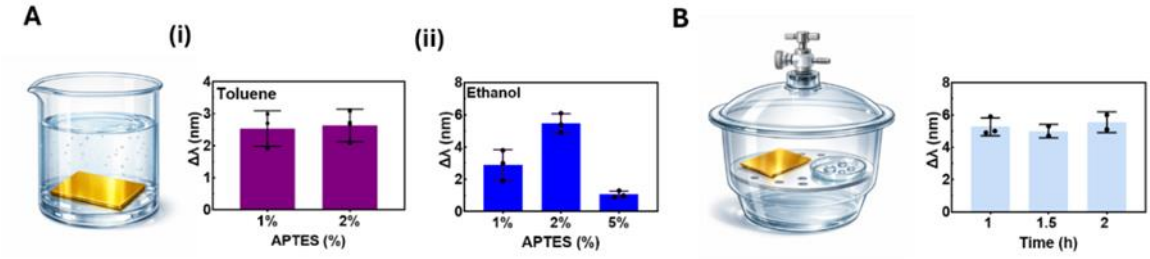


Figure A.1 (DNA probe immobilization signals (Δλ) measured on SiO_2-coated SPR chips for the optimization of the APTES silanization route. **(A)** APTES deposited in liquid phase: (i) in anhydrous toluene (1 % and 2 % v/v) and (ii) in ethanol (1, 2 and 5 % v/v). **(B)** APTES deposited in vapoor phase.

A.3. Optimization of the crosslinking chemistry

Once a reproducible amine-terminated interface was available, two amine-to-thiol crosslinking chemistries were compared on SPR (**Figure A.2**): the aromatic homobifunctional crosslinker PDITC, and the heterobifunctional spacer NHS-PEG-MAL.

PDITC forms stable thiourea linkages between the surface amines and the thiolated probe. Because its isothiocyanate groups require organic media to preserve their reactivity, activation was performed *ex situ* in DMF (20 mM). Extending the activation time from 1 h to 2 h, with mixing, increased the immobilization signal from Δλ ≈ 4 nm to ≈ 6 nm, consistent with a higher density of surface-bound crosslinker available for thiol coupling. Its short, rigid structure is not a limitation for oligonucleotide probes, which provide their own vertical spacing, and *ex situ* activation is compatible with batch processing and storage of pre-functionalized chips.

NHS-PEG-MAL combines an NHS ester for amine coupling with a terminal maleimide for thiol-selective probe attachment, and operates under aqueous conditions, which is attractive for in-flow workflows. *In situ* and *ex situ* activation were compared at 20 and 50

mM in sodium bicarbonate buffer ($NaHCO_3$, pH 9); both routes yielded strong, fully acceptable signals, with the best performance at 20 mM. Increasing the concentration to 50 mM reduced immobilization, likely due to excessive PEG-layer formation and decreased accessibility of the maleimide groups.[200–202]

Both chemistries therefore provide viable routes to the silicon-compatible interface: PDITC offers robust, scalable *ex situ* activation with high immobilization efficiency, whereas NHS-PEG-MAL provides an aqueous-compatible alternative based on widely established NHS/maleimide chemistry. The 2 h PDITC condition was selected for transfer to the BiMW platform in Chapter 4, with the 20 mM NHS-PEG-MAL condition retained as an alternative route.

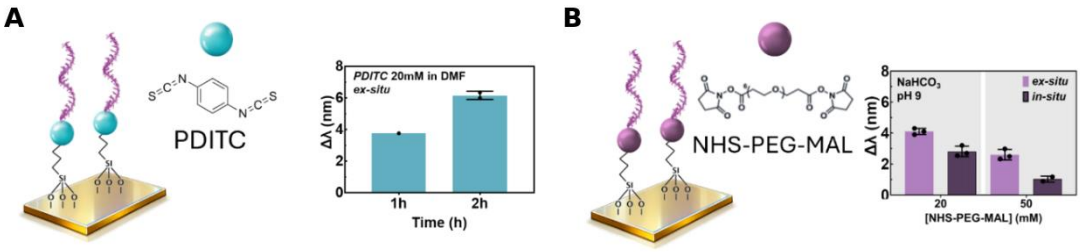


Figure A.2 DNA probe immobilization signals (Δλ) measured on SiO_2-coated SPR chips for the optimization of the crosslinking chemistry. **(A)** PDITC crosslinking performed *ex situ* (20 mM in DMF) for 1 and 2 h. **(B)** NHS-PEG-MAL crosslinking under *in situ* and *ex situ* conditions (20 and 50 mM in $NaHCO_3$, pH 9).

A.4. Analytical comparison of the optimized configurations

Combining the two optimization steps, the analytical performance of the four most promising biofunctionalization configurations was compared by recording calibration curves for the model RNA target: 2 % APTES in ethanol or vapor-phase APTES, each coupled through PDITC or NHS-PEG-MAL (**Figure A.3**). The hybridization conditions were those established for the model probe–target pair in Chapter 4. All four surfaces detected the target in the picomolar range, but their sensitivities differed markedly. Vapor-phase APTES combined with PDITC gave the lowest limit of detection (117 pM), consistent with the structural uniformity of the vapor-phase silane layer and the efficient covalent coupling provided by PDITC. The remaining configurations gave higher LODs (between ≈ 400 and ≈ 650 pM), reflecting the less ordered ethanol-deposited silane layer or the less efficient surface coupling under the conditions tested. This comparison identified vapor-phase APTES with PDITC as the best-performing combination, which was the configuration carried forward to the BiMW platform.

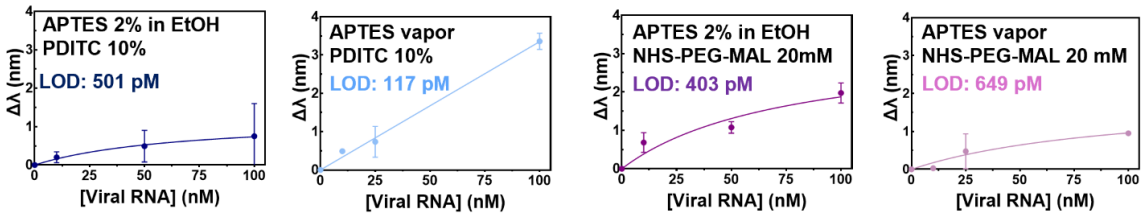


Figure A.3 Standard calibration curves for the model RNA target measured on the four biofunctionalized SPR surfaces, with the limit of detection (LOD) indicated for each. From left to right: 2 % APTES in ethanol with PDITC (501 pM), vapor-phase APTES with PDITC (117 pM), 2 % APTES in ethanol with NHS-PEG-MAL (403 pM), and vapor-phase APTES with NHS-PEG-MAL (649 pM).

A.5. Conclusions

This Annex extended the silicon-surface biofunctionalization work of Chapter 4 by screening, on the SPR biosensor, the APTES silanization and probe-crosslinking conditions used to build the silicon-compatible interface. Among the silanization routes, vapor-phase APTES deposition gave the most reproducible amine layer (CV ≈ 11.9 %, compared with ≈ 30.8 % for toluene and ≈ 20.0 % for ethanol). For the probe-coupling step, 2 h *ex situ* PDITC activation produced the highest immobilization signal, with 20 mM NHS-PEG-MAL as a viable aqueous-compatible alternative. When the resulting surfaces were compared by calibration of the model RNA target, vapor-phase APTES with PDITC gave the lowest limit of detection (117 pM); this combination was therefore selected and transferred to the BiMW platform, where it was applied to nucleic acid detection.

Part of this study, together with the biofunctionalization study and the coronavirus (chapter 5) and sexually transmitted bacteria (chapter 6) applications presented in this Thesis, is currently under peer review for publication.

Publications

Journal Articles

Rapid screening of animal coronaviruses in livestock and wildlife using a silicon photonics biosensor

Serrano, B., Soler, M., Courtillon, C. *et al.* Rapid screening of animal coronaviruses in livestock and wildlife using a silicon photonics biosensor. *npj Biosensing* **3**, 26 (2026). https://doi.org/10.1038/s44328-026-00091-0

Coronaviruses (CoVs) pose a persistent global health threat, with animal reservoirs such as bats, rodents, and poultry driving their emergence. Rapid, field-deployable detection tools are urgently needed to monitor these viruses at the animal-human interface, where spillover events are most likely. We present a nanophotonic interferometric biosensor for label-free, amplification-free detection of alpha/beta- and gamma-CoVs in animal reservoirs. The biosensor achieves limits of detection below 10 copies/µL for in vitro transcribed (IVT) RNA samples, strongly correlating with PCR assays. Field validation using RNA extracts from bats and chickens yielded sensitivities of 72–90% and specificities of 83–90%, confirming robust performance across diagnostic relevant ranges. Fabricated on silicon microchips via standard techniques, the biosensor platform is scalable, cost-effective, and compatible with miniaturized components suitable for point-of-care and decentralized use. Our biosensor device addresses a critical gap in veterinary diagnostics, supporting early surveillance and pandemic preparedness under a One Health framework.

Engineering the Biochemical Interface of Silicon Photonic Biosensors for Robust Nucleic Acid Detection

Serrano, B.; Ramírez-Priego, P.; Lechuga, L. M.; Soler, M.

Manuscript submitted for publication, 2026.

Silicon photonic biosensors offer label-free, sensitive and real-time detection of all types of nucleic acids, but their analytical performance is often limited by the molecular architecture of the bio-interface rather than by the photonic architecture. We present a biochemical strategy to engineer efficient nucleic acid hybridization on silicon-compatible surfaces, linking interfacial chemistry and analytical methodology with integrated photonic sensors. Using SiO_2-coated surface plasmon resonance (SPR) sensor as a gold-standard optimization platform, we evaluated silanization methods, crosslinking chemistries, and hybridization conditions to maximize probe immobilization, accessibility, and reproducibility. Vapor-phase deposition of 3-aminopropyltriethoxysilane (APTES) combined with p-phenylene diisothiocyanate (PDITC)-mediated probe coupling yielded a uniform, robust bio-interface, while buffer composition, ionic strength, denaturing additives, and lateral probe spacing were optimized for efficient duplex formation. The engineered sensor surfaces supported selective, reversible, and reproducible hybridization, achieving picomolar sensitivity and stable performance across multiple regeneration cycles.

Transferring this interface directly to a silicon nanophotonic interferometer enabled detection of viral RNA and bacterial DNA with a threefold improvement in detection limits relative to standard SPR. This work demonstrates that careful bio-interface design can enhance the analytical performance of silicon photonic sensors, providing a scalable, transferable platform for next-generation diagnostics and advancing the integration of molecular recognition into semiconductor technologies.

Abbreviations and Acronyms

ACE2	Angiotensin-converting enzyme 2
ADE	Antibody-dependent enhancement
AMR	Antimicrobial resistance
APTES	(3-Aminopropyl)triethoxysilane
AST	Antimicrobial susceptibility testing
AUC	Area under the curve
BiMW	Bimodal waveguide (interferometer)
BPPL	Bacterial Priority Pathogens List
C6	Hexamethylene (six-carbon) spacer
CCD	Charge-coupled device
CDC	Centers for Disease Control and Prevention
CHIKV	Chikungunya virus
CoV	Coronavirus
COVID-19	Coronavirus disease 2019
Ct	Cycle threshold
CV	Coefficient of variation
DENV	Dengue virus
DEPC	Diethyl pyrocarbonate
DIPEA	N,N-Diisopropylethylamine
DMF	Dimethylformamide
DMSO	Dimethyl sulfoxide
DNA	Deoxyribonucleic acid
EDC	N-(3-Dimethylaminopropyl)-N'-ethylcarbodiimide hydrochloride
EDTA	Ethylenediaminetetraacetic acid
EOT	Extraordinary optical transmission

FA	Formamide
FN	False negatives
FP	False positives
GBD	Global Burden of Disease (study)
GDP	Gross domestic product
gyrA	DNA gyrase subunit A gene
HGT	Horizontal gene transfer
HIV	Human immunodeficiency virus
HO-PEG-SH	Hydroxyl-terminated thiolated polyethylene glycol (lateral spacer)
IBV	Infectious bronchitis virus
ICN2	Catalan Institute of Nanoscience and Nanotechnology
ICTS	Singular Scientific and Technical Infrastructures
IgA	Immunoglobulin A
IgG	Immunoglobulin G
IgM	Immunoglobulin M
IMB-CNM	Microelectronics Institute of Barcelona – National Microelectronics Centre
IVT	In vitro transcribed (RNA)
LFA	Lateral flow immunoassay
LMIC	Low- and middle-income country
LoC	Lab-on-a-chip
LOD	Limit of detection
LOQ	Limit of quantification
LSPR	Localized surface plasmon resonance
MALDI-TOF	Matrix-assisted laser desorption/ionisation time-of-flight (mass spectrometry)
MDR	Multidrug-resistant
MES	2-(N-Morpholino)ethanesulfonic acid (buffer)
miRR	Microring resonator

MOMP	Major outer membrane protein
MPXV	Mpox (monkeypox) virus
MRSA	Methicillin-resistant Staphylococcus aureus
MZI	Mach–Zehnder interferometer
NAAT	Nucleic acid amplification test
NanoB2A	Nanobiosensors and Bioanalytical Applications (group)
NGS	Next-generation sequencing
NHS	N-Hydroxysuccinimide
NHS-PEG-MAL	N-Hydroxysuccinimide–polyethylene glycol–maleimide
NPV	Negative predictive value
OHHLEP	One Health High-Level Expert Panel
ompA	Major outer membrane protein gene (*Chlamydia trachomatis*)
opa	Opacity-associated gene (*Neisseria gonorrhoeae*)
PBS	Phosphate-buffered saline
PCR	Polymerase chain reaction
PDITC	p-Phenylene diisothiocyanate
PDR	Pan-drug-resistant
PEG	Polyethylene glycol
PhC	Photonic crystal
PID	Pelvic inflammatory disease
PoC	Point-of-care
PolyT / polyT15	Poly-thymine (15-mer) vertical spacer
PPV	Positive predictive value
Q factor	Quality factor
qPCR	Quantitative (real-time) polymerase chain reaction
RdRp	RNA-dependent RNA polymerase
RDT	Rapid diagnostic test
RIU	Refractive index unit
RNA	Ribonucleic acid

ROC	Receiver operating characteristic
RT-PCR	Reverse transcription polymerase chain reaction
RT-qPCR	Reverse transcription quantitative polymerase chain reaction
SARS-CoV-2	Severe acute respiratory syndrome coronavirus 2
SD	Standard deviation
SDS	Sodium dodecyl sulfate
SE	Sensitivity
Si_3N_4	Silicon nitride
SiO_2	Silicon dioxide
SOI	Silicon-on-insulator
SP	Specificity
SPF	Specific pathogen-free
SPP	Surface plasmon polariton
SPR	Surface plasmon resonance
SSC	Saline-sodium citrate (buffer)
ssDNA	Single-stranded deoxyribonucleic acid
STI	Sexually transmitted infection
TB	Tuberculosis
TBE	Tris-borate-EDTA (buffer)
TE	Tris–EDTA (buffer)
TE (polarization)	Transverse electric
Tm	Melting temperature
TM (polarization)	Transverse magnetic
TMAC	Tetramethylammonium chloride
TP	True positives
WHO	World Health Organization
WOAH	World Organisation for Animal Health
XDR	Extensively drug-resistant
Xpert	Cepheid GeneXpert (assay)

ZIKV	Zika virus

List of figures

Figure 1.1 Worldwide leading causes of death. 9

Figure 1.2 Schematic representation of PCR, RT-PCR and qPCR. Adapted from Adams et al.[56] 15

Figure 1.3 Schematic representation of a lateral flow immunoassay (LFA). 16

Figure 1.4 Schematic representation of culture-based methods workflow for bacterial identification. 18

Figure 1.5 Schematic representation of a biosensor. 19

Figure 1.6 Schematic representation of an evanescent-wave biosensor. DNA probes (cyan) immobilized on the sensor surface hybridize with their complementary targets (yellow); the evanescent field (red) decays exponentially away from the interface. 20

Figure 1.7 Schematic representation of a surface plasmon polariton (SPP) propagating along a metal–dielectric interface, illustrating: (**a**) the surface confined collective oscillation of free charges and (**b**) the transverse evanescent electromagnetic field extending..... 23

Figure 1.8 SPR biosensor based on prism-coupling Kretschmann configuration. 23

Figure 1.9 Spectral reflectivity dip and sensogram from SPR measurement methodology by wavelength-based interrogation. 24

Figure 1.10 Schematic representation of SPR (**a**) grating coupling and (**b**) waveguide coupling. 25

Figure 1.11 Schematic comparison of (**a**) SPR , (**b**) LSPR , and (**c**) EOT-based sensing, illustrating propagating vs localized fields and nanostructured platforms. 26

Figure 1.12 Schematic figure of (**a**) microring resonators (miRRs) and (**b**) photonic crystals (PhCs). 29

Figure 1.13 Schematic figure of (**a**) Mach–Zehnder interferometers (MZI) and (**b**) Bimodal waveguide (BiMW) interferometers. 30

Figure 1.14 (**a**) Schematic illustration of the BiMW biosensor configuration. (**b**) Representative BiMW readout response: (**i**) raw Iup and Idown intensity signals; (**ii**) periodic interferometric signal associated with the sensor response during refractive index variation; and (**iii**) linearized sensor response obtained after all-optical modulation.[100]..... 32

Figure 3.1 Photograph and schematic representation of the experimental SPR platform, showing the halogen light source, collimator, injection valve, syringe pump, prism coupling system, flow cell, plasmonic chip, and CCD spectrometer. 39

Figure 3.2 Screenshots of the homemade SPR readout software showing: (a) the wavelength reflectivity spectrum and (b) the sensogram tracking the SPR response in real time as wavelength shift, Δλ. 39

Figure 3.3 Photograph of the experimental BiMW platform and light-coupled BiMW waveguide, showing the diode laser, syringe pump, injection valve, flow cell, temperature controller, photodetector, and chip holder. 41

Figure 3.4 Screenshots of the homemade BiMW readout software showing the interferometric signal, SR values, and the real-time sensogram tracking the BiMW response as phase shift, Δϕ. 41

Figure 3.5 (**a**) Photography and (**b**) schematic overview of the BiMW interferometric sensor chip, showing the longitudinal layout of the single-mode and bimodal sensing regions. .. 42

Figure 4.1 Schematic representation of DNA probe immobilization and hybridization process. 47

Figure 4.2 Schematic overview of DNA probe design parameters evaluated. (**a**) Influence of vertical spacers on probe orientation and target accessibility. (**b**) Influence of GC content on duplex stability, hybridization efficiency, and risk of secondary structures or 50

Figure 4.3 Surface coverage scheme: high, low, and optimum probe density 51

Figure 4.4 Schematic figure of thiolated single-stranded DNA probe with a vertical spacer (PolyT) and thiolated lateral spacer (HO-PEG-SH) immobilized on the gold surface. 51

Figure 4.5 (**a**) Immobilization of DNA probe with different concentrations (1, 2 and 5 μM) and (**b**) lateral spacer ratios (1:1, 1:2, 1:5, 1:7, 1:10, 1:15). 53

Figure 4.6 100 nM RNA sample hybridization signal with different (**a**) lateral spacer ratios (1:1, 1:2, 1:5, 1:7, 1:10) and (**b**) DNA probe concentrations (1, 2 and 5 μM). 53

Figure 4.7 SPR hybridization response after injection of a 100 nM 50-nt complementary RNA model target and a 100 nM non-complementary RNA control on functionalized sensor surfaces. 54

Figure 4.8 (**a**) Schematic representation and (**b**) SPR biosensor sensogram of regeneration of the DNA probe layer on gold surfaces using 35% formamide. (**c**) Repeated hybridization–

regeneration cycles were performed to evaluate the stability and reusability of the sensing surface. 55

Figure 4.9 General scheme of the silanization reaction on Si_3N_4 surfaces: hydrolysis of the silane hydrolysable groups to silanols and subsequent condensation with surface hydroxyls to yield siloxane (Si–O–Si) bonds. 56

Figure 4.10 Schematic representation of the three PEG-silanes evaluated and their corresponding immobilization chemistries: PEG–silane–COOH/EDC–NHS/NH_2-DNA, PEG–silane–biotin/neutravidin/biotin-DNA, and PEG–silane–NH_2/PDITC/modified DNA probe. 58

Figure 4.11 Schematic of PEG–silane–COOH functionalization, EDC/NHS activation, and NH_2-DNA probe immobilization. 58

Figure 4.12 (**a**) Immobilization signals with different probe concentration (2, 5, 10, 20 and 30 µM) and (**b**) hybridization signals obtained using PEG–silane–COOH. 59

Figure 4.13 Schematic of PEG–silane–NH_2 functionalization, PDITC activation, and DNA probe immobilization. 60

Figure 4.14 DNA probe immobilization on PEG–silane–NH_2 surfaces activated with PDITC. (bar plot of immobilization signal for the tested probe (-SH and -NH2)..... 60

Figure 4.15 Schematic of PEG–silane–biotin functionalization, neutravidin immobilization, and biotin-DNA probe attachment. 61

Figure 4.16 (**a**) Neutravidin immobilization saturation and (**b**) Biotin-DNA probe immobilization study. 62

Figure 4.17 Effect of buffer composition on biotin-DNA probe immobilization. 63

Figure 4.18 Sensogram showing DNA probe immobilization and subsequent hybridization with 100 nM RNA target on PEG–silane–biotin/neutravidin surfaces. 63

Figure 4.19 DNA probe immobilization sensor signals with different APTES silanizations: dilluted in toluene, ethanol, and vapor phase. 66

Figure 4.20 Hybridization response after injection of 100 nM RNA target on BiMW sensors functionalized with APTES/PDITC using toluene, ethanol, or vapor-phase silanization. ... 66

Figure 4.21 Regeneration with NaOH 5 mM using the BiMW sensor functionalized with vapor-phase APTES/PDITC. 67

Figure 4.22 Regeneration with FA 35% using the BiMW sensor functionalized with vapor-phase APTES/PDITC. 68

Figure 4.23 pH effect in target hybridization. 69

Figure 4.24 Salinity effect in target hybridization. 70

Figure 4.25 Formamide effect in target hybridization. 70

Figure 4.26 TMAC effect in target hybridization. 71

Figure 5.1 Schematic overview of coronavirus genera, main animal reservoirs, and surveillance targets addressed in this chapter. 74

Figure 5.2 Schematic representation of the SPR biosensor system for coronavirus RNA detection. 78

Figure 5.3 Sensograms of DNA probe immobilization. 79

Figure 5.4 Effect of Formamide in SSC 5 × hybridization buffer on sensor response for different CoV RNA targets. Hybridization signals obtained for 100 nM RNA targets corresponding to SARS-CoV-2 N gene, E gene, alpha/beta-coronavirus, and gamma-coronavirus assays 80

Figure 5.5 Effect of addtives in SSC 5 × hybridization buffer on sensor response for different CoV RNA targets. Hybridization signals obtained for 100 nM RNA targets corresponding to SARS-CoV-2 N gene, E gene, alpha/beta-coronavirus, and gamma-coronavirus assays. . 81

Figure 5.6 Sensograms of viral target detection SARS-CoV-2 (**a**) N and (**b**) E genes RNA. . 81

Figure 5.7 Calibration curves for (**a**) gene E and (**b**) N RNA detection. 82

Figure 5.8 Sensograms showing specificity for (**a**) E gene and (**b**) N gene RNA detection. 82

Figure 5.9 (**a**) Immobilization response and (**b**) calibration curve for gene E + N RNA detection. 83

Figure 5.10 Calibration curves for alpha/beta-RNA detection and specificity sensogram.84

Figure 5.11 Calibration curves for gamma-RNA detection and specificity sensogram. 84

Figure 5.12 Illustration of Anti-DNA-RNA amplification strategy. 86

Figure 5.13 DNA probe spacing optimization for amplification assay. 87

Figure 5.14 Evaluation of anti-DNA-RNA antibody concentrations for the optimization of the amplification assay, ... 88

Figure 5.15 Calibration curve alpha/beta-CoV amplification assay. 88

Figure 5.16 Calibration curve gamma-CoV amplification assay..... 89

Figure 5.17 Amplification signal obtained for negative-control RNA sequences. 89

Figure 5.18 Preliminary validation of the alpha/beta-CoV amplification assay RNA extracted from bat feces: (**a**) discrimination between positive and negative samples and (**b**) statistical analysis (Kruskal–Wallis test, $p < 0.0001$). 91

Figure 5.19 BiMW sensograms of DNA probe immobilization in different waveguides of the BiMW sensor chip over 2500 s. 92

Figure 5.20 . Synthetic RNA target for α/β-CoV assay (blue histograms) and negative control (grey histograms) signals obtained with different formamide percentage (FA at 1, 5, and 10%)..... 93

Figure 5.21 (**a**) Standard calibration curve using a synthetic RNA target at concentration range of 0.5-100 nM for the α/β-CoV biosensor assay; (**b**) Representative sensograms of the synthetic RNA targets for the α/β-CoV assay; (**c**) Standard calibration curve using a synthetic RNA target at concentration range of 0.5-100 nM for the γ-CoV biosensor assay; (**d**) Representative sensograms of the synthetic RNA targets for the γ-CoV assay. 94

Figure 5.22 BiMW biosensor responses (orange) to serial 10-fold dilutions of gamma-CoV IVT RNA (from 10-2 to 104 copies/µL) compared with RT-qPCR results (purple). 95

Figure 5.23 Calibration curve of biosensor signal versus RNA concentration fitted to a one-site specific binding model..... 96

Figure 5.24 Benchmarking of the biosensor against RT-qPCR. All sensor signals are measured in duplicate. 96

Figure 5.25 Validation of the BiMW biosensors: (**a**) Sensor signals for alpha/beta-CoV RNA extracted from bat feces samples (37 positive (blue) and 9 negative (grey), classified by the BiMW biosensor results). Negative samples according to RT-PCR are highlighted inside the grey box and (**b**) signal distribution and statistical analysis. 97

Figure 5.26 Statistical ROC analysis of alpha/beta-CoV BiMW assay..... 97

Figure 5.27 (**a**) Sensor signals for gamma-CoV RNA extracted from chicken swab samples (16 positive (orange) and 10 negative (grey), classified by the BiMW biosensor), negative samples according to RT-PCR are highlighted inside the grey box , and (**b**) signal distribution and statistical analysis..... 99

Figure 5.28 Statistical ROC analysis of gamma-CoV BiMW assay..... 99

Figure 6.1 Schematic representation of *Chlamydia trachomatis* and *N. gonorrhoeae* structure. 104

Figure 6.2 BiMW sensograms of the *N. gonorrhoeae* (NG) and *C. trachomatis* (CT) DNA probe immobilization. 108

Figure 6.3 Bars graph with SSC salinity with NG and CT. 109

Figure 6.4 Calibration curve for (**a**) *N. gonorrhoeae* and for (**b**) *C. trachomatis*. 110

Figure 6.5 Specificity assay for (**a**) *N. gonorrhoeae* and (**b**) *C. trachomatis* synthetic DNA detection using non-complementary DNA controls. 110

Figure 6.6 Calibration curve for detection of the ciprofloxacin resistance-associated *gyrA* sequence using 2× SSC + 1% FA. 112

Figure 6.7 Optimization of hybridization stringency for discrimination between resistant and wild-type gyrA sequences..... 113

Figure 6.8 Calibration curve of *N. gonorrhoeae* AMR with optimized buffer. 113

Figure 6.9 Evaluation of lysozyme-based lysis and lysis-buffer compatibility of 10^7 CFU/mL sample. 116

Figure 6.10 10^6 CFU/mL sample lysed with SDS 1% and 10min incubation at 95ºC..... 117

Figure 6.11 Antifouling additives effect in hybridization buffer for 10^6 CFU/*mL N. gonorrheae* samples. 118

Figure 6.12 Sensograms of *N. gonorrhoeae* and negative control (*P. aeruginosa*) detection. 119

Figure 6.13 Calibration curve for *N. gonorrhoeae* real samples. 120

Figure A.1 (DNA probe immobilization signals (Δλ) measured on SiO_2-coated SPR chips for the optimization of the APTES silanization route. **(A)** APTES deposited in liquid phase: (i) in anhydrous toluene (1 % and 2 % v/v) and (ii) in ethanol (1, 2 and 5 % v/v). **(B)** APTES deposited in vapoor phase. 129

Figure A.2 DNA probe immobilization signals (Δλ) measured on SiO_2-coated SPR chips for the optimization of the crosslinking chemistry. **(A)** PDITC crosslinking performed *ex situ* (20 mM in DMF) for 1 and 2 h. **(B)** NHS-PEG-MAL crosslinking under *in situ* and *ex situ* conditions (20 and 50 mM in $NaHCO_3$, pH 9). 130

Figure A.3 Standard calibration curves for the model RNA target measured on the four biofunctionalized SPR surfaces, with the limit of detection (LOD) indicated for each. From

left to right: 2 % APTES in ethanol with PDITC (501 pM), vapor-phase APTES with PDITC (117 pM), 2 % APTES in ethanol with NHS-PEG-MAL (403 pM), and vapor-phase APTES with NHS-PEG-MAL (649 pM). 131

List of tables

Table 4.1 Comparison of different silanization strategies for DNA probe immobilization and RNA target detection on BiMW sensors. 64

Table 5.1 Target RNA and DNA probe sequences for SPR biosensor. 77

Table 5.2 Target RNA and DNA probe sequences for BiMW biosensor. 78

Table 5.3 LODs obtained for the different coronavirus RNA assays. 85

Table 6.1 DNA probes and target DNA sequences. 107

Bibliography

1. Global Health Estimates 2021: Deaths by Cause, Age, Sex, by Country and by Region, 2000–2021. World Health Organization; 2024.

2. Naghavi M, Kyu HH, Bhoomadevi A, et al. Global burden of 292 causes of death in 204 countries and territories and 660 subnational locations, 1990–2023: a systematic analysis for the Global Burden of Disease Study 2023. Lancet. 2025;406(10513):1811-1872. doi:10.1016/S0140-6736(25)01917-8

3. Global Tuberculosis Report 2024. World Health Organization; 2024.

4. Lim YB, Parr L, Popescu S, Rezzonico A, Van Beck L, Zarfos MR. Addressing the Threat of Disease Spillover: U.S.-Based Best Practices at the Nexus of Ecological and Biological Security. Council on Strategic Risks; 2023.

5. Weekly Epidemiological Update on COVID-19 — 1 September 2023. World Health Organization; 2023. https://www.who.int/publications/m/item/weekly-epidemiological-update-on-covid-19---1-september-2023

6. Ten Threats to Global Health in 2019. World Health Organization; 2019.

7. Liu Q, Liu M, Liang W, et al. Global distribution and health impact of infectious disease outbreaks, 1996–2023: a worldwide retrospective analysis of World Health Organization emergency event reports. J Glob Health. 2025;15:04151. doi:10.7189/jogh.15.04151

8. Jones KE, Patel NG, Levy MA, et al. Global trends in emerging infectious diseases. Nature. 2008;451(7181):990-993. doi:10.1038/nature06536

9. Carroll D, Daszak P, Wolfe ND, et al. The Global Virome Project. Science. 2018;359(6378):872-874. doi:10.1126/science.aap7463

10. Sanjuán R, Nebot MR, Chirico N, Mansky LM, Belshaw R. Viral mutation rates. J Virol. 2010;84(19):9733-9748. doi:10.1128/JVI.00694-10

11. Li X, Giorgi EE, Marichannegowda MH, et al. Emergence of SARS-CoV-2 through recombination and strong purifying selection. Sci Adv. 2020;6(27):eabb9153. doi:10.1126/sciadv.abb9153

12. Andersen KG, Rambaut A, Lipkin WI, Holmes EC, Garry RF. The proximal origin of SARS-CoV-2. Nat Med. 2020;26(4):450-452. doi:10.1038/s41591-020-0820-9

13. Hoffmann M, Kleine-Weber H, Schroeder S, et al. SARS-CoV-2 cell entry depends on ACE2 and TMPRSS2 and is blocked by a clinically proven protease inhibitor. Cell. 2020;181(2):271-280.e8. doi:10.1016/j.cell.2020.02.052

14. Lan J, Ge J, Yu J, et al. Structure of the SARS-CoV-2 spike receptor-binding domain bound to the ACE2 receptor. Nature. 2020;581(7807):215-220. doi:10.1038/s41586-020-2180-5

15. Hoffmann M, Kleine-Weber H, Pöhlmann S. A multibasic cleavage site in the spike protein of SARS-CoV-2 is essential for infection of human lung cells. Mol Cell. 2020;78(4):779-784.e5. doi:10.1016/j.molcel.2020.04.022

16. Chinazzi M, Davis JT, Ajelli M, et al. The effect of travel restrictions on the spread of the 2019 novel coronavirus (COVID-19) outbreak. Science. 2020;368(6489):395-400. doi:10.1126/science.aba9757

17. Msemburi W, Karlinsky A, Knutson V, Aleshin-Guendel S, Chatterji S, Wakefield J. The WHO estimates of excess mortality associated with the COVID-19 pandemic. Nature. 2023;613(7942):130-137. doi:10.1038/s41586-022-05522-2

18. Levin AT, Owusu-Boaitey N, Pugh S, et al. Assessing the burden of COVID-19 in developing countries: systematic review, meta-analysis and public policy implications. BMJ Glob Health. 2022;7(5):e008477. doi:10.1136/bmjgh-2022-008477

19. Micah AE, Bhangdia K, Cogswell IE, et al. Global investments in pandemic preparedness and COVID-19: development assistance and domestic spending on health between 1990 and 2026. Lancet Glob Health. 2023;11(3):e385-e413. doi:10.1016/S2214-109X(23)00007-4

20. World Economic Outlook, April 2021: Managing Divergent Recoveries. International Monetary Fund; 2021.

21. Carabelli AM, Peacock TP, Thorne LG, et al. SARS-CoV-2 variant biology: immune escape, transmission and fitness. Nat Rev Microbiol. 2023;21(3):162-177. doi:10.1038/s41579-022-00841-7

22. Influenza (Seasonal). World Health Organization; 2025.

23. Garg S, Reinhart K, Couture A, et al. Highly pathogenic avian influenza A(H5N1) virus infections in humans. N Engl J Med. 2025;392(9):843-854. doi:10.1056/NEJMoa2414610

24. Cumulative Number of Confirmed Human Cases for Avian Influenza A(H5N1) Reported to WHO, 2003–2025, 20 January 2025. World Health Organization; 2025.

25. Ebola Disease. World Health Organization; 2025.

26. Ebola Outbreak 2014–2016 — West Africa. World Health Organization; 2016.

27. Nipah Virus Infection. World Health Organization; 2026.

28. Katzelnick LC, Gresh L, Halloran ME, et al. Antibody-dependent enhancement of severe dengue disease in humans. Science. 2017;358(6365):929-932. doi:10.1126/science.aan6836

29. Liu Q, Liu M, Liang W, et al. Global distribution and health impact of infectious disease outbreaks, 1996–2023: a worldwide retrospective analysis of World Health Organization emergency event reports. J Glob Health. 2025;15:04151. doi:10.7189/jogh.15.04151

30. Zika Virus Disease Outbreak 2015–2016. World Health Organization; 2016.

31. Ryan SJ, Carlson CJ, Mordecai EA, Johnson LR. Global expansion and redistribution of Aedes-borne virus transmission risk with climate change. PLoS Negl Trop Dis. 2019;13(3):e0007213. doi:10.1371/journal.pntd.0007213

32. Zumla A, Rosenthal PJ, Sam-Agudu NA, et al. The 2024 Public Health Emergency of International Concern: a global failure to control mpox. Am J Trop Med Hyg. 2025;112(1):17-20. doi:10.4269/ajtmh.24-0606

33. Hantavirus Cluster Linked to Cruise Ship Travel, Multi-Country. World Health Organization; 2026.

34. Baker RE, Mahmud AS, Miller IF, et al. Infectious disease in an era of global change. Nat Rev Microbiol. 2022;20(4):193-205. doi:10.1038/s41579-021-00639-z

35. Marani M, Katul GG, Pan WK, Parolari AJ. Intensity and frequency of extreme novel epidemics. Proc Natl Acad Sci U S A. 2021;118(35):e2105482118. doi:10.1073/pnas.2105482118

36. One Health Joint Plan of Action, 2022–2026: Working Together for the Health of Humans, Animals, Plants and the Environment. FAO, UNEP, WHO, WOAH; 2022.

37. Adisasmito WB, Almuhairi S, Behravesh CB, et al; One Health High-Level Expert Panel (OHHLEP). One Health: a new definition for a sustainable and healthy future. PLoS Pathog. 2022;18(6):e1010537. doi:10.1371/journal.ppat.1010537

38. Ikuta KS, Swetschinski LR, Robles Aguilar G, et al. Global mortality associated with 33 bacterial pathogens in 2019: a systematic analysis for the Global Burden of Disease Study 2019. Lancet. 2022;400(10369):2221-2248. doi:10.1016/S0140-6736(22)02185-7

39. Murray CJL, Ikuta KS, Sharara F, et al. Global burden of bacterial antimicrobial resistance in 2019: a systematic analysis. Lancet. 2022;399(10325):629-655. doi:10.1016/S0140-6736(21)02724-0

40. Naghavi M, Vollset SE, Ikuta KS, et al. Global burden of bacterial antimicrobial resistance 1990–2021: a systematic analysis with forecasts to 2050. Lancet. 2024;404(10459):1199-1226. doi:10.1016/S0140-6736(24)01867-1

41. Poudel AN, Zhu S, Cooper N, et al. The economic burden of antibiotic resistance: a systematic review and meta-analysis. PLoS One. 2023;18(5):e0285170. doi:10.1371/journal.pone.0285170

42. Annex to the GLG Report: Estimating the Return on Investment from Tackling Antimicrobial Resistance Using a Package of One Health Interventions. Global Leaders Group on Antimicrobial Resistance; 2024.

43. Drug-Resistant Infections: A Threat to Our Economic Future. World Bank; 2017.

44. Partridge SR, Kwong SM, Firth N, Jensen SO. Mobile genetic elements associated with antimicrobial resistance. Clin Microbiol Rev. 2018;31(4):e00088-17. doi:10.1128/CMR.00088-17

45. Munita JM, Arias CA. Mechanisms of antibiotic resistance. Microbiol Spectr. 2016;4(2):VMBF-0016-2015. doi:10.1128/microbiolspec.VMBF-0016-2015

46. Queenan AM, Bush K. Carbapenemases: the versatile β-lactamases. Clin Microbiol Rev. 2007;20(3):440-458. doi:10.1128/CMR.00001-07

47. Paterson DL, Bonomo RA. Extended-spectrum β-lactamases: a clinical update. Clin Microbiol Rev. 2005;18(4):657-686. doi:10.1128/CMR.18.4.657-686.2005

48. Bush K, Bradford PA. Epidemiology of β-lactamase-producing pathogens. Clin Microbiol Rev. 2020;33(2):e00047-19. doi:10.1128/CMR.00047-19

49. Peacock SJ, Paterson GK. Mechanisms of methicillin resistance in Staphylococcus aureus. Annu Rev Biochem. 2015;84(1):577-601. doi:10.1146/annurev-biochem-060614-034516

50. Hooper DC, Jacoby GA. Mechanisms of drug resistance: quinolone resistance. Ann N Y Acad Sci. 2015;1354(1):12-31. doi:10.1111/nyas.12830

51. Vasala A, Hytönen VP, Laitinen OH. Modern tools for rapid diagnostics of antimicrobial resistance. Front Cell Infect Microbiol. 2020;10:308. doi:10.3389/fcimb.2020.00308

52. Global Action Plan on Antimicrobial Resistance. World Health Organization; 2015.

53. Rapid Diagnostics: Stopping Unnecessary Use of Antibiotics. Review on Antimicrobial Resistance; 2015.

54. Schmitz JE, Stratton CW, Persing DH, Tang YW. Forty years of molecular diagnostics for infectious diseases. J Clin Microbiol. 2022;60(10):e02446-21. doi:10.1128/jcm.02446-21

55. Yang S, Rothman RE. PCR-based diagnostics for infectious diseases: uses, limitations, and future applications in acute-care settings. Lancet Infect Dis. 2004;4(6):337-348. doi:10.1016/S1473-3099(04)01044-8

56. Adams G. A beginner's guide to RT-PCR, qPCR and RT-qPCR. Biochem (Lond). 2020;42(3):48-53. doi:10.1042/BIO20200034

57. Diao Z, Han D, Zhang R, Li J. Metagenomics next-generation sequencing tests take the stage in the diagnosis of lower respiratory tract infections. J Adv Res. 2022;38:201-212. doi:10.1016/j.jare.2021.09.012

58. Chiu CY, Miller SA. Clinical metagenomics. Nat Rev Genet. 2019;20(6):341-355. doi:10.1038/s41576-019-0113-7

59. Koczula KM, Gallotta A. Lateral flow assays. Essays Biochem. 2016;60(1):111-120. doi:10.1042/EBC20150012

60. Liu Y, Zhan L, Qin Z, Sackrison J, Bischof JC. Ultrasensitive and highly specific lateral flow assays for point-of-care diagnosis. ACS Nano. 2021;15(3):3593-3611. doi:10.1021/acsnano.0c10035

61. Espejo AP, Akgun Y, Al Mana AF, et al. Review of current advances in serologic testing for COVID-19. Am J Clin Pathol. 2020;154(3):293-304. doi:10.1093/ajcp/aqaa112

62. Khan ZA, Siddiqui MF, Park S. Current and emerging methods of antibiotic susceptibility testing. Diagnostics (Basel). 2019;9(2):49. doi:10.3390/diagnostics9020049

63. Singhal N, Kumar M, Kanaujia PK, Virdi JS. MALDI-TOF mass spectrometry: an emerging technology for microbial identification and diagnosis. Front Microbiol. 2015;6:791. doi:10.3389/fmicb.2015.00791

64. Lagier JC, Edouard S, Pagnier I, Mediannikov O, Drancourt M, Raoult D. Current and past strategies for bacterial culture in clinical microbiology. Clin Microbiol Rev. 2015;28(1):208-236. doi:10.1128/CMR.00110-14

65. Oliver JD. Recent findings on the viable but nonculturable state in pathogenic bacteria. FEMS Microbiol Rev. 2010;34(4):415-425. doi:10.1111/j.1574-6976.2009.00200.x

66. Tacconelli E, Carrara E, Savoldi A, et al. Discovery, research, and development of new antibiotics: the WHO priority list of antibiotic-resistant bacteria and tuberculosis. Lancet Infect Dis. 2018;18(3):318-327. doi:10.1016/S1473-3099(17)30753-3

67. Soler M, Huertas CS, Lechuga LM. Label-free plasmonic biosensors for point-of-care diagnostics: a review. Expert Rev Mol Diagn. 2019;19(1):71-81. doi:10.1080/14737159.2019.1554435

68. Thévenot DR, Toth K, Durst RA, Wilson GS. Electrochemical biosensors: recommended definitions and classification. Biosens Bioelectron. 2001;16(1-2):121-131. doi:10.1016/S0956-5663(01)00115-4

69. Soler M, Lechuga LM. Label-free photonic biosensors: key technologies for precision diagnostics. ChemistryEurope. 2025;3(4):e202400106. doi:10.1002/ceur.202400106

70. Morales MA, Halpern JM. Guide to selecting a biorecognition element for biosensors. Bioconjug Chem. 2018;29(10):3231-3239. doi:10.1021/acs.bioconjchem.8b00592

71. Soler M, Estevez MC, Cardenosa-Rubio M, Astua A, Lechuga LM. How nanophotonic label-free biosensors can contribute to rapid and massive diagnostics of respiratory virus infections: COVID-19 case. ACS Sens. 2020;5(9):2663-2678. doi:10.1021/acssensors.0c01180

72. Estevez MC, Otte MA, Sepulveda B, Lechuga LM. Trends and challenges of refractometric nanoplasmonic biosensors: a review. Anal Chim Acta. 2014;806:55-73. doi:10.1016/j.aca.2013.10.048

73. Soler M, Lechuga LM. Biochemistry strategies for label-free optical sensor biofunctionalization: advances towards real applicability. Anal Bioanal Chem. 2022;414(18):5071-5085. doi:10.1007/s00216-021-03751-4

74. Estevez MC, Alvarez M, Lechuga LM. Integrated optical devices for lab-on-a-chip biosensing applications. Laser Photonics Rev. 2012;6(4):463-487. doi:10.1002/lpor.201100025

75. Homola J. Surface plasmon resonance sensors for detection of chemical and biological species. Chem Rev. 2008;108(2):462-493. doi:10.1021/cr068107d

76. Cooper MA. Label-free screening of bio-molecular interactions. Anal Bioanal Chem. 2003;377(5):834-842. doi:10.1007/s00216-003-2111-y

77. Soler M, Lechuga LM. Principles, technologies, and applications of plasmonic biosensors. J Appl Phys. 2021;129(11):111102. doi:10.1063/5.0042811

78. Yu H, Peng Y, Yang Y, Li ZY. Plasmon-enhanced light–matter interactions and applications. npj Comput Mater. 2019;5(1):45. doi:10.1038/s41524-019-0184-1

79. Homola J, Yee SS, Gauglitz G. Surface plasmon resonance sensors: review. Sens Actuators B Chem. 1999;54(1-2):3-15. doi:10.1016/S0925-4005(98)00321-9

80. Kretschmann E, Raether H. Notizen: radiative decay of non radiative surface plasmons excited by light. Z Naturforsch A. 1968;23(12):2135-2136. doi:10.1515/zna-1968-1247

81. González-Guerrero AB, Maldonado J, Herranz S, Lechuga LM. Trends in photonic lab-on-chip interferometric biosensors for point-of-care diagnostics. Anal Methods. 2016;8(48):8380-8394. doi:10.1039/C6AY02972H

82. Olaru A, Bala C, Jaffrezic-Renault N, Aboul-Enein HY. Surface plasmon resonance (SPR) biosensors in pharmaceutical analysis. Crit Rev Anal Chem. 2015;45(2):97-105. doi:10.1080/10408347.2014.881250

83. Kumbhat S, Sharma K, Gehlot R, Solanki A, Joshi V. Surface plasmon resonance based immunosensor for serological diagnosis of dengue virus infection. J Pharm Biomed Anal. 2010;52(2):255-259. doi:10.1016/j.jpba.2010.01.001

84. Soler M, Belushkin A, Cavallini A, Kebbi-Beghdadi C, Greub G, Altug H. Multiplexed nanoplasmonic biosensor for one-step simultaneous detection of Chlamydia trachomatis

and Neisseria gonorrhoeae in urine. Biosens Bioelectron. 2017;94:560-567. doi:10.1016/j.bios.2017.03.047

85. Peláez EC, Estevez MC, Mongui A, et al. Detection and quantification of HspX antigen in sputum samples using plasmonic biosensing: toward a real point-of-care (POC) for tuberculosis diagnosis. ACS Infect Dis. 2020;6(5):1110-1120. doi:10.1021/acsinfecdis.9b00502

86. Calvo-Lozano O, Aviñó A, Friaza V, et al. Fast and accurate Pneumocystis pneumonia diagnosis in human samples using a label-free plasmonic biosensor. Nanomaterials (Basel). 2020;10(6):1246. doi:10.3390/nano10061246

87. Ghosh N, Gupta G, Boopathi M, et al. Surface plasmon resonance biosensor for detection of Bacillus anthracis, the causative agent of anthrax from soil samples targeting protective antigen. Indian J Microbiol. 2013;53(1):48-55. doi:10.1007/s12088-012-0334-3

88. Riedel T, Rodriguez-Emmenegger C, de los Santos Pereira A, et al. Diagnosis of Epstein-Barr virus infection in clinical serum samples by an SPR biosensor assay. Biosens Bioelectron. 2014;55:278-284. doi:10.1016/j.bios.2013.12.011

89. Mauriz E, Calle A, Manclús JJ, et al. Optical immunosensor for fast and sensitive detection of DDT and related compounds in river water samples. Biosens Bioelectron. 2007;22(7):1410-1418. doi:10.1016/j.bios.2006.06.016

90. Ramirez-Priego P, Mauriz E, Giarola JF, Lechuga LM. Overcoming challenges in plasmonic biosensors deployment for clinical and biomedical applications: a systematic review and meta-analysis. Sens Biosensing Res. 2024;46:100717. doi:10.1016/j.sbsr.2024.100717

91. Fernández Gavela A, Grajales García D, Ramirez J, Lechuga L. Last advances in silicon-based optical biosensors. Sensors (Basel). 2016;16(3):285. doi:10.3390/s16030285

92. Luan E, Shoman H, Ratner DM, Cheung KC, Chrostowski L. Silicon photonic biosensors using label-free detection. Sensors (Basel). 2018;18(10):3519. doi:10.3390/s18103519

93. Fan X, White IM, Shopova SI, Zhu H, Suter JD, Sun Y. Sensitive optical biosensors for unlabeled targets: a review. Anal Chim Acta. 2008;620(1-2):8-26. doi:10.1016/j.aca.2008.05.022

94. Ramirez-Priego P, Alonso-Fernández A, Soler M, Lechuga LM. Silicon photonic biosensors in clinical diagnostics: emerging opportunities and challenges. Annu Rev Biomed Eng. Published online January 13, 2026. doi:10.1146/annurev-bioeng-103023-030143

95. Iqbal M, Gleeson MA, Spaugh B, et al. Label-free biosensor arrays based on silicon ring resonators and high-speed optical scanning instrumentation. IEEE J Sel Top Quantum Electron. 2010;16(3):654-661. doi:10.1109/JSTQE.2009.2032510

96. Prieto F, Sepúlveda B, Calle A, et al. An integrated optical interferometric nanodevice based on silicon technology for biosensor applications. Nanotechnology. 2003;14(8):907-912. doi:10.1088/0957-4484/14/8/312

97. Zinoviev KE, González-Guerrero AB, Domínguez C, Lechuga LM. Integrated bimodal waveguide interferometric biosensor for label-free analysis. J Lightwave Technol. 2011;29(13):1926-1930. doi:10.1109/JLT.2011.2150734

98. Domínguez Horna C, Zinoviev K, Lechuga Gómez LM. Interferometer and Sensor Based on Bimodal Optical Waveguides, and Detection Method. US patent 8279445 B2. October 2, 2012.

99. Torrijos-Morán L, Lisboa BD, Soler M, Lechuga LM, García-Rupérez J. Integrated optical bimodal waveguide biosensors: principles and applications. Results Opt. 2022;9:100285. doi:10.1016/j.rio.2022.100285

100. Calvo Lozano O. Nanophotonic Point-of-Care Biosensors for Innovative Clinical Diagnosis of Respiratory Diseases. Dissertation. Universitat Autònoma de Barcelona; 2022.

101. Bassols-Cornudella B, Ramirez-Priego P, Soler M, et al. Novel sensing algorithm for linear read-out of bimodal waveguide interferometric biosensors. J Lightwave Technol. 2022;40(1):237-244. doi:10.1109/jlt.2021.3118103

102. Grajales García D. Lab-on-a-Chip Integration of the Bimodal Waveguide Nanointerferometric Biosensor. Dissertation. Universitat Autònoma de Barcelona; 2012.

103. Leys C, Ley C, Klein O, Bernard P, Licata L. Detecting outliers: do not use standard deviation around the mean, use absolute deviation around the median. J Exp Soc Psychol. 2013;49(4):764-766. doi:10.1016/j.jesp.2013.03.013

104. Sassolas A, Leca-Bouvier BD, Blum LJ. DNA biosensors and microarrays. Chem Rev. 2008;108(1):109-139. doi:10.1021/cr0684467

105. Huertas CS, Calvo-Lozano O, Mitchell A, Lechuga LM. Advanced evanescent-wave optical biosensors for the detection of nucleic acids: an analytic perspective. Front Chem. 2019;7:724. doi:10.3389/fchem.2019.00724

106. SantaLucia J, Hicks D. The thermodynamics of DNA structural motifs. Annu Rev Biophys Biomol Struct. 2004;33(1):415-440. doi:10.1146/annurev.biophys.32.110601.141800

107. Huertas CS. Nanophotonic Biosensors for Deciphering Cell Regulation Pathways. Dissertation. Universitat Autònoma de Barcelona; 2016.

108. Peterson AW. The effect of surface probe density on DNA hybridization. Nucleic Acids Res. 2001;29(24):5163-5168. doi:10.1093/nar/29.24.5163

109. Kim S, Im J, Wang SX, Lee JR. Design and validation of specific oligonucleotide probes on planar magnetic biosensors. Anal Chem. 2024;96(49):19447-19455. doi:10.1021/acs.analchem.4c03973

110. Cholko T, Chang C. Modeling effects of surface properties and probe density for nanoscale biosensor design: a case study of DNA hybridization near surfaces. J Phys Chem B. 2021;125(7):1746-1754. doi:10.1021/acs.jpcb.0c09723

111. Kavand A, Robin P, Mayoraz L, Mensi M, Gerber-Lemaire S. Achieving high hybridization density at DNA biosensor surfaces using branched spacer and click chemistry. RSC Adv. 2023;13(48):34003-34011. doi:10.1039/D3RA04928K

112. Kimura-Suda H, Petrovykh DY, Tarlov MJ, Whitman LJ. Base-dependent competitive adsorption of single-stranded DNA on gold. J Am Chem Soc. 2003;125(30):9014-9015. doi:10.1021/ja035756n

113. Ravan H, Kashanian S, Sanadgol N, Badoei-Dalfard A, Karami Z. Strategies for optimizing DNA hybridization on surfaces. Anal Biochem. 2014;444:41-46. doi:10.1016/j.ab.2013.09.032

114. Dallaire AM, Patskovsky S, Vallée-Bélisle A, Meunier M. Electrochemical plasmonic sensing system for highly selective multiplexed detection of biomolecules based on redox nanoswitches. Biosens Bioelectron. 2015;71:75-81. doi:10.1016/j.bios.2015.04.011

115. Huertas CS, Soler M, Estevez MC, Lechuga LM. One-step immobilization of antibodies and DNA on gold sensor surfaces via a poly-adenine oligonucleotide approach. Anal Chem. 2020;92(18):12596-12604. doi:10.1021/acs.analchem.0c02619

116. Maldonado J, Estévez MC, Fernández-Gavela A, González-López JJ, González-Guerrero AB, Lechuga LM. Label-free detection of nosocomial bacteria using a nanophotonic interferometric biosensor. Analyst. 2020;145(2):497-506. doi:10.1039/C9AN01485C

117. Ramirez-Priego P, Estévez MC, Díaz-Luisravelo HJ, Manclús JJ, Montoya Á, Lechuga LM. Real-time monitoring of fenitrothion in water samples using a silicon nanophotonic biosensor. Anal Chim Acta. 2021;1152:338276. doi:10.1016/j.aca.2021.338276

118. Ruiz-Vega G, Soler M, Estevez MC, et al. Rapid and direct quantification of the SARS-CoV-2 virus with an ultrasensitive nanobody-based photonic nanosensor. Sens Diagn. 2022;1(5):983-993. doi:10.1039/D2SD00082B

119. Wickramathilaka MP, Tao BY. Characterization of covalent crosslinking strategies for synthesizing DNA-based bioconjugates. J Biol Eng. 2019;13(1):63. doi:10.1186/s13036-019-0191-2

120. Huertas CS, Domínguez-Zotes S, Lechuga LM. Analysis of alternative splicing events for cancer diagnosis using a multiplexing nanophotonic biosensor. Sci Rep. 2017;7(1):41368. doi:10.1038/srep41368

121. Green NM. Avidin. 1. The use of [14C]biotin for kinetic studies and for assay. Biochem J. 1963;89(3):585-591. doi:10.1042/bj0890585

122. Kamperman T, Koerselman M, Kelder C, et al. Spatiotemporal material functionalization via competitive supramolecular complexation of avidin and biotin analogs. Nat Commun. 2019;10(1):4347. doi:10.1038/s41467-019-12390-4

123. Fuchs J, Dell'Atti D, Buhot A, Calemczuk R, Mascini M, Livache T. Effects of formamide on the thermal stability of DNA duplexes on biochips. Anal Biochem. 2010;397(1):132-134. doi:10.1016/j.ab.2009.09.044

124. Calvo-Lozano O, García-Aparicio P, Raduly LZ, et al. One-step and real-time detection of microRNA-21 in human samples for lung cancer biosensing diagnosis. Anal Chem. 2022;94(42):14659-14665. doi:10.1021/acs.analchem.2c02895

125. Huertas CS, Fariña D, Lechuga LM. Direct and label-free quantification of microRNA-181a at attomolar level in complex media using a nanophotonic biosensor. ACS Sens. 2016;1(6):748-756. doi:10.1021/acssensors.6b00162

126. Antoniou M, Tsounidi D, Petrou PS, Beltsios KG, Kakabakos SE. Functionalization of silicon dioxide and silicon nitride surfaces with aminosilanes for optical biosensing applications. Med Devices Sens. 2020;3(5):e10072. doi:10.1002/mds3.10072

127. Sypabekova M, Hagemann A, Rho D, Kim S. Review: 3-aminopropyltriethoxysilane (APTES) deposition methods on oxide surfaces in solution and vapor phases for biosensing applications. Biosensors (Basel). 2023;13(1):36. doi:10.3390/bios13010036

128. Yadav AR, Sriram R, Carter JA, Miller BL. Comparative study of solution-phase and vapor-phase deposition of aminosilanes on silicon dioxide surfaces. Mater Sci Eng C. 2014;35:283-290. doi:10.1016/j.msec.2013.11.017

129. Fiorilli S, Rivolo P, Descrovi E, et al. Vapor-phase self-assembled monolayers of aminosilane on plasma-activated silicon substrates. J Colloid Interface Sci. 2008;321(1):235-241. doi:10.1016/j.jcis.2007.12.041

130. Karakoy M, Gultepe E, Pandey S, Khashab MA, Gracias DH. Silane surface modification for improved bioadhesion of esophageal stents. Appl Surf Sci. 2014;311:684-689. doi:10.1016/j.apsusc.2014.05.136

131. Wetmur JG. DNA probes: applications of the principles of nucleic acid hybridization. Crit Rev Biochem Mol Biol. 1991;26(3-4):227-259. doi:10.3109/10409239109114069

132. Owczarzy R, You Y, Moreira BG, et al. Effects of sodium ions on DNA duplex oligomers: improved predictions of melting temperatures. Biochemistry. 2004;43(12):3537-3554. doi:10.1021/bi034621r

133. Blake R. Thermodynamic effects of formamide on DNA stability. Nucleic Acids Res. 1996;24(11):2095-2103. doi:10.1093/nar/24.11.2095

134. Wood WI, Gitschier J, Lasky LA, Lawn RM. Base composition-independent hybridization in tetramethylammonium chloride: a method for oligonucleotide screening of

highly complex gene libraries. Proc Natl Acad Sci U S A. 1985;82(6):1585-1588. doi:10.1073/pnas.82.6.1585

135. Serra-Cobo J, Frutos R. Pandemics: the challenge of the twenty-first century. In: Núñez-Delgado A, ed. Planet Earth: Scientific Proposals to Solve Urgent Issues. Springer International Publishing; 2024:7-23. doi:10.1007/978-3-031-53208-5_2

136. Meurens F, Dunoyer C, Fourichon C, et al. Animal board invited review: risks of zoonotic disease emergence at the interface of wildlife and livestock systems. Animal. 2021;15(6):100241. doi:10.1016/j.animal.2021.100241

137. Miłek J, Blicharz-Domańska K. Coronaviruses in avian species – review with focus on epidemiology and diagnosis in wild birds. J Vet Res. 2018;62(3):249-255. doi:10.2478/jvetres-2018-0035

138. Woo PCY, Lau SKP, Lam CSF, et al. Discovery of seven novel mammalian and avian coronaviruses in the genus Deltacoronavirus supports bat coronaviruses as the gene source of Alphacoronavirus and Betacoronavirus and avian coronaviruses as the gene source of Gammacoronavirus and Deltacoronavirus. J Virol. 2012;86(7):3995-4008. doi:10.1128/JVI.06540-11

139. Compton SR. Overview of coronaviruses in veterinary medicine. Comp Med. 2021;71(5):333-341. doi:10.30802/AALAS-CM-21-000007

140. Family: Coronaviridae. International Committee on Taxonomy of Viruses; 2024.

141. Kirchdoerfer RN, Ward AB. Structure of the SARS-CoV nsp12 polymerase bound to nsp7 and nsp8 co-factors. Nat Commun. 2019;10(1):2342. doi:10.1038/s41467-019-10280-3

142. Callison SA, Hilt DA, Boynton TO, et al. Development and evaluation of a real-time Taqman RT-PCR assay for the detection of infectious bronchitis virus from infected chickens. J Virol Methods. 2006;138(1-2):60-65. doi:10.1016/j.jviromet.2006.07.018

143. Ar Gouilh M, Puechmaille SJ, Diancourt L, et al. SARS-CoV related Betacoronavirus and diverse Alphacoronavirus members found in western old-world. Virology. 2018;517:88-97. doi:10.1016/j.virol.2018.01.014

144. Corman VM, Landt O, Kaiser M, et al. Detection of 2019 novel coronavirus (2019-nCoV) by real-time RT-PCR. Euro Surveill. 2020;25(3):2000045. doi:10.2807/1560-7917.ES.2020.25.3.2000045

145. Lu X, Wang L, Sakthivel SK, et al. US CDC real-time reverse transcription PCR panel for detection of severe acute respiratory syndrome coronavirus 2. Emerg Infect Dis. 2020;26(8):1654-1665. doi:10.3201/eid2608.201246

146. Kang T, Lu J, Yu T, Long Y, Liu G. Advances in nucleic acid amplification techniques (NAATs): COVID-19 point-of-care diagnostics as an example. Biosens Bioelectron. 2022;206:114109. doi:10.1016/j.bios.2022.114109

147. Hoffmann B, Beer M, Reid SM, et al. A review of RT-PCR technologies used in veterinary virology and disease control: sensitive and specific diagnosis of five livestock diseases notifiable to the World Organisation for Animal Health. Vet Microbiol. 2009;139(1-2):1-23. doi:10.1016/j.vetmic.2009.04.034

148. Calvo-Lozano O, Sierra M, Soler M, et al. Label-free plasmonic biosensor for rapid, quantitative, and highly sensitive COVID-19 serology: implementation and clinical validation. Anal Chem. 2022;94(2):975-984. doi:10.1021/acs.analchem.1c03850

149. Giarola JF, Soler M, Estevez MC, et al. Validation of a plasmonic-based serology biosensor for veterinary diagnosis of COVID-19 in domestic animals. Talanta. 2024;271:125685. doi:10.1016/j.talanta.2024.125685

150. Vicenti I, Zazzi M, Saladini F. SARS-CoV-2 RNA-dependent RNA polymerase as a therapeutic target for COVID-19. Expert Opin Ther Pat. 2021;31(4):325-337. doi:10.1080/13543776.2021.1880568

151. Markov PV, Ghafari M, Beer M, et al. The evolution of SARS-CoV-2. Nat Rev Microbiol. 2023;21(6):361-379. doi:10.1038/s41579-023-00878-2

152. Monchatre-Leroy E, Boué F, Boucher JM, et al. Identification of Alpha and Beta coronavirus in wildlife species in France: bats, rodents, rabbits, and hedgehogs. Viruses. 2017;9(12):364. doi:10.3390/v9120364

153. Jelinek HF, Mousa M, Alefishat E, et al. Evolution, ecology, and zoonotic transmission of betacoronaviruses: a review. Front Vet Sci. 2021;8:644414. doi:10.3389/fvets.2021.644414

154. Reijns MAM, Thompson L, Acosta JC, et al. A sensitive and affordable multiplex RT-qPCR assay for SARS-CoV-2 detection. PLoS Biol. 2020;18(12):e3001030. doi:10.1371/journal.pbio.3001030

155. Qiu G, Gai Z, Tao Y, Schmitt J, Kullak-Ublick GA, Wang J. Dual-functional plasmonic photothermal biosensors for highly accurate severe acute respiratory syndrome coronavirus 2 detection. ACS Nano. 2020;14(5):5268-5277. doi:10.1021/acsnano.0c02439

156. Chang S, Liu L, Mu C, et al. An ultrasensitive SPR biosensor for RNA detection based on robust GeP5 nanosheets. J Colloid Interface Sci. 2023;651:938-947. doi:10.1016/j.jcis.2023.08.064

157. Arnaout R, Lee RA, Lee GR, et al. The limit of detection matters: the case for benchmarking severe acute respiratory syndrome coronavirus 2 testing. Clin Infect Dis. 2021;73(9):e3042-e3046. doi:10.1093/cid/ciaa1382

158. Holbrook MG, Anthony SJ, Navarrete-Macias I, Bestebroer T, Munster VJ, Van Doremalen N. Updated and validated pan-coronavirus PCR assay to detect all coronavirus genera. Viruses. 2021;13(4):599. doi:10.3390/v13040599

159. Schmieder S, Weißpflog J, Danz N, Klotzbach U, Sonntag F. Detection of miRNA using a surface plasmon resonance biosensor and antibody amplification. Curr Dir Biomed Eng. 2016;2(1):135-138. doi:10.1515/cdbme-2016-0032

160. Boguslawski SJ, Smith DE, Michalak MA, et al. Characterization of monoclonal antibody to DNA·RNA and its application to immunodetection of hybrids. J Immunol Methods. 1986;89(1):123-130. doi:10.1016/0022-1759(86)90040-2

161. Diao W, Tang M, Ding S, et al. Highly sensitive surface plasmon resonance biosensor for the detection of HIV-related DNA based on dynamic and structural DNA nanodevices. Biosens Bioelectron. 2018;100:228-234. doi:10.1016/j.bios.2017.08.042

162. Courtney S, Stromberg Z, Myers y Gutiérrez A, et al. Optical biosensor platforms display varying sensitivity for the direct detection of influenza RNA. Biosensors (Basel). 2021;11(10):367. doi:10.3390/bios11100367

163. Chen Z, Li J, Li T, et al. A CRISPR/Cas12a-empowered surface plasmon resonance platform for rapid and specific diagnosis of the Omicron variant of SARS-CoV-2. Natl Sci Rev. 2022;9(8):nwac104. doi:10.1093/nsr/nwac104

164. Koo B, Jin CE, Lee TY, et al. An isothermal, label-free, and rapid one-step RNA amplification/detection assay for diagnosis of respiratory viral infections. Biosens Bioelectron. 2017;90:187-194. doi:10.1016/j.bios.2016.11.051

165. WHO Bacterial Priority Pathogens List 2024: Bacterial Pathogens of Public Health Importance, to Guide Research, Development, and Strategies to Prevent and Control Antimicrobial Resistance. World Health Organization; 2024.

166. Price MJ, Ades A, Soldan K, et al. The natural history of Chlamydia trachomatis infection in women: a multi-parameter evidence synthesis. Health Technol Assess. 2016;20(22):1-250. doi:10.3310/hta20220

167. Brunham RC, Gottlieb SL, Paavonen J. Pelvic inflammatory disease. N Engl J Med. 2015;372(21):2039-2048. doi:10.1056/NEJMra1411426

168. Sadarangani M, Pollard AJ, Gray-Owen SD. Opa proteins and CEACAMs: pathways of immune engagement for pathogenic Neisseria. FEMS Microbiol Rev. 2011;35(3):498-514. doi:10.1111/j.1574-6976.2010.00260.x

169. AbdelRahman YM, Belland RJ. The chlamydial developmental cycle. FEMS Microbiol Rev. 2005;29(5):949-959. doi:10.1016/j.femsre.2005.03.002

170. Centers for Disease Control and Prevention. Recommendations for the laboratory-based detection of Chlamydia trachomatis and Neisseria gonorrhoeae—2014. MMWR Recomm Rep. 2014;63(RR-02):1-19.

171. Unemo M, Del Rio C, Shafer WM. Antimicrobial resistance expressed by Neisseria gonorrhoeae: a major global public health problem in the 21st century. Microbiol Spectr. 2016;4(3):EI10-0009-2015. doi:10.1128/microbiolspec.EI10-0009-2015

172. Buckley C, Trembizki E, Donovan B, et al. A real-time PCR assay for direct characterization of the Neisseria gonorrhoeae GyrA 91 locus associated with ciprofloxacin susceptibility. J Antimicrob Chemother. 2016;71(2):353-356. doi:10.1093/jac/dkv366

173. Hemarajata P, Yang S, Soge OO, Humphries RM, Klausner JD. Performance and verification of a real-time PCR assay targeting the gyrA gene for prediction of ciprofloxacin resistance in Neisseria gonorrhoeae. J Clin Microbiol. 2016;54(3):805-808. doi:10.1128/JCM.03032-15

174. Allan-Blitz LT, Wang X, Klausner JD. Wild-type gyrase A genotype of Neisseria gonorrhoeae predicts in vitro susceptibility to ciprofloxacin: a systematic review of the literature and meta-analysis. Sex Transm Dis. 2017;44(5):261-265. doi:10.1097/OLQ.0000000000000591

175. Workowski KA, Bachmann LH, Chan PA, et al. Sexually transmitted infections treatment guidelines, 2021. MMWR Recomm Rep. 2021;70(4):1-187. doi:10.15585/mmwr.rr7004a1

176. Unemo M, Ross J, Serwin A, Gomberg M, Cusini M, Jensen J. 2020 European guideline for the diagnosis and treatment of gonorrhoea in adults. Int J STD AIDS. Published online October 29, 2020. doi:10.1177/0956462420949126

177. Astúa A, Estevez MC, Ramírez-Lázaro MJ, Calvet X, Lario S, Lechuga LM. Identification and ultrasensitive quantification of H. pylori infections on gastric and stool human samples with a photonic label-free nanobiosensor. Biosens Bioelectron. 2025;281:117459. doi:10.1016/j.bios.2025.117459

178. Maldonado J, González-Guerrero AB, Fernández-Gavela A, González-López JJ, Lechuga LM. Ultrasensitive label-free detection of unamplified multidrug-resistance bacteria genes with a bimodal waveguide interferometric biosensor. Diagnostics (Basel). 2020;10(10):845. doi:10.3390/diagnostics10100845

179. Geraats-Peters CWM, Brouwers M, Schneeberger PM, et al. Specific and sensitive detection of Neisseria gonorrhoeae in clinical specimens by real-time PCR. J Clin Microbiol. 2005;43(11):5653-5659. doi:10.1128/JCM.43.11.5653-5659.2005

180. Verma R, Sood S, Singh R, et al. Coupling electrochemical response of a DNA biosensor with PCR for Neisseria gonorrhoeae detection. Diagn Microbiol Infect Dis. 2014;78(1):16-23. doi:10.1016/j.diagmicrobio.2013.09.010

181. Sayada C, Denamur E, Orfila J, Catalan F, Elion J. Rapid genotyping of the Chlamydia trachomatis major outer membrane protein by the polymerase chain reaction. FEMS Microbiol Lett. 1991;67(1):73-78. doi:10.1016/0378-1097(91)90447-i

182. Brunelle BW, Sensabaugh GF. The ompA gene in Chlamydia trachomatis differs in phylogeny and rate of evolution from other regions of the genome. Infect Immun. 2006;74(1):578-585. doi:10.1128/IAI.74.1.578-585.2006

183. Stothard DR, Boguslawski G, Jones RB. Phylogenetic analysis of the Chlamydia trachomatis major outer membrane protein and examination of potential pathogenic determinants. Infect Immun. 1998;66(8):3618-3625. doi:10.1128/IAI.66.8.3618-3625.1998

184. Aldred KJ, Kerns RJ, Osheroff N. Mechanism of quinolone action and resistance. Biochemistry. 2014;53(10):1565-1574. doi:10.1021/bi5000564

185. Drlica K, Zhao X. DNA gyrase, topoisomerase IV, and the 4-quinolones. Microbiol Mol Biol Rev. 1997;61(3):377-392. doi:10.1128/mmbr.61.3.377-392.1997

186. Belland RJ, Morrison SG, Ison C, Huang WM. Neisseria gonorrhoeae acquires mutations in analogous regions of gyrA and parC in fluoroquinolone-resistant isolates. Mol Microbiol. 1994;14(2):371-380. doi:10.1111/j.1365-2958.1994.tb01297.x

187. Unemo M, Shafer WM. Antimicrobial resistance in Neisseria gonorrhoeae in the 21st century: past, evolution, and future. Clin Microbiol Rev. 2014;27(3):587-613. doi:10.1128/CMR.00010-14

188. Maldonado J, Estévez MC, Fernández-Gavela A, González-López JJ, González-Guerrero AB, Lechuga LM. Label-free detection of nosocomial bacteria using a nanophotonic interferometric biosensor. Analyst. 2020;145(2):497-506. doi:10.1039/C9AN01485C

189. Sakai J, Maesaki S. A new real-time quantitative polymerase chain reaction method using locked nucleic acids to detect Neisseria gonorrhoeae infection and point mutation on gyrA associated with quinolone susceptibility. J Microbiol Methods. 2022;203:106619. doi:10.1016/j.mimet.2022.106619

190. Kumar R, Sumana G, Choudhary A, Sood S, Rajesh. Liquid crystal assisted optical DNA biosensor for the selective detection of bacterium Neisseria gonorrhoeae. Liq Cryst. 2024;51(5):857-867. doi:10.1080/02678292.2024.2337021

191. Kaur G, Paliwal A, Tomar M, Gupta V. Detection of Neisseria meningitidis using surface plasmon resonance based DNA biosensor. Biosens Bioelectron. 2016;78:106-110. doi:10.1016/j.bios.2015.11.025

192. Joung HA, Lee NR, Lee SK, et al. High sensitivity detection of 16s rRNA using peptide nucleic acid probes and a surface plasmon resonance biosensor. Anal Chim Acta. 2008;630(2):168-173. doi:10.1016/j.aca.2008.10.001

193. Cotton S, McHugh MP, Etherson M, Shepherd J, Templeton KE. Evaluation of the molecular detection of ciprofloxacin resistance in Neisseria gonorrhoeae by the ResistancePlus GC assay (SpeeDx). Diagn Microbiol Infect Dis. 2021;99(4):115262. doi:10.1016/j.diagmicrobio.2020.115262

194. Gaydos CA. Review of use of a new rapid real-time PCR, the Cepheid GeneXpert (Xpert) CT/NG assay, for Chlamydia trachomatis and Neisseria gonorrhoeae: results for patients while in a clinical setting. Expert Rev Mol Diagn. 2014;14(2):135-137. doi:10.1586/14737159.2014.871495

195. Gopal A, Yan L, Kashif S, et al. Biosensors and point-of-care devices for bacterial detection: rapid diagnostics informing antibiotic therapy. Adv Healthc Mater. 2022;11(3):2101546. doi:10.1002/adhm.202101546

196. Batool R, Soler M, Colavita F, Fabeni L, Matusali G, Lechuga LM. Biomimetic nanoplasmonic sensor for rapid evaluation of neutralizing SARS-CoV-2 monoclonal antibodies as antiviral therapy. Biosens Bioelectron. 2023;226:115137. doi:10.1016/j.bios.2023.115137

197. Azadbakht B, Afarideh H, Ghannadi-Maragheh M, Bahrami-Samani A, Asgari M. Preparation and evaluation of APTES-PEG coated iron oxide nanoparticles conjugated to rhenium-188 labeled rituximab. Nucl Med Biol. 2017;48:26-30. doi:10.1016/j.nucmedbio.2016.05.002

198. Saengdee P, Promptmas C, Thanapitak S, et al. Optimization of 3-aminopropyltriethoxysilane functionalization on silicon nitride surface for biomolecule immobilization. Talanta. 2020;207:120305. doi:10.1016/j.talanta.2019.120305

199. Wang L, Qian Y, Sun Y, Liu B, Wei G. Single-molecule force spectroscopy: a facile technique for studying the interactions between biomolecules and materials interfaces. Rev Anal Chem. 2020;39(1):116-129. doi:10.1515/revac-2020-0115

200. Hermanson GT. Bioconjugate Techniques. 3rd ed. Elsevier/Academic Press; 2013.

201. Boutureira O, Bernardes GJL. Advances in chemical protein modification. Chem Rev. 2015;115(5):2174-2195. doi:10.1021/cr500399p

202. Chudasama V, Maruani A, Caddick S. Recent advances in the construction of antibody–drug conjugates. Nat Chem. 2016;8(2):114-119. doi:10.1038/nchem.2415